Near-net shaping of dense ceramics via freeze-casting

By

Samuel Pinches

Oct, 2020

A thesis submitted in total fulfilment of the requirements
of the degree of Doctor of Philosophy

Supervisor: Prof. George Franks

Department of Chemical Engineering

The University of Melbourne

Parkville, Victoria 3010

Australia

Abstract

At present, producing dense complex-shaped ceramic parts require time-consuming and labour intensive processes, that are unsuitable for large-scale mass production. This results in prohibitively expensive part costs, in turn limiting the range of practical applications for complex-shaped dense ceramic materials. With process modifications, the freeze-casting process has potential as a suitable near-net shaping process for this application. In freeze-casting, a well-dispersed suspension of particles, such as a dispersion of ceramic powder in a carrier solvent, is frozen in a mould to produce a solid part. The frozen solvent can then be removed by sublimation in a freeze dryer, to produce a ceramic green body. Sintering this part enables us to produce a dense ceramic part retaining the shape of the mould.

Current research in the field of freeze-casting elsewhere is primarily focused on tailoring the freezing process, to create solvent-crystals of various morphologies, for use as pore-forming templates in the production of highly porous components. In this thesis, freeze-casting was performed with highly loaded non-aqueous alumina ceramic suspensions, primarily with submicron alumina in cyclohexane carrier solvent, with the end-goal of producing dense ceramic components. Previous progress in this research area has been hindered by the samples exhibiting severe internal cracking.

In this thesis the mechanisms and key factors responsible were identified for crack formation within samples, and applied this new understanding to explore selected avenues for mitigating the formation of cracks through changes to the process and to the suspension composition. In this work, the role of each of the primary freeze-casting process steps (freezing, freeze-drying and pressureless sintering) were systematically explored relating to both microstructure development and crack formation. A range of techniques were used to examine internal sample microstructures, including micro computed-tomography (micro-CT) and SEM imaging, with specific attention being given to the effects of freeze-drying conditions on samples.

The key conclusions are as follows. By performing dense freeze-casting with highly loaded suspension, and by maximising the freezing rate (using pre-chilled moulds to minimise the templated pore size), it was demonstrated that dense and complex-shaped objects can be formed via this process. The formation of undesirable internal cracks in this process was identified and proven to occur during the freeze-drying step, with cracks being absent in the frozen state, and present prior to sintering. It was found that the rate of sublimation drying influences both the distribution and configuration of the crack network, with fast drying rates (rapid sublimation under vacuum) resulting in both external radial ‘spoke’ cracking and internal discontinuous cracking, while slow drying rates (self-sublimation of samples in a freezer at ambient pressure) resulted in ‘onion-like’ concentric ring cracks. While cracks occur during drying, it was identified that the development of cracks occurs towards the start of drying, and significantly, that crack development occurs independently to the progress of drying and solvent removal. Addition of an acrylic binder to the suspension was shown to significantly increase the mechanical green body strength, and this reduced but did not eliminate cracks. With regards to crack mitigation, the combination of both using slow drying rates, and adding an acrylic binder to the suspension, was demonstrated to successfully mitigate crack formation. Finally, the use of cyclooctane as an alternative carrier solvent also resulted in reduced cracking, confirming that the solvent selection is integral to the effectiveness of the dense freeze-casting process.

In this way, the viability of a dense freeze-casting process for rapid production of complex shaped ceramic components was critically evaluated, and potential limitations of this process were identified and considered.

Summary Table of Contents

Table of Contents

List of figures

Statement

This is to certify that:

I. the thesis comprises only my original work towards the PhD,
II. due acknowledgement has been made in the text to all other materials used,
III. the thesis is less than 100,000 words in length, exclusive of tables, figures, bibliographies and appendices.

Samuel Pinches
October 2020

Acknowledgement

This thesis has been by far the greatest challenge in my life, and it certainly would not have been possible on my own abilities alone.

Firstly, my sincere thanks go to my PhD supervisors, Prof. George V. Franks, and Dr Carolina Tallon for their expertise and assistance throughout this project. Your generosity with your time, you care with providing considered and insightful feedback, and your patience and encouragement throughout, have all been invaluable and deeply appreciated. I am so grateful and fortunate to have had your support, and there is much that I have learned under your guidance.

I am grateful to the University of Melbourne, and the Australian Research Council, for the provision of funding and resources that have enabled this research to be possible.

Thank you to the community that has supported me during this time; I am especially grateful to Dr Silvia Leo for laying the foundations of this work and showing me the ropes with freeze-casting, to Laura Jukes for her generous help in the lab and much encouragement, and to Dr Catherine Sutton for your time and careful feedback. Special thanks go to Dr Mitchell Sesso for being an encouraging friend and wise sounding board, and for putting up with my terrible sense of humour in the office. Thanks to all the members of the ceramics and mineral processing group immensely for your roles in this project. Thanks also go to Oktay Balkis and the staff from the Engineering workshop, for their technical support and fabrication skills. To Dr Jay Black, thank you for your time, expertise and care with Micro-CT analysis, which was a critical instrument for the success of this project. I would also like to express thanks and gratitude to my PhD committee, for their careful and critical feedback that has shaped the project and guided it to completion.

To my mum and my brother, thank you deeply for your continual care, support, and encouragement over many years of this journey. Finally, I give thanks to my heavenly father for the opportunities that I have been blessed with, and for the inexhaustible wonders that I have had the privilege to examine for the past six years.

1 Introduction

The rapid growth of research in material science has resulted in a proliferation of new materials via unique and novel processes, that are in turn enabling new applications and opening the door to new and innovative products. In high-value applications, components with complex shapes are frequently found, and a key engineering challenge is to find suitable processes for shaping materials, that meet the requirements for mass production; namely low time and cost. For this reason, it is a requirement that new processing techniques are explored alongside the development of new materials.

For ceramic materials, there has been an absence of processes that are suitable for mass-producing dense complex shaped ceramic components. The purpose of this project is to explore the suitability of the freeze-casting process for this application, continuing on from the foundational work of Dr Silvia Leo in the area of shaping processes, producing dense ceramic components via colloidal processing techniques[1]. While freeze-casting technology has been thoroughly explored in the literature for producing porous ceramic components[2–9], Dr Leo's work successfully demonstrated the shaping of dense ceramic components via freeze-casting. However, it was identified that the dense samples that were produced featured significant internal defects.

The goal of this project, therefore, is to continue to investigate dense freeze-casting for the production of complex-shaped dense ceramics, and to uncover the primary factors responsible for achieving both micro- and macro-structural control, including identification of the cause of internal cracking. Finally, where possible, the knowledge gained should be applied towards the eliminating or mitigation of cracks and other internal sample defects, with the end goal of either demonstrating the production of high-quality complex shaped ceramic components, or otherwise identifying limitations of the dense freeze-casting process for this purpose.

The primary project objectives are introduced in detail in chapter 3.

2 Literature Review

The purpose of this project is seeking to find a new process to enable ceramics to be formed into complex shapes ready for use with minimal finishing ("near-net-shape"). The intention is to examine if this can be potentially achieved using a freeze-casting process to produce dense, near-net-shape ceramic pieces.

This project, though it has different primary objectives, follows on from Dr Silvia Leo's research efforts investigating the near-net shaping of advanced ceramics. Her work included an investigation of freeze-casting for this purpose. The research scope in this thesis is different, with a concentrated focus freeze-casting specifically, and on understanding the details of each step in the freeze-casting process. For this chapter, a new literature review has been prepared, to enable a deeper look at the theory and mechanisms behind each of the process steps involved in freeze-casting.

2.1 Material Processing

2.1.1 Applications for Advanced Ceramic Materials

The material family considered to be 'ceramics' encompasses a broad range of materials. The term is commonly associated with traditional ceramics, such as sanitaryware, whitewares, and structural clay-based products. However, the term extends far beyond this, encompassing glasses, refractories, as well a range of materials classified as 'advanced ceramics'. In direct contrast with earthenware goods that often are present in ancient archaeological finds, advanced ceramics are a far more recent innovation, and are considered to have been developed approximately within the last century alone[10]. Advanced ceramics are typically distinguished from other materials by the rare or highly application-specific combinations of properties they offer, including high compressive strength, extreme hardness, resistance to high temperatures, and resistance to corrosive chemicals[11]. It is often that when referring to material selection charts (as shown below), while metals may be generally 'good' for a broad range of applications, ceramics are often featured at the extreme limits of performance. It is often the rare combinations of high-performance properties that these materials can offer, that results in them being well suited for specialised applications, such as in electronics, aerospace, chemical processing, or medical devices. Continual innovation across these fields consistently results in ever greater performance requirements being demanded of their materials, and it innovation in ceramics materials have enabled many recent developments, such as fluoride glasses for extreme optics[12], or gallium nitride for power efficient energy conversion[13].

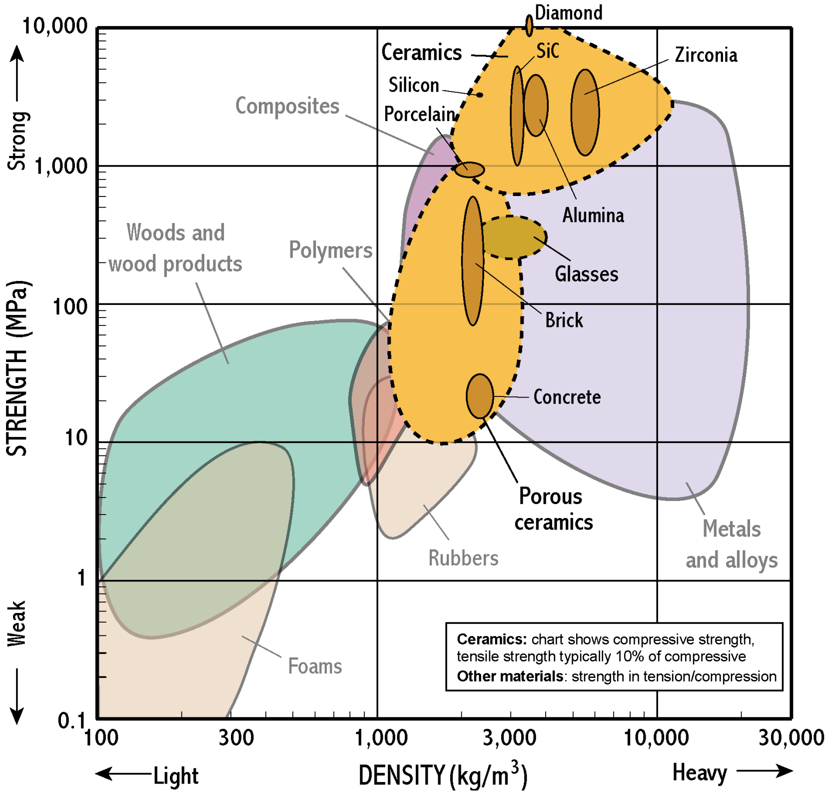

Figure 2.1.a: Material selection, indicating the high compressive strength generally possessed by Ceramics, at lower density than some metals. The family of ceramic materials are highlighted in yellow[14].

2.1.2 Introduction to Materials Shaping

Continual research into material science continues to result in new materials possessing unique combinations of properties, that have potential to enable new possibilities for designers and engineers. However, without the availability of suitable processes for working with and shaping these materials, the use of these materials becomes critically halted.

The importance of materials shaping has continued to grow in importance in modern production processes. A recent example of the significance of material shaping capabilities can be observed in the trend towards “unibody” construction in many products, where multiple parts, screws and assemblies are integrated into a single part, that not only provides the same mechanical functions, whilst also providing superior component strength alongside a reduction in the overall component weight. This trend has been especially evident in high value products where strength to weight ratio is a priority, as seen in carbon-fibre composite exotic sports cars and racing bicycles. More recently, this trend has begun to carry over to mainstream products, with the emergence of flagship smartphones and ultraportable laptops incorporating unibody designs machined from aluminium blocks.

Figure 2.1.b: Complex shaping is required to produce these unibody laptop[15] and smartphones components[16].

Whilst using a unibody construction results in a reduced part count, it simultaneously significantly increases the shape complexity of parts. The ability to produce such complex-shaped parts, is only possible when specialised materials are available alongside compatible complex shaping techniques. With exception to certain industries (such as defence) and some exceptionally large corporations (such as Apple[17]), the broader availability of these products is further challenged by the requirement for processes to be suitable for practical mass production, where consideration must be given to concerns of cost, yield, energy, labour, equipment and lead-time.

To date, the commercial use of advanced ceramics in novel high-performance mass-produced applications has been hindered by a lack of suitable shaping techniques. This is not to say that no processes exist; rather that the shaping techniques used by other materials are generally unsuitable or far from ideal for use for ceramics, and the existing shaping techniques that are available are either too expensive for mass production, or unable to produce the complex component shapes required for advanced applications. For example, while casting processes can be used to produce steel or aluminium components, many ceramics have very high melting points, and may oxidise at high temperatures; for these and other reasons, alternative processes are typically used for producing shaped ceramic components[18]. One commercial example of a mass produced complex shaped ceramic component can be found in the Apple Watch. In 2016, Apple produced a special version of their Apple Watch featuring a white ceramic Yttria-sensitized Zirconia case, for toughness and scratch resistance[19, 20]. This case was formed by a multi-step processing operation, including powder dry-pressing with binder, hot isostatic pressed (HIP) to sinter and densify, followed by 6-hours of diamond machining and polishing steps to achieve the finished watch body. While the final product is both complex in shape and produced to a high standard, the overall device cost is three times the price as the same identical product available in an aluminium housing.

Figure 2.1.c: Manufacturing of the Apple Watch Ceramic Edition involved production of multiple complex shaped ceramic components, includes the body, buttons, and dial. [19]

Even though this increase in price may will not directly represent the additional manufacturing cost incurred by Apple in making a luxury product, this kind of extensive machining time required per part would be cost-prohibitive for most other mass-produced applications. It is desirable to find a process alternative that can produce a complex shaped part without machining, or at a minimum, a process able to produce a **near-net shaped part** that requires minimal manufacturing effort to finish for its final commercial use.

2.1.3 Ceramic Shaping Processes

From a comprehensive perspective, the production of advanced ceramic components is possible by a broad range of techniques [21–23]. However, many of these techniques are hindered by limitations, in the shape, type, or kind of ceramic product that they can form. For example, select processes such as Chemical Vapour Deposition (CVD) are only practically suitable for forming thin ceramic coatings, and their slow deposition rates means that they are not suitable for forming bulk components[21]. Other production processes are highly specific to producing select ceramic compounds, such as through specific liquid/solid reaction chemistry, or via reaction sintering from specific pre-ceramic materials. Without discounting those production techniques and their specific benefits, for this project the objective is to obtain a flexible process that would be applicable to the forming of a broad range of bulk ceramic components, for a wide range of applications. In particular for a process to have broad suitability for commercial ceramic production, this requires that the process be compatible with the use of a range of ceramic materials, and that the process be capable of forming precise, complex shaped components as required for use in modern highly-engineered systems and products.

To produce bulk advanced ceramic components, for most ceramic shaping processes the raw materials are typically supplied as a fine powder. These powders are then consolidated into a weak solid form known as a green body, before undergoing sintering at high temperature, to achieve particle fusion to produce a solid component that ideally possesses a dense (low porosity) and homogenous microstructure[24]. For high strength ceramics, a typical powder feedstock contains particles ranging between 100nm to 10μm in size, and the particle size distribution is typically very well controlled and monodisperse, as this is critical to ensure correct densification during sintering operations[24]. For most applications, the purity must also be maintained above 99% or higher, in order to achieve the required properties from the selected material.

At present, existing commercial bulk ceramic shaping processes from powder feed-stocks commonly take one of three multi-step processing routes, differentiated by their ratio of liquid carrier solvent (often water) to dry ceramic powder[21]:

1. **Dry powder processes (none or very low fraction of binder or carrier solvent)**
2. **Ceramic paste processes (medium quantity of binder or solvent added)**
3. **Wet colloidal processes (saturation in carrier solvent)**

2.1.3.1 *Dry Pressing & Cold Isostatic Pressing*

Dry powder processing routes include simple techniques such as dry pressing, where a die and uniaxial pressing ram are used to form components into the shape of a mould, to produce green body ceramic compacts[23]. While fast and cost effective, dry pressing is widely used in industry for the production of ceramic components with simple geometries. However, while dry pressing is suited for producing prismatic or simple extruded geometries, it is not well suitable for manufacturing complex shaped components, as variations in thickness or geometry can result in variations in the consolidated packing density. When density variations occur in green body samples, during sintering this can cause differential densification, and may result in undesirable warping, cracking or inhomogeneities in microstructure. While considered ‘dry’, a small percentage (<10%) of binder may be added, to enhance the structural integrity of the green body component after pressing and ensure it is durable enough for subsequent handling. Frictional forces between the powder and the die walls can also result in density variations[24], so lubricants may also be added to the feedstock mixture. For production of complex shaped components via dry pressing, first simple ceramic compacts must be produced, and then those compacts must be individually machined to reach the desired shape, either while in the green state or after sintering – or both. Both of these approaches have significant disadvantages: Green state sintering has the potential to introduce flaws into the green body[25] which is undesirable for part reliability. Post-machining after sintering is also undesirable, as it is expensive and time consuming. The high hardness of most ceramic materials necessitates the use of diamond tooling, so any forming process that requires shaping of sintered ceramics via subtractive processes will be inefficient for mass production.

Cold isostatic pressing (CIP) seeks to overcome many of the shaping limitations of dry pressing by using a flexible mould for shape forming[23]. After filling a mould with ceramic powder, the flexible mould can be placed under high external pressure using a fluid, enabling compacting forces to be applied from all directions. This process yields a more uniform ceramic compact, and the mould form also enables more complex shapes to be achieved. CIP is capable of forming parts with detailed features, such as threaded components, or regions of tapering or varying thickness. While this process is commercially used, the requirement for a single-part flexible mould results in some shaping limitations remaining; the process is typically only used for elongated and cylindrical shapes, such as in the production of spark plugs insulators.

2.1.3.2 *Ceramic Paste Processing*

Ceramic paste shaping processes and wet colloidal processes both depend on the use of additions to the ceramic powder, to enable material flow while undergoing shaping or forming via various techniques. This enables the use of more conventional mass-production material forming processes such as extrusion and injection moulding, as used for other materials that deform plastically.

For paste based techniques, the powder is blended with a significant fraction of binder or plasticiser, in order to then shape the component through plastic deformation techniques, such as via injection moulding, or other extrusion based processes[26]. While this enables flexible processing in complex shaped moulds, the large fraction of plasticising carrier phase must be removed during sintering to form the final solid ceramic component. As a result, the large amount of bunder burnout required means that during sintering these samples undergo a significant degree of consolidation shrinkage, which can cause issues with warping, distortion or cracking[24]. The binder used must also be carefully selected to ensure that it burns out cleanly and does not leave behind ash or other residues, which can compromise the performance of the final material[27, 28]. The injection of ceramic mixture under high pressure also results in high wear rates on the mould and tooling, increasing the cost per part.

2.1.3.3 Colloidal Processing

For colloidal processes, typically a liquid phase carrier solvent is added (in place of the plasticiser of paste processes) to a fine (<1um) ceramic powder. Sufficient solvent is added for the particles to be able to be dispersed in liquid, to form a fluid-particulate suspension. When preparing a colloidal suspension, a key goal is to achieve a well-dispersed (homogenously distributed particles) suspension free of powder agglomerates. Colloidal preparation methods include the use of ultrasonics to break up aggregates, the addition of additives to control inter-particle attractive and repulsive forces, and mixing and agitation to prevent particle settling and maintain a homogenous particle dispersion[29]. During drying and solidification, a homogenous dispersion can be used to produce a dry powder compact with fewer defects or variation in density. Such a dispersion is essential for achieving homogenous microstructures after sintering, which are required for high-strength components [25], as well as reducing defects to ensure consistency of product quality [1130].

Once a stable colloidal suspension has been prepared, a range of processes are available to obtain a green body compact, which primarily depend on the viscosity of the suspension, any additives that are used, and the specific processing steps selected. Putting aside processes unsuitable for forming bulk components (such as tape casting), common colloidal ceramic shaping processes include slip casting, gel casting and freeze-casting.

2.1.3.4 Slip Casting

Slip casting primarily involves the build-up of ceramic components via filter-drying techniques using porous moulds[24]. While it is possible to produced detailed and complex components via slip casting [11], the rate of part formation is inherently limited by the rate of filtration of solvent through the part itself, due to Darcy's Law[29], limiting the part geometry in other ways. While formation of thin-wall components (<10mm) is possible within acceptable per-part production rates for commercial production, to produce solid bulk components the low-permeability of thick components may result in excessively long drying times. This process has been augmented through the use of external applied pressure to accelerate drying rates through 'pressure slip casting'[28], but even so, this process must also overcome dimensional limits.

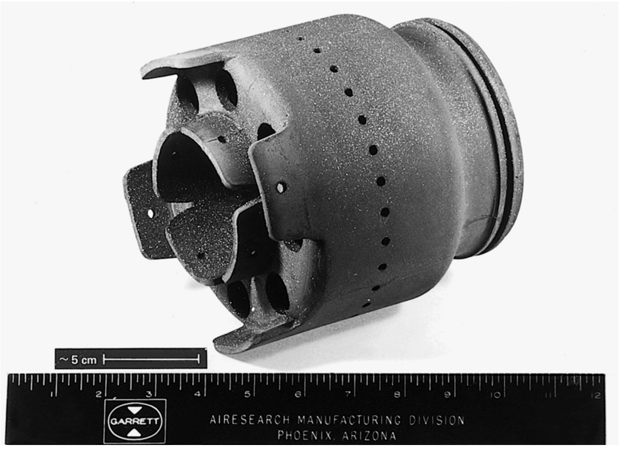

Figure 2.1.d: An example of a complex-shaped gas turbine combustor formed via slip-casting, taken from [24]

2.1.3.5 Gel Casting

For practical commercial production of bulk components, an alternative shaping process is needed that can achieve solidification within a more concise timeframe. One such process is gel-casting, where a gel-ceramic mixture is solidified to take on the shape of a mould via chemical means. This process has the advantage that it is largely material insensitive; most ceramic materials can be cast via gel-casting, and it is well suited for formation of complex shapes via use of detailed moulds [31]. However, the large fraction of added gel required for solid polymerisation results in similar challenges as for paste-processing, with high additive loadings resulting in compromised mechanical properties in the final components. In addition, the gelation monomers commonly used are associated with significant health hazards. Surface reactions also typically result in a poor quality part surface finish[27].

2.1.4 Summary of Ceramic Forming Processes

A simplified tabulated summary matrix of the ceramic processes discussed so far is provided in Table 2.1.a below, evaluating the performance of each process on its ability to:

a) Produce complex shaped ceramic components
b) Have a low cost per part
c) Have a low processing time per part
d) Maintain high-performance material properties of ceramic material
e) Produce solid (bulk/monolith) ceramic components

When considering the ceramic processes presented so far, none can offer a satisfactory solution to all of the identified commercial requirements. As a result, a need exists to identify an alternative process to meet these requirements.

Table 2.1.a: Evaluative comparison of common ceramic forming processes, considered for mass production of complex shaped dense ceramic components.

Ceramic forming processes for mass-production	a) Complex Shaping	b) Low Cost	c) Fast Forming	d) Material Properties	e) Produce Solid Parts
Dry Pressing	✕	✓	✓	✕	✓
Injection moulding	✓	✕	✓	✕	✓
Extrusion	✕	✓	✓	✕	✓
Gel Casting	✓	✓	✓	✕	✓
Slip Casting	½	½	½	✓	½
CIP & Green Machining	½	½	✓	✓	✓

2.1.5 Freeze-Casting

The process of freeze-casting is another colloidal-based forming technique for forming and consolidation of components from powder feedstocks; including from ceramic powder materials. Fine ceramic powder is first dispersed in a fluid carrier solvent to prepare a colloidal suspension, which can then be injected into a mould of desired shape. The mould is then subsequently cooled below the freezing temperature of the solvent, to yield a solid frozen ceramic compact in the desired shape [27]. The frozen part is then demoulded, and freeze-dried. This step removes the frozen solvent from the formed part via sublimation, to yield a dried green body ceramic compact of the desired shape, ready to be fired and sintered into a solid ceramic component. During sintering, the part will shrink in size and densify, while retaining the original complex shape from the casting mould used.

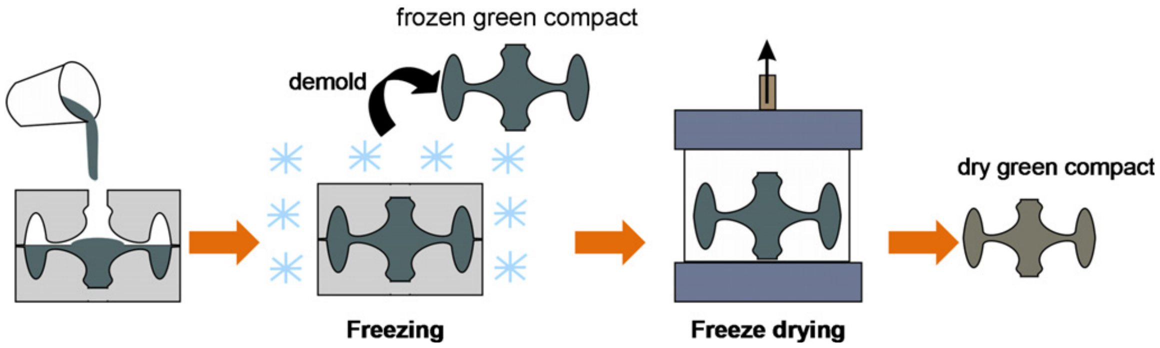

Figure 2.1.e: Freeze-casting process [27]

Freeze-casting is not a new technique; the process of freeze drying has existed since the 1950's[11], while patents on the core freeze-casting process were previously granted in 1991[32]. Recently, interest in freeze-casting has re-emerged following a greater interest in controlling the microstructure of porous materials, which is possible to accomplish with freeze-casting by tailoring the solvent solidification conditions[11].

2.1.5.1 Advantages of Freeze-casting for Dense Ceramic Shaping

Freeze-casting provides several advantages over other ceramic processing techniques for producing complex shaped components. As a colloidal process, freeze-casting benefits from the ability to prepare a well-dispersed suspension, in order to ensure a homogenous density is achieved in the compact before sintering. Freeze-casting has similarities with gel-casting, in that it enables complete solidification of near-net shaped monolithic solid components using complex shaped moulds. However, unlike gel casting or ceramic injection moulding, a key advantage of freeze-casting is that the process requires a significantly reduced quantity of additives. The freeze-solidification process eliminates the need for gelation additives, and as a result, this avoids the issues around binder burn-out residues potentially compromising the properties of the final ceramic. Similarly, the relatively fluid viscosity of a colloidal suspension also eliminates the need for plasticiser additives, again improving sintering performance as well as reducing capital costs by avoiding the need for high pressure injection moulding equipment.

Instead, the carrier solvent itself is solidified via phase change (is frozen) to provide a solid frozen body in the shape of the mould. The frozen compact is then freeze-dried (sublimation) to remove the solvent and yield a near-net shaped green-body ready for sintering. Freeze-casting also provides additional benefits beyond enabling net-shaping; the viscosity of the suspension is significantly lower than that of pastes used in other injection moulding processes, and this enables lower pressures to be used during injection moulding, which reduces the cost of moulding equipment required for commercial applications.

Similar to gel casting, freeze-casting is broadly possible to perform with a range of powder materials, including both oxide[2] and non-oxide[3, 33] ceramics, metals[4, 5, 34, 35], as well as composites with fibres [36, 37], ceramic/metal mixtures[38–40] or other insoluble additives[41].

2.1.5.2 History of Freeze-casting for Dense Shaping

The original freeze-casting research memo published by process was initially pursued by the US NACA agency for the casting of turbosupercharger blades from a range of ceramic and metallic powders[42]. Their study used an aqueous suspension highly-loaded with powdered material, and with a 2wt% starch binder added to provide sufficient green strength for handling. The shaping and casting process was indicated to be successful in most aspects, with radiographic imaging used to verify that a satisfactory part quality (flaw-free) was achieved. However, the results also showed that the achieved part density was not fully dense, with $MoSi_2$ samples achieving 90% of theoretical density. Samples were also successfully prepared with in TiC, but since Inconel melt infiltration was successfully performed post-sintering on these samples, it is reasonably inferred that even after sintering a high porosity was still obtained.

2.1.5.3 Disadvantages of Freeze-casting for Dense Ceramic Shaping

Considering the stated goal of producing dense components, freeze-casting intrinsically has a disadvantage for this purpose as it is inherently a pore-forming process. The process of freezing results in the production of a distributed matrix of frozen solvent crystals and powder particles. Following freeze-drying of a frozen compact, the solvent phase is removed, resulting in a distributed network of pores corresponding to a negative of the previous solvent crystal geometry.

For this reason, the freeze-casting process is also commonly known by the term 'ice-templating' [43–45]. It has been repeatedly shown that the growth and geometry and distribution of the solvent crystals can be affected by changing the freezing conditions, to produce templated porous networks of various configurations. For this reason, most recent research on freeze-casting has focused on applying and optimising the process to produce components with tailored porous microstructures for specific desired applications, such as for biomaterials [6, 7, 46, 47], insulation[48], catalysts[49], or filtration[49, 50].

While porous materials have a range of benefits including lighter weight and reduced component material costs, with regard to mechanical properties, porous internal microstructures are deleterious, as pores can act as crack initiation sites, reducing the mechanical strength of the component [8, 51].

For this reason, since the pores are produced during solvent removal, and the goal is to produce dense components, the ratio of carrier solvent addition should be minimised, to produce a highly-loaded suspension with a high solids-loading of ceramic particles[52, 53]. This will assist by reducing the overall volume fraction of pores, but it is inevitable that some porosity will be present in the green component after drying.

2.1.5.4 Freeze-casting Suspension Composition

In the early 90's, the need for a process of producing high-quality dense complex near-net shaped parts via powder processing was again identified, with pressure slip casting considered to be state of the art for this purpose at the time [28]. The freeze-casting process was again revisited, with patents granted covering two key innovations primarily relating to solvent selection in the freeze-casting system [32, 53, 54]. Many of the properties of water make it well suited as a carrier solvent, such as having a conveniently accessible phase change temperature, a low viscosity, a reasonable vapour pressure, and low toxicity. It is unremarkable then to discover the majority of freeze-casting is explored with aqueous based suspensions [53, 55]. However, in other aspects the use of water as a carrier solvent is inherently problematic for dense freeze-casting. During solidification, water has a tendency to form large ice crystals, which when removed result in macroscopic pores in the sample, pores that are too large to eliminate during pressureless sintering and remain in the final product[56]. The primary innovation here was the addition of a cryoprotectant to the suspension, to disrupt the crystal growth, in order to produce an evolved pore microstructure that is amenable to densification during sintering.

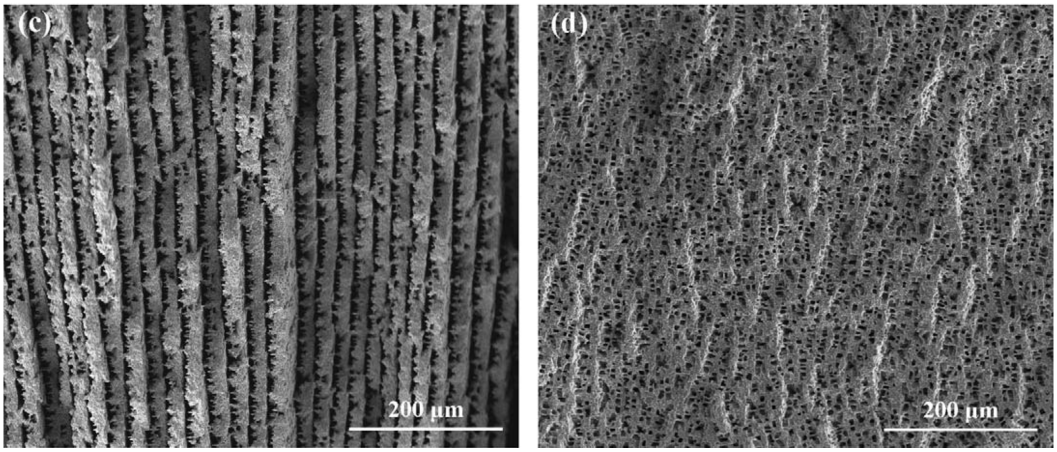

Figure 2.1.f: Comparison of porous 30 vol.% alumina freeze-cast microstructures, prepared with (d) and without (c) addition of glycerol. Figure from [57]

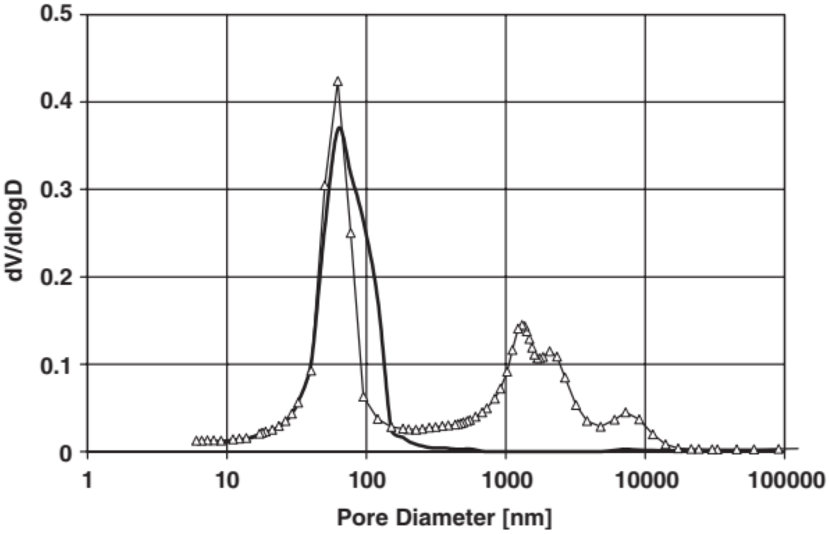

Figure 2.1.g: Pore size distribution in freeze-dried green body, prepared by freeze-casting an aqueous alumina suspension both with (solid bold line) and without (triangle thin line) glycerol addition. Figure reproduced from [52].

The use of cryoprotectants within aqueous freeze-casting systems has been well explored since, with glycerol demonstrated to be highly effective for this purpose [52, 56–58], especially as a low-toxicity ceramic shaping alternative to gel-casting systems.

Optimising the suspension chemistry through tailored additives, such as solvents, binders, dispersants, templating agents, cryoprotectants, have all been shown to have transformative impacts on the solidification process[53] and this remains an area that has significant potential from discoveries yet to come. During freezing, while the solvent is rejected into inter-dendritic spaces, the various suspension additives may be adsorbed onto the physical ceramic particle surfaces, so it is expected that a significant portion of the additive may remain after freeze-drying.

2.1.5.5 Freezing-rate & Microstructure

Interest in freeze-casting has been maintained through the past twenty years, and has continued to provide further insights into both the suitable operating conditions and process parameters, as well as developing a deeper understand of the mechanisms responsible [11, 44, 45, 53, 59–61]. In addition to both selecting a suitable carrier solvent system, and ensuring a highly-loaded ceramic slurry is used, the importance of freezing-rate on part microstructure has been comprehensively explored. Fukasawa et al [49] showed this effect clearly early on, by using controlled temperature freezing baths to prepare and compare part microstructure when alumina slurry was frozen at -20°C and -80°C. While the size of frozen pores in those samples was observed to vary with freezing-temperature, the overall porosity was not affected, with porosity measured by mercury porosimetry to be constant a 62% for both samples presented in Figure below.

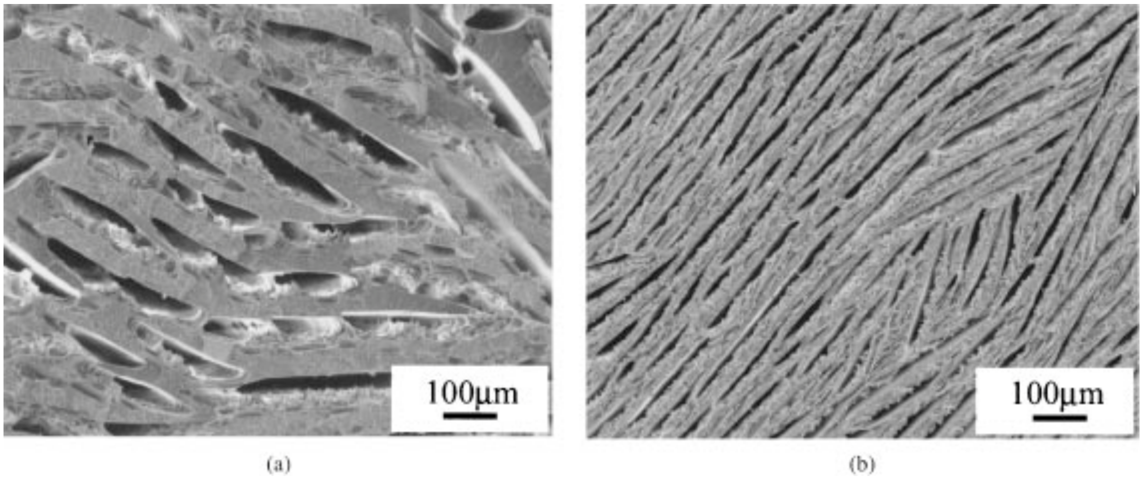

Figure 2.1.h: Comparison of freeze-cast microstructure for freezing of 28 vol% alumina, frozen at (a) -20°C and (b) -80°C respectively. Figure from [49].

The reason for the relationship between freezing-rate and pore size has since been explained as due to competition between the growth of solvent crystals, and rate of rejection of powder particles from the freezing front[45, 56, 62]. The present understanding of suspension solidification is a dynamic interplay between the progress of a 'freezing front', and the desire (energetically favourable) of solid frozen solvent crystals to be free of internal trapped particles. For a simplified case of a single frozen particle being surrounded by a growing solid phase, the interfacial energies must be considered for each of the particle-solvent and particle-ice and solvent-ice phases, and evaluation of these energies permits a calculation of both the attractive and repulsive (and therefore net) forces the particle experiences. This net force is responsible for the motion of the particle and resulting rejection of particles from the solid frozen phase. When considering many particles, in cases where particle rejection force is low, and the freezing front velocity is high, it is possible for particles to be engulfed into the frozen solvent matrix without significant deflection as the freezing front overtakes. In the opposite case, with low freezing front velocity, it is possible for a filtration effect to occur, where particle repulsion results in a concentration of particles in front of the freezing front. This particle accumulation in front of the freezing front continues, until the compacted layer becomes sufficiently thick that rejection no longer becomes possible, and encapsulation or engulfment of the particles at the front occurs. The expression for this can be derived in terms of a critical velocity, v_{cr} for the suspension, where the ratio of freezing front velocity (v) to critical velocity (v_{cr}) determines the mode of solvent growth and particle interactions that are occurring.

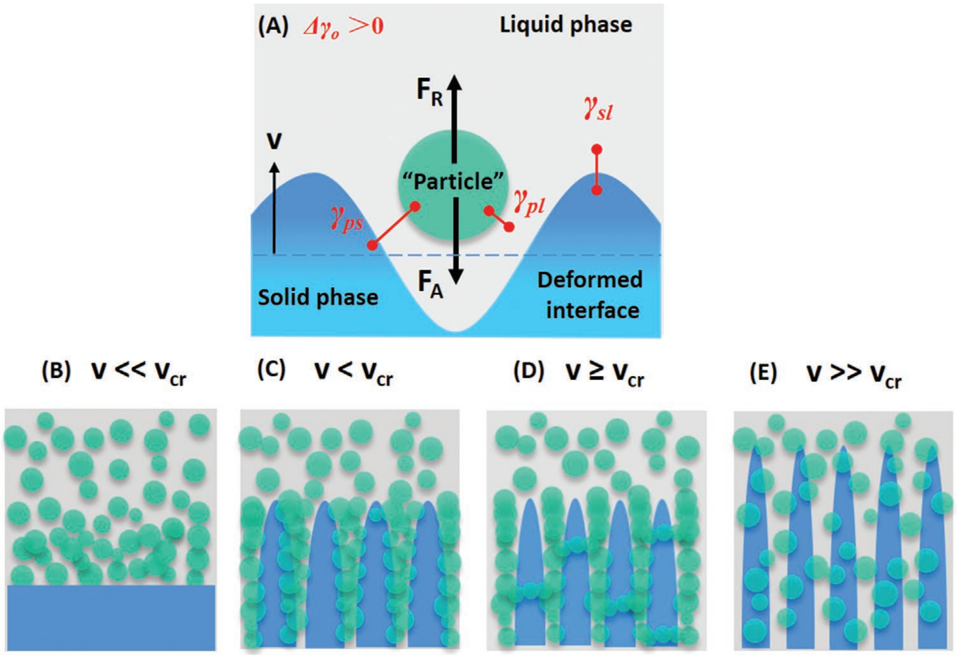

Figure 2.1.i: Illustration of different solidification modes depending on $v:v_{cr}$ solidification velocity ratio. Figure reproduced from [45].

This demonstrates that it is particle rejection from the solvent phase due to crystal growth that is responsible for the development of large pores after freeze-drying. In order to produce a microstructure with small pores, it is desirable to maximise the freezing-front velocity during freezing. Toward this goal, in order to maximise freezing rates, several studies use a pre-chilled mould, brought to a low temperature prior to the addition of suspension[58, 62]. Doing so provides the greatest initial temperature gradient between suspension freezing temperature and driving freezing temperature, which helps to achieve the highest solidification velocity. The drawback with fast-freezing is that maintaining a high freezing front velocity requires a high thermal gradient, which is difficult to maintain over large freezing distances. If freezing rate decreases, larger pores may form, resulting in a inhomogeneous distribution of pore sizes within the component. Because of this, the thickness of fast-freeze cast samples may be limited due to the associated practical considerations of temperature difference. Alternatively, a non-constant freezing temperature can be used to varying the exterior driving thermal gradient, in order to maintain a constant internal freezing front velocity[63]. However, while it is an impressive technical achievement to do so, the complexity of this dynamic temperature setup for anything other than the simplest geometry is likely to render it impractical. Using a pre-chilled mould also introduces second a practical challenge; since freezing begins immediately upon suspension addition, it requires the injection procedure to be capable of filling the mould completely in a short amount of time. Failure to fill the mould fully with a pre-chilled mould is likely to result in significant surface defects on the frozen component as frozen-suspension regions come into contact with liquid suspension.

In summary, the freezing process is core to freeze-casting, as it is the primary process step responsible for obtaining the desired microstructure in the green body. Whether through incorporating additives, or developing advanced thermal control processes, a broad range of techniques and approaches remain open to modify the effective freezing rate through both intrinsic and extrinsic means; acting to affect the forces present during freezing and solidification, or by acting to counteract those forces through external means [60].

By using highly loaded aqueous ceramic suspensions, and utilising fast-freezing using pre-chilled moulds, successfully dense freeze-cast samples have been successfully demonstrated. Wildhack & Aldinger [58] reported achieving 98% of theoretical density (%T.D) from a 55 vol% AlN aqueous suspension, using glycerol as cryoprotectant (14% of liquid wt.), 2 wt.% Dolapix PC 33 as dispersant, 0.4 wt.% Optapix AC 112 as binder, and with 2 wt.% Y_2O_3 added as sintering aid. This demonstrates the potential of an optimised freeze-casting process to produce dense ceramic components.

2.1.5.6 Non-Aqueous Carrier Solvent for Dense Freeze-casting

The second significant limitation with aqueous ceramic processing, is that of material chemical compatibility. While aqueous systems may be suitable for oxide ceramics such as alumina, a broad range of non-oxide materials are incompatible with water and upon exposure will oxidise or otherwise react. Although it has been shown that some materials can be ‘chemically protected’ to enable sufficient short-term aqueous-suspension compatibility for freeze-casting[58, 64], this is not guaranteed to be possible for all materials in all processing conditions. For this reason, there is a need for alternative non-aqueous carrier solvents to enable colloidal systems to be prepared using a broader range of materials. Within the past two decades, a number of non-aqueous solvents have been explored within the context of both the freeze-casting and dense freeze-casting processes. For a solvent to be suitable, it should possess physical properties within a desirable range, including an accessible phase transition temperature, low toxicity, low vapour pressure, and good chemical compatibility with materials, additives and dispersants. For a solvent to be well suited for dense freeze-casting, it is also essential that it can provide a low viscosity, to promote the ease of achieving high solids loadings. At present, Camphene and Tert-Butyl Alcohol are the most commonly studied non-aqueous carrier solvents for freeze-casting [53], in addition to others including Naphthalene/Camphor [65] and Cyclohexane [27, 33, 66, 67].

Araki & Halloran demonstrated dense freeze-casting early on, using a eutectic mixture of Naphthalene and Camphor that offers an accessible solidification temperature of 31°C. By using such a carrier solvent system with a highly loaded suspension with 48 vol.% alumina, they were able to achieve near-dense ceramic bodies of >99.5%T.D. Similar to the cryoprotectant effects of glycerol in aqueous suspensions, the eutectic mixture was thought to reduce particle rejection from the freezing front, helping to avoid formation of large pores in the green body. Similarly, using a Camphene based suspension with 51 vol.% Alumina, Araki & Halloran achieved a 98.4%T.D [68]

Cyclohexane has been explored on several instances within our research group as a suitable non-aqueous suspension carrier solvent for dense freeze-casting. Highly loaded 54 vol.% suspensions of ‘difficult-to-densify’ ZrB2 were pressureless sintered, achieving 91.5%T.D measured in cylindrical test coupons. However, after cutting these samples, significant internal cracking was revealed. Proposed theories for the origins of this cracking primarily involve concerns related to the freeze-drying and sintering process steps. Partial melting during freeze-drying could result in capillary forces being present, resulting in significant internal forces during drying. Cracking during sintering could occur where densification occurs anisotropically, resulting in differential shrinkage. Variations in internal pore size, with smaller pores distributed in the sample centre, could result in inhomogeneous densification, and the stresses that arise under those conditions could contribute to the formation of cracks. Cyclohexane is also known to have several different crystal states, with ice phases I occurring at 6.3°C, phase II at -87°C, and phase III at high pressure (500 bar) and -75°C.

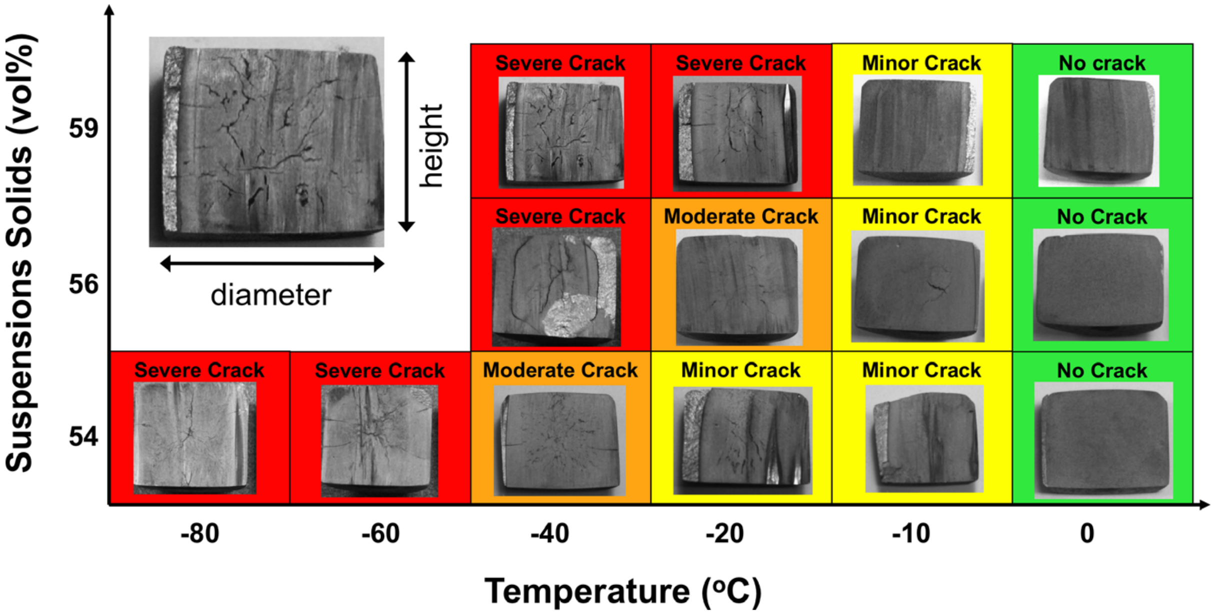

Figure 2.1.j: Severe internal cracking observed within dense freeze-cast test samples. Figure from [33]

Table 2: Table of common non-aqueous freeze-casting solvents

Solvent	**Freezing Temp (°C)**	**Boiling Temp (°C)**	**Vapour Pressure**	**Viscosity**	**Dielectric Constant**	**Vol. Change on Freezing**
Cyclohexane	6.5[69]	80.8[69]	13 kPa at 25°C [70]	–	2.0 [71]	–
Naphthalene/Camphor	31[65]	–	–	–	–	–
Cyclooctane	14.6[69]	149[69]	–	–	2.12[72]	–
Camphene	51.5[69]	159[69]	2 kPa at 55°C [43]	1.4 mPa.s at 47°C [43]	2.33[73]	-3.1%[43]
Tert-Butyl Alcohol	24[69]	82[69]	6.4 kPa at 40°C [43]	–	10.9[74]	-2%[43]
Dodecane	-10[69]	216[69]	18 Pa at 25°C [75]	–	2.00[76]	–

Using the same suspension formulation, the production of complex shaped objects was also demonstrated, with test pieces dense freeze-cast in various novelty confectionery silicone moulds. Density for those components varied between 65-80%T.D.

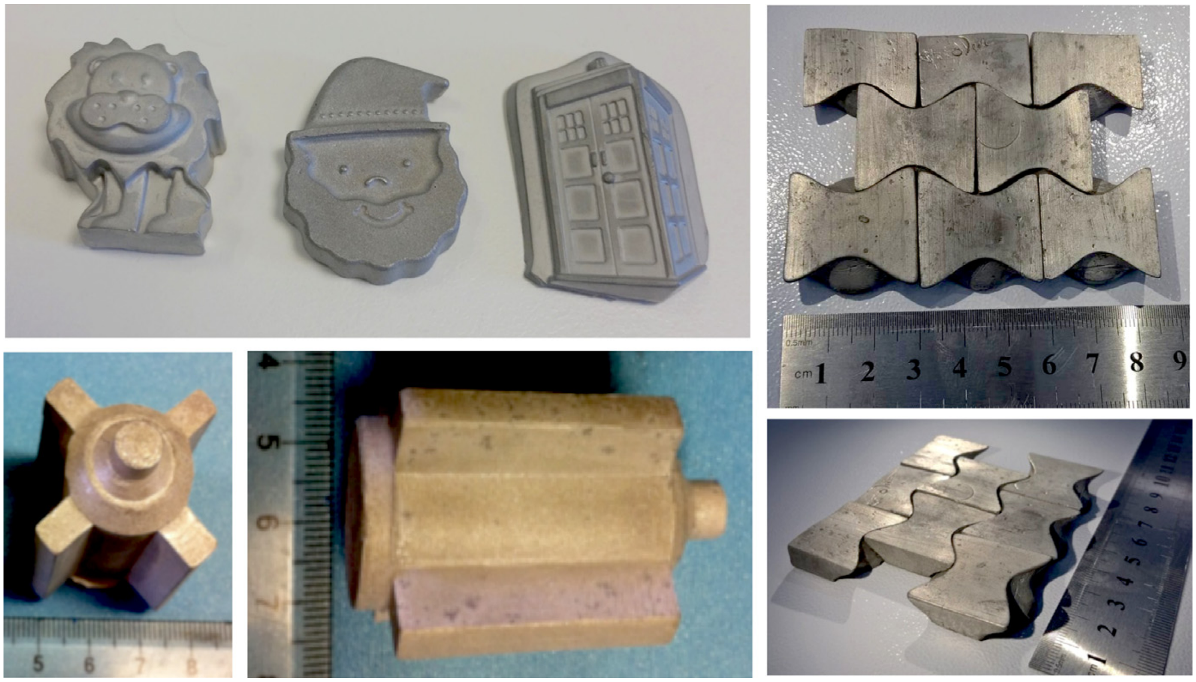

Figure 2.1.k: Examples of complex-shaped ceramic pieces produced by dense freeze-casting. Figure from [33]

The examples above indicate that a range of suspension composition options are available for preparing dense freeze cast components, while also highlighting present challenges surrounding producing crack-free components.

2.1.6 Conclusion

A survey of the freeze-casting literature has provided clear impetus to explore the potential of dense freeze-casting for production of dense, complex shaped ceramic components, to unlock further applications of advanced ceramic materials. In comparison to traditional freeze-casting, where porosity is valued, for dense freeze-casting several strategies can be elucidated. Firstly, the use of highly-loaded suspensions assists to minimise the total porosity found in the final ceramic shaped green component. The use of fast-freezing with pre-chilled moulds is also beneficial, as this helps to maximise the freezing front velocity, thus minimising the time available for large dendritic crystal growth, and hence minimising the size of pores in the shaped green-body prior to sintering. In this way, an optimised microporous component microstructure can be obtained that is favourable for densification during sintering. A key remaining challenge to overcome is mitigating the cracking that has previously been observed within some dense freeze cast samples. Towards this goal, control of freezing rate should also be explored to achieve a constant homogenously pore size throughout the part, to ensure that densification occurs isotopically, to minimise any potential warping or cracking within shaped components. Finally, while the use of aqueous-based suspensions has been successfully demonstrated, to enable a broad range of oxide and non-oxide ceramics to be processed it is essential that suitable alternative non-aqueous carrier solvents for this process are also be identified. In this way, from a review of the literature it appears that the dense freeze-casting process is plausibly viable as a process suitable for mass-production complex shaping of dense ceramic components.

3 Aims and Objectives

3.1 Research Opportunities

A key conclusion from the literature review (previous chapter) was the identified need for a new dense ceramic shaping process. The availability of shaping processes for metals and plastics have been key to both their broad adoption and use, but it is the availability of complex-shaping processes that has enabled advanced integrated product designs with complex features.

The aim of this thesis is to examine the suitability of the freeze-casting process for producing dense, near-net shaped ceramics. To both constrain the complexity of the study, and to examine the simplest possible process, the sintering process used was pressureless sintering, which is well understood, and this capability is already available within the research facility.

As shown in the literature review, previous work on using freeze-casting for producing dense non-oxide ceramics was found to result in parts containing a significant number of severe cracks, both on the exterior of the part and internally. These cracks are undesirable, as according to Griffith's crack theory they are expected to provide weak points for material failure under load, significantly reducing the mechanical strength of the parts.

The cause of these cracks is not known at this point, and these severe cracks would be unacceptable if present in production parts. As such, the following primary aims of this project are in both identifying the specific cause of cracks, and then once new understanding has been achieved, to investigate options for crack mitigation. In addition to identifying the cause of cracks, an understanding of the factors affecting part microstructure is also sought.

3.2 Primary Project objectives:

1) **Demonstrate dense freeze-casting, to produce complex shape dense ceramics**
    a. Produce parts via dense freeze-casting to demonstrate shaping capability.
    b. Produce parts from oxide and non-oxide materials to demonstrate material flexibility and verify that cracks are not exclusive to previously studied materials.
2) **Develop understanding of factors responsible for microstructural control**
    a. Examining the primary process steps, identify the mechanisms and key process parameters responsible for controlling the evolution and development of micro- and macro-structures in freeze-cast parts
    b. Identify process step responsible for formation of cracks, and investigate cause of cracks
3) **Apply understanding to optimise process and identify limitations**
    a. Investigate methods of reducing or eliminating cracks
    b. Apply learnings obtained throughout study, to select optimal process conditions, with the goal of producing dense, crack-free parts.

In the following section, each of these primary objectives is discussed in further detail, to explain the proposed method to achieve each objective.

1) Demonstrate dense freeze-casting, to produce complex shape dense ceramics

For freeze-casting to be a useful dense shaping process, it must be capable of reproducing a wide range of shapes, with good feature accuracy. All shaping processes have some shaping constraints, and moulding processes are no exception, with limitations expected such as minimum feature size, or minimum wall thickness. Identifying all aspects of the shaping limitations of freeze-casting is valuable to evaluate suitable applications for the process.

While some shrinkage is to be expected during sintering, this can generally be accounted for by adjusting the initial object size. Other details, such as surface finish or texture, can be time consuming to add by post processing, whereas they may be readily and rapidly transferred from a mould.

Typically, for injection moulding, the applied pressure will determine how the material will flow into the mould shape, determining the quality of the details captured, such as sharp edges. For this project, sample injection is performed by hand, which limits the moulding pressure availably. Instead, the viscosity of the suspension should be reduced to provide sufficient fluidity so as to permit a rapid injection and satisfactory detail capture. This implies then that the maximum solids loading permissible for an ideal industrial process would be higher than that used in this study.

It is worthwhile to measure both the shrinkage and the density of the sintered parts.

For parts requiring high dimensional accuracy, some post-sintering grinding may still be required, but a preliminary near-net shaping still provides a very significant saving in time and cost. In the metals industry, casting and post-machining are still a commonly paired set of production processes.

It was previously shown that the cracks observed in samples differed significantly between different ceramic materials. For ease of processing, the primary materials studied in this thesis are oxide ceramics, as sintering can be performed in air, at lower temperature. However, it is expected that at a later stage, there may be significant value in applying the knowledge obtained to also evaluate the shaping of non-oxide ceramics.

2) Develop understanding of factors responsible for microstructural control

As a multi-step process, it is expected that within each step there will be parameters and conditions to be selected, that will affect the final product. Furthermore, some of these parameters are linked, with the results from each step, affecting the influence and effects of downstream parameters.

Some of the Freeze-casting process steps are well understood; for example, the literature has many examples of controlling the freezing process to tailor the size, distribution, and morphology of pores within the sample[44, 77–79]. There are several examples of incorporating additives into the suspension to modify the freezing behaviour, which in turn also affects the pore microstructure. However, there is a conspicuous lack of literature examining the impact of the drying step of the process on microstructure. Some parameters in the process are readily adjustable, while others may require modifications to equipment or methodology. Conversely, some parameters may not be adjustable at all, but may still be important to monitor to relate with observations.

A clear obstacle for the use of freeze-casting as a shaping process, is the observation from previous work by Silvia Leo, of undesirable large cracks being present within samples. A key challenge for this project, is of identification of both the specific process step(s) where these cracks are evolved, and of the factors that cause and affect the morphology of cracks.

3) Apply understandings to optimise process and identify limitations

Following the knowledge gained relating to identifying the cause of cracks, the next challenge is to investigate methods to, as much as possible, minimize or eliminate the presence of cracks.

It was noted, that cracks have not been reported in work relating to porous ceramics. In cases where cracks cannot be eliminated in dense samples, it may be useful to examine samples produced with reduced solids loadings, in order to identify the critical solids loading where cracks start to appear.

Finally, while gathering understanding surrounding the factors influencing each process step provides useful learnings, there is significant value to be obtained by applying this knowledge, to provide an evaluation of both the capability and limitations of the overall process.

To demonstrate the overall outcome from key learnings from this project, an optimized process will be prepared, with the aim of producing dense, complex-shaped parts, while minimizing cracks and defects. The quality of parts obtained could then provide a benchmark for the performance of the process to be compared to other ceramic shaping processes, and such a benchmark could serve well to use in exploring potential specific applications.

3.3 Chapter Outline

To introduce the structure of the thesis, and provide context for the reader, a summary of each subsequent chapter is outlined below.

Chapter 4: Methods

The experimental method section contains details of both the laboratory practical work performed, as well as the procedures used for image analysis. This chapter introduces the experimental techniques used, providing a detailed explanation of the methods used for both the preparation of samples, and the analysis of samples. This includes the designs of custom equipment, the setup of laboratory experiments, and the tools and packages used on the computer for the analysis of numerical data, SEM and optical images, and tomographic data.

Chapter 5: Preliminary study of dense freeze-casting process

This first brief experimental chapter investigates the preparation of suspension used for the freeze-casting study, optimising the suspension to maximise the density of green-body samples, followed by optimising the sintering regime for achieving maximal sintered density via a pressureless sintering regime.

Chapter 6: Study of freezing-rate and microstructure via dense freeze-casting

This second experimental chapter presents a study examining microstructural formation during freezing and relating the freezing rate to variations in microstructure. Experimental samples, produced across a range of freezing rates, are imaged both optically, and via SEM and micro CT. Measurements were taken using in-situ probes to obtain a quantitative measurement of the freezing-rate under different conditions, and to provide further insight regarding the difference of fast-freezing and slow-freezing methods.

Chapter 7: Study of drying-rate and cracking in dense freeze-casting

The third experimental chapter demonstrates a series of microstructural analysis of parts produced by freeze-casting, across different steps in the process. The results from this analysis are used to confirm that the cracks observed in product parts, are introduced during the sample drying process.

A time series study was used to image one sample while drying, to examine the sequence of crack evolution.

Chapter 8: Study of modified suspension composition for mitigation of freeze-drying cracks

The fourth experimental chapter investigates methods to mitigate crack development through two avenues. This includes investigating the effect of binder addition and process conditions on green mechanical strength, suspension rheology and cracking formation, as well as examining the effect of the carrier solvent in crack formation and morphology.

Chapter 9: Conclusions

This section summarises the main research findings, incorporates an evaluation of the results obtained relative to the research aims and objectives, and collates the recommendations for opportunities for future work.

4 Methods

This chapter provides a description of the standard methodology, processes and techniques used, that are common to each of the research studies that follow. This chapter is ordered as follows:

- Experimental Preparation techniques
- Experimental Analysis techniques
- Imaging analysis techniques

4.1 Freeze-casting Process Steps

The freeze-casting process comprises several individual process operations, with the details of each step described in the following sections.

4.1.1 Suspension Preparation

The freeze-casting process begins with preparing a colloidal suspension of ceramic particles in solvent. A summary of the suspension preparation process is as follows

1. Dissolve dispersant completely in carrier solvent
2. Add binder(s) and/or other solvent
3. Add ceramic powder gradually, mixing intermittently.
4. Sonicate suspension
5. Homogenise

Details of each of these process preparation steps are explained in subsequent sections further below. However, the first task required before preparing a suspension involves identifying and selecting compatible materials for formulating the suspension. Typical active components of the suspension include:

- Ceramic Feedstock
- Carrier Solvent
- Dispersant
- Binder
- Sintering Aids

4.1.1.1 Ceramic Feedstock

For the production of ceramics, the starting material is a ceramic powder. In this work, the primary ceramic feedstock used was an alumina (Al_2O_3) AKP-15 high purity powder (Sumitomo, Japan), which has a mean particle size of 0.65 µm. For chapter 5, the other ceramic used for some experiments was titanium carbide, TiC (H.C Starck, Munich, Germany), with a mean particle size of 1.5 µm.

The size distribution of particles is significant; as in order to produce a stable, well dispersed suspension, a narrow distribution is desirable. Particles must not be too large (>10 µm), or they will rapidly settle, nor can they be too small as they will agglomerate and be difficult to disperse.

4.1.1.2 Alumina Ceramic Powder

The majority of experiments in this thesis were performed with Alumina (Al_2O_3). Alumina has several advantages that make it practically easier to work with. The primary advantage is that it is relatively easy to densify, in comparison with other ceramic materials. High sintered densities (>98%TD) can be achieved using simple pressureless sintering in an open-air furnace. Secondly, as is typical for an oxide ceramic, it does not require a special protective atmosphere during sintering. Additionally, the sintering temperature for Alumina is lower (relative to the other non-oxide ceramics studied), which means that an air furnace of simpler construction can be used. The sintering profile used for Alumina was 1550°C for 2 hours. While it is known that MgO additives can be used to achieve a higher final density [80] , for simplicity no sintering aids were used.

The specific powder used was high-purity AKP-15 alumina supplied by Sumitomo Chemical Co., Ltd. (Tokyo, Japan). This is a fine powder produced by aluminium alkoxide hydrolysis, producing homogeneous alpha-alumina crystal particles. The AKP-15 product was used features a mean particle size of 0.65 µm [81]. SEM images of this powder are provided on the following page. This powder was characterised under SEM to examine the typical particle shape, and also examined in a Mastersizer (Malvern Panalytical, Malvern, UK) to obtain an analysis of the particle size distribution. The size distribution is primarily monomodal, within a narrow size range from 0.3 to 6 µm. A small fraction of particles found to be greater than 6 µm, of which a portion is likely to be due to agglomerated particles.

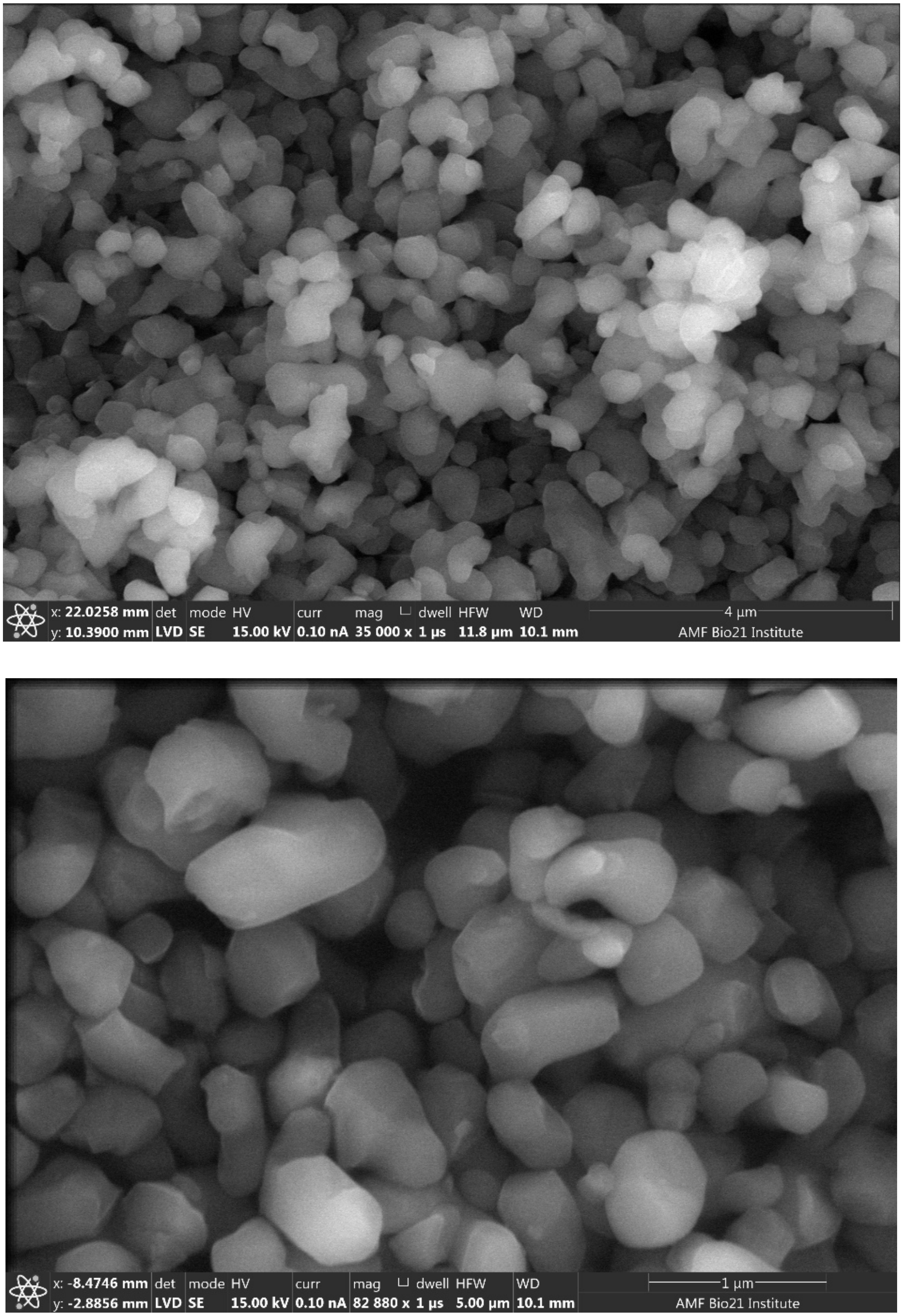

Figure 4.1.a: SEM images of Alumina powders used (top) and (bottom).

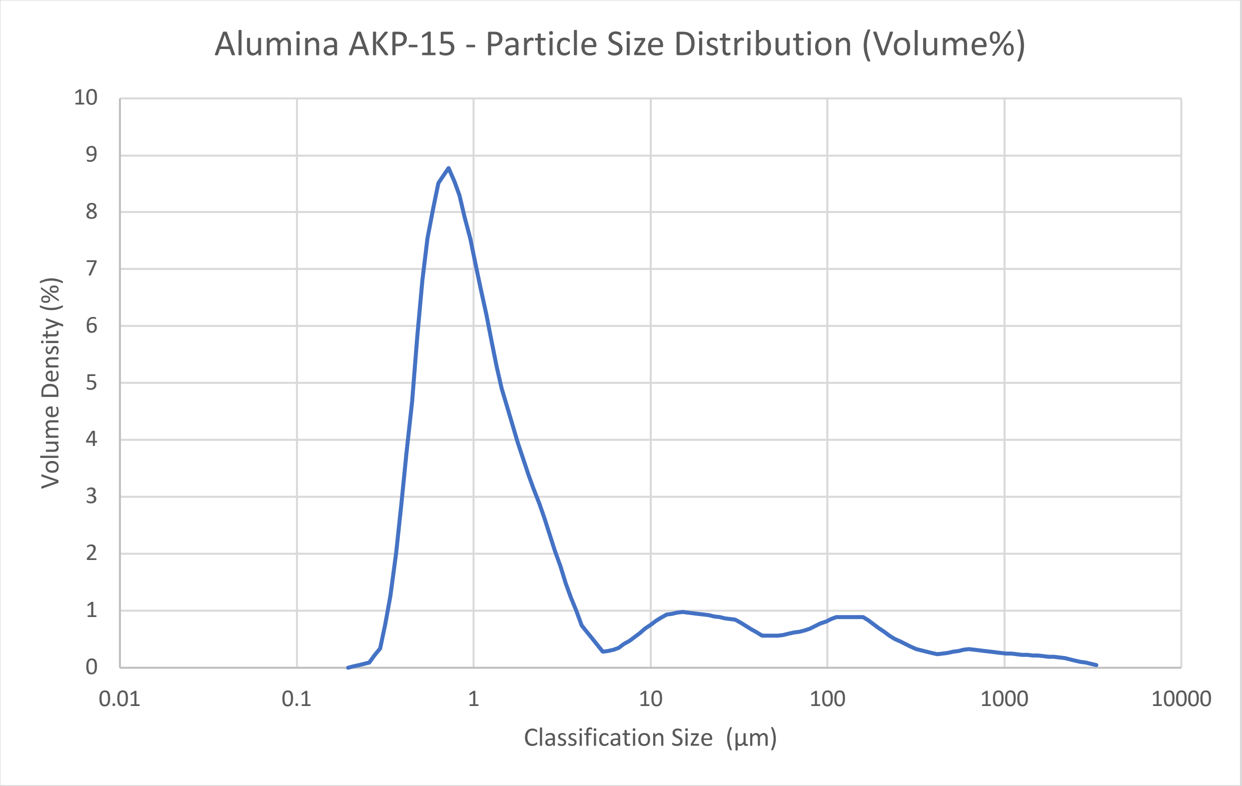

Figure 4.1.b: Particle size distribution for alumina AKP-15 powder.

4.1.1.3 Titanium Carbide Ceramic Powder

The second material used was Titanium Carbide (TiC), provided by H.C.Starck GmbH (Goslar, Germany). The specific product used was TiC HV 120. In order to minimise moisture adsorption or oxidation after opening, care was taken to reseal the container when not in use to.

4.1.1.4 Carrier Solvent

In order to suspend the ceramic powder, a carrier solvent and dispersant combination must be selected. The difficulty of achieving small pores from aqueous-based suspensions via freeze-casting, has been clearly seen in the literature[56, 57, 64, 66]. As a result, for this reason the focus was exclusively on non-aqueous suspensions. Additionally, by using non-aqueous solvents this also enables the possibility of performing work with both oxide, and non-oxide ceramics, since non-oxide ceramics may otherwise react or oxidise when processed in an aqueous formulation.

The choice of solvent may seem arbitrary, but with several selection criteria prioritised, the range of suitable solvents becomes rapidly constrained. For these studies, the priorities were specified:

- Low toxicity and low hazard risk
- High vapour pressure for easy solvent removal during freeze drying
- Convenient phase change temperature close to room temperature
- Low viscosity at room temperature

When applying these constraints, an examination of the literature resulted several different solvents being identified that appear suitable, including:

- Cyclohexane
- Cyclooctane
- Tert-Butyl-Alcohol
- Camphene
- Dodecane
- Naphthalene / Camphor Eutectic mixture

For these studies, the primary solvent selected was cyclohexane (Sigma-Aldrich, North Ryde, Australia),, a saturated non-aromatic hydrocarbon with low relative polarity, insoluble in water. It has a range of material properties that make it favourable for freeze-casting, including low viscosity, an accessible melting point of 6.6ºC, and a high vapour pressure enabling rapid solvent removal. Of note, cyclohexane in the frozen state forms a ‘rubbery’ solid, quite distinctly different to the ‘hard solid crystal’ that forms when water freezes.

Suspensions were prepared in a plastic polypropylene container with a polyethylene lid, as this was acceptably solvent resistant to the solvents used. 120 mL flat containers from TechnoPlas (St Marys , Australia, cat. item P9246UUUV) were most commonly used, with 92 mm height and 46 mm diameter. These containers were used for all preparation steps prior to suspension mould injection.

4.1.1.5 Dispersant

The dispersant used in these studies was Hypermer A70 (Croda, Snaith, UK), which was selected based on successful past work preparing highly-loaded ceramic suspensions with this solvent [27, 66, 82–84]. This dispersant is a non-ionic high molecular weight polymeric surfactant, soluble in non-polar liquids. The dispersant is apportioned by weight as a thick high-viscosity liquid, after which, the suspension container is closed and vigorously agitated, shaking by hand for two to three minutes, until the dispersant appears fully dissolved in the solvent.

4.1.1.6 Binder Addition

Before firing, the component being produced must possess sufficient green strength to enable it to be removed from the mould and transferred between both the freeze dryer and the furnace, without damage or crumbling of the part. In the frozen state, the carrier solvent provides a solid matrix that supplies the strength of the part. However, once the carrier solvent is removed in the freeze dryer, the remaining ceramic powder alone will not have enough strength, so an additive must be used to provide additional mechanical support. In some cases, the dispersant used may be able to contribute some mechanical support through inter-particle adhesion, however this will depend on both the properties and concentration of the additive used. If the part green strength is still insufficient, then a binder additive must also be incorporated when preparing the ceramic suspension.

In later studies, the effect of adding a dedicated binder additive was explored, and the binder selected was Elvacite 2045 (Lucite International, Newton Aycliffe, UK) [85]. This binder is an acrylic resin, specified for offering clean burnout, while compatibility with ceramics and solubility in cyclohexane were both indicated.

The binder is supplied as a granular powder with a particle size of approximately 0.3mm. The solubility of the binder in cyclohexane solvent was observed to be lower than for the dispersant. To fully dissolve the binder, first the suspension was manually agitated by shaking vigorously for 1 minute, before the suspension was then placed on a mechanical roller (c.a. 250rpm). Rolling was performed for approximately 15 minutes, until individual binder particles were no longer observable in the suspension.

4.1.1.7 Ceramic addition

After preparing the carrier solvent and required additives, the ceramic powder can be added to produce a ceramic suspension. First, the required weight of ceramic powder is initially apportioned into a separate container. Then, powder is then gradually added into the solvent, with intermittent manual mixing performed using a thin stainless-steel spatula, in order to assist with incorporation of powder.

4.1.1.8 Solvent Top-up

While it is desirable to use a high-vapour pressure solvent for speed of freeze-drying, this also results in rapid solvent loss during suspension preparation steps that have the suspension exposed to the atmosphere. By recording the weight of the container, and the weight of each component (ceramic, dispersant, binder), the target weight of the prepared suspension with carrier solvent can be calculated. From this, before sealing the container, the container can be ‘topped-up’ to restore the desired quantity of solvent after evaporation. Since the solvent loss is primarily a function of time, and since the time required to manually mix in the powder into suspension can vary significantly, by making-up the lost solvent by weight, a consistent suspension solids concentration was able to be maintained from batch to batch.

4.1.1.9 Sonication

During the preparation of the ceramic suspension, a key goal is ensuring the suspension is well dispersed. Particle aggregates will naturally be present within the raw dry ceramic powder feedstock, and these must be broken down to avoid resulting in aggregates of low bulk solid density being included in the final product. The severity of aggregation will vary with both the surface charge of particles in suspension, and with the size of particles.

After all the suspension components are added, a Misonix S-4000 Sonicator (Qsonica, LLC, Newton, CT, USA) was used in order to break up large particle aggregates. Typically, for maximum energy application the sonicator horn is immersed into the suspension directly. The sonicator delivers significant acoustic energy (10-100W) into the suspension, which is then converted to heat, resulting in heating of the suspension. Again, here the high solvent vapour pressure presented an issue, as directly immersing the sonicator resulted in solvent loss, along with deposition of dried ceramic caking onto the sonicator horn, in turn resulting in an undesirable increase in particle aggregation. For each suspension sonication, the sonicator was set to on 40-60% power, and run for 5 minutes. Energy input was pulsed in 1s intervals.

Under these high suspension loading solids concentrations, even small losses of solvent significantly impact the properties of the suspension. To mitigate this effect, the both the sonicator horn and sealed plastic container of suspension were immersed in a small ice water dish. The addition of both water and plastic container wall between the horn and suspension significantly reduces the energy delivered to the suspension, so a higher sonication power (80%) was applied in order to maximise the energy transferred to the suspension. Ice cubes were also added as required to the water, in order to counteract the heating of the water occurring during sonication.

While the suspension was typically prepared and contained within a polypropylene container, with a polyethylene lid (as described in 4.1.1.4) the seal on the lid is not vapour-proof, and evaporation was observed to occur over time. To minimise evaporation, after sonication, the container of suspension was externally sealed by wrapping the lid and container interface with 6-8 layers of parafilm, in order to minimise vapour leakage.

4.1.1.10 Rolling

After sonication, the suspension container was placed on low-speed (c.a. 250 rpm) mechanical rollers (Ratek Instruments Pty Ltd, Victoria, Australia) for a minimum of 12 h, in order to maintain a homogeneous suspension composition. Rolling was not allowed to exceed 24 h, as gradual solvent evaporation results in an alteration of the expected suspension composition.

4.1.1.11 Verification of Solids Concentration

Before injection into the freeze-casting mould, the solids concentration of the suspension was measured, and compared to the calculated concentration. A small glass Petri dish was first labelled and weighted beforehand. A small portion of suspension (ca. 10-20 g) was delivered to the dish, and the weight immediately recorded using an analytical balance. While the weight measurement accuracy of the scale is within 10mg, some rapid solvent evaporation can occur between dispensing the sample onto the dish and recording the weight. By measuring the weight of the suspension container before and after delivering the sample, over a selection of measurements the solvent loss was calculated to be less than 100 mg in 98% of cases. After weighing the dish with sample, it was then dried in an oven at 80ºC for a minimum of 12 h, before a dried weight is recorded. With these measurements, the mass loss of solvent, and original suspension mass can then be used to calculate an accurate solids content concentration (dry weight fraction) for that suspension, as prepared:

$$Solids\ content\ (by\ weight) = \frac{container\ weight - \ dried\ weight}{container\ weight - \ wet\ weight}$$

4.1.2 Freeze-Casting Process

In order to examine the freezing step of the freeze-casting process, a set of processes were used to allow repeatable experiments, while still enabling a range of process conditions to be examined.

Firstly, the cold temperatures required for freezing are achieved by using an Operon DFC-84CE ultra-low temperature freezer (Gyeonggi-do, Korea), which features an adjustable temperature control down to -84°C. The temperature setpoint was measured by a thermocouple attached to the wall, in the corner of the internal freezer chamber. For more precise verification of the actual freezer and mould temperatures, an independent temperature measuring system was used. Multiple K-type thermocouples were connected to a National Instruments (Austin, Texas, USA) 16-channel thermocouple digital to analogue acquisition device (ADC), which is then connected to a PC with a National Instruments LabVIEW program running, which both displays and records the sensor temperature data over time. The use of multiple probes, enables the temperature to be recorded at several points, including:

- The temperature of the internal freezer wall
- The internal freezer air temperature
- The surface temperature of the mould, measured via a probe attached to the mould surface
- The bulk temperature of the mould, measured with a probe inserted internally
- The ambient laboratory temperature.

The accuracy of these probes was examined by measuring the freezing point of Millipore (Burlington, Massachusetts, USA) water (calibration test results provided in supplementary data) and were found to be accurate within ±1ºC.

In order to exert control of the rate of freezing over a broad range of speeds, two different freezing methods were used; pre-cooled mould freezing (fast), and ambient mould freezing (slow). Using two different methods enabled examining structures across a wide range of timescales, from a few seconds, to more than several minutes. The different methods used are explained below.

4.1.2.1 Fast Freezing: Precooled mould

For ‘fast’ freezing, the mould was first placed in the freezer, which is set to the desired freezing temperature. The bulk mould temperature was measured until the mould reaches the desired freezing temperature. 10mL of suspension was drawn up into a syringe (60mL), and the syringe was then tapped to dislodge any large bubbles in the suspensions, with the tip pointed upward. The mould was then removed from the freezer, and the syringe tip inserted into the port on the bottom of the mould. The suspension was then smoothly injected into the mould over approximately 3 seconds, until resistance was felt. The mould, with syringe inserted, was then slowly inverted so that the syringe was pointing downwards into the mould, and the mould and syringe returned to the freezer. Depending on the mould temperature, full solidification with a prechilled mould was typically complete in under a minute. After freezing, the sample was left in the mould for 5 to 10 minutes to continue to decrease in temperature, to ensure that the sample does not melt during removal and handling. The sample was then removed, with the mould being returned to the freezer to prechill again, before the freezing cycle was repeated for a new sample.

To reduce the incidence of sample sticking to the mould, the aluminium mould was plated with a nickel-Teflon coating. Additionally, to further assist with sample release after freezing, a thin layer of Krytox GPL204 PTFE-based low-temperature grease (Wilmington, Delaware, USA) was also applied to the mould surface.

4.1.2.2 Slow Freezing: Ambient mould

For ‘slow’ freezing, the freezer was first set to the desired freezing temperature, and the temperature was confirmed on the independent temperature measurement system. The mould remains at ambient room temperature (21±3°C) before the suspension was injected into the mould. After injection, the mould was then placed in the freezer to solidify. Depending on the freezer temperature, the full cooling and freezing process can take between approximately 0.5 to 2.0 h to complete. After freezing the sample can be removed, and then the mould warmed up, cleaned, and regreased, after which the cycle can be repeated.

After the freezing of each sample, the frozen part was placed in a labelled 20 mL polypropylene container, which is closed, and stored in the freezer while awaiting the next processing step.

4.1.3 Mould Design

The shaping of dense freeze cast samples was achieved using an aluminium mould. The shape of the samples produced were a simple cylinder shape. A cylindrical form was selected for the shape to be moulded, as this geometry results in a high degree of symmetry. This enables the freezing process to be considered approximately equivalent to a 1-D radial freezing process, freezing from the outside to the inside. This geometrical symmetry in turn provides a symmetry in the forces generated during most processing operations, avoiding stress concentrations at sharp internal corners or edges. This enables the ‘best-case’ evaluation of the dense freeze-casting process. Put simply, if it were not possible by any method to produce cylindrical boules without cracks, then the freeze-casting process would not be suitable for consideration for complex shaping.

For ease of injection, the mould cavity is fed by a tapered injection port, in turn leading to a conical sprue expanding to the full diameter of the mould. The injection port was designed to friction-fit with the tip of standard 60cc slip syringes. Injection is performed with the mould inverted, gradually filling the mould cavity via the port from top to bottom against gravity. Two air channels were incorporated into the bottom of the mould, to enable the displacement of air during suspension injection.

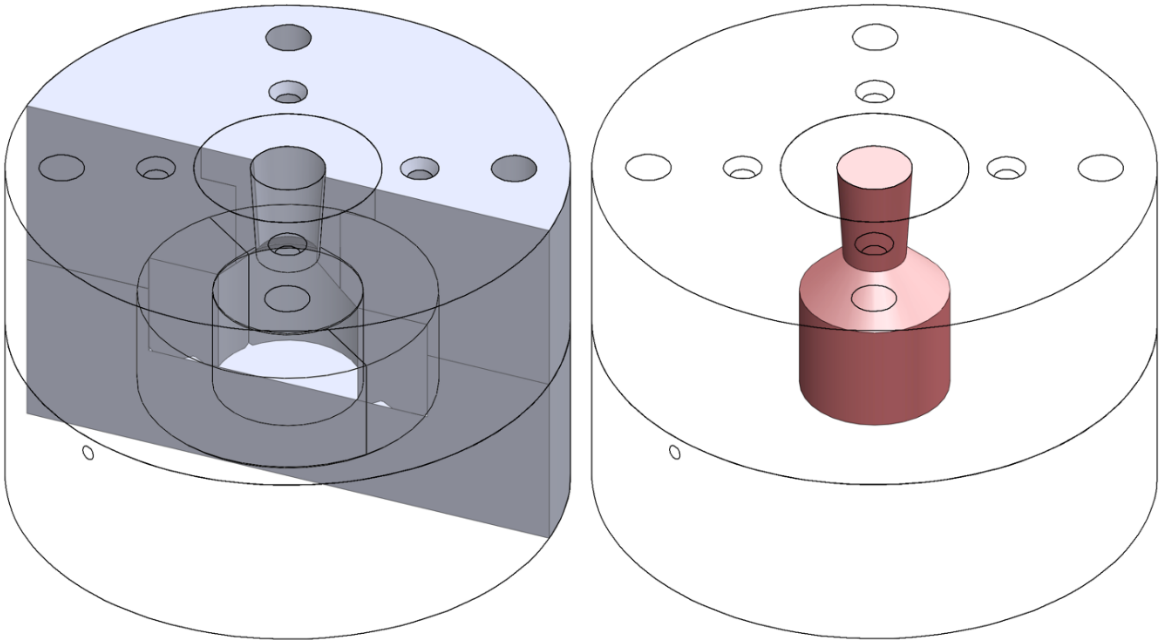

Figure 4.1.c: Cutaway of freeze-casting mould (left), and visualization of internal mould cavity (right)

The mould is comprised of multiple parts, to enable easy removal of the parts after casting. The standard configuration produces samples with a cylindrical region 20 mm in diameter (r_{max} = 10 mm), and 15 mm in height, while the mould is 75 mm in diameter and 50 mm in height. The large thermal mass of the mould, and good thermal conductivity of aluminium help to ensure the symmetry of the freezing conditions, and to minimise any non-isotropic effects from external air convection on the mould surface.

4.1.4 Freeze Drying

The solvent removal process is performed by placing samples into a freeze dryer (Telstar, Spain) for 26 h, at 0.1mBar. To load samples into the freeze dryer, first a metal tray is placed into the freezer to chill. The samples are then placed onto the tray, and the tray loaded into the freeze dryer. While the freeze dryer has multiple shelves, in order to minimise sample heating, close proximity to the warm freeze dryer compressor is avoided, so that only the middle and upper shelves are used for frozen samples. After drying, the samples can be removed from the dryer, and placed into labelled plastic containers and stored at room temperature before proceeding to the next processing step.

4.1.5 Sintering

After solvent removal, the green body samples must be sintered to achieve their final working strength. For oxide samples, this is completed using a high-temperature furnace (Tetlow Kilns & Furnaces Pty Ltd, Melbourne, Victoria Australia). For non-oxide samples, these samples are sintered in a graphite Red Devil RD-G furnace (R.D Webb, Natick, MA, USA).

The sintering process as used consists of five main steps:

1. Primary heating (10ºC/min)
2. Binder burnout (400ºC)
3. Secondary heating (10ºC/min)
4. Sintering at constant temperature (depends on material)
5. Cool-down (10ºC/min)

4.1.5.1 Dense Firing

For oxide ceramics, sintering is performed under conventional atmosphere, while for non-oxide ceramics, sintering is performed under argon above 1800ºC.

For oxide ceramics (Alumina and Zirconia), the temperature profile used includes a binder burn out at 400ºC, held for two hours, and a maximum temperature during sintering of 1550ºC. The maximum temperature was maintained for one hour, to prevent excessive grain growth. The temperature ramp set during heating was 10ºC per minute.

For non-oxide ceramics, the same binder burnout was performed at 400ºC, and held for two hours, followed by a temperature ramp set during heating of 10ºC per minute. For Titanium carbide, the maximum temperature was 2100ºC, held for one hour.

4.1.5.2 *Bisque Firing*

For some analyses, such as optical or SEM examination of the internal microstructure, samples must first be cut to reveal access to internal surfaces. While cutting of sintered samples is possible using a diamond saw, green samples are too fragile, and do not have sufficient integrity to allow being cut. As a compromise, samples can be partially sintered, or "bisque fired", using a lower temperature and a shorter sintering time to add sufficient strength for sample handling and cutting, without undergoing full densification. The full binder burnout process is still maintained, but by changing the sintering step conditions, densification of the microstructure can be minimised.

Bisque firing of oxide samples (Alumina and Zirconia) was performed by sintering at 1100ºC for one hour. This imparts sufficient strength into green samples, to allow cutting and polishing of samples, as required to prepare samples for examination under SEM and HEIM.

4.2 Sample analysis

After samples are produced, they may be examined by a range of non-destructive, and destructive tests.

4.2.1 Cutting & Polishing

In order to examine the internal sample microstructure under a scanning electron microscope (SEM), the samples must be cut, and polished to achieve a highly flat and smooth surface. Cutting is achieved with a diamond blade using a Struers Accutom-5, with cutting speeds of 3000 rpm, and feed rates of 20 mm/min.

After cutting, samples are fixed with epoxy (Epofix, Struers) into 30 mm sample pucks. The epoxy is then allowed to cure for 24 h, in order to harden sufficiently before proceeding with polishing.

To help highlight large cracks after polishing, a fluorescent dye may also be added to the resin.

Polishing of the cut surface is achieved using a Struers TegraPol-21 with TegraForce 5 polishing head, and TegraDoser 5 lubricant supply controller. In general, the same regimes were used independent of the ceramic material, however, the number of cycles required at a particular grit level was higher for polishing of harder materials. For polishing bisque samples, to avoid excessive material removal, a reduced number of cycles were used, especially when using coarser grits.

4.2.1.1 Polishing Procedure

1. Sample flattening and parallel grinding of both top and bottom using Piano magnetic sheet. Sheet is initially cleaned using a brief pass with an alumina cleaning stone.
2. The sample surface is smoothed and scratches are gradually removed, by stepping through a series of sandpaper grades, from 800, 1200, 2000, 3000.
3. The sample surface is then finely ground using MD-largo with green lubricant
4. Sample surface is polished using MD-Dur polishing cloth and various diamond polishing sprays, of 6 and 3 micron sizes.
5. The sample is finely polished to a high shine using OP-S and a MD-Nap polishing cloth.

4.2.2 Bulk density measurement

The bulk density of samples can be measured both before and after sintering, via two different methods.

For samples that have been sintered and that are dense, the sample bulk density can be measured via the Archimedes method, by weighing in air, and weighing while submerged in water.

The un-fired “green” bulk density can be obtained by coating the sample with paraffin wax, and then by measuring the weight via the Archimedes method, submersing in water on a balance scale. This is necessary, as if unfired samples are submerged, they rapidly absorb moisture and lose their structural integrity, mixing with the water to form an aqueous suspension.

The paraffin wax coating is applied by repeatedly dipping the sample in liquid wax that is heated to liquid state (approx.. 60-80ºC), and then removing the sample and allowing the sample to cool and the coating to harden. The first coating is applied with care to minimise bubbles being trapped on the sample surface, which would introduce error into the measured result.

The sintered samples have densified, and do not require this coating process before measurement. After the sample is submerged, stream of bubbles may exit the sample, indicating internal voids within the sample. The sample is left to remain submerged until the evolution of bubbles stops, before a measurement is taken.

The calculation of the bulk density of is as follows:

Bulk density = weight ÷ total occupied volume
= dry weight ÷ ((dry weight – wet weight) ÷ true density of water)

For the wax coated samples this is modified:

Bulk density = weight ÷ total occupied volume
= dry weight ÷ ((dry weight – wet weight) ÷ true density of water – wax weight ÷ true density of wax)

4.3 Sample Imaging & Imaging Analysis

Physical inspection of the samples plays a key role in this study; examining details including surface texturing, macroscopic cracking and voidage, internal microstructural features, porosity distribution, and the ceramic grain structure. Due to the broad span of length scales, and the range of both 2D and 3D features under study, a range of sample imaging techniques are required.

4.3.1 Optical Imaging

For capturing macroscopic images of samples, a digital camera was used, either as a dedicated device, or as integrated into a mobile device such as smartphone. Where possible, consideration was given to providing sufficient lighting to minimise noise and image shake issues, to produce clear and sharp images. A large depth of field is possible so this was used where optical images of curved surfaces were required.

For higher magnification images with a field of view spanning between 10 to 30 mm, microscopes fitted with digital cameras were used for image acquisition. The microscopes used include a “premier” microscope with up to 4.5x magnification, and a Nikon microscope fitted with a range of objectives up to 100x.

The depth of field achievable with microscopy is significantly reduced, and this limits using the technique to imaging details found on flat surfaces only. Image stacking was infrequently used in some circumstances, using the “ToupView” software provided by the microscope camera manufacturer.

4.3.2 SEM imaging

Higher magnification is required to study details including the microstructure and grain structure, and these details were obtained using SEM imaging. Cylindrical samples were prepared via cutting in half down the axis of symmetry, followed by polishing. Due to the lack of strength, unfired “green” samples are unable to remain intact after such a cutting process, so for SEM imaging, samples were bisque-fired, in order to impart sufficient strength for cutting and polishing.

Some samples were imaged uncoated, which was acceptable for titanium carbide samples. However, gold coating the samples was found to significantly improve the quality of images achievable, especially for Alumina samples. A high acceleration voltage of 10kV was used to provide sufficient contrast for the uncoated samples, with a low-vacuum used to minimise charging effects.

4.3.3 Micro-CT imaging

In order to gather 3D structural sample data, the use of micro-computed tomography (micro CT) was an essential technique used for this study. In this process, X-rays are passed through the sample, and the resulting shadow projection is recorded on a digital sensor. The sample is then rotated by a series of small angles to capture a complete rotational image series of projections, which is computed and reconstructed to synthesized a complete virtual 3D model of the sample. This process is non-destructive, and the resulting computed model can then be virtually cut or sliced to examine internal sample features, while leaving the original physical sample intact for further treatment or processing. This means that this technique is uniquely well-suited for imaging the internal structure of fragile unfired “green” samples.

Micro-CT scanning was performed with a Phoenix Nanotom m (GE Sensing & Inspection Technologies GmbH, Wunstorf, Germany) operated using xs control and Phoenix datos|x acquisition software (both GE Sensing & Inspection Technologies). This instrument features a square detector with resolution of 1200x1200 pixels.

Wet Al ceramic casts of 2.5 cm diameter were mounted on an Al disc attached to the end of a Deben cooling stage chilled by a peltier to ~-10°C. Dry casts were mounted on the same stage, but were not chilled. The position of the stage relative to the X-ray source and detector was optimized to achieve a resolution of 8.938 µm on a region of interest 2.7 cm wide and 2.15 cm high on the micro-CT detector. Samples were scanned for 10 minutes (timing = 500 mS, av = 1, skip =0) at 70 kV and 320 µA, collecting 1199 X-ray projections of each sample through 360° of rotation. Smaller Al ceramic casts (4 mm diameter) were mounted on a glass rod with the same diameter allowing for a higher resolution of 2.67 µm to be achieved. The smaller specimens were scanned for 15 minutes (timing = 500 mS, av = 1, skip =0) at 50 kV and 220 µA, collecting 1798 X-ray projections of each sample through 360° of rotation.

Volume reconstruction of the micro-CT data was performed using Phoenix datos|x reconstruction software (GE Sensing & Inspection Technologies) and data was exported as 16-bit volume files. Reconstructed data was exported as a stack of .tiff images for further analysis.

4.3.3.1 Sample Mounting

Sintered, bisque, or unfired “green” samples are placed on a vertical glass column, which was gripped in the rotating mount by a 3 jaw chuck.

The non-destructive nature of the micro-CT process also enabled the possibility to image samples that were still frozen. As a scan could typically take 10 minutes or more, and X-ray energy absorbed would heat the sample, this introduces a problem of sample melting. To avoid this occurring, samples were transported to the micro CT facility in dry ice, and continuously monitored to ensure they maintained temperatures below -20ºC (<30ºC typically). Inside the scanner, a specimen cooling unit was used. This unit has a refrigerated chiller providing cooling water, which in turn was connected to a primary thermoelectric cooler mounted on the sample rotation stage. A small metal disk was attached to this cooler to provide a flat and stable stage for which to mount the sample for scanning. The sample stage surface was measured at being stable around -5ºC, and after placing the sample on the stage, a plastic sample container was placed over the sample as a cover to thermally isolate the sample from the warmer atmospheric air. This setup was successful at maintaining the cold temperature, and successful at avoiding melting occurring in frozen samples.

4.3.4 Micro-CT Analysis Workflow: Reconstruction and Processing

Subsequent to capturing a projection series, several software tools were used to process, analyse, and visualise the captured dataset.

An example sequence of processing steps is outlined below, for exporting the internal crack microstructure as an 3D mesh file, suitable for animation.

4.3.4.1 Example Micro-CT Processing Workflow

1. The reconstruction and alignment correction of projection images was performed in the GE software called Phoenix Datos.
2. The resulting reconstruction was exported from the proprietary GE format, into a series of TIFF image slices, readily suitable for use in a range of software packages.
3. To reduce the size of the resulting model, the detail in the scan was reduced by a factor of three. This was achieved by a pre-processing step in the software "XNConvert", via a batch operation with the following parameters:
    a. **Sharpen** with intensity of 43. This was to increase the sharpness of edges and boundaries.
    b. **Median cross filter** of 3x3, and **Median box filter** of 3x3: These were used to reduce the noise in the images.
    c. **Resize** to 33.33%. Reducing the size of two dimensions by 3 reduces the size of the model by a factor of 9.
    d. **Masking Watermark**. A masking watermark was used to clear the data outside of the sample geometry. This mask was manually prepared in Paint.net from a slice near the centre of the sample, slightly overlapping the edge of the sample. After this step, the outer sample surface is removed, leaving only the inner microstructure. **A figure showing this step is below**
    e. **Levels**. A levels adjustment was used to rescale the black and white levels, in order to increase the contrast, such that ceramic sample regions were white, and that air or voidage regions were black
        i. White point: 68
        ii. Black point: 48
    f. **Adjust**. An adjust filter was used to segment the image slices into solid black and white regions.
        i. Brightness: 0
        ii. Contrast 127
        iii. Gamma: 1.00

The processed image stacks are then loaded into the software “ImageJ”, and processed with the following workflow, in this case to produce a 3D mesh of the internal void space.

1. ImageJ - image-> stacks -> tools -> reduce (or import with interval 3)
2. ImageJ -> process -> binary -> erode 8
3. ImageJ -> process -> binary -> erode 7
4. ImageJ -> plugin -> particle remover
    a. size: 15-infinity
    b. circularity 0-0.6
    c. show masks
    d. exclude on edges
5. ImageJ -> Edit->invert
6. BoneJ -> isosurface
7. ImageJ -> Edit->invert
8. 3d surface
9. export to STL

The STL that is produced requires a clean-up step. This is performed in the software “MeshLab”

1. MeshLab -> quadrature reduction
2. MeshLab -> select small component selection ratio 0.003
3. -> selected -> delete selected faces and vertices

This cleaned file can then be saved for visualisation or animation, which can be performed in any software capable of working with STL files, such as “ParaView” or “Blender”.

5 Preliminary study of dense freeze-casting process

5.1 Abstract

To date, freeze-casting has been primarily explored as a method for producing porous components. In this chapter, the viability of performing freezing-casting with a high solids-loading suspension was demonstrated to successfully produce near-dense components with complex shapes. Preparation of a highly loaded ceramic suspension with non-aqueous solvent was explored, and the maximum solids volume loading achieved was 55%, using 0.9wt% of Hypermer A70 as dispersant. By a dense freeze-casting process and pressureless sintering, near-dense alumina samples were produced with relative density exceeding 97% t.d.

5.2 Introduction

When novel materials are discovered or created, it is common for these developments to be communicated and promoted, by providing examples of the kinds of applications that their properties make them uniquely suited for. However, while unique physical properties may enable new applications, the mere existence of a material with desirable properties is insufficient to enable its practical use. For practical applications, in order to produce a part in the desired geometry, a material must be paired to a compatible process for shaping the material. It not always a certainty that the ideal shaping process for that material will be known at the time of discovery, and the development of an improved shaping process (such as improved efficiency or greater flexibility) has the potential to transform the suitability of the material for a wider range of applications.

The family of ceramic materials are a tantalising example of this; while they have many desirable properties, at present there is an absence of shaping processes available for economical, efficient mass-production of complex-shaped ceramic parts. Interest in freeze-casting as a shaping process has significantly increased over the last two decades, as it has been successfully demonstrated to be a powerful shaping tool in the production of porous materials across a range of material classes, including ceramics [86]. A significant attraction of the freeze-casting process is found in its demonstrated ability to create complex-shaped parts, while offering simultaneous co-ability to control and generate tailored porous microstructures within parts [44].

Across the field of freeze-casting, to date the majority of research has focused on exploring the capabilities of the process for the production of porous components [6, 44, 87], while the capability to control microstructure to produce dense components through the freeze-casting of highly loaded suspensions has been less extensively explored[56, 58, 79]. Another less-examined pathway for pursuing dense component shaping involves the use of non-aqueous solvents[9, 65, 66, 68]. By using alternative solvents with different crystal morphologies, the formation of large ice crystals observed with aqueous systems can be avoided, which is desirable for evolving fine pore microstructures that promote densification processes during sintering.

A preliminary investigation into the potential of specifically tailoring the freeze-casting process to produce dense components (referred to as "dense freeze-casting"), was previously performed by Silvia Leo, in 2014[27]. The results of her work confirmed the potential of the dense freeze-casting process, by successfully producing near-dense ceramic shapes from a selection of materials. However, these results also indicated potential critical process limitations, where internal examination of the dense freeze-cast revealed the presence of internal cracks of varying severity. The cause and mechanism responsible for these cracks is yet to be uncovered.

5.3 Aims

In this thesis, the intention is to restart a detailed exploration of the dense freeze-casting process using different ceramic materials. The focus of the preliminary study in this chapter is to establish fundamental processing parameters, including optimising the composition of the non-aqueous suspensions used for dense freeze-casting, and investigating optimal sintering conditions. The primary outcome desired is to identify maximum sintered bulk density achievable via the dense freeze-cast process. While working towards this goal, it is also of interest to identify the maximum solids loading possible while maintaining acceptable suspension viscosity. Additives will be used to assist with achieving a stable particle dispersion, and the optimal (minimum required) proportion of additive will also be evaluated. Finally, it is desirable to demonstrate the complex shaping capabilities of the process.

The studies in subsequent chapters then focus on exploring the relationship between other key process parameters and the resulting sample properties, including attempting to understand the previous findings related to internal sample cracking with different ceramic materials.

5.4 Theory

5.4.1 Suspension optimisation

From the review of the literature on conventional freeze-casting, several relevant processing factors were identified that affect the final bulk density of samples.

The first processing parameter identified was the solids concentration, or solids loading (volume fraction of solids) of ceramic particles in suspension. Previous reviews of freeze-casting studies indicate a close relationship between the suspension solids loading and the degree of porosity observed in the final sintered product [86]. Since the process of removing frozen solvent crystals is responsible for the evolution of pores in freeze cast samples, by reducing the volume fraction of solvent in the suspension, this consequently effects a direct reduction in the resulting volume fraction of pores in the dried samples, and hence an increase in the density of sintered samples. Since for dense freeze-casting it is desirable to maximise the sintered density, then it follows that it is also useful to achieve a maximal solid loading in the prepared suspension, with a minimum of added solvent.

For an ideal case with homogeneous monodisperse spherical particles, the maximum fraction of solids in suspension cannot exceed the ideal volume fraction of spheres in a random close packing (approximately 64%[88]), and will become limited at some solids concentration below this point, that depends on the magnitude of interparticle friction coefficients[89]. However, the ideal case is typically a lower limit: for most non-ideal cases the critical packing density can exceed 70%, such as for suspension with non-spherical particle geometries (e.g. ellipsoidal) [90, 91] and polydisperse, bimodal [92] or skewed particle size distributions [88]. However, for this work, the powders were simply used as supplied, and these factors were not explored further.

5.4.2 Suspension stability

It is well understood, that the performance of a colloidal system in a process, heavily depends on the preparation of the ceramic suspension, where a stable and homogenous colloidal dispersion is key towards achieving a high bulk density final product [93, 94]. For example, if settling occurs in suspension prior to freeze-casting, this could lead to anisotropy or inhomogeneities in the frozen component microstructure. This in turn can result in uneven densification occurring during sintering, leading to warping or flaws in the in the final sintered component. For high quality components to be successfully produced, a homogeneous particle dispersion is desirable, and particle setting or agglomeration in suspension must be minimised.

In preparing the ceramic suspension, the combination of exclusively non-aqueous solvent and ceramic particles alone was not pursued, as it was evaluated as unlikely to result in an optimum suspension. However, through the addition of a suitable dispersant, the stability of the suspension can be tuned. For non-aqueous solvents (with low dielectric constants) this addition typically involves the adsorption of dispersant polymers onto particle surfaces, thus increasing steric repulsive forces [95, 96].

The dispersant selected should be soluble in the solvent used, as well as having an affinity for the specific material that is being dispersed. Finally, while sufficient dispersant is required to ensure all the solid is well dispersed and that the suspension is stable, the addition of excess dispersant should also be minimised as this will result in an unnecessary increase in the suspension viscosity.

5.4.3 Viscosity Limitations

With the intention to optimise the suspension composition for maximum product bulk density, this goal was constrained by the essential requirement to also maintain a suspension viscosity suitable for processing. While it was desirable to minimise the fraction of solvent in the suspension, competing demands required that sufficient solvent be retained in suspension so that the suspension viscosity remained suitably fluid for the injection process. However, the challenge of maintaining a suitable suspension viscosity was especially complex. In addition, the suspension concentration influences the degree of non-Newtonian rheological behaviour observed[97, 98]. Highly loaded particulate suspensions typically are strongly shear-thinning at lower shear rates, while at very high shear rates can become shear-thickening [99, 100] . For this reason, the expected shear rates that the suspension is exposed to were also given consideration, as the injection conditions and mould design significantly impact the resulting flow behaviour, and hence affect both the limiting suspension solids concentration and define the pressure requirements for injection moulding equipment.

For suspension injection to be economically feasible under mass production, the injection and casting should ideally be possible under low-pressure injection. Under the shear conditions experienced during low-pressure injection, the suspension behaviour must still be suitably fluid, so that it is able to flow into the mould to capture fine details, while also enabling air to be evacuated. If the suspension is at too high a solids concentration, under high injection pressure the suspension may shear-thicken and jam, preventing flow. The suspension viscosity must also be sufficiently fluid, that it is possible to complete the entire mould injection process rapidly – typically within seconds. The speed of injection mould filling is important, as it ensures that that the progression of the freezing-front occurs continuously. For traditional plastic injection moulding, a high rate of injection must be maintained, to prevent early-solidification of the hot melt occurring before mould-filling is complete. Similarly, if a high-throughput freeze-casting process is imagined, the fastest way to freeze samples would be using actively cooled (i.e. pre-chilled) moulds; in that scenario, a fast injection rate would also be required to ensure complete mould-filling before solidification occurs. If the mould filling speed is not fast enough, the motion of the freezing front may overtake and solidify prematurely, potentially resulting in incomplete mould filling, or discontinuities in solidification microstructure as liquid suspension flows over solidified features.

5.5 Method

In the preparation of the ceramic suspension, a non-aqueous solvent and dispersant system was selected, as this enables the examination of both oxide and non-oxide ceramics. The ceramic materials studied were TiC (H.C Starck, Munich, Germany) and alumina (AKP-15, Sumitomo Co., Tokyo, Japan[81]) powders. The mean particle size for these powders were 1.5 µm and 0.65 µm, respectively.

The carrier solvent selected for this preliminary study was cyclohexane, as it possesses several attributes that make it highly suitable for use as a carrier solvent for freeze-casting, including:

- Non-aqueous solvent, for compatibility with both oxide and non-oxide ceramics
- Low viscosity at 25ºC (0.892 mPa.s) [101]
- Easily-accessible freezing point of 6ºC [102]
- High vapour pressure for rapid solvent removal via sublimation [102]
- Readily available industrial solvent [103]
- Manageable safety and health risks, non-carcinogenic [104, 105]

Hypermer A70 (Croda, England) was selected as a dispersant, the family of which are known to offer good rheological performance at high solids loadings [100]. This specific dispersant is a high-

MW non-ionic polymeric surfactant, that is both soluble in the solvent, and also indicated as suitable for use with ceramic suspensions [106]. Past experience working with this carrier solvent and dispersant system with different ceramic materials has been successful at achieving suitable viscosities at a dispersant concentration of 0.5 wt.%, relative to the weight of solid ceramic in suspension. For this study an initial dispersant concentration range up to 1.5 wt% was explored[33]. Similarly, previous suspension formulations at 50 vol.% of ceramic powder were able to be prepared successfully, so concentrations starting slightly below this were used for the initial suspension ceramic concentration in this study. Following an optimisation of the dispersant concentration, the maximum practical solids concentration can then be determined experimentally for these ceramic materials studied. Following optimisation of the suspension formulation, the subsequent process steps can be demonstrated, including freeze-casting, freeze drying, and sintering.

Performing freeze-casting requires both a mould, and a method for cooling the suspension below the freezing point of the carrier solvent. Casting of samples was performed by injecting suspension into a cylindrical aluminium mould of 20mm internal diameter. Suspension injection and freezing was performed both with the mould at ambient room temperature, and with the mould pre-chilled to the freezer temperature. Samples were placed into an ultra-low temperature blast freezer (DFC-84CE Operon, Korea) at three different temperatures (-80ºC, -40ºC, -20ºC). More details of the mould, other apparatus and procedures are given in Chapter 3.

After solidification was completed, solvent removal was achieved via sublimation, by drying samples in a freeze-dryer (Telstar, Spain), for a minimum of 24 h at 0.1 mBar.

The alumina green body samples were sintered in an oxide air furnace (Tetlow Kilns & Furnaces Pty Ltd, Australia, max temperature of 1700°C). Typical process conditions for producing dense alumina samples were obtained from the literature, with sintering temperatures of 1500°C, and hold times of 2 h generally indicated [107], times as long as 5 h [56], and temperatures as hot as 1700°C [108] have also previously been demonstrated. While our primary goal on this study is the maximisation of sintered bulk density, consideration should also be made to minimise excessive sintering durations in order to avoid coarsening or large grain growth.

Previous work in our group with pressureless alumina sintering was performed at 1500°C for 2 h, achieving 97.1% of theoretical density (%T.D.)[109]. Araki and Halloran achieved 98.4%T.D. by the freeze-casting of non-aqueous 50.8 vol.% alumina suspension, with sintering at 1600°C for 4 h. A high sintered bulk density of 99.5% T.D. was recorded in the literature for slip cast samples sintered at 1550°C for 2 h[110], and this sintering profile was selected for this study. Before sintering, a binder burnout step was performed by holding at 400°C for 2 h, with heating rates of 5°C per minute during temperature ramps.

Following sintering, samples were then cut using an Accutom-50 diamond saw (Struers, Denmark) and then polished via TegraPol-21 (Struers, Denmark) for macro- and micro-structural imaging under optical microscopy and SEM. As green body samples are too fragile to cut without damaging the region of interest, a selection of green body samples was first bisque fired at 1100ºC for 1 h. This was done in order to impart sufficient strength for samples to survive cutting and polishing, thus enabling examination of the un-densified microstructures.

Additional (uncut) samples were used for bulk density measurement via the Archimedes method in water. For undensified (bisque-fired) samples, samples were first coated in paraffin wax before bulk density measurement.

In addition to the samples prepared by casing in the cylindrical mould, the same suspension was used to prepare complex-shaped samples, by pouring the suspension into silicone ice-cube and confectionary moulds before placing filled moulds in the freezer. These samples underwent the sample sintering regime as the standard geometry test samples.

5.5.1.1 Rheological Measurement

The rheological properties of the prepared suspension were quantified through experimental measurement using an AR-G2 rheometer (TA Instruments, New Castle, Delaware), operating as a Couette viscometer. The geometry used for this test was a concentric cylindrical (DIN standard Bob and Cup, with 27.7 mm dia., 40 mm length Bob and 30.0 mm dia. Cup) shear cell. As the inner cylinder rotates, this induces drag on the fluid, and by measuring the drag resistance the flow behaviour can be characterised under a specific shear rate. The rheometer records the applied torque to the inner cylinder, while recording the resulting rotational shear rate, A continuous shear ramp of 1 s^{-1} to 1000 s^{-1} , was used to characterise the relationship between shear rate and viscosity, which is typically non-newtonian for highly loaded suspensions[98]. Each shear rate condition was sampled for 10 s, and 10 points were sampled per log decade. 20 mL of fresh suspension were used for each test.

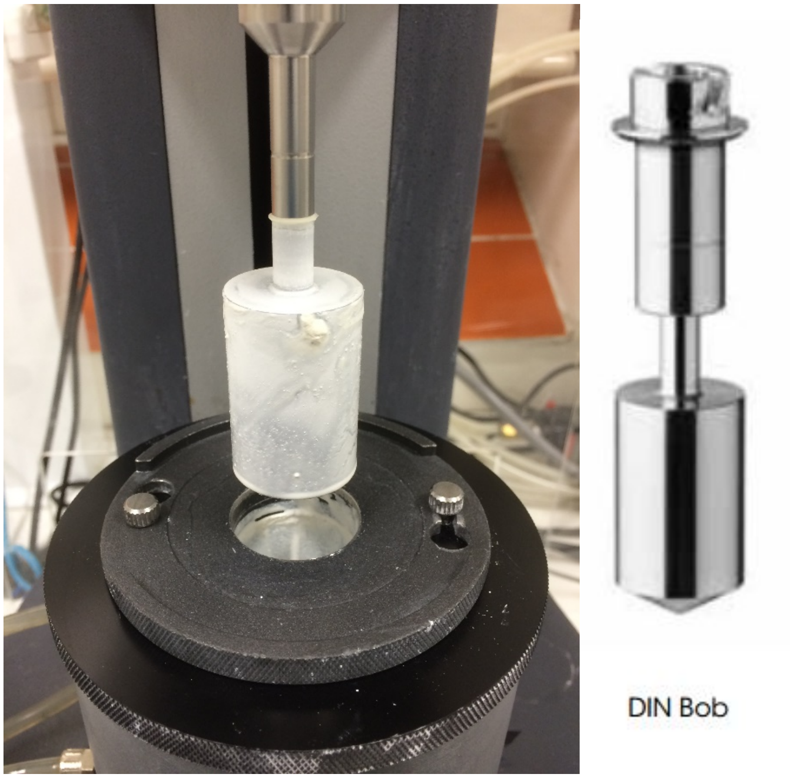

Figure 4: (left) Photo of DIN Bob and Cup following suspension rheology test. (right) Standard DIN Bob

5.6 Results

5.6.1 Rheology Results

The combination of cyclohexane solvent and Hypermer dispersant were successful in producing a stable suspension at a moderate loading of 40 wt.% solids concentration, for both TiC and alumina ceramics. First, the relationship between dispersant concentration and viscosity was examined using an AR-G2 rheometer (TA Instruments, Delaware). Initial testing indicated that for 40 wt.% TiC suspension the minimum viscosity was obtained for a dispersant concentration of 1 wt.% (see Figure 5.8.a), while increasing the concentration of dispersant did not significantly increase the viscosity until the dispersant concentration exceeded 2 wt.%. For 40 wt.% Alumina suspensions, the lowest measured viscosity again was found to occur with the addition of 1 wt.% of dispersant (see Figure 5.8.b), however higher dispersant concentrations resulted in significant measurable increases in suspension viscosity at all shear rates. The higher dependence of the alumina suspension viscosity on dispersant concentration may in part be due to the lower starting viscosity of the alumina suspension. This in turn could be due to both differing particle surface interactions, as well as due to differences in particle shape and size distributions between the ceramic powder feedstocks.

Further tests were performed in order to obtain a more precise optimal dispersant concentration. The relationship of dispersant concentration and viscosity can be measured with more highly loaded suspensions, as at higher solids loadings the effect of varying dispersant concentration on viscosity is amplified, enabling the optimal concentration to be determined more accurately.

After establishing a baseline dispersant concentration of 1 wt.%, the preparation of suspensions with higher solids concentration was examined. Firstly, new suspensions were prepared at a range of higher ceramic solid loadings using 1 wt.% dispersant.

For TiC even at moderate solids loadings (40 vol.%) the suspension flow properties were already observed to be noticeably viscous, and when increasing the concentration further above 58 vol.% the viscosity increased rapidly (see Figure 5.8.c and Figure 5.8.b). This higher viscosity resulted in difficulties in achieving a homogenous well-mixed suspension, as well as making the suspension unsuitable for practical mould injection by hand. For this reason, TiC suspensions were found to be practically limited to 54 vol.% solids content. For 54 vol.% TiC suspension, a concentration of around 1.5 wt.% Hypermer A70 resulted in the lowest measured suspension viscosity over higher shear rates (see Figure 5.8.b and Figure 5.8.d).

During the measurement of these suspension viscosities, it was found that the data obtained at higher shear rates would become noisy and unreliable. It was determined that this was a limitation of the equipment, where the maximum torque limit of the viscometer was exceeded for highly viscous suspensions being sheared at such high rates. An alternate MCR702 rheometer (Anton Paar, Graz, Austria) was used for subsequent measurements, so regrettably not all rheology series are directly comparable.

To improve the accuracy of viscosity measurements, lower viscosities of 45 wt.% were used to optimise the alumina suspension concentration. For 45 vol.% alumina suspensions, 0.9 wt.% Hypermer A70 was determined optimal, resulting in the lowest measured suspension viscosity (see Figure 5.8.e and Figure 5.8.b). The rheology at higher suspension concentrations was then investigated, with well-dispersed alumina suspensions successfully prepared up to 55 vol.% (see Figure 5.8.f and Figure 5.8.b), and found to possess reasonable viscosity for practical injection by hand.

5.6.2 Freeze-Casting

Frozen samples were prepared via injection into both ambient temperature moulds and prechilled moulds. A range of freezer temperatures were used to provide some control over freezing rate during solidification. Following freezing, the solvent was sublimated, and the samples sintered. Both sintered and bisque fired samples were successfully prepared for each process condition. Further information related to the influence of freezing conditions on the bulk density, microstructure and cracking are presented in chapter 6.

5.6.3 Complex Shaping

Using simple non-porous silicone confectionary moulds, samples were prepared following the dense freeze-casting procedure. Generally, very good detail reproduction was obtained from the mould (see Figure 5.6.a and Figure 5.6.b), with even the mould surface texture being well reproduced. Some void defects from bubbles were observed on the cast samples, and this was attributed to the simple moulding method. For samples with complex or deep features, demoulding the samples without damage was challenging. Using a mould release agent would be expected to assist with this process.

Frozen-state sample

Dense sample after sintering

(White appearance due to ice build-up)

Figure 5.6.a: "Han Solo In Carbonite", Dense Freeze Cast in Titanium Carbide, approx. 22x52x6mm after sintering.

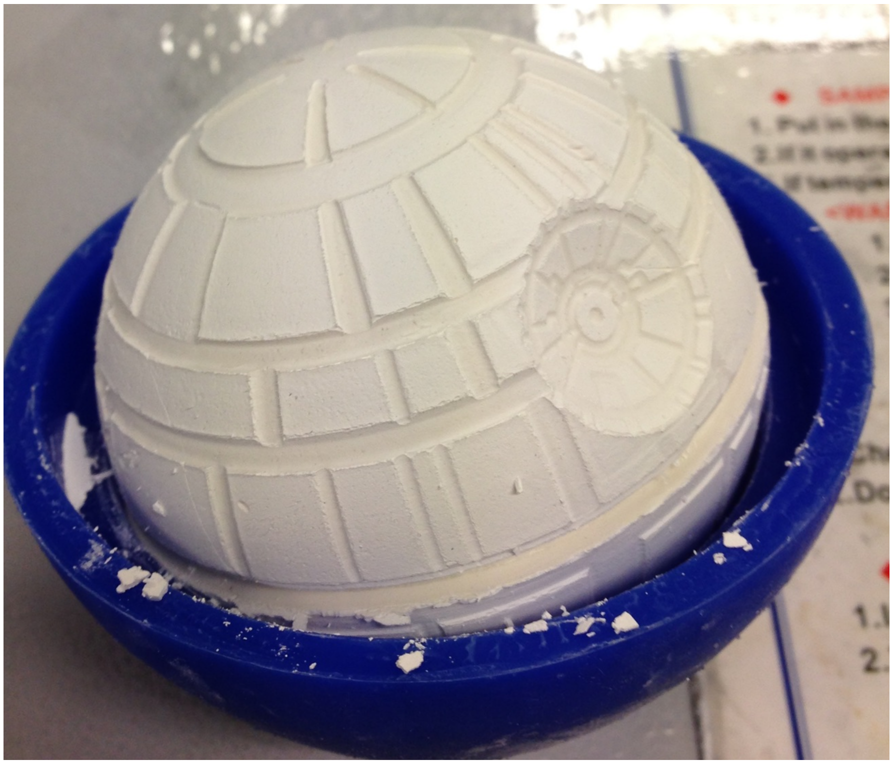

Figure 5.6.b: "Death Star", Dense Freeze Cast in Alumina.

5.6.4 Sintering

Testing the bulk density of sintered samples via Archimedes method showed (plotted in Figure 5.8.g) that the highest sample density was achieved for 55 vol.% suspension frozen in an ambient mould at -40ºC, with a bulk density of 3865 kg/m^3 measured, corresponding to 97.8 %.T.D. For TiC, pressureless sintering in a graphite furnace in argon resulted in lower densities of 91.5%. Further information related to the influence of freezing conditions on the bulk density, microstructure and cracking are presented in chapters 5 and 6. Sample shrinkage was observed post-sintering due to densification of around 14-15 vol.% (see Figure 5.8.h: Dimensional shrinkage of 1550ºC sintered alumina samples, by feed-suspension solids loading and by casting freezer temperature.Figure 5.8.h) , but no issues were encountered with warping, and detail reproduction from the green-body cast sample was well replicated without loss in the sintered sample (Figure 5.6.a).

5.7 Discussion

In consideration of the goal to produce smaller ice crystals, a higher solidification velocity was pursued by using a lower freezer temperature and injecting under pre-chilled mould conditions. However, as the temperature was below -85°C at all times, only the cyclohexane ice phase I could form. After freeze drying, this is expected to result in corresponding smaller pores in the dried microstructure. In turn these smaller pores would be expected to result in greater densification rates during sintering, resulting in higher final sample densities. Contrary to expectations, as seen in Figure 5.8.g, the highest observed densities were obtained for samples frozen at the 'medium' freezing temperature, -40ºC. While only one sample was prepared for each condition, there does seem to be consistent results when examining both the sintered (top) and bisque-fired (bottom) samples, with a measurable increase in bulk density observed at -40ºC. Additionally, for the 55 vol.% suspension, the ambient-temperature mould samples produced a consistently higher density product than the pre-chilled mould samples, and this trend is consistent across both the bisque and sintered samples. This challenges the theory that faster freezing would result in a more favoured microstructure for obtaining samples with higher bulk density. This unexpected phenomenon may be due to larger cracks in the slow-frozen samples enabling internal porosity to be accessed during density measurement, unlike for fast-frozen. However, it was also observed that using a higher solids loading does have a corresponding positive relationship with product bulk density, as was expected.

This suggests that the microstructure produced by pre-chilled moulds may not be favourable for densification, or, that perhaps the significantly faster freezing rate in pre-chilled moulds has resulted in internal air bubbles or other defects being trapped during solidifications, and thus resulting in lower effective measured final densities. As discussed later in chapter 5, the use of non-aqueous cyclohexane solvent was successful in resulting in smaller dendrite sizes than observed in aqueous prepared suspensions.

Sample shrinkage following sintering was observed, and this shrinkage would need to be accounted for in the preparation of the freezing-mould geometry, in order to produce a sintered part of the correct desired dimensions. This would likely require further investigation to optimise.

5.8 Conclusions

This chapter has demonstrated that the Freeze-Casting process can be used with hard or flexible complex shaped moulds, to produce dense complex shaped ceramic components that capture both the mould geometry and surface finish. For alumina ceramic parts, atmospheric pressureless sintering at 1500°C was able to result in fully dense parts, with relative densities approaching 98%. Well-dispersed non-aqueous alumina ceramic suspensions were prepared with high solids loading of 55 vol.% using 0.9 wt.% dispersant, while maintaining sufficient fluidity for manually injecting suspension into moulds via a syringe. For TiC, the maximum practical solids loading obtained was 54 vol.%, with 1.5 wt.% dispersant. This study also indicates future examination of sintered samples should be pursued via cross-sectional cutting and/or X-ray imaging could potentially to reveal if large pores are present internally as is presented later in chapter 5.

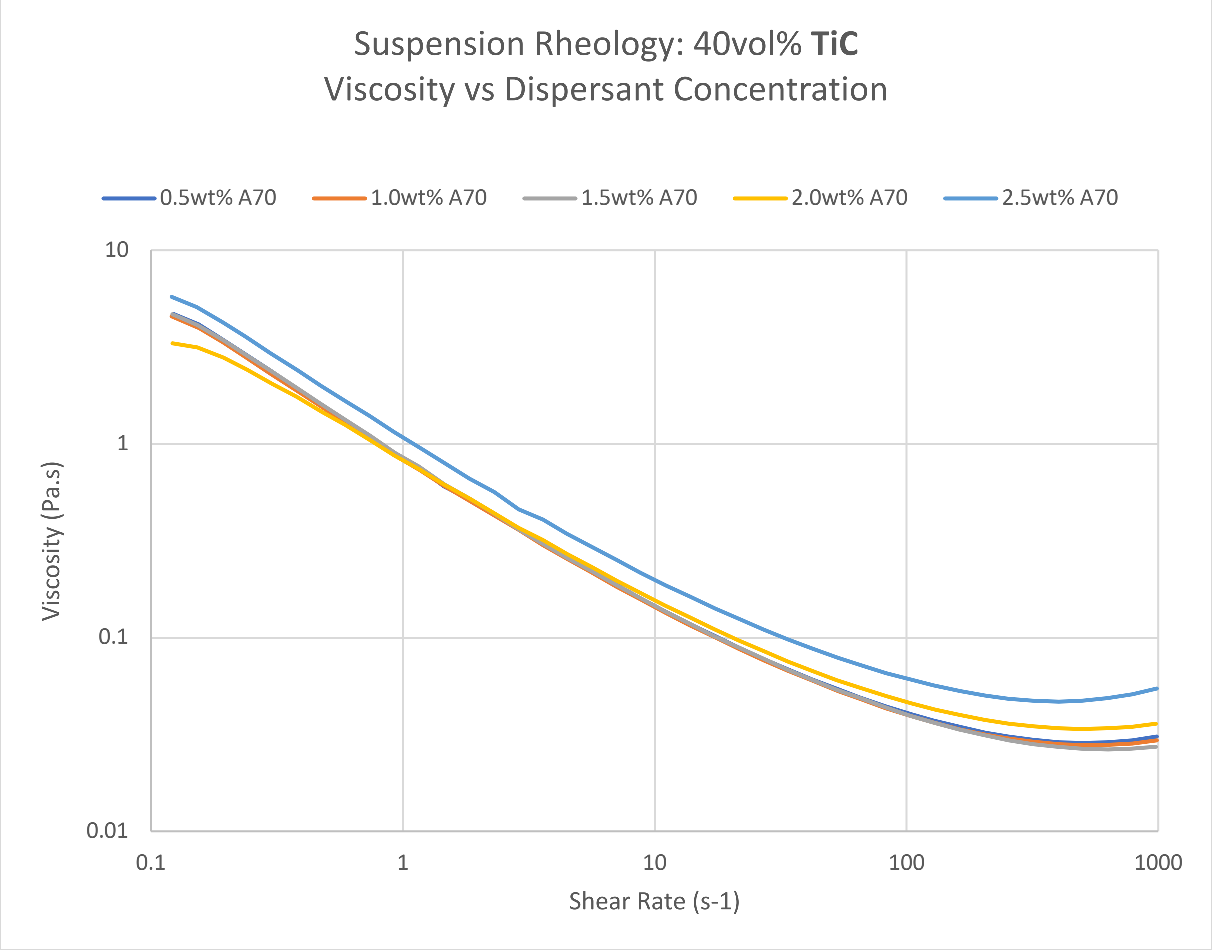

Figure 5.8.a: Rheology of moderately-loaded (40 wt.%) TiC non-aqueous suspensions: Dispersant Concentration vs Viscosity, measured via AR-G2 rheometer.

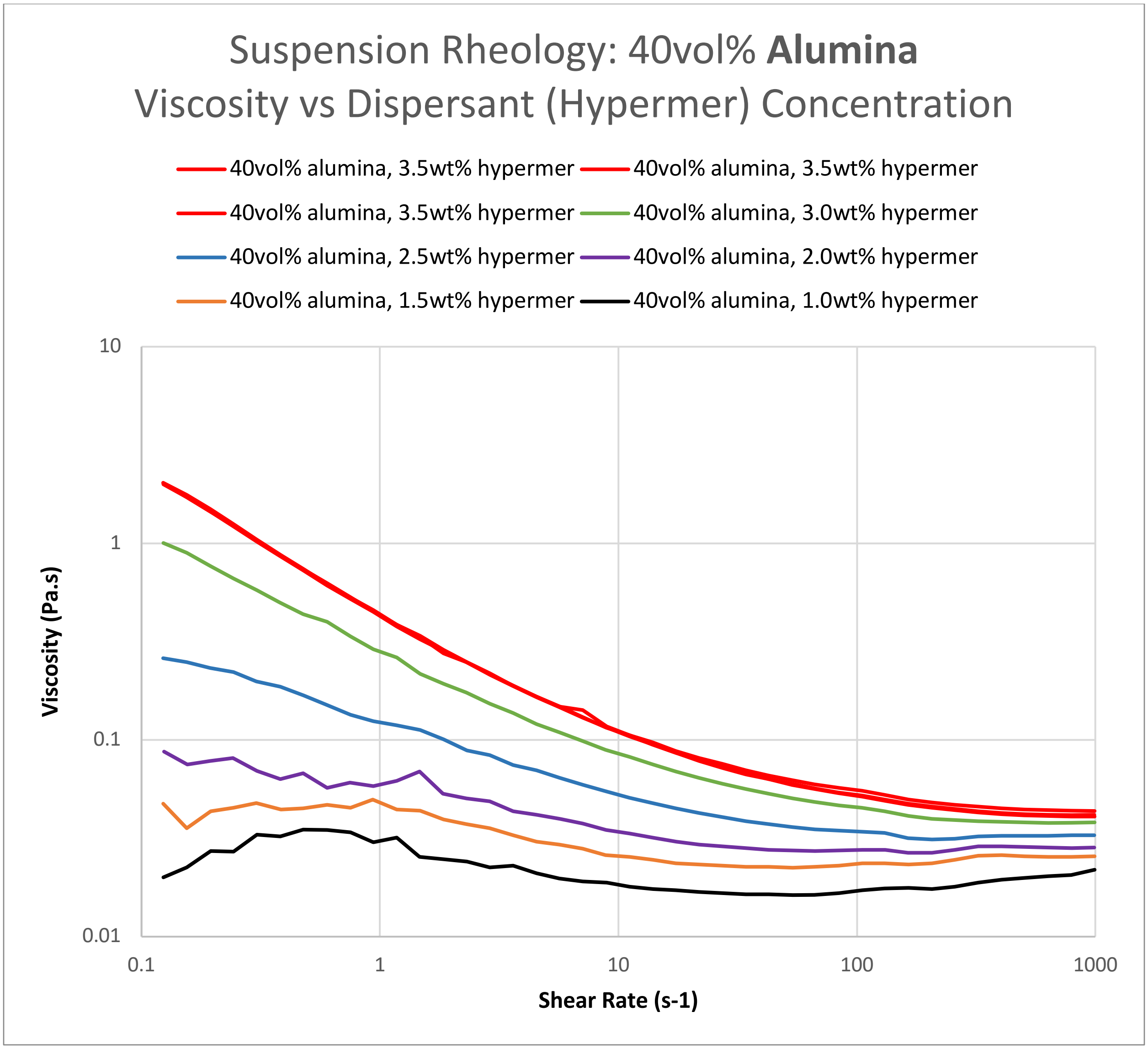

Figure 5.8.b: Rheology of moderately-loaded (40 wt.%) Alumina non-aqueous suspensions: Dispersant Concentration vs Viscosity, measured via AR-G2 rheometer.

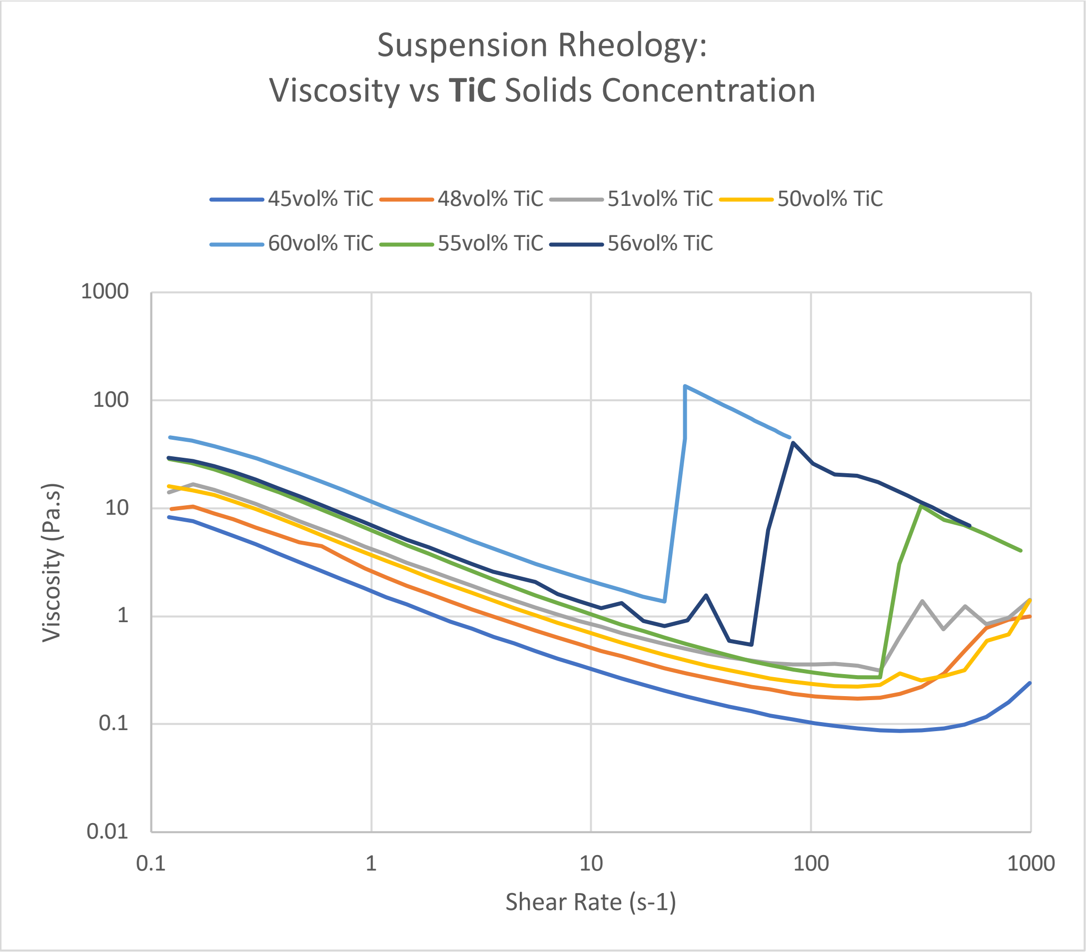

5

Figure 5.8.c: Determining maximum practical solids loading: Rheology of highly-loaded TiC non-aqueous suspensions with 1 wt.% dispersant: Solids Concentration vs Viscosity, measured via AR-G2 rheometer.

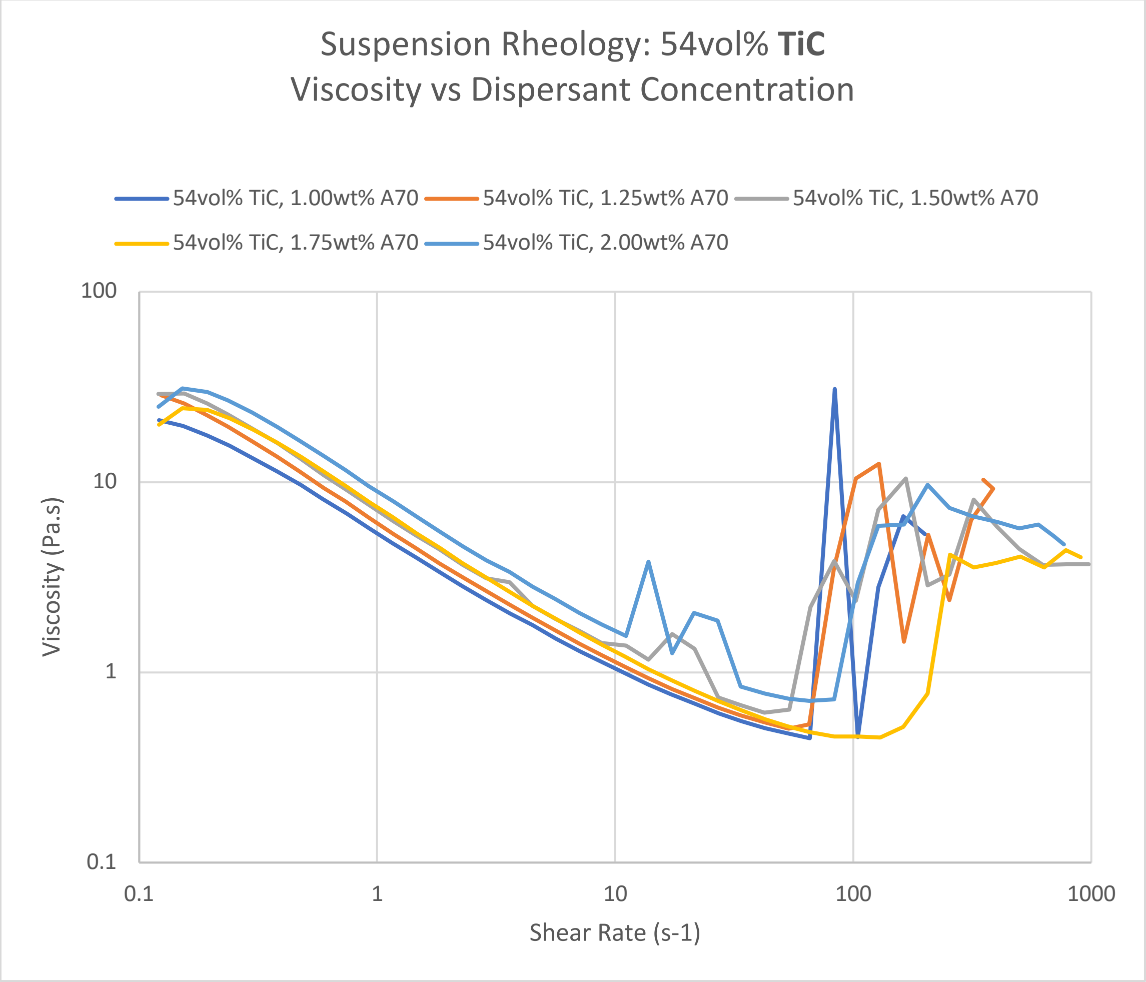

Figure 5.8.d: Rheology of TiC non-aqueous highly-loaded suspensions: dispersant concentration vs Viscosity, measured via AR-G2 rheometer.

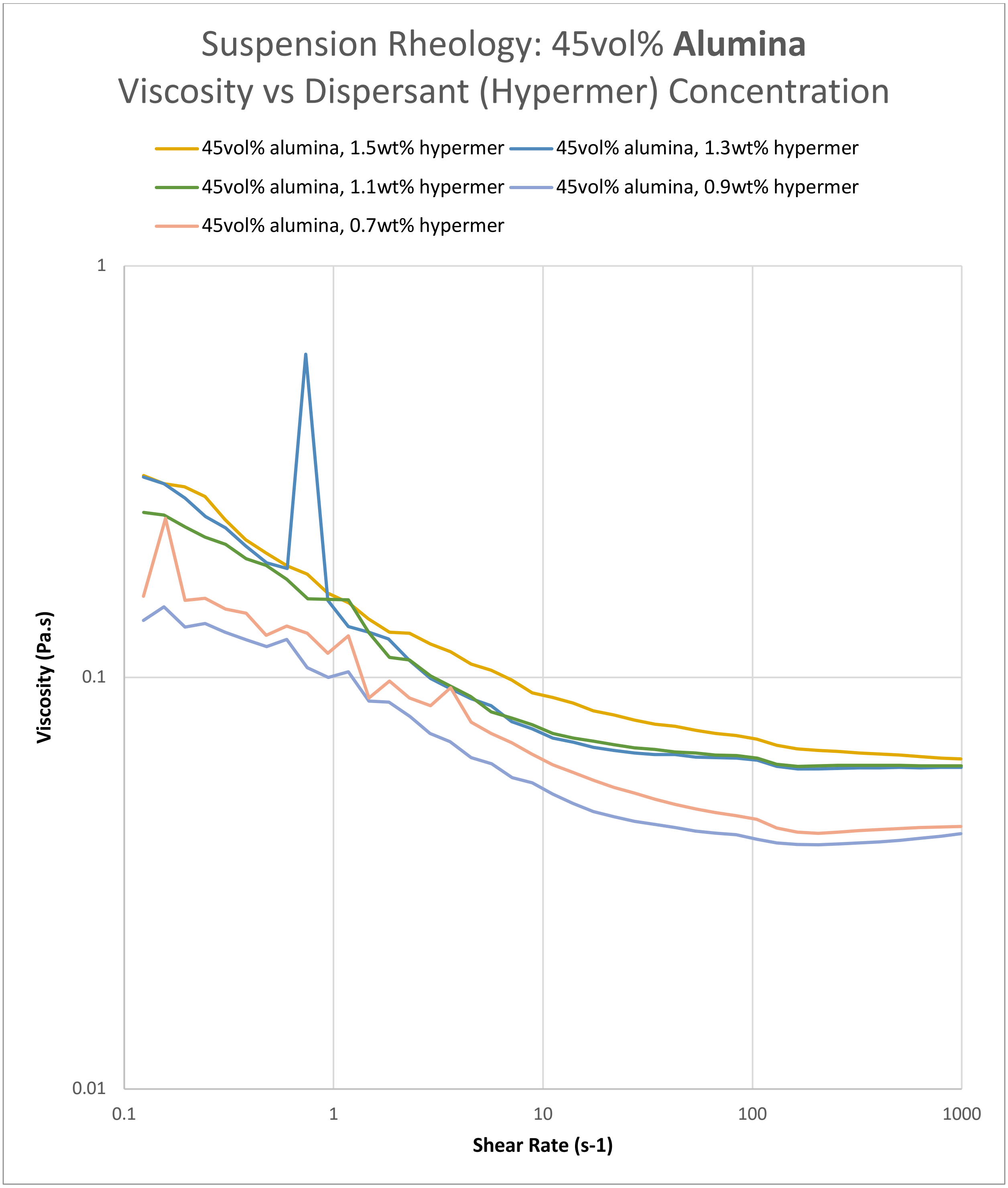

Figure 5.8.e: Rheology of Alumina non-aqueous highly-loaded suspensions: dispersant concentration vs Viscosity, measured via AR-G2 rheometer.

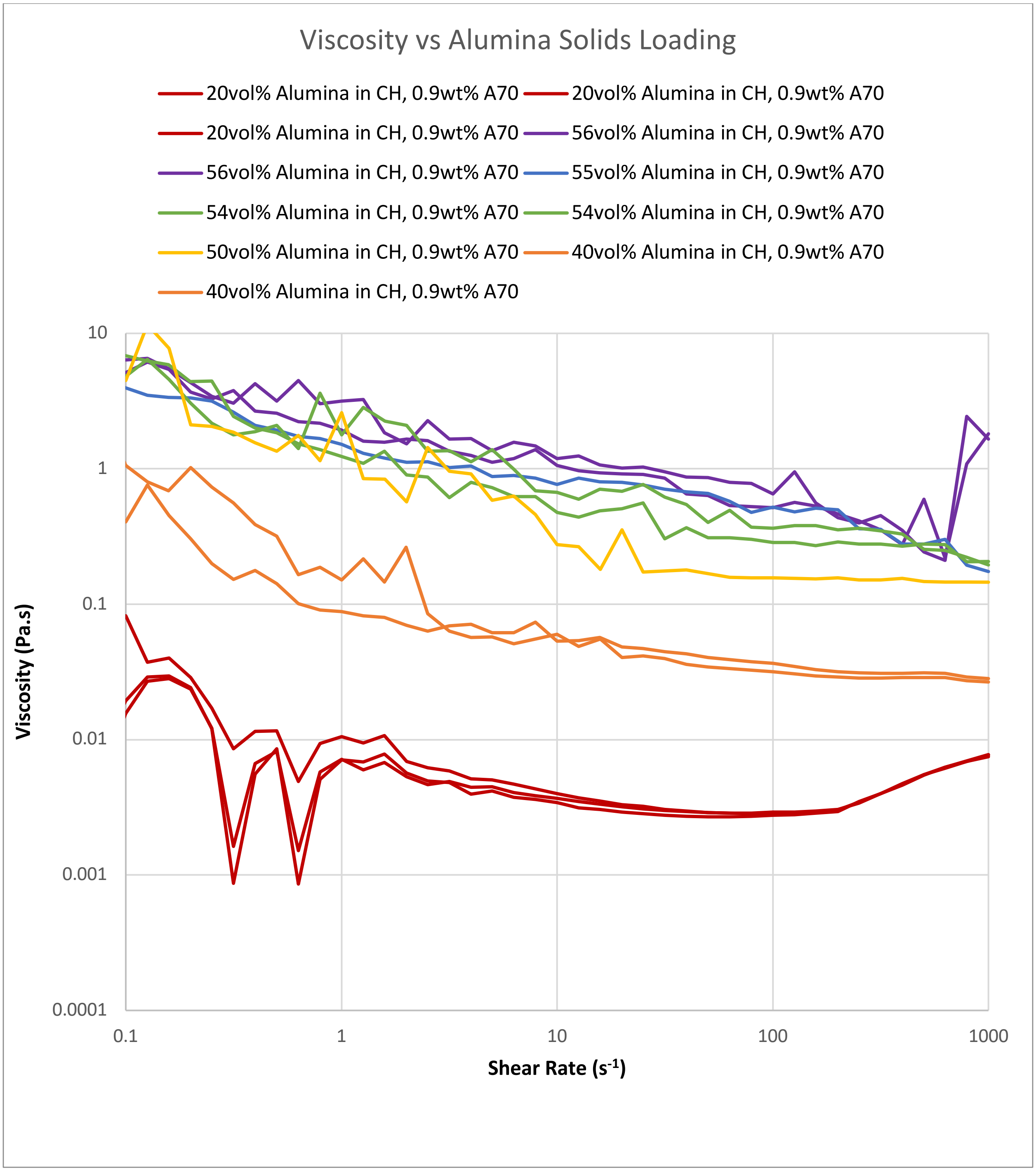

Figure 5.8.f: Rheology of Alumina non-aqueous suspensions, across a range of solids concentration vs Viscosity, measured via MCR702 rheometer.

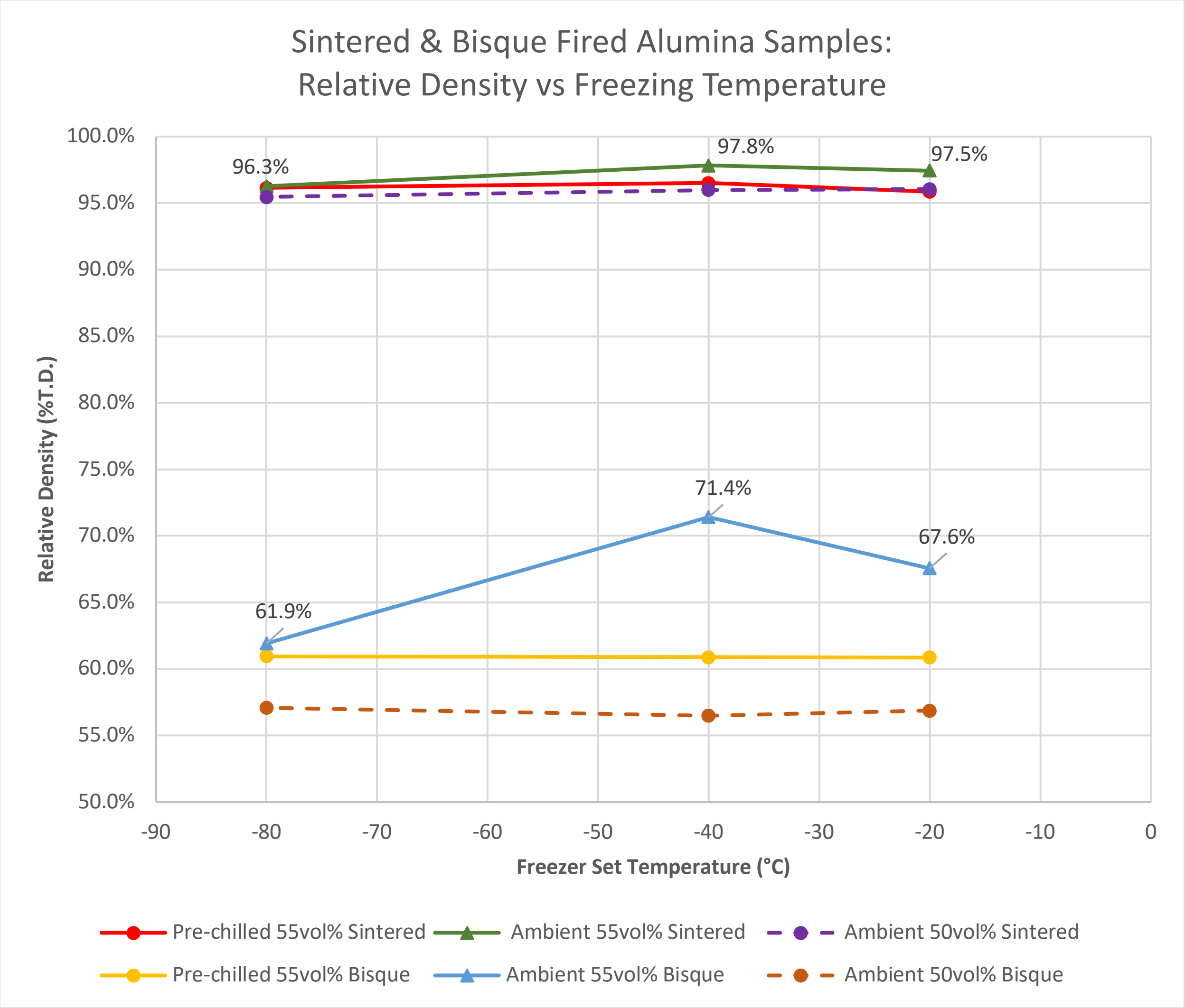

Figure 5.8.g: Bulk density of Alumina samples after sintering and bisque firing, at 1550°C and 1100°C respectively.

Sample #	120	125	130	135	138	141	142	163	168
Target Ceramic Solids Loading (vol.%)	50%	50%	50%	55%	55%	55%	55%	55%	55%
Actual Ceramic Solids Loading (vol.%)	53%	53%	53%	58%	58%	58%	58%	58%	58%
Freezer Temperature (ºC)	-20	-80	-40	-80	-40	-20	-40	-20	-80
Green Sample Diameter (mm)	19.8	19.93	19.92	20	19.93	20	20.07	19.99	19.99
Sintered Sample Diameter (mm)	16.86	16.98	16.84	17.2	17.19	17.19	17.18	17.15	17.15
Sample Diameter Shrinkage (%)	15%	15%	15%	14%	14%	14%	14%	14%	14%

Table 3: Sample Dimensions, before and after sintering, Alumina, sintered 1550°C for 1h.

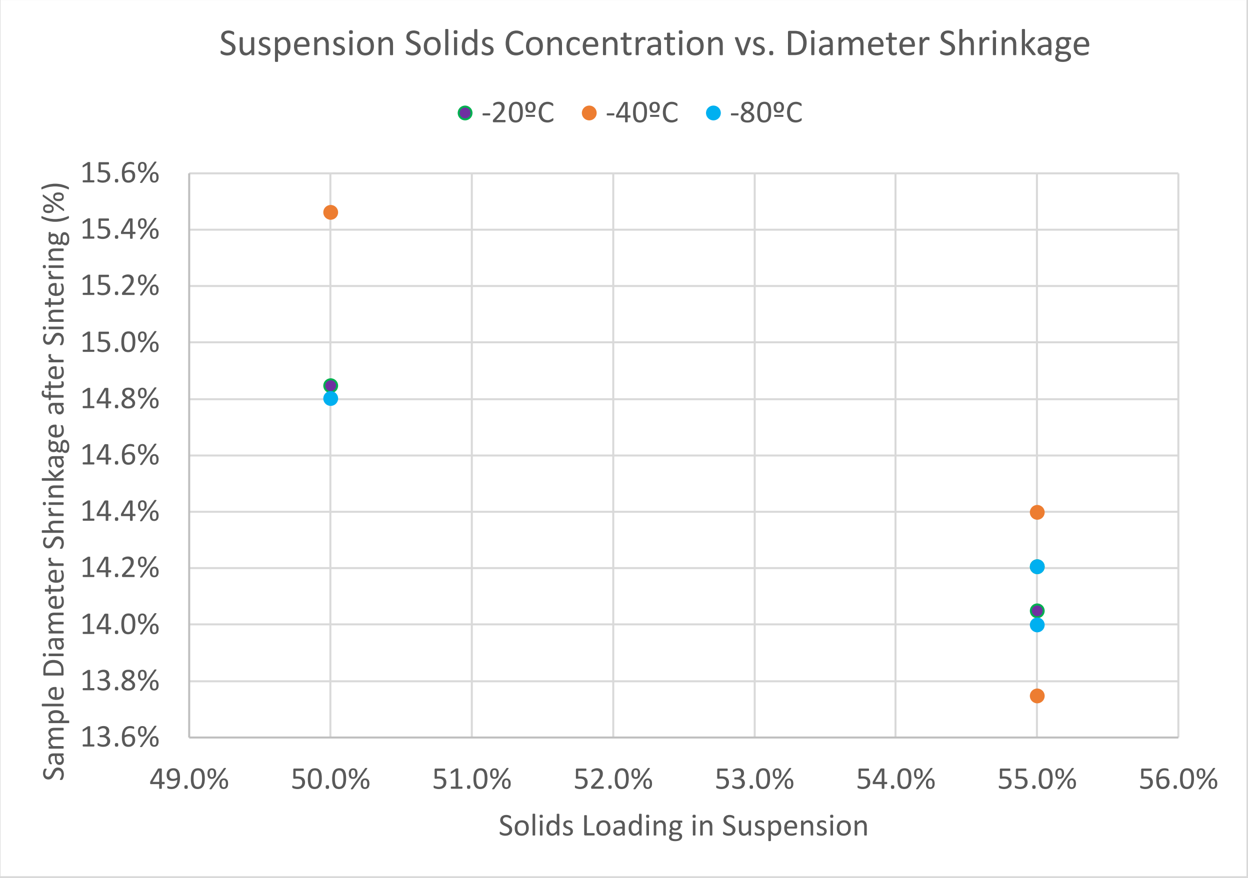

Figure 5.8.h: Dimensional shrinkage of 1550°C sintered alumina samples, by feed-suspension solids loading and by casting freezer temperature.

6 Study of freezing-rate and microstructure via dense freeze-casting

- *Effect of Freezing Temperature Control on Microstructural formation in Freeze Cast Dense Ceramics*
- *Role of Freezing Rate on Templated Pore Structures in Dense Freeze Cast Ceramics*

6.1 Abstract

This thesis investigates dense freeze-casting as a technique for producing complex near-net shaped dense ceramic parts. Previous work producing porous ceramics identified the rate-of-freezing as a major factor affecting the distribution and morphology of pores produced via freeze-casting.

In this chapter the result of varying freezing-rate on freeze-cast microstructures was studied in sintered samples observed via SEM. Samples were prepared from dispersed non-aqueous ceramic suspensions with high solids loadings of 56 vol.%, and were freeze-cast in cylindrical moulds at temperatures between 0 and -80°C. In addition, the initial freezing rate was further controlled by casting in moulds prepared at either ambient or pre-chilled temperatures.

Variation in freezing rate was observed to generate two primary classes of microstructural features: templated pores, alongside crack-like voids. These features differed in their morphology, distribution and size.

6.2 Aims

The purpose of this chapter is to demonstrate dense freeze-casting, via two major changes to conventional freezing casting practice; using highly-loaded ceramic suspensions to minimise the void fraction during solvent removal, and using high-speed freezing, with the aim of minimising the size of the pores produced during freezing. The desired objective of this work is to develop an understanding of the relationship relating freezing rate conditions applied during suspension solidification, to the resulting microstructure obtained in the formed part, specifically for freeze-cast highly loaded suspensions.

This knowledge obtained has the potential to extend the practical understanding of the suitability of the freeze-casting process beyond the production of porous components alone, as a valuable technique to achieve the rapid and accurate forming of both porous and dense complex-shaped components, from a range of powder-based materials, including ceramics.

6.3 Introduction

Presently, few mass-production processes are suitable to produce complex-shaped dense ceramic components. While complex-shaped forming of ceramic components can be achieved via other shaping processes such a CNC machining, this is both cost prohibitive and time consuming, and as a result this hinders broader adoption of ceramic materials in novel applications. Other existing shaping techniques such as powder processing techniques are limited in their shaping capability, creating a market need for a new commercial complex-shaping process for ceramic materials. Presently, other new processes such as ceramic injection moulding, and gel casting appear to be promising potential solutions. However, these alternative processes require the inclusion of a significant fraction of additives, which limit the ultimate part strength obtainable. In contrast, freeze-casting has the potential to offer near-net shaping capability for ceramics, without requiring significant additive loading, and without compromising the final material properties. As a colloidal processing technique, dispersing particles in a suspension offers the potential for reducing the incidence of defect-prone aggregates, as can occur in powder-pressed parts[84].

The term freeze-casting refers to a multi-step moulding process that can be used to produce a shaped component from a liquid suspension. By loading a suspension of particles (in this case ceramic material) into a mould, the temperature can be reduced causing the suspension to solidify to produce a solid shaped component. The frozen phase can then be eliminated via freeze drying to produce a green body part, and subsequently finished with sintering to produce a solid component. The absence of capillary forces during freeze drying enables the shape that was cast to be maintained after the removal of the solvent, resulting in freeze-casting being well suited for the shaping of complex shaped components by using an appropriately shaped mould. However, the process of removing the frozen solvent crystals inherently results in the generation of pores, which are left throughout the green body, typically resulting in a porous final component microstructure.

A review of the literature involving freeze-casting reveals a significant portion of research interest is focused around the discovery that freeze-casting can be used to create tailored porous microstructures, such as microstructures with highly ordered pores with specific morphologies, or microstructures with structured or graded directional porosity[67, 77, 78, 111]. This has been achieved by modifying the freeze-casting processing conditions, affecting the size, shape and morphology of the frozen solvent crystals, which in turn can be used as in-situ pore-formers or pore-templates. The capability to tailor the product microstructure in turn enables the potential for porous components to be produced to meet specific properties required for a broad range of novel applications, from biomaterials to filtration. However, for other applications the highest priority (with respect to material properties) is mechanical strength, and hence for these applications the production of parts with low porosity is preferable. For this reason, the study scope was defined to explore the necessary conditions required to produce dense near-net shaped ceramic parts via freeze-casting, for which only select examples can be found in the literature[42, 52, 65, 112]. While freeze-casting has long been considered for use as a ceramic shaping process [28], recent interest has been largely confined to exploring porous materials [6, 86, 87]. The specific exception to this has been recent work in our group from Leo et al, exploring the production of dense ceramic components for body armour applications[27, 66, 33]. Even at present, there exist a limited number of studies involving studies with suspensions above 40v% solids fraction, and as a result, few examples available of high bulk density components produced by freeze-casting [86].

In the previous study a deeper investigation into dense freeze-casting was begun, by examining the role of solids loading on product bulk density. From previous studies in the literature, the porosity of the final product was been shown to be primarily determined by the solids volume fraction of the suspension[28, 33, 64, 65]. However, as the solids fraction of the suspension is increased, the viscosity also increases non-linearly, requiring the dispersant selection and concentration to be optimised in order to maximise the suspension solids loading, while maintaining a practical viscosity, suitable to inject at a reasonable rate without requiring inconveniently high pressures. In the previous chapter, it was found that by optimising the suspension composition, by maximising the solid loading, optimising the dispersant concentration, and balancing the need to maintain a suitable viscosity, total porosity in freeze-cast samples could be minimised, to successfully enable the production of components close to the full theoretical density.

Examination of the freeze-casting literature produces numerous examples demonstrating the importance of maintaining control over process parameters during the solidification process, as this process has been identified as key to controlling the evolution of the porous microstructure[113, 114]. Of relevance to this study, it has been shown that by controlling the solidification direction and freezing front velocity, a range of microstructures of varying morphology can be obtained[51, 63, 111, 115–118], and correlations are readily observed between the applied freezing rate and evolved pore sizes[4, 78, 119].

However, the relationship between freeze-casting parameters, and observed microstructure has not yet been studied for dispersed suspensions of high solids loading. Under these conditions, particle-particle interactions are more frequent, and may contribute to differing results than observed for studies of more dilute suspensions.

While the overall porosity of the final product is a major factor affecting the mechanical strength of the part, the microstructural configuration of the pores is also of significance. For example, if the processing conditions result in aligned structures consisting of high aspect ratio pores, or clusters of large pores, this could result in anisotropic material properties, or otherwise areas of locally reduced strength.

In this chapter the microstructure produced via the dense freeze-casting process was investigated, examining whether this capability to tailor microstructure can be harnessed to assist with producing fully-dense ceramic components, such as by optimising the microstructure to further promote the densification during sintering.

Providing that the pores evolved in the sample are small enough in size relative to the powder particle size, then, the densification that occurs during sintering may be promoted, to result in pore reduction and elimination. In contrast, the production of larger pores is undesirable, as these may be consolidated during sintering to become large defects in the final part. Hence, it is important to be able to *maintain* control of the freezing process parameters (and hence the developed microstructure) throughout the entire part, and not simply at the surface of the mould. In this study the range of action was investgated; the distance from the mould surface over which satisfactory control is able to be maintained to promote the desired fine-pore microstructure.

6.4 Experimental setup

6.4.1 Ceramic Suspension Composition

The ceramic feedstock used was alumina AKP-15 (Sumitomo, Japan). A suspension was prepared with Hypermer A70 (Croda, Snaith, UK) added as dispersant, and cyclohexane as solvent. As discussed in the previous chapter, an alumina solids-loading of 55v% and a dispersant concentration of 0.9wt% were found to be optimal for producing a suspension with an acceptable rheology, suitable for low pressure suspension injection. While a higher solids loading would have been desirable, ensuring that the suspension was well-dispersed and free of aggregates was a priority.

6.4.2 Mould Design & Injection Process

The primary sample shape produced for most of our freeze-casting experiments is a small cylindrical prism. By producing samples with a high degree of symmetry, this allows the work from experimental studies to be compared with the results from simulation studies that examine a simplified 1D geometry.

To produce this shape, a mould for injection casting was designed, and CNC machined from aluminium (6061 alloy). The mould was designed to be relatively large, with a sufficiently high thermal mass (approx.. 500 g) and high thermal conductivity, so that the suspension freezing would occur with the mould remaining largely isothermal.

For a typical frozen freeze-cast sample, it contains 13 g of alumina, and 2 g (0.02376 mol) of cyclohexane suspension.

Cyclohexane thermal heat capacity: 105.3 J mol^{-1} K^{-1} , Alumina thermal heat capacity: : 0.880 J g^{-1} K^{-1} , Cyclohexane enthalpy: 2.68 kJ/mol

A sample going from 20°C to -80°C, requires:

100K*(105.3 J mol^{-1} K^{-1} *0.02376 mol + 13g*0.880 J g^{-1} K^{-1}) + 0.02376mol *2680 J/mol = **1458J**

Mould change in temperature: = $\frac{1458\ J}{0.9\ Jg^{-1}K^{-1}*500g}$= **Δ3.3K** increase in temperature.

The top of the mould features an injection port, with a tapered channel that leads to the mould cavity. This results in cast parts featuring a conical sprue on the top of the part produced, from suspension flowing from the injection port into the top of the mould and then into the mould cavity.

This mould consists of several components that fit together to provide an encapsulated chamber for suspension to be injected into, which can then be disassembled after freezing, allowing frozen samples to be removed without damage to the mould or sample.

The lining of the mould is plated with Nickel-Teflon, to increase the ease of removing cast samples. To help maintain a sealed injection chamber, and to aid removal of the samples after freezing, the mould was also lightly greased on all internal surfaces with Krytox GPL 205 (Dupont, Delaware USA).

In order to cast samples with a range of different diameters, the mould design features removable aluminium inserts. A range of inserts were produced to enable the casting of 20 mm (standard size), 10 mm (medium size), and 5 mm (small size) diameter samples. All samples are 15 mm high, in addition to the feeder sprue.

The injection inlet port is constructed from Teflon, which helps to reduce heat transfer from the mould to the nozzle, preventing freezing from occurring in the syringe nozzle. The mould design also includes two 1.8 mm air vents, that allow air to be displaced as the mould cavity is filled with suspension. These small air vents provide significant resistance to flow for the high viscosity suspension. During injection, once the main cavity is filled, the injection pressure required increases significantly due to these smaller vents, providing feedback that the mould cavity has been filled.

Injection of suspension into the mould is performed with the mould inverted, with the injection port at the bottom facing downwards and the air vents at the top, and with suspension injected from the bottom to top. A 60 cc slip-nozzle syringe is used to draw up suspension, which is then tapped several times to dislodge and eliminate any large bubbles, before being inserted into the injection port. While injection is performed manually, with reasonable pressure on the syringe plunger the rate of injection is primarily limited by the viscosity of the suspension, and generally takes approximately 4 seconds to complete injection.

6.4.2.1 Freezing

Freezing was performed using an ultra-low temperature chest freezer (Operon DFC-84, Korea), pre-set to selected fixed temperatures. A porous rubber grid mat was placed on the floor of the freezer, to avoid significant heat transfer through conduction from the base of the mould, which would affect the symmetry of the freezing process. For a similar reason too, during freezing the mould was positioned towards the centre of the freezing chamber in order to avoid thermal gradients across the mould laterally.

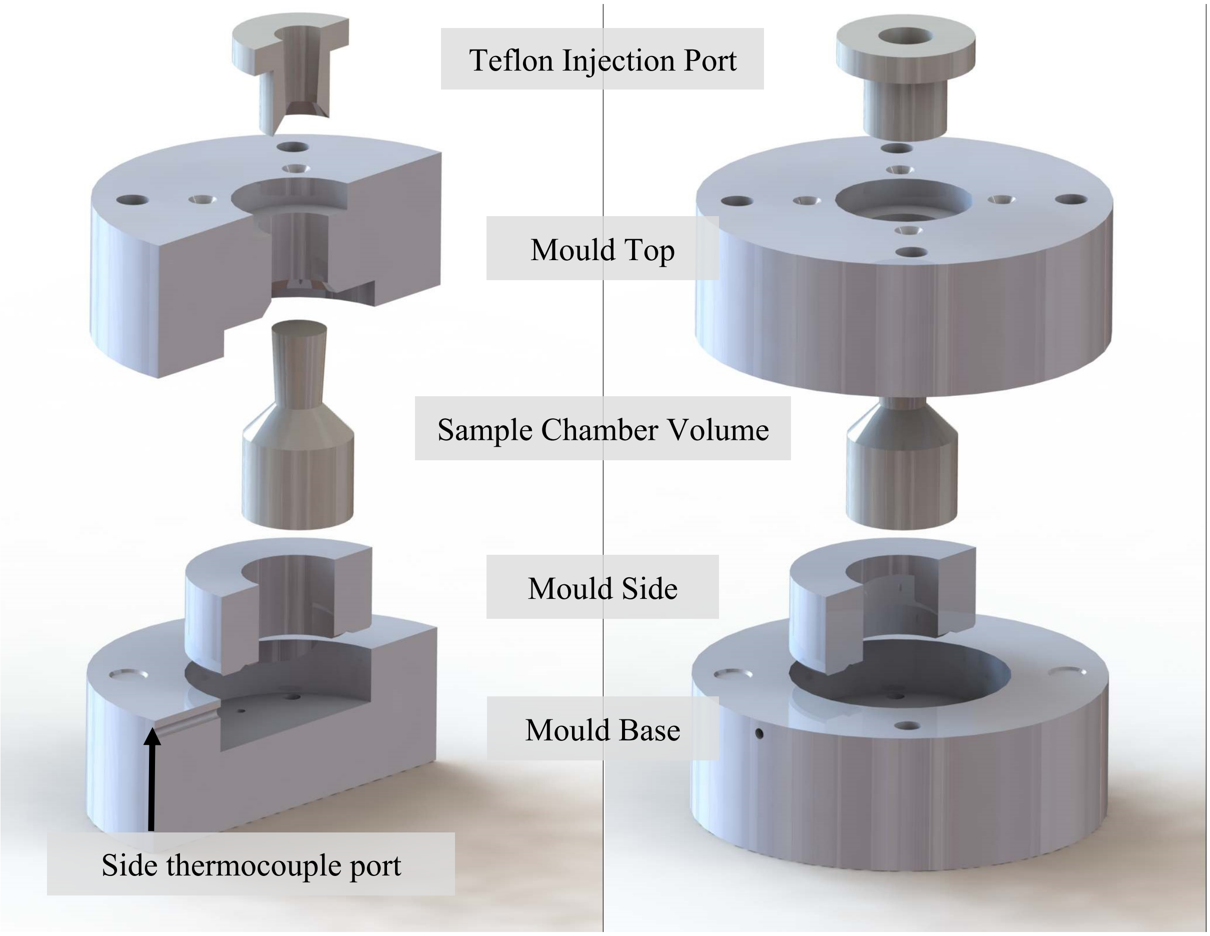

Figure 6.4.a: Exploded View of Mould Assembly.

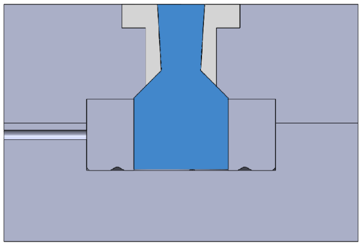

Figure 6.4.b: Cross-section view of the mould design, showing mould chamber injection volume highlighted in blue.

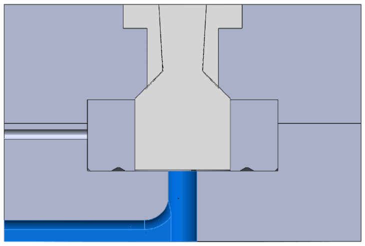

Figure 6.4.c: Cross-section view of the mould, showing modified mould base with thermocouple port highlighted in blue.

6.4.3 Freezing Conditions

In order to examine a broad range of freezing rates, samples were produced with casting temperatures that spanned the operating temperature range of the blast freezer, from -20°C to -80°C. To cover a broad range of freezing rates, two different freezing regimes were used. For slow-freezing, moulds at ambient room temperature were injected with suspension, and then placed into the freezer until frozen. Under the slow-freezing regime, the large thermal mass of the mould, and the thick mould walls, results in a delay between when the mould is placed in the freezer, and the point at which freezing begins to occur in the mould cavity. The fast-freezing regime involves placing the mould into the freezer first, to pre-chill. The chilled mould is then taken out of the freezer, and the suspension injected into the cavity. Because the mould cavity surface is below the freezing point of the suspension, the freezing process begins immediately when injected suspension contacts the mould walls.

6.4.4 Measurement of Freezing Rates

In order to obtain a quantitative measure of the freezing-rate experienced under different freezing-conditions, a thermal logging system was used to record temperatures during freeze-casting, and temperature profiles were recorded under each of the different conditions used. This system consisted of multiple thermocouples connected to a 16-channel differential ADC interface (National Instruments NI9202, Austin, Texas, USA), and connected to a computer-based logging system running NI-LabView (National Instruments NI9202, Austin, Texas, USA). K-type thermocouples were used to sample multiple temperature points, and the stated ±1.0°C accuracy of the thermocouples were verified by measuring the freezing point of water.

The measurements recorded during the freeze-casting process included:

- Ambient lab environment
- Freezer internal temperature
- Mould Internal Temperature (via thermocouple inserted inside port)
- In-situ Sample Internal Temperatures (via in-situ thermocouple probe)
- Mould side surface temperature
- Mould top surface temperature

Figure 6.4.d:Thermocouple probes attached on side and top of mould.

6.4.4.1 Mould In-situ Thermocouple Probe

The sample in-situ thermocouple probe setup consisted of a modified mould base, with a secondary port. A thermocouple array of seven probes was assembled and inserted into the mould base port. The height of the probes was arranged in a staggered sequence spaced at 3 mm intervals within the mould cavity. This was intended to enable local measurements of the temperature within the centre region of the samples during freeze-casting. The thermocouple tips were exposed to the suspension, and the wiring was shielded with stainless steel tubing.

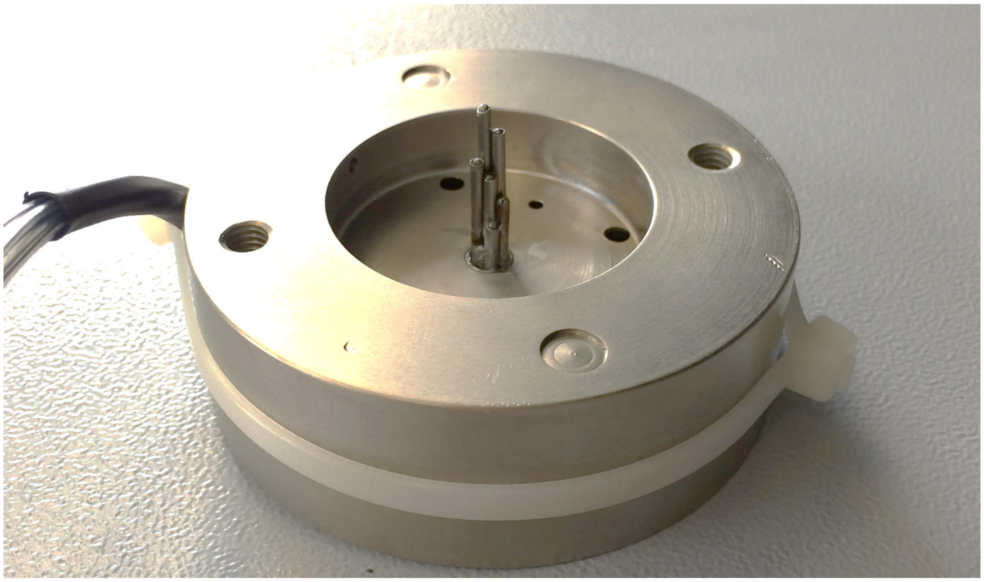

Figure 6.4.e: In-situ thermocouple probe assembly installed in modified mould base

Figure 6.4.f: Failed suspension injection illustrating in-situ probe within sample injection chamber.

6.5 Results

6.5.1 Measurement of Freezing Rates

The in-situ probe was used to measure temperature profiles over time under each of the freezing rates and freezing regimes examined in this study

On these profiles, the transition from chilling to freezing can be observed by the slope of the graph, where a constant temperature represents phase change occurring (latent heat removal), while a varying temperature corresponds with cooling (sensible heat removal). The temperature measurement from the centre thermocouple was used selectively to monitor when complete sample solidification had occurred. Typically, a 'knee' or dwell was observable in the temperature-time diagram during solidification at the solvent solidification temperature, prior to the temperature dropping further towards the freezer set temperature. The actual freezer internal temperature was also recorded using a separate thermocouple placed inside the freezer.

Total duration of freezing time was calculated as from the start of injection, until the time taken for the measured temperature to reach the end of the 'knee' on the temperature plot, indicating complete freezing has been achieved. While temperature changes follow a logarithmic curve depending on the difference in temperature, for high differences in temperature, the initial change in temperature will approach a linear decrease. For this reason, for simplicity, a linear "average rate of cooling" for the sample centre point was calculated as the average rate of temperature drop, between 20.0°C and the corresponding temperature where freezing was determined to begin at the centre. This provides a simple quantitative measure for comparing the freezing velocity between the different conditions explored.

These corresponding calculated thermal profile values of significance are tabulated on the following page, and the temperature plots for these tests are presented on Figure 6.5.a, on page 84.

Table 6.5.a: Thermal profiles from in-situ probe during freeze-casting solidification

Freezing Regime	Set T	Measured T	Start t (s)	End t (s)	Average Cooling Rate (°C/s)
Ambient	-20°C	-16°C	1552	1622	0.012°C/s
Ambient	-40°C	-34°C	1142	1196	0.015°C/s
Ambient	-60°C	-55°C	668	694	0.027°C/s
Ambient	-80°C	-70°C	542	570	0.033°C/s
Pre-Chilled	-20°C	-17°C	54	*	0.35°C/s
Pre-Chilled	-40°C	-33°C	44	*	0.43°C/s
Pre-Chilled	-60°C	-57°C	36	*	0.53°C/s
Pre-Chilled	-80°C	-73°C	30	*	0.63°C/s

- *Set T =Freezer Set Temp. (°C)*
- *Measured T = Actual Measured Start Temp. (°C)*
- *Start t = Starting time for centre to reach freezing temperature (s)*
- *End t = Ending time for freezing at centre (s)*
- *Cooling rate = Average rate of cooling (°C/s)*

* Note: The pre-chilled samples did not display a temperature dwell during solidification, as they completed solidification at the centre probe in under 2 seconds.

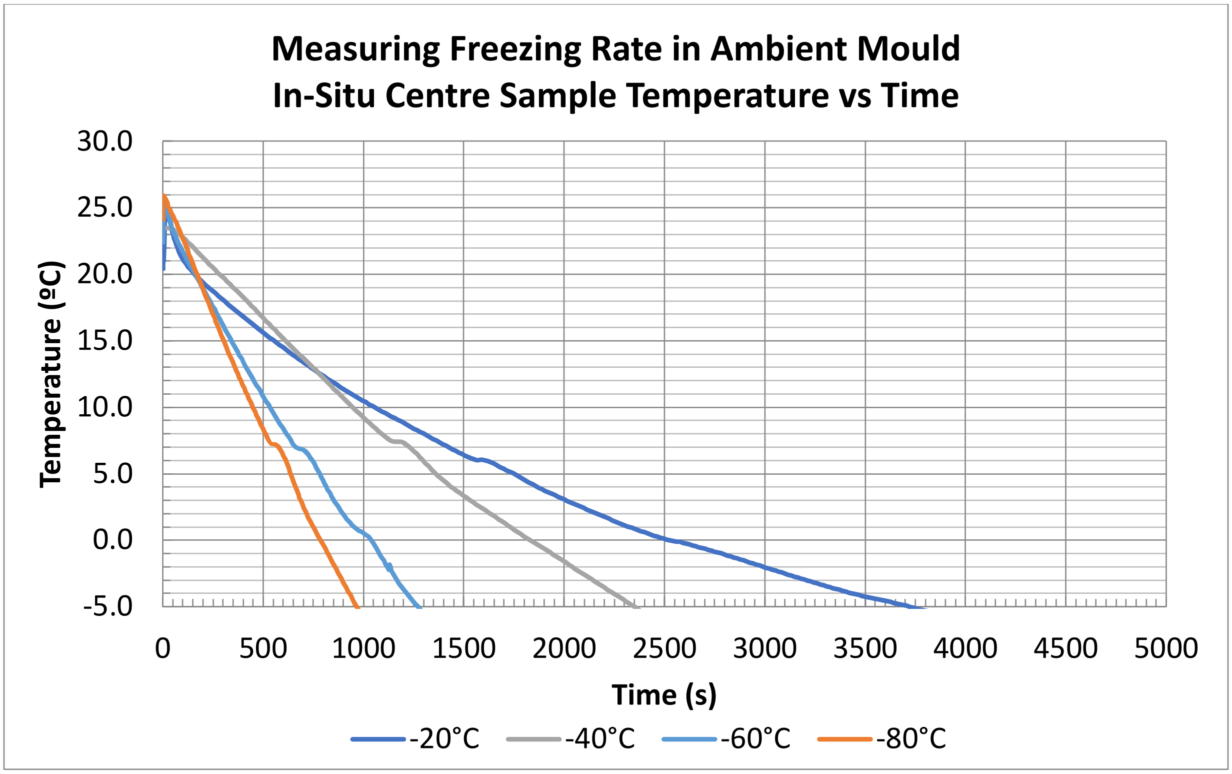

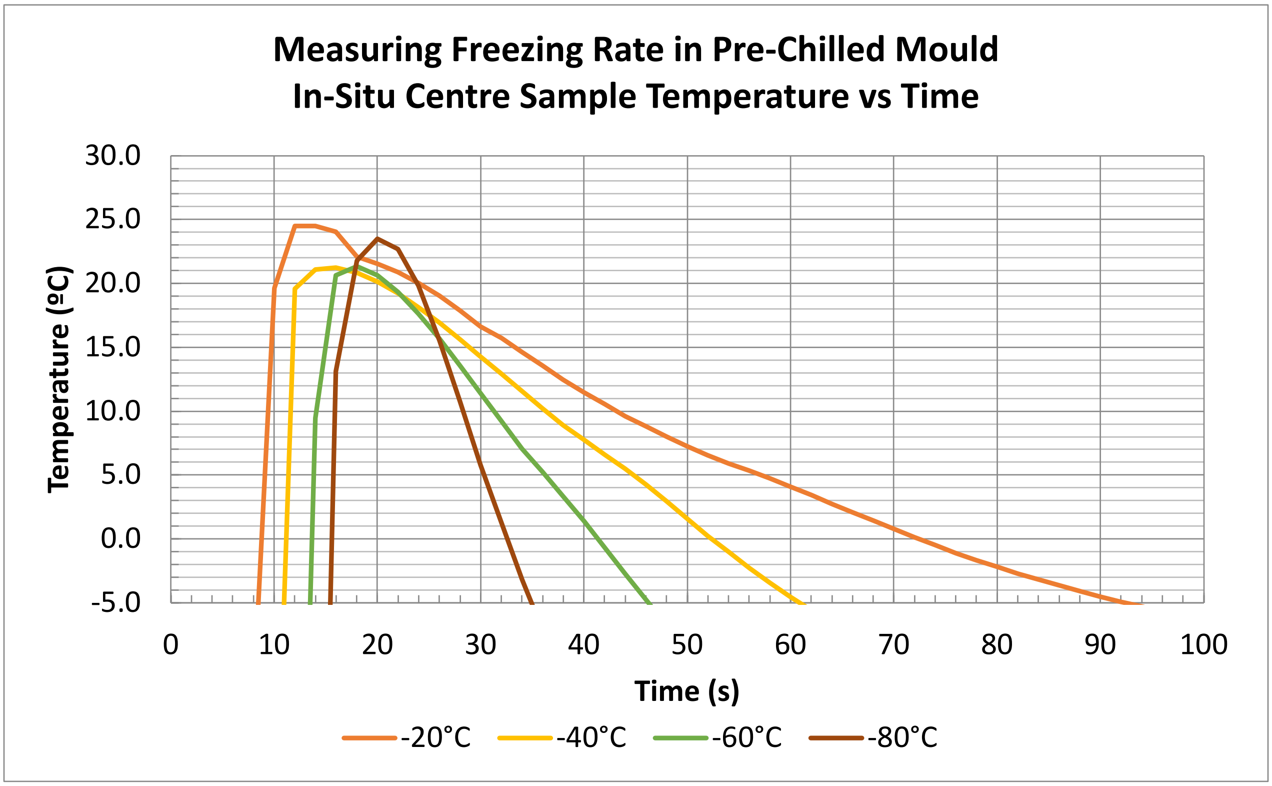

Figure 6.5.a: Graphs of Temperature vs Time under different freezing conditions, for ambient moulds (top) and pre-chilled moulds (bottom), under freezing temperatures between -20°C to -80°C.

6.5.2 Freeze-Casting under varying freezing-rates

To study the microstructure evolved under different freezing conditions, a set of samples were prepared, with two samples prepared for each specific condition for the purpose of visual analysis. For each pair of samples, one sample was bisque-fired, and the other sample fully sintered. After sintering, each sample was cut in half and cold-mounted in epoxy. Then, the internal cut face was highly polished prior to imaging.

A summary table of the conditions examined are listed below:

Freezer Temperature	Mould Temperature	Sintering	Sample #
-20°C	Ambient Mould	Bisque Fired	147
		Fully Sintered	148
	Pre-Chilled Mould	Bisque Fired	162
		Fully Sintered	163
-40°C	Ambient Mould	Bisque Fired	141
		Fully Sintered	142
	Pre-Chilled Mould	Bisque Fired	153
		Fully Sintered	155
-80°C	Ambient Mould	Bisque Fired	134
		Fully Sintered	135
	Pre-Chilled Mould	Bisque Fired	167
		Fully Sintered	168

Table 6.5.b: List of Dense Freeze-cast Sample Conditions Studied

6.5.3 Overview Imaging

After samples were cut, an overview photo was taken using a digital camera. Due to the inherently low contrast of the material, the practical purpose of these images is to simply indicate the presence of large internal features. An additional image edited with enhanced contrast is provided alongside to assist with the identification of macroscopic cracks and internal voids. Enlarged reproductions of these overview images are provided in Appendix 11.2.

Table 6.5.c: Overview images of dense freeze cast alumina samples, listed with processing conditions

Freezer Temp	Mould Temp	Sintering	Sample #	Photograph of Sample	Photograph of Sample (Enhanced Contrast)
-20°C	Ambient Mould	Bisque Fired	147	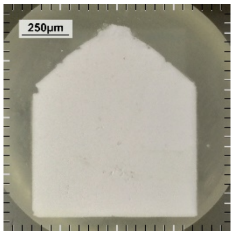	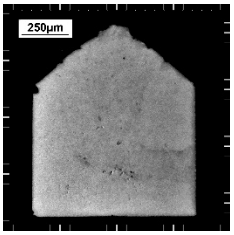
		Fully Sintered	148	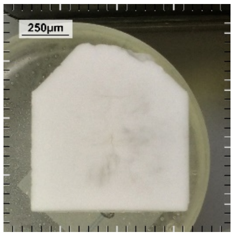	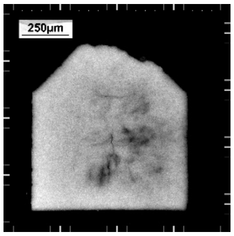
	Pre-Chilled Mould	Bisque Fired	162	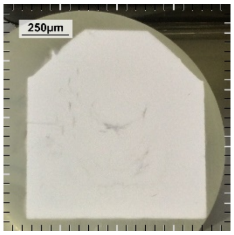	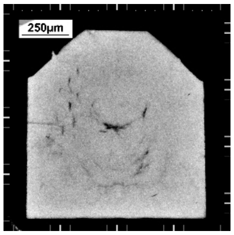

Freezer Temp	**Mould Temp**	**Sintering**	**Sample #**	**Photograph of Sample**	**Photograph of Sample (Enhanced Contrast)**
		Fully Sintered	163	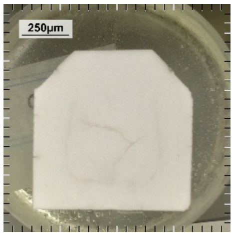	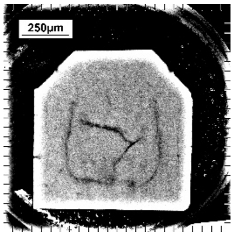
-40°C	Ambient Mould	Bisque Fired	141	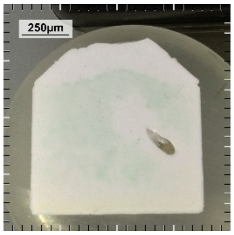	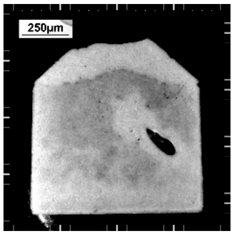
		Fully Sintered	142	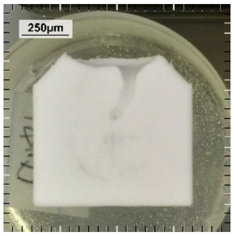	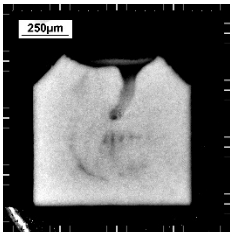
	Pre-Chilled Mould	Bisque Fired	153	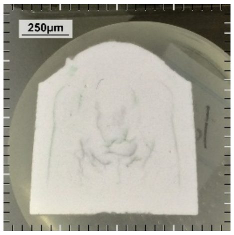	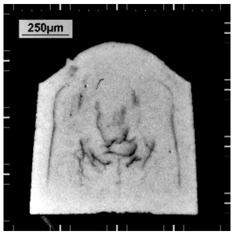
		Fully Sintered	155	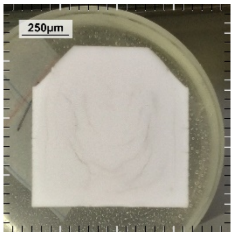	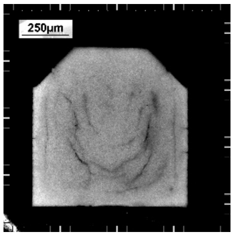

Freezer Temp	**Mould Temp**	**Sintering**	**Sample #**	**Photograph of Sample**	**Photograph of Sample (Enhanced Contrast)**
-80°C	Ambient Mould	Bisque Fired	134	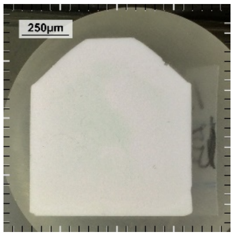	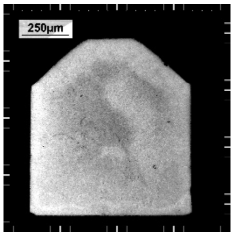
		Fully Sintered	135	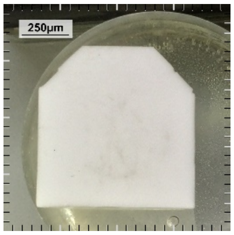	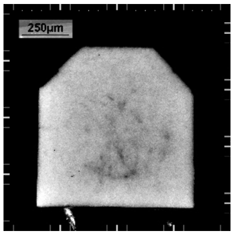
	Pre-Chilled Mould	Bisque Fired	167	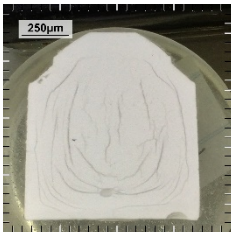	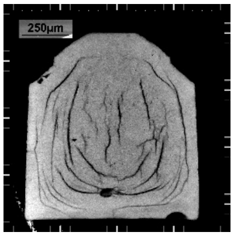
		Fully Sintered	168	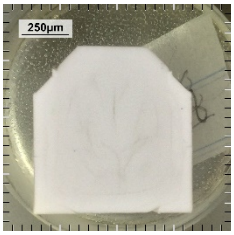	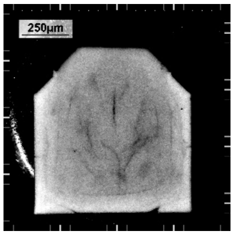

6.5.4 Microscopy results

The full set of microscopy photos for both optical and SEM are shown in Appendix 11.2 on page 233. Selected images are reproduced in the discussion section that follows to highlight certain points.

6.5.5 Microscope Imaging

For each sample, images were obtained at higher magnification using a trinocular microscope equipped with an imaging camera. For each sample, images were taken using both 5x and 20x objectives. Two areas of the sample were selected for study, specifically focusing on the centre of the sample, and the side of the sample. These regions were selected to enable both the regions of the sample with the fastest and slowest freezing rates to be studied. The regions studied are shown schematically below.

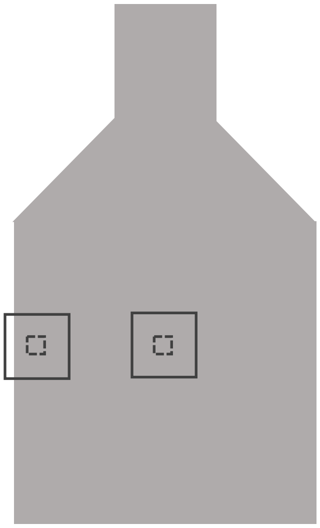

Figure 6.5.b: Schematic view of optically imaged regions

The full set of sample micrograph images are provided in Appendix 11.2.1.

6.5.6 SEM Images

In order to examine the microstructure of samples at high magnification, SEM imaging was used. For this process, images were obtained from different locations compared with the optical images. Initial observation under SEM revealed a visible directionality of the freezing process from the bottom of the sample, towards the centre. As a result of this, SEM images were acquired the bottom region of the sample, and from the centre of the sample. One additional location was also studied, and images were acquired at the top corners of the sample. At each area studied, images were captured at 100x, 800x, and 4000x magnification. The regions studied are again shown schematically below.

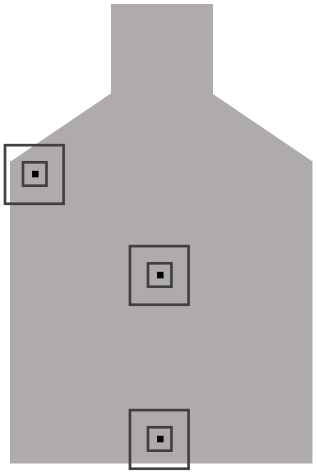

Figure 6.5.c: Schematic view of SEM imaged regions

6.5.7 Sintering Grain Structure

While SEM images were obtained of the microstructure, high-magnification images were also captured of the grain structure.

Bisque Fired	Fully Sintered
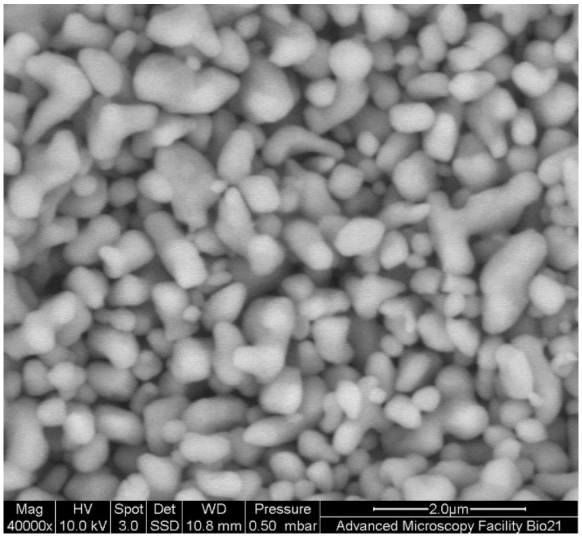	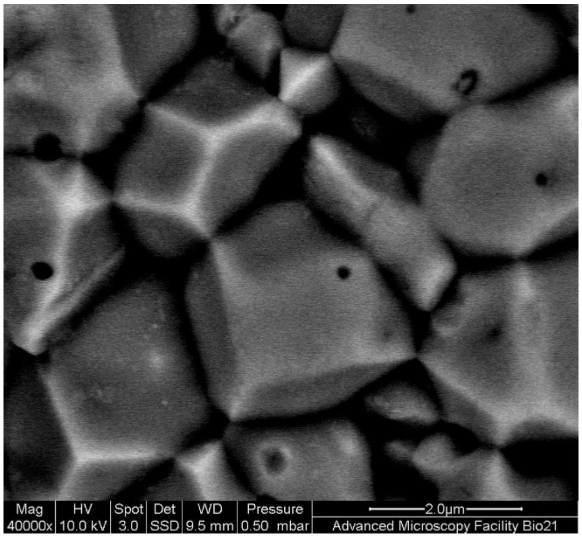

Figure 6.5.d: Comparison of sintered vs bisque fired grain size, for Alumina freeze cast samples. Images taken at 40000x. Left: sample 135, Right: sample 167.

The bisque firing microstructure can be contrasted against the high-purity alumina (HPA AKP-15) feedstock, and this powder was also imaged under SEM. In comparison to the as-supplied feedstock, after bisque firing there is no significant visual difference in particle shape or size, and only minimal particle interdiffusion appears to have occurred.

<table>
<tr><th>Alumina AKP-15 – powder feedstock as supplied (0.60µm mean particle diameter)</th><th>Alumina AKP-15 – Bisque Fired</th></tr>
<tr><td>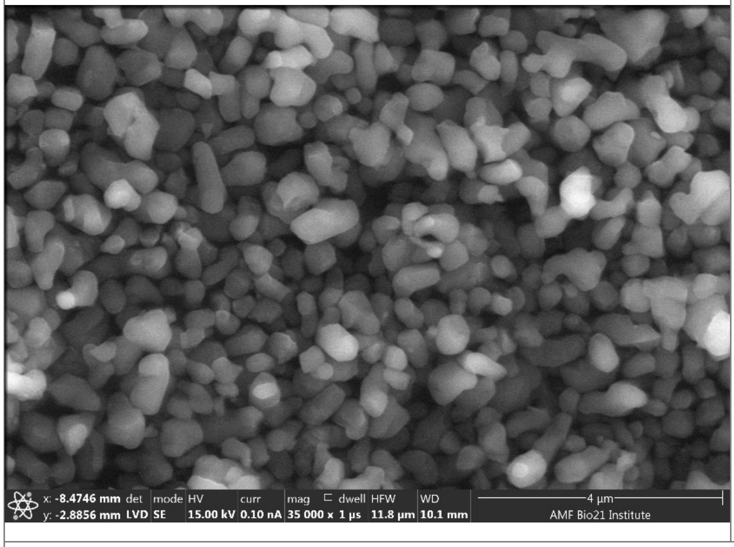
</td><td>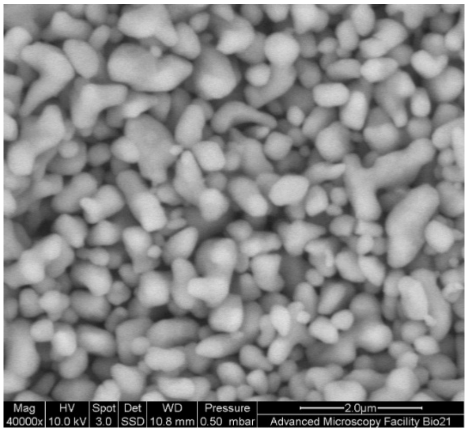
</td></tr>
<tr><td colspan="2">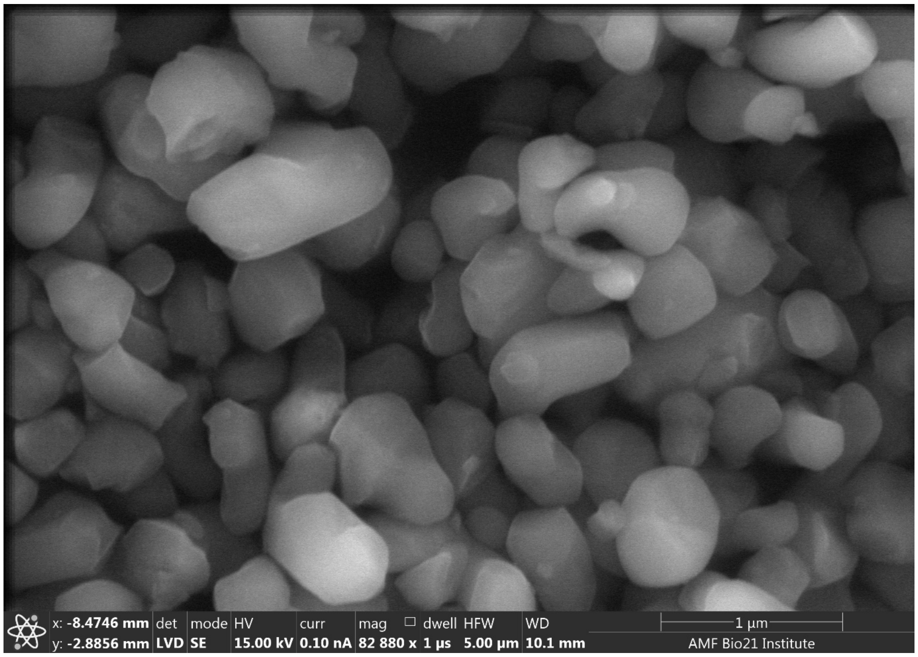
</td></tr>
</table>

Figure 6.5.e: Comparison of as-supplied Alumina AKP-15 powder (top left and bottom) with freeze-cast sample microstructure after bisque-firing (top right). Top images presented at equivalent scale.

6.6 Discussion

6.6.1 Freezing Control

From the plot of temperature over time, and the corresponding calculations of freezing rate, it is apparent that the goal of varying freezing rate has been reasonably achieved under the limitations of the present experimental setup. The time required for freezing, and the calculated average initial cooling rate at the sample centres, both approached variation over two orders of magnitude. These rates correspond to the centre of the sample where freezing will be slowest; at the sample edges, the peak rate of freezing would far exceed these measured rates. This presents a suitable opportunity to study the effects of these variations on the sample microstructures, across the sample geometry.

6.6.2 Freezing of Samples

The manually freeze-casting process was successfully demonstrated with the ceramic suspension as prepared, and consistent well-shaped samples were produced with good surface finish and satisfactory mould filling. However, after sintering and cutting, significant variation in internal features was observed between samples. The aluminium moulds were greased to produce an air-tight seal, and to allow easy disassembly and removal of samples. Variations in both mould greasing, and minor variations in manual suspension injection, may have contributed to the inconsistencies observed in the set of optical images of the cut samples. If the process was automated, as in a commercial mass-production process, the frequency of these inconsistencies may have been reduced.

For each studied condition, several samples were produced. The samples selected for study were selected from samples with fewer externally visible large voids. However, some samples were observed to possess large internal voids. A key limitation of this study is its dependence on destructive examination. Since the cutting of samples is irreversible, it is not possible to examine both the same region of a sample in both the green and sintered states. For the same reason, it is not readily possible to easily pre-select samples free of internal voids, as these voids are not visible until after the sintering and cutting of samples had been completed. Fortunately, in most cases, large voids were present primarily on only one side of the sample, and the regions around large voids were generally able to be avoided.

6.6.3 Optical Low-magnification Imaging

While it was found to be possible to use optical imaging to identify voids, the examination of small pores was hindered due to the low visual contrast of alumina. When examined with a microscope under high optical magnification, the resulting shallow depth of field also proved limiting for detailed visual analysis. The use of SEM imaging enabled these limitations to be overcome and offered greater detail at higher magnifications.

Examining the optical image set, when comparing the internal structure with the mould temperature, several differences were able to be observed. Various void geometries are also visible in these samples; attributable to minor variations in mould filling behaviours.

The first notable difference in the cracking can be seen when comparing pre-chilled and ambient-temperature moulds. Cracks are visibly present in the optical overview images, for of all the samples produced by fast freezing with pre-chilled mould. In contrast, these same cracks are not visible in the samples produced by slow freezing with ambient temperature moulds. This demonstrated that the rate of solidification was involved with the sequence of processes that affect the generation of large internal cracks.

Additionally, for the pre-chilled samples conditions, cracks are visible in bisque samples 153, 162, and 167. The presence of cracks occurring in both sintered and bisque-fired samples, confirms that cracks must be developing during one of the freeze-casting process steps occurring prior to sintering and densification.

The final observation is that the most severe cracking is observed in the sample frozen at the lowest pre-chilled mould temperature, which is the sample that would have experienced the highest freezing rates.

6.6.4 Bulk Phase Microstructure

Examining the grain structures of both the bisque and fully-sintered samples (Figure) enables us to understand the length scales that are significant for the material before and after the sintering process. The manufacturer specification for the average particle size of the ceramic powder feed is 0.6µm. Examining the bisque-fired image, many of the individual ceramic particles of this size can still be clearly seen. While the bisque sample is solid and can be successfully cut, it was not possible to achieve the same kind of polished surface as can be achieved for the sintered material. The limited interparticle connectivity results in a relatively weak material that is easily scratched, even with a relatively soft fingernail. Examining the grain structure of the dense sintered material, the grain size is approximately 2-3 µm which indicates that grain growth has occurred. Further inspection of the sintered microstructure revealed that most of the bulk ceramic material is low or free of porosity, indicating that the sintering conditions used are adequate for successful densification of this material with pressureless sintering, suitable for testing the hypothesis. However, while the bulk phase may appear to be dense, an examination of the SEM images shows both pores and large voids remain present in the sintered microstructure in all the test samples. The small pores seen in Figure 6.5.d on the surface of the grains (<200 nm) could be due to air trapped inside during grain growth from sintering.

6.6.5 Microstructure Classification

Examining both the SEM and optical images of both the bisque and sintered microstructures reveals three classes of features observable:

- Internal voids
- Dendritic pores
- Crack-like features

The internal voids observed are generally defined by a smooth curved contour, and generally these voids either are continuous and extend to the sample surface (e.g. sample 142), or they feature some directionality that appears to originate from the surface. In some samples, an internal void is present that appears as a bubble or near the centre of the sample. (e.g. sample 167). The cause of these voids is not known, but their appearance is similar to a gas bubble, and which could have been formed by several routes; via solvent evaporation, via the introduction of air into the mould, or from dissolved nitrogen in the solvent (from the atmosphere). As previously mentioned, the inconsistent presentation of these voids could be due to inconsistencies with the manual process of injecting the suspension into the mould.

Under optical imaging the dendritic pores are difficult to distinguish from the cracks or from the bulk material, but the dendrites can be clearly seen under SEM imaging in the sintered samples. Dendritic structures can also be observed in the bisque fired samples, confirming that these features are present before the sintering process. Freeze-casting is well understood to be a pore forming process[120], and these dendritic features appear to correspond to the templated pores left behind by the cyclohexane carrier solvent, as formed by solidification followed by sublimation. The scale of these pores is observed to strongly vary with both position and freezing condition.

For ambient temperature moulds, the dendritic voids can be readily seen, extending from the surface of the sample, towards the centre of the sample. For pre-chilled moulds, the dendrites are difficult to see, unless viewed under higher magnification. These smaller dendrites only become identifiable at some distance away from the surface, linearly growing in size towards the centre of the sample.

When looking at the pre-chilled samples large cracks are prominently visible, and these cracks can be readily differentiated from the dendritic pores by their orientation, morphology, and size. As is consistent with results observed in the literature[67, 108], the dendrites are consistently aligned with the freezing orientation and pointing from the surface of the sample towards the centre, while in contrast the cracks appear to occur in a range of orientations, with most cracks observed to be parallel with the surface of the sample. In contrast, for the ambient mould samples there does not appear to be any cracks. However, for the ambient mould samples the dendrites are large, so in those samples it is difficult to create a distinction between any large observed dendrites and any minor cracks that may also be present.

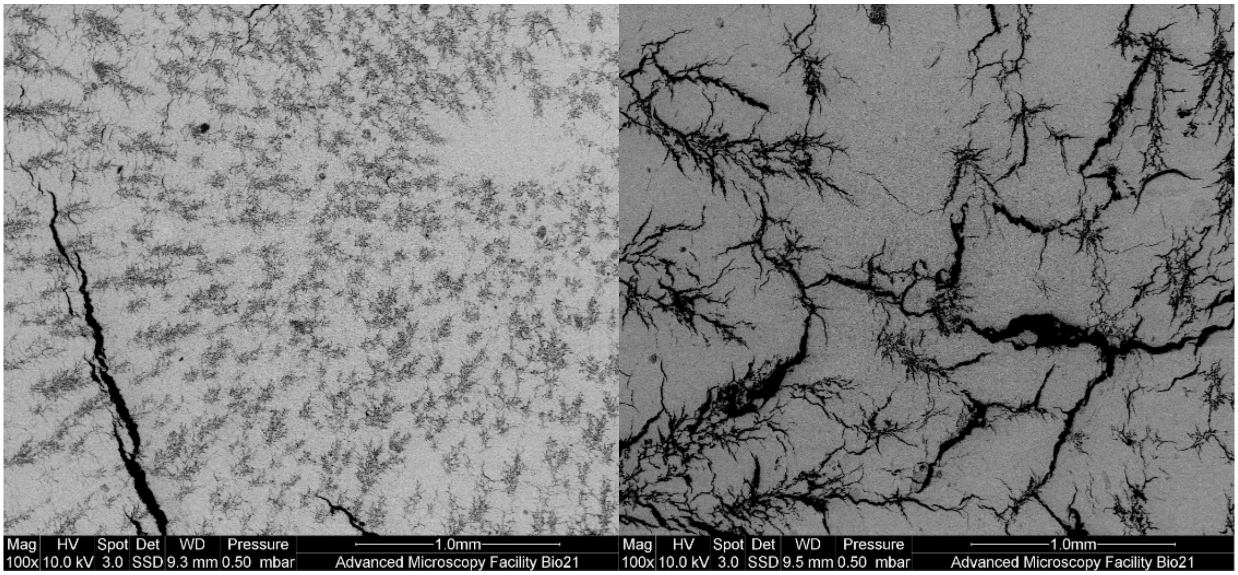

Figure 6.6.a: SEM images of centre region from fast-frozen (left, cast in pre-chilled mould) and slow-frozen (right, cast in ambient mould) samples. Both cast using a freezer at -80°C and are displayed at 100x magnification. Fast-frozen sample shows a large crack running perpendicular to small dendrites, while the slow-frozen sample shows the presence of large dendritic voids.

The apparent absence of large cracks in the ambient-temperature moulds suggests that the rate of solidification is a factor involved in the formation of cracks. However, it may be the case that the large dendritic voids present in the slow-frozen samples act as stress concentrators, where the dendrites allow the crack-generating forces to be alleviated by the crack propagating from the dendrite tips.

6.6.5.1 Comparison of previously observed cracking behaviour

These internal cracks are not unexpected, as cracking in samples was previously observed in dense freeze cast samples studied by Dr Leo[33], which were all produced using fast freezing with pre-chilled moulds.

When comparing the sample images in Figure 6.6.b, to the overview images in Table 6.5.c (on page 86), there does appear to be a difference visible in the crack patterns. In Figure 6.6.c it can be seen that when examining the cracks observed in the left sample, there are two cracking styles evident; (a) onion-like cracks, where the cracks are parallel with the sample surface, that are inset from the surface, and (b) starburst fracture, cracks that appear to propagate from the centre of the sample outwards. Examining the cracks Figure 6.6.b, most of the cracks appear to be of style (b), starburst fractures. In contrast, for most of the cracks observed in the samples from the present study, more of the cracks of style (a), onion-like cracks are present. The main difference between these two studies is the ceramic used, where this study uses alumina, and the previous study uses zirconium diboride.

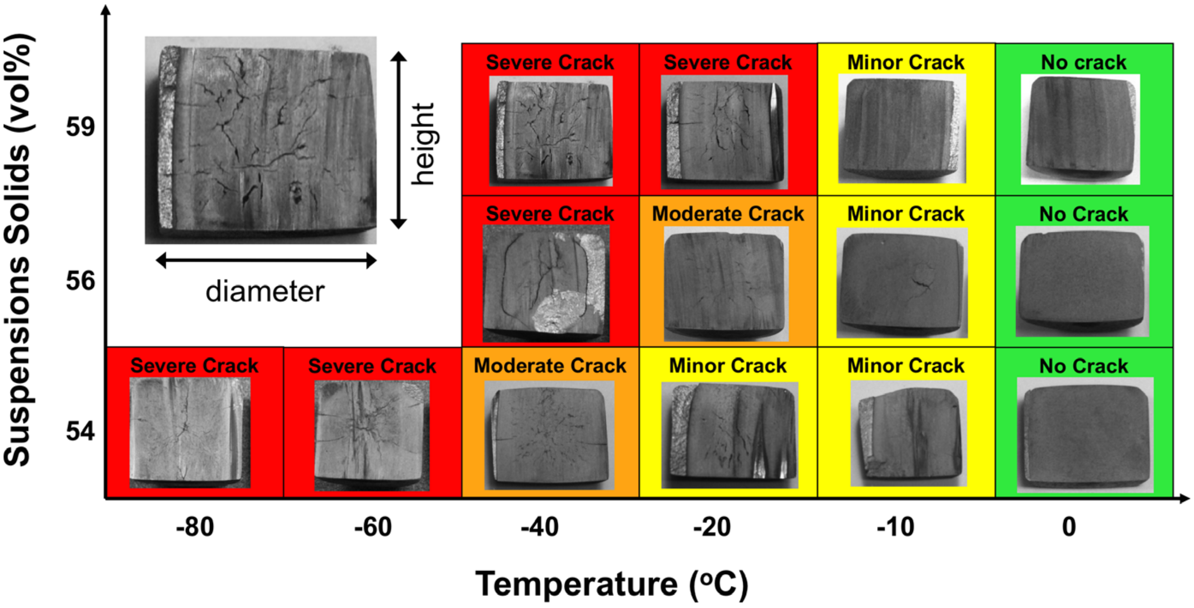

Figure 6.6.b: Display of internal cracks in dense freeze cast ZrB2 samples [33].

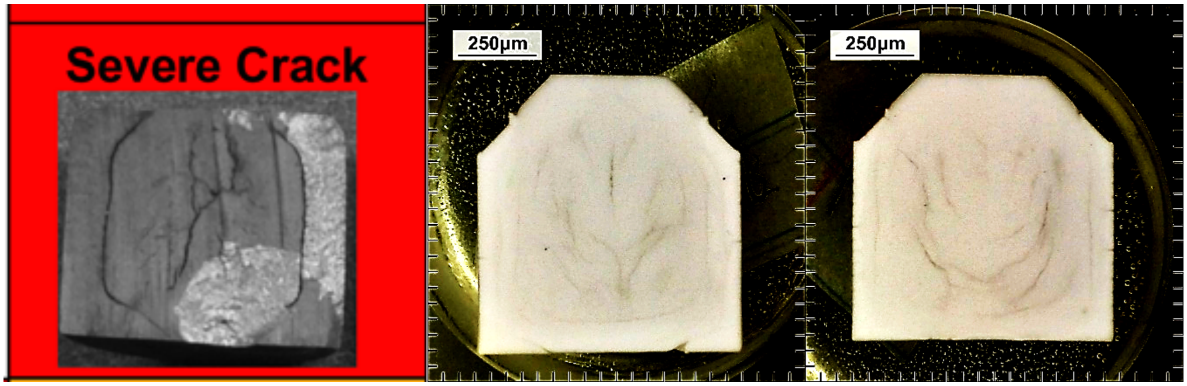

Figure 6.6.c: (from left to right) Comparison of ZrB2 sample (56 vol.%, -40°C) with sample 167 (56 vol.%, -80°C) and sample 155 (56 vol.%, -40°C).

These results suggest that the material used may affect the crack evolution. As the cracks are present in the bisque fired samples, this difference is not suspected to be due to the sintering processes.

6.6.5.2 Microstructure variation with freezing rate

When SEM images obtained of the microstructure are examined, several preliminary observations can be made. As previously mentioned, clear visible trends are observable when comparing samples from different mould conditions, with larger dendrites visible for ambient moulds with slower freezing rate, and significantly smaller dendrites observable for prechilled moulds with correspondingly higher freezing rates, as shown in Figure 6.6.a.

It has been previously observed in the literature that different regimes of solidification modes exist depending on the local freezing rate[114, 121–123]. At some critical freezing rate, solidification is expected to transition from a regular periodic sequence of macroscopic layers of compacted particles followed by layers of ice-lenses, transitioning through a mode of chaotic microstructure, and then transitioning to a microstructure with a microscopic segregation of particle compacts and ice layers[124, 125].The goal of this study was to operate within the fast-freezing solidification mode, in order to generate a fine pore morphology that is optimised for densification during sintering. The specific morphology observed is known to vary significantly depending on the suspension composition and processing conditions, resulting in ice-banding[124], dendritic branching or lamellar patterning[126]. This ability to tailor microstructure of freeze-casting has been well explored for producing porous structures [2, 6, 87].

Due to the wide range of freezing rates explored in this study, it may be expected that a range of microstructures would be observed. Even comparing the images obtained from a single sample, it becomes clear that the microstructure within is heavily dependent on the position within the sample. This observation was expected, as for freezing with an (approximately) constant mould surface temperature, the freezing rate across the sample is predicted to vary as a function of the distance from the mould surface[113, 127, 128].

However, the sequence of morphologies observed, do not match the typical trends seen in porous freeze cast samples as a function of freezing rate. This phenomenon of particle compaction that causes ice-banding depends on the ability of particles to concentrate to a critical concentration in order to form compacts. For the highly loaded suspensions under study, it was expected that the high starting solids concentration would reduce the length of the compaction region. Thus, it was expected that a fine pore microstructure would be observed, even under a slow freezing rate.

Araki and Halloran demonstrated that under lower solids loading conditions, templated ice voids typically replicated the typical crystal structure of the carrier solvent studied[9]. For cyclohexane, the typical crystal structure is dendritic, but the highly-aligned dendritic structures observed in their work shown in Figure 6.6.d, differ greatly from those seen in this study.

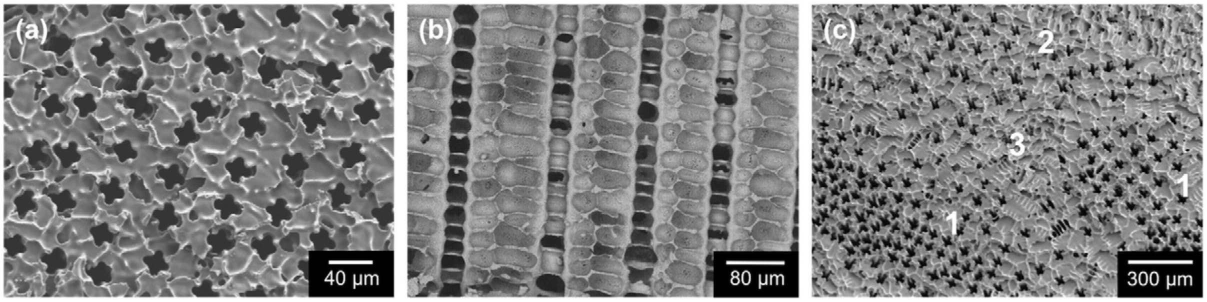

Figure 6.6.d: Figure reproduced from [129], of highly aligned dendritic structures in freeze-cast samples, produced using Cyclohexane as a carrier solvent. From left to right: (a) primary dendrites in the transverse view, (b) secondary dendrites from the longitudinal view, (c) regions of aligned porosity in various domains.

In this study, at the centre of the -20°C ambient mould sample (the slowest freezing-rate condition), the presence of large dendrite free regions with a dense microstructure can be observed, with the largest contiguous dendrite-free region observed to be approximately 0.5 mm in diameter, as shown in Figure 6.6.e. The limitation of this observation was that only a 2D plane through the sample was examined, without considering the 3D nature of the dendrite pore network. Additionally, these microstructures did not match the structures previously observed in porous freeze-cast pore networks at any length scale.

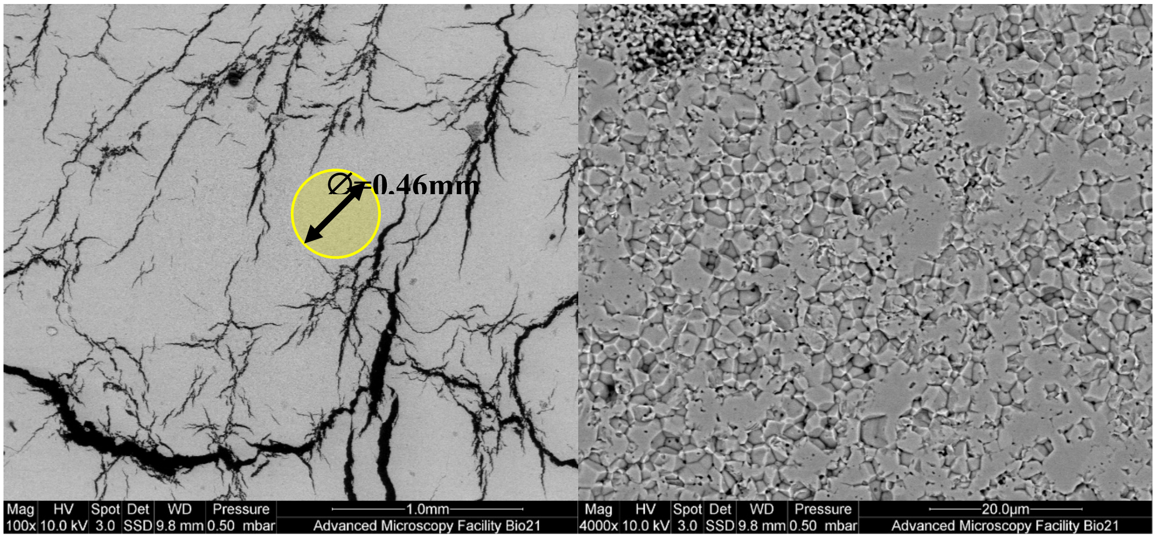

Figure 6.6.e: (Left) SEM image of the centre of sample 148, frozen in ambient mould at -20°C, highlighting dendrite-free zone. (Right) 4000x magnification of dendrite-free zone, showing dense bulk microstructure.

For dense freeze-casting, there are limited examples of microstructure available in the literature[56, 65]. For non-aqueous dense freeze-cast suspensions using a hypereutectic naphthalene/camphor mixture as a carrier solvent, Araki and Halloran describe observing "distorted dendrite-shaped voids surrounded by almost fully dense regions"[15]. The conditions studied could be reasonably classified as slow-freezing, due to the long solidification times indicated. While their carrier solvent was different, the description of the morphology generally matches the observed microstructure seen in the centre region of the slow frozen sample from this study. However, with the limited details available it is difficult to directly compare the results from that study here. This suggests the possibility that the morphology of the "dendrites" seen here may not be an intrinsic function of the solvent, but may be related to a processing aspect, such as the very high solids concentration.

Other possible contributing factors for the generation of the dendrite voids observed could include the volume change of the solvent that occurs during phase change, since cyclohexane shrinks on freezing. At 25°C, the molar volume of cyclohexane is 99.8 cm^3/mol [130], and the volume change on melting is recorded as +5.2 cm^3/mol[131]. This equates to an approximate volume shrinkage on freezing of 5.4%; this is significantly less than water (9% expansion), but significantly greater than for other demonstrated carrier solvents such as Camphene (3.1% shrinkage) and Tert-butyl alcohol (2% shrinkage)[43].

When examining the outer regions of the slow-frozen samples a similar microstructure morphology is observed, but on a reduced length scale. For the centre region of the -20C slow-frozen sample (#148, Figure 6.6.e), the diameter of the secondary dendrite arms diameter (SDAD) is approximately 10-30 µm, the secondary dendrite arm spacing (SDAS) varies between 200-500 µm, and dendrite clusters are approximately 500-1000 µm in size. At the outer regions of this sample, the SDAD is reduced to 2-10 µm, the SDAS is reduced to 20-100 µm, and the cluster size is reduced to 100-200 µm. Examining the -40°C and -80°C slow frozen samples, the same morphologies are present. However, for each temperature step, the dimensions of the dendritic features are incrementally reduced further. The dendrites located at the outer sample surface have SDAD of approximately 1-10 µm, which is on the same length scale as the sample grain size of approximately 2 µm. Near the sample surface these features become indistinguishable as dendrites, while at the sample surface a 100 µm thick region is present that appears to be dense and free of dendrites. These results demonstrate that using ambient temperature moulds for a 20 mm diameter sample results in a sufficiently large range of freezing rates to produce a strong gradient in the dimensions of microstructural features.

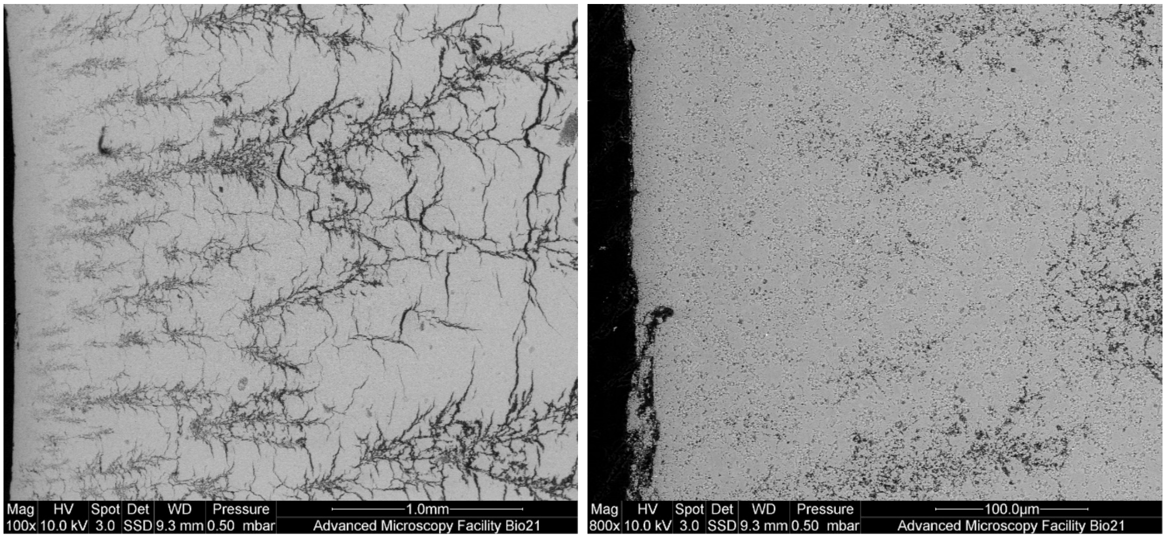

Figure 6.6.f: (Left) 100x view of sample #142 (-40°C, slow frozen) with bottom of sample oriented on the left side of image, showing scaling of dendritic features away from the sample surface. (Right) 800x view of sample #142, showing region of dense microstructure at the sample surface.

Comparing the microstructure of the slow-freezing samples with that of the fast-freezing samples, both similarities and differences are observed. When examining regions of samples that experience similar freezing conditions, similar microstructures are typically observed. Examining the centre regions of the fast-frozen samples (Figure 6.6.g, right), another dendritic microstructure with small dendritic clusters is visible, very similar to the microstructure observed on the outer regions of the slow-frozen samples. The similar microstructure and similar length scales of these features suggests that these regions experienced similar freezing rates during solidification. However, these dendritic clusters of 100-150 μm in diameter are observed alongside of large macroscopic crack-like voids on the order of 500 μm in diameter. Near the surface of the fast-frozen samples a different homogenous microstructure is visible, that appears near-dense with some evenly distributed porosity visible. These observations regarding the microstructure appear consistent across all the pre-chilled mould samples, while the appearance of the crack like voids vary in size, location and geometry.

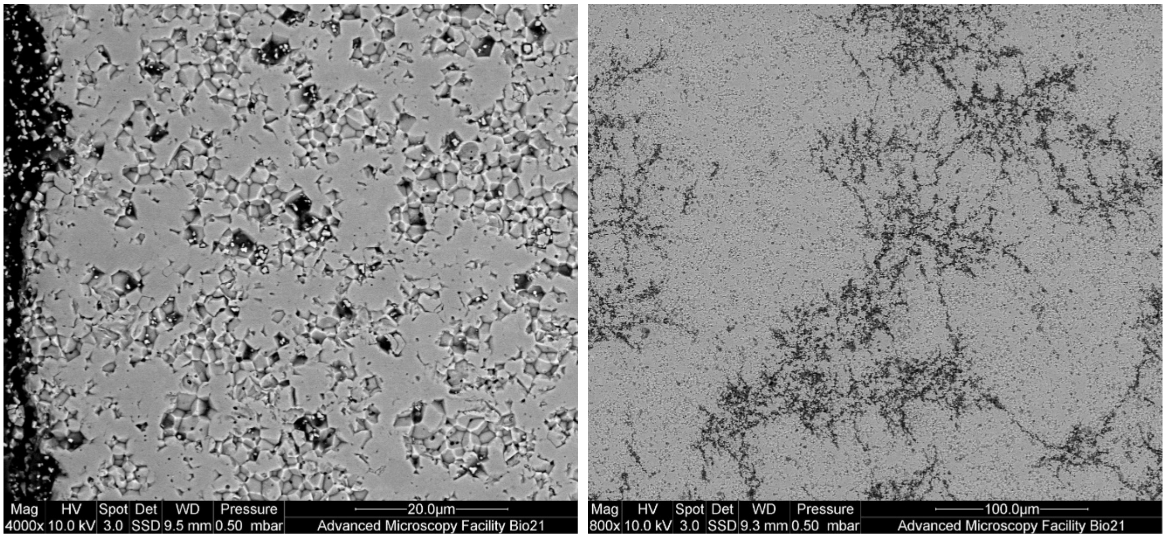

Figure 6.6.g: (Left) 4000x view of microstructure of sample #155 (-40°C, fast frozen), showing homogenous microstructure with visible porosity. (Right) 800x view of centre region, showing dendritic clusters.

Between the two aforementioned regions in the fast-frozen samples, a different microstructure is observed, with thin (1-3 µm) porous stripes repeating at intervals between regions of dense ceramic. The freezing direction in Figure 6.6.h is from left to right, showing that the stripes run perpendicular to the freezing front direction. Larger perpendicular voids are also visible intermittently, that may be cracks or fractures. These elongated striped pores would offer a favourable path for cracks to propagate.

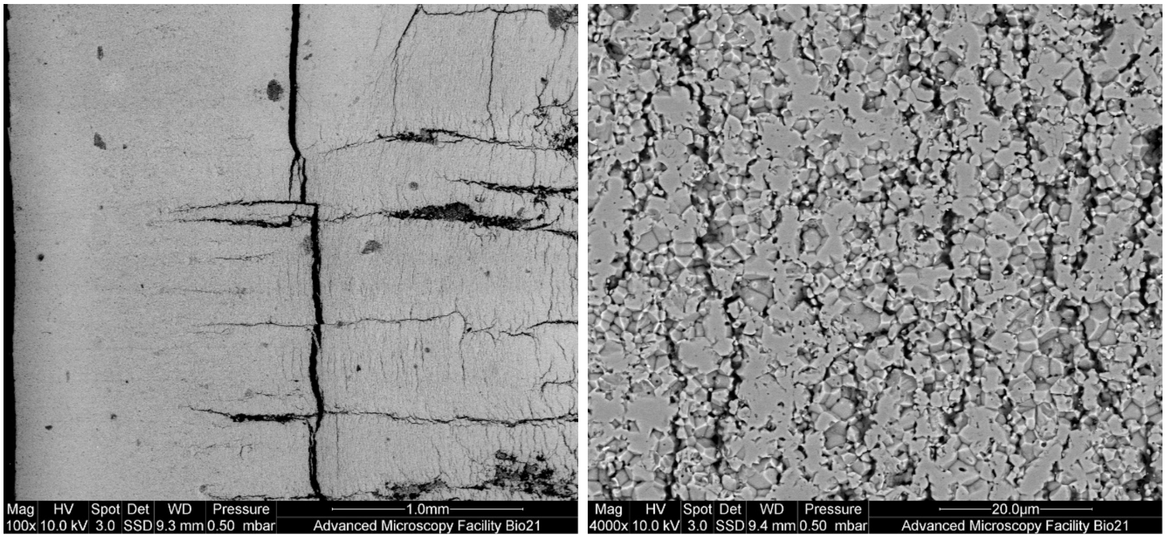

Figure 6.6.h: (Left) 100x view of lower region of fast-frozen sample #155, showing microstructure transition region. (Right) 4000x close up view of centre area of left image, showing striped pore microstructure.

In addition to these porous strips, some long larger voids are visible which run parallel with the direction of freezing. These parallel voids appear to have formed during freezing, as they appear to transition into starting points for the dendritic clusters to develop from.

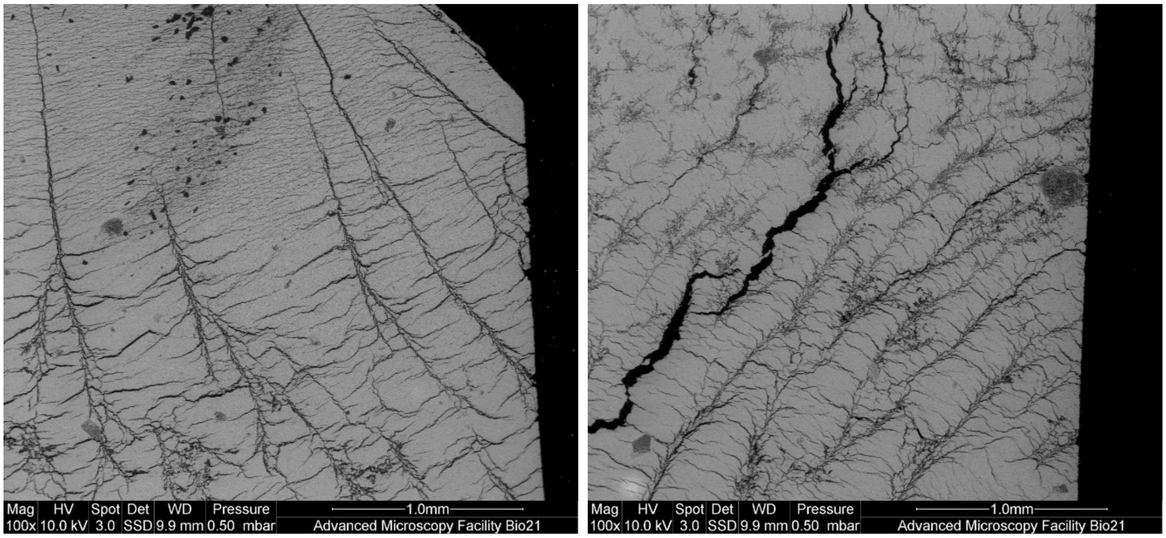

Figure 6.6.i: (left) 100x image of sample #163 (-20°C fast-frozen) showing development of parallel voids into dendritic voids. (Right) 100x image of sample #168 (-80°C fast-frozen). These images show the freezing direction moving from the top and bottom of the images, to the bottom right and top right respectively. This corresponds with freezing propagating from the sides of the sample at the mould wall, and moving towards the top of the sample, which has an insulated Teflon insert where the injection port is located.

Examining the transition region between the striped dendrites and dendritic clusters, the results are inconsistent, making it is difficult to draw direct conclusions. However, there does appear to be at least five distinguishable morphologies occurring as a function of freezing rate. The following table (Table 6.6.a) lists these observations, by fastest-freezing to slowest-freezing.

Table 6.6.a: Observed microstructure sorted by freezing rate. Where 1 is the fastest freezing rate and 6 is the slowest freezing rate.

Microstructure observed	Representative sample of morphology	Image Magnification
1. Near-dense microstructure with homogenous distributed fine (<5 µm) porosity	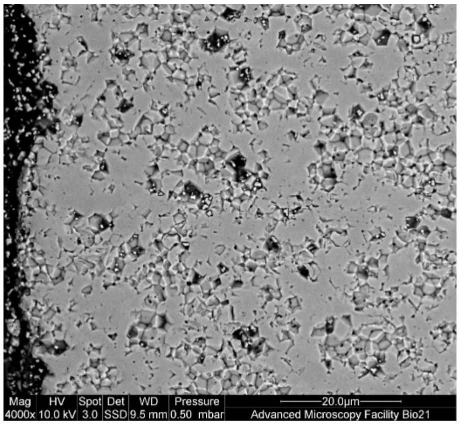	4000x
2. Thin (1-5 µm) elongated pore stripes perpendicular to direction of freezing.	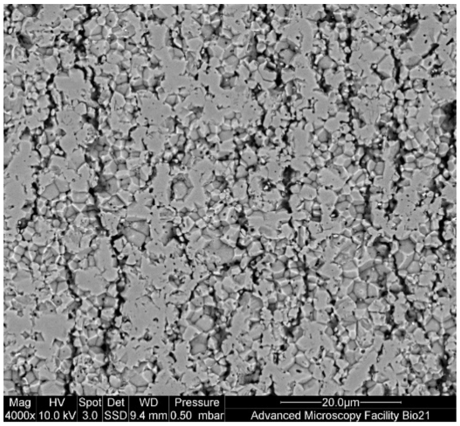	4000x
3. Thin (1-5 µm) elongated pore stripes perpendicular to direction of freezing, with thin elongated pore stripes perpendicular to direction of freezing, with intermittent larger pores parallel with freezing direction. Parallel pores vary in size significantly.	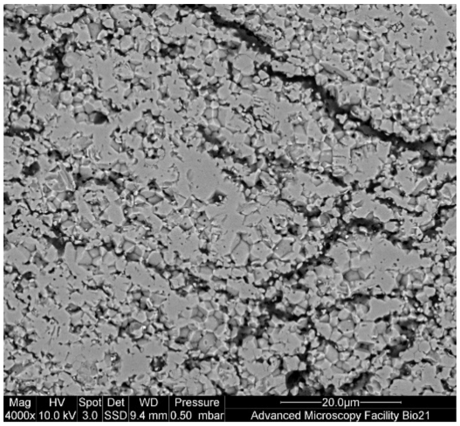	800x

Microstructure observed	Representative sample of morphology	Image Magnification
4. Long parallel pores develop into dendritic pores with perpendicular arms. SDAD varying from 5-20 µm.	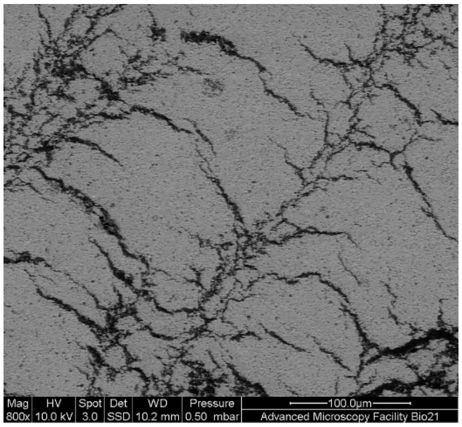	800x
5. Dendritic pores develop into small branching dendritic clusters (100-250 µm)	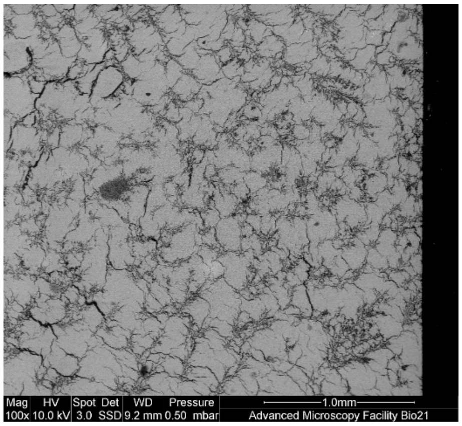	100x
6. Branched dendritic clusters grow in size (300 µm+), with SDAD of 5-20 µm. As the freezing rate decreases, there is an observed increase in SDAD and corresponding decrease in SDAS.	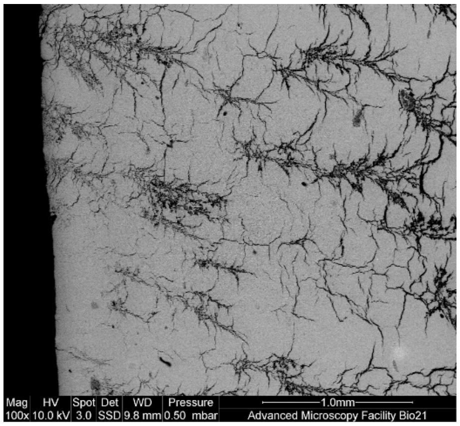	100x

While there does appear to be an observable trend relating the pore microstructure to freezing rate, the large crack-like voids are inconsistent in their presentation and distribution. From these results it has not yet been determined whether they formed during the freezing process, or in a subsequent processing step. The formation mechanism behind these diverse microstructures is also not speculated here, as it is discussed subsequently in Chapter 6. Further future investigation of heat transfer may be appropriate to determine the freezing front velocity, and the degree of supercooling present at the point of evolution for each of these structures.

6.7 Conclusion

Using a temperature-controlled freezer, and by applying pre-chilled and ambient mould freezing regimes, dense freeze cast samples were able to be produced under a range of freezing rates varying at the sample centre in excess of one order of magnitude. By studying the role of freezing rate on dense freeze-cast microstructure, the feasibility of producing dense microstructures from pressureless sintering of fast freeze cast samples was able to be evaluated. Specifically, by analysing the green and sintered microstructures of dense freeze cast ceramic samples via SEM, the effect of freezing rate on microstructure was able to be clarified.

For cyclohexane-based highly loaded alumina ceramic suspensions, the formation of dendritic pores was observed under most conditions, alongside dense bulk ceramic. However, as expected, the size of dendrites varied inversely with the speed of the solidification process. Under slow freezing, the diameter of some secondary dendritic arms was observed to exceed 20μm, while under fast freezing the diameter of dendritic arms became smaller than sintered ceramic grain size of 2μm, giving the appearance of a near-dense homogenous microstructure. While small pores were successfully formed via fast freezing using pre-chilled moulds, it was found that under pressureless sintering, complete elimination of small pores was not achieved.

However, in addition to dendrites produced from pore templating, in samples that were fast-frozen the formation of large crack-like voids was also observed. This indicates the possibility of significant forces being present during the freezing processes, the drying processes, or both. This in turn suggests that future detailed investigation into the solidification and drying processes may be appropriate.

7 Study of drying-rate and cracking in dense freeze-casting

7.1 Aim

While the presence of internal cracking within dense freeze-cast samples has been previously identified [33], the previous chapters have confirmed the existence of these cracks within formed green-body samples, prior to undergoing the sintering process step. These cracks are undesirable and will result in parts of reduced strength, significantly limiting the potential applications for the process. The purpose of this study is to identify the contributing causes behind crack development, and the relationship of process conditions to crack formation, distribution and microstructure.

7.2 Introduction

From a fundamental perspective, the presences of cracks within samples can be taken as evidence of a sufficiently strong force (or stress) having been applied to the material, that it exceeded the limit of the material's constitutional properties. Examining the orientation and morphology of cracks can be used to obtain inferential knowledge about the orientation and type of origin forces, but this information alone does not immediate reveal the cause behind these forces. This is the challenge that this study is seeking to address; to identify the source of the crack-generating forces (stresses) responsible for the evolution of cracks.

Regarding cracks in freeze-cast samples, multiple hypotheses were identified as possible causes resulting in the formation of cracks within samples. The freeze-casting process involves several process steps, and until sintering, samples are quite fragile and easily damaged. The weak interparticle bond strength prevents samples from being cleanly sectioned prior to sintering, which limits the ability to examine the internal microstructure at intermediate stages, preventing potential theories from being evaluated.

Initially, the hypothesis proposed for crack generation involved differential shrinkage that was thought to be occurring during the sintering process. It was posited that the gradient of pore sizes previously identified in the porous microstructure could result in non-isotropic densification during sintering, and thus generating significant internal stresses within samples. While the existence of these proposed forces during sintering was not disproven, in chapter 6 internal cracks of similar magnitude were identified within sectioned bisque-fired samples. As those samples had not undergone significant densification, this suggested that crack formation is occurring prior to sintering, possibly in either the freeze-solidification and/or freeze-drying process steps.

Cracking has previously been observed to occur during some freeze-solidification processes involving particulate or porous materials, resulting in observations such as frost-damage, freeze-thaw cracks, and froze-heave cracking. Models now exist to explain the mechanical behaviour of freezing processes in porous and particulate materials[132], that have been validated to hold with non-aqueous solvents[133].

Similarly, the observation of cracks within freeze-dried objects is also not a new phenomenon, with examples found in literature across a range of different frozen media:

- Fissures in the dried matrix were observed after freeze-drying of a range of different solutions of biological interest[134].
- Internal cracking in frozen potatoes was observed after freeze drying [135]
- Bones exposed to low temperatures were observed to have the most severe forms of micro and macroscopic cracking when subjected to freeze drying[136]
- Gel-cast samples developed internal cracks after subjected to freeze-drying, with the freeze-drying process proposed as the cause, along with a hypothesis for mechanism [137].
- An extensive study of freeze-drying effects on pharmaceutical product cakes showed both extensive shrinkage and internal cracking[138–141].

Figure 7.2.a: Internal cracking in freeze dried potatoes [1]

Due to the fragile nature of examining fractured materials, Micro-computed-tomography (micro-CT) has been proven to be a valuable technique as it allows non-destructive internal examination of internal features and cracks within samples, even enabling crack propagation to be studied [142]. For this reason, Micro-CT was used extensively for the present study. In the past, micro-CT imaging has been successfully applied for examination of cracking phenomenon, including both freeze-thaw cracks [143], and freeze-drying cracks[137, 138]. Micro-CT has also previously been applied for imaging freeze-cast samples, however the focus has been primarily on the solidification process only[79, 114, 144–148].

7.3 Methods

In this study, a sequence of three experiments was executed to test the following:

Experiment 1: Examine the microstructure both before and after freeze-drying, to determine whether the freeze-solidification or freeze-drying process were responsible for crack evolution.

Experiment 2: Investigate if the process conditions during freeze-drying *(the process step identified as responsible for cracks in Experiment 1)* affect the development of cracks, using ambient pressure freeze-drying (slow-drying), and conventional freeze-drying (fast-drying).

Experiment 3: Investigate the development of cracks during freeze-drying, over time by using 4D Micro-CT imaging.

Experiment 4: Investigate the effect of freezing rate on the crack morphology observed within freeze-dried samples.

7.3.1 Experiment 1: Comparing internal microstructure before and after freeze-drying

7.3.1.1 Preparation of Freeze-cast Samples

As developed in the previous chapter, the primary suspension used for this study is a highly loaded alumina suspension of 55 vol.% solids fraction, dispersed in cyclohexane solvent, using 0.9 wt.% of Hypermer A70 dispersant relative to the weight of ceramic used. The primary advantages of this solvent is the high vapour pressure enabling rapid drying through the freeze-drying, and a conveniently accessible freezing point of 6ºC[102].

Four samples were prepared in total: two with the mould pre-chilled to -80°C, and two with the mould prechilled to -20°C. The standard size mould inserts were used, which produces samples with a 20mm diameter.

The samples were prepared and frozen using an ultra-low temperature freezer (Operon, Korea), using the pre-chilled mould technique, where moulds were first cooled to the desired temperature, and suspension then injected into the cold mould. The temperature of the moulds can be monitored during freezing using thermocouple probes attached to the mould surface, that are connected to a thermocouple data acquisition device (National Instruments NI-9213, Austin TX) attached to a desktop computer for the recording of temperature freezing profiles.

After freezing is complete, the frozen samples were removed and placed into individual sealed screw-lid containers and loaded into in an ultra-low temperature freezer for short term storage, before being removed and transported for imaging. During transport, the samples were kept frozen in a container cooled by dry ice, with the temperature in the container monitored and maintained below -20ºC.

7.3.1.2 Pre-fractured sample

Since the underlying cause of sample cracking is unknown, and since the freezing and drying processes are dynamic and challenging to analyse the cracking in real time, an additional test sample was prepared. This sample was prepared with an artificial split passing through the centre of sample, intended to provide additional insight into the crack formation mechanism. This cast-in split was achieved by preparing the mould chamber with a strip of Kapton tape passing through the centre of the mould, dividing it in two vertically. This film divider is both temperature and chemically resistant and the frozen suspension does not adhere strongly to the tape. Because of this, the tape film acts a mechanical interruption inside the sample. However, because the Kapton tape is also very thin, effects on heat transfer inside the sample are minimised. The addition of this divider was expected to affect the distribution of any residual stresses left within the sample as a result of the freezing process. This divider will also affect the freeze-drying process, both by providing mechanical interruption, but also by providing an additional exposed interface for sublimation to proceed from. This is expected to affect the distribution of resulting cracks, which in turn could provide further insight towards the origins of the stresses. For this study, one of the -80°C samples were prepared with a split through the middle of the sample, using this method.

7.3.1.3 Sample Micro-CT Imaging

For all experiments, samples were imaged in 3D using a micro-CT instrument, as this technique allows the fine internal crack structures to be observed non-destructively without disturbing the sample matrix, for both frozen samples before freeze-drying, and green-body samples after freeze-drying.

Micro-CT scanning was performed with a *phoenix nanotom m* (GE Sensing & Inspection Technologies GmbH, Wunstorf, Germany) operated using *xs control* and *phoenix datos|x* acquisition software (both GE Sensing & Inspection Technologies).

The position of the stage relative to the X-ray source and detector was optimized to achieve a resolution of 8.938 µm on a region of interest 2.7 cm wide and 2.15 cm high on the micro-CT detector. Samples were scanned for 10 minutes (timing = 500 mS, av = 1, skip =0) at 70 kV and 320 µA, collecting 1199 unique X-ray projections of each sample through 360° of rotation.

7.3.1.4 Imaging of Frozen Samples

While the process of imaging frozen samples is non-contact, depending on samples it may not necessarily be non-destructive, as if frozen samples are simply exposed to atmospheric ambient conditions they will melt. In order to prevent melting occurring during imaging, a chilled sample stage was prepared to provide cold environment for samples during imaging. This stage consists of a thermoelectric cooling element (TEC) system (Debyn CT160 Coolstage, Suffolk, UK[149]), which offers a threaded mounting stud that is able to be actively cooled to -20°C. Due to the relatively large size of samples (20 mm diameter) the standard sample chamber was unsuitable. An aluminium disk (25 mm diameter) was prepared with a suitable threaded mount, for use as a sample stage. The cooling finger assembly can be mounted in the micro-CT rotational axis, to provide continuous cooling during the imaging process. The resulting hot side of the TEC is in turn cooled via an external water chiller. Using this chilled stage, the samples are kept frozen indefinitely, with the unloaded surface plate temperatures measured at around -5°C using an external thermocouple sensor.

A small clear polyethylene sample container was placed over the samples while on the cooling stage, in order to provide additional thermal insulation from ambient convective air temperatures. The cover fits the outer diameter of the aluminium stage disc and does not contact the samples. A small hole was made in the top of the container to allow atmospheric pressures within the sample chamber to be maintained. Since the cooling capacity of the stage is limited, additional cooling was provided by placing dry-ice pellets on top of the sample cover, outside of the imaged field of view. No significant frost build-up was observed on the sample cover. A similar method of cooling has been successfully demonstrated for imaging of large frozen samples, with the disadvantage of dry ice requiring periodic replacement[150].

After imaging, frozen samples were returned to their individual sample storage containers, and then placed back into the cooled transport container. Samples were then returned to the main sample freezer for short-term storage, before undergoing low-pressure freeze-drying followed by re-imaging.

7.3.1.5 Imaging of Freeze-dried samples

For imaging of freeze-dried ceramic samples, the same imaging parameters were used. Dried samples were either placed on a 25 mm glass rod, or placed on the cooling platform, with the cooling component disabled (at ambient temperature).

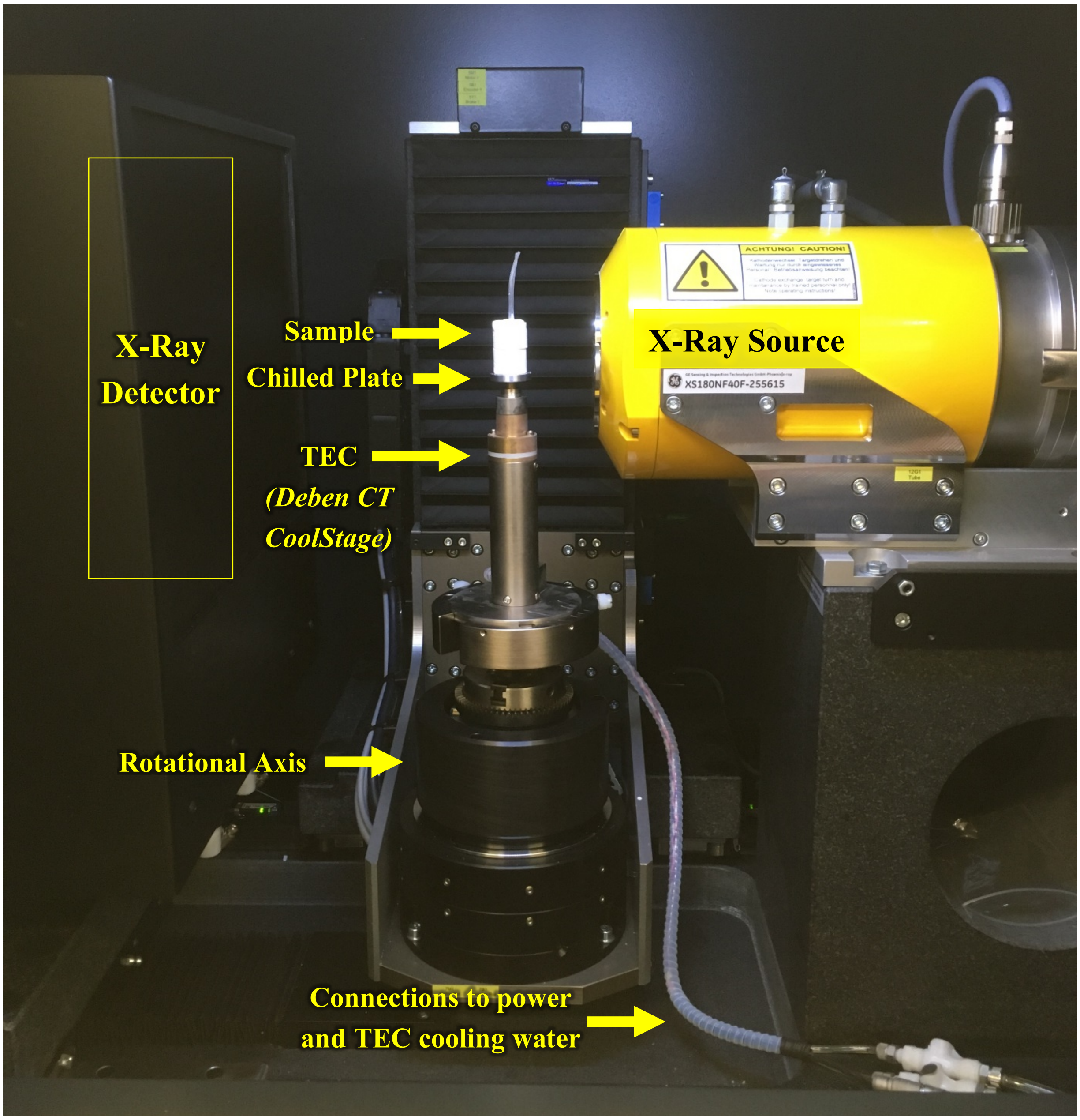

Figure 7.3.a: Sample placed on cooling stage, inside micro-CT instrument. Plastic sample cover not in place.

7.3.1.6 Volume Reconstruction & Image Processing

Volume reconstruction of the micro-CT data was performed using Phoenix datos|x reconstruction software (GE Sensing & Inspection Technologies) and data was exported as 16-bit volume files. Reconstructed data was exported as a stack of .tiff images for further analysis. The image stack sequences were pre-processed using XnConvert, to optimise contrast, brightness, as well as applying mild image sharpening. The image set was then imported into ImageJ for analysis and segmentation. Sample image sets can be aligned via internal features, in order to directly compare between frozen and freeze-dried states for the same sample.

Provided that the minimum size of any features of interest exceeds the effective voxel resolution of the reconstruction, and providing that there is sufficient contrast between phases, features of interest can be segmented by thresholding the pixel values within the image stack. This allows the internal pore space to be determined and extracted as 3D volume and can be visualised to show the geometry of internal cracks and pores. The surface of this volume can then be exported as an STL mesh file for postprocessing using MeshLab. MeshLab enables the mesh file to be cleaned and reduced, creating a simplified mesh requiring less computational resources for post processing. This software also enables minor void volumes (generally small, disconnected pores) to be removed if required, to improve clarity in order to ensure that the configurations of the primary void structures are easy to identify. ParaView was used to prepare the visual animations provided in the supplementary material.

7.3.2 Experiment 2: Examining freeze-drying process conditions effect on microstructure

7.3.2.1 Freeze-Drying of Samples

In order to remove the solvent from samples without liquid-phase solvent being formed, the process of drying via sublimation can be performed, commonly via a freeze-dryer[32]. A freeze-dryer works by places the samples under vacuum. By reducing the pressure below the solvent's triple-point (5.4 kPa for Cyclohexane[151]), the solvent cannot exist in the liquid phase, resulting in any phase change occurring via sublimation. Some freeze-dryers also offer temperature controlled heated platforms, where heat can be added to drive the gas/solid phase equilibrium forwards, and hence maximise the rate of solvent removal by sublimation.

However, sublimation can also occur at pressures above the triple point, where at temperatures below the freezing point, stochastic kinetic processes at the gas/solid equilibrium interface can also provide sufficient energy to solid solvent molecules for them to undergo sublimation. This enables the solid sample solvent to self-sublimate, even while the samples are in storage in a freezer at below the sample freezing point. The higher pressure and lower temperatures result in slower rates of sublimation than compared to drying in a freeze-dryer, but the high vapour pressure of Cyclohexane results in sufficiently significant self-sublimation rates that consideration is required during the preparation and scheduling of frozen non-dried samples for later examination.

These two methods of sublimation provide two different freeze-drying process conditions, resulting in two different freeze-drying rates that can be compared to examine the impacts of the freeze-drying process conditions on internal cracking. For examining fast drying rates, a commercial freeze-dryer was used under vacuum at ambient temperatures, while for slow drying rates, self-sublimation was performed in an ultra-low temperature freezer, with samples at ambient atmospheric pressure.

For reduced pressure drying, samples are dried in a commercial freeze dryer. The freeze-dryer (Telstar, Spain) is configured to operate at 0.1 mBar, with no shelf heating. Before drying, samples are placed on a cold tray stored the freezer at -20ºC or lower, before the tray is transferred to the freeze-dryer. This process avoids the possibility of samples melting before the freeze-drying process begins. Samples were freeze-dried for a minimum of 26 h, after which all samples were fully dried.

For freeze-drying at ambient pressure, samples were first transferred to a tray and placed in a conventional freezer, maintained at -18ºC. The sample weight was measured once a week, and the sample was considered dry once no change in weight was observed between measurements. A significantly slower rate of drying was observed for samples dried via this method, as drying generally took 3 to 4 weeks to complete.

After freeze-drying via any method, samples were transferred to individual containers for storage at ambient lab temperature and pressure, before being transported to the micro-CT facility for imaging.

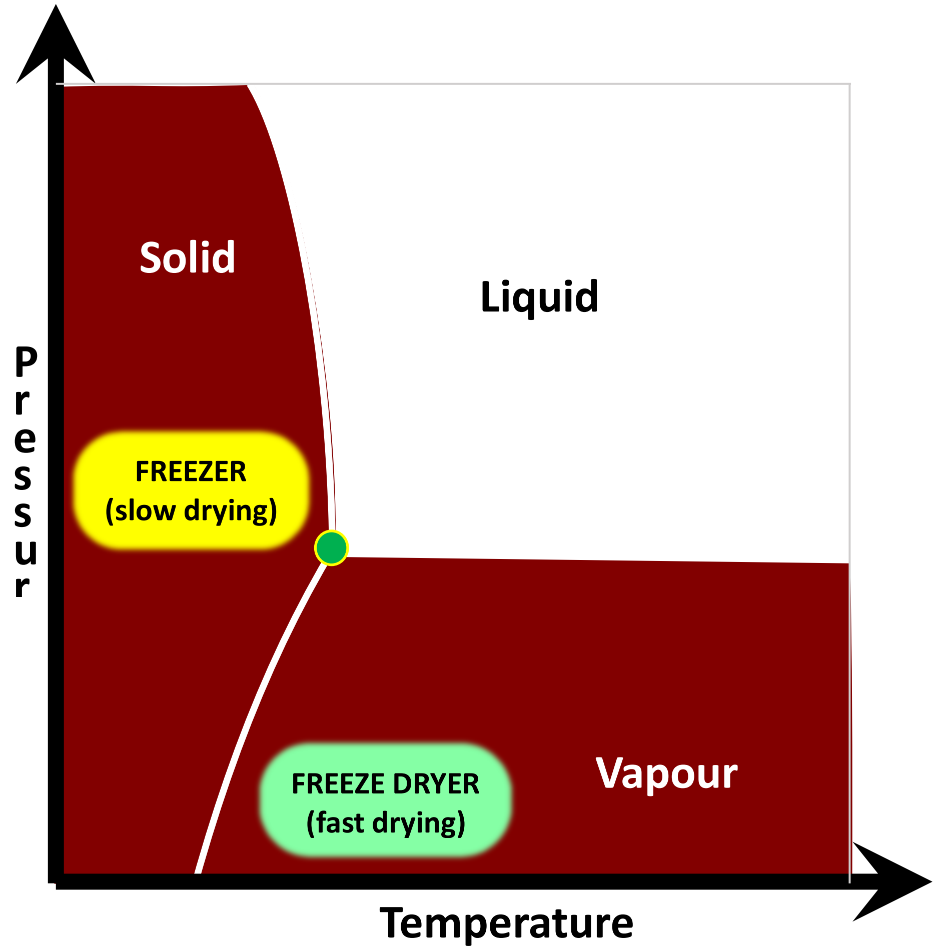

Figure 7.3.b:Representation of different freeze-drying methods, plotted on pressure vs temperature phase diagram.

7.3.3 Experiment 3: Investigate the development of cracks during the identified process over time, using 4D imaging

In order to observe the effect of freeze drying on the internal structures as a function of time, a single freeze-cast sample was prepared for study over an extended time period. For this experiment, a sample was frozen at -40°C, using the pre-chilled mould method. After demoulding, this sample was immediately transported to the micro-CT facility for imaging, using the chilled stage and the same acquisition parameters as for other samples. This sample remained on the chilled stage continuously with active cooling. This sample was reimaged six times over the course of five days at increasing time intervals, while undergoing slow freeze-drying.

7.3.4 Experiment 4: Investigate the effect of freezing rate on the crack morphology observed within freeze-dried samples.

For this final experiment, samples were freeze-cast under varied freezing rates using ambient and pre-chilled moulds. Samples were then weighed, and then imaged in the frozen state via micro-CT. Then, placed into a freezer at -20°C, and left to self-sublimate. After 10 days, samples were re-weighted to confirm drying, and then re-imaged via micro-CT.

7.4 Results

7.4.1 Experiment 1: Comparing internal microstructure before and after freeze-drying

In this experiment, micro-CT imaging proved to be a valuable and flexible imaging technique for non-destructive inspection. With the use of a chilled stage, samples that were thermally sensitive were able to be sufficiently stabilised for a complete high resolution (ca. 9µm voxel) reconstruction to be obtained.

The micro-CT process was successfully able to capture the internal structure of samples, in both frozen and freeze-dried conditions. For each sample, the reconstructions of the sample in frozen and freeze-dried states were manually matched using microstructural features, allowing samples to be aligned in 3D for direct feature comparisons. Datasets were not resized or scaled, allowing direct dimensional comparison. Cross-sectional slices in the xy-plane were extracted from the centre of each sample, and these are displayed in Table 1 below.

It is important to consider the actual resolution of the captured microstructure, as features that are smaller than this unable to be clearly isolated and segmented for analysis. While the captured theoretical voxel resolution was calculated as 9 µm, for some samples, some sample movement was detected during the reconstruction process, and both automatic and manual correction tools were applied to correct for this. Where significant correction was required (typically cases where correction factors exceed 3 voxel units) it was generally observed that the fidelity of the resulting reconstruction was poor. Those samples were then re-imaged to achieve an acquisition of satisfactory acuity, in order to obtain a high-quality reconstruction for microstructural analysis. Issues with sample movement were generally only encountered during imaging of frozen samples, and not during imaging of dried samples. For this reason, it is proposed that the observed sample movement may be due to frost build-up and dissipation both on the sample surface, and on the imaging platform.

Examining the frozen samples, a relatively homogenous structure was observed, free of large pores or voids. For the two samples frozen at -20ºC in pre chilled moulds (samples 58-1 and 58-2), a patterned feature could be observed towards the centre of the sample. Those features are dendrites, the size of which correspond to the local freezing rate. Toward the centre of the -20°C frozen samples, the lower freezing rate results in dendrites that become visible with micro-CT imaging. While the previous study (Study of freezing-rate and microstructure via dense freeze-casting) confirmed the presence of dendrites in other regions, those features were too small and could not be resolved at that resolution. In the sample frozen more quickly at -80°C in a prechilled mould (57-2) there were no large dendrites visible in the centre of the sample.

Table 7.4.a: Cross section (xy-slices) showing internal features of freeze-cast samples, in both frozen (left) and freeze-dried (right) states. The freeze drying was at ambient temperature and 0.1 mBar vacuum.

Sample #	Frozen	Freeze-Dried
57-2 (frozen at -80°C, pre-chilled)	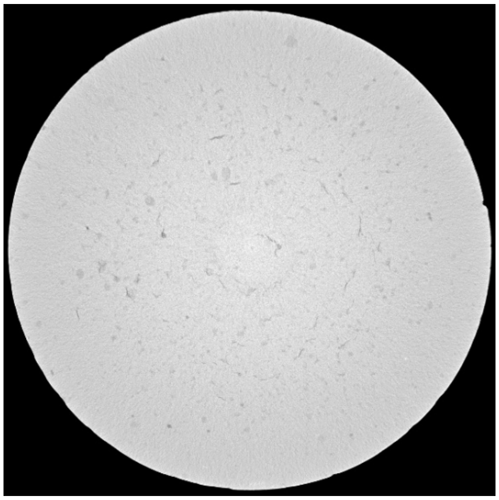	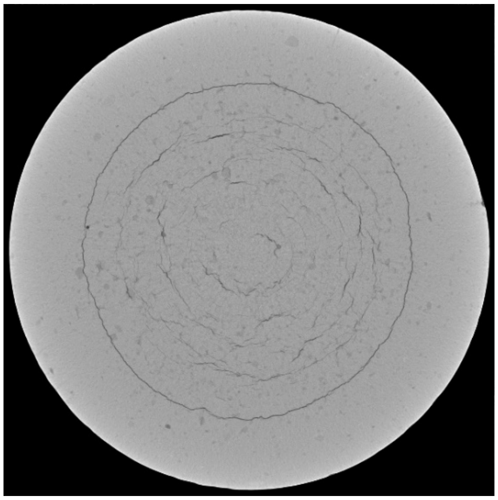
58-1 (frozen at -20°C, pre-chilled)	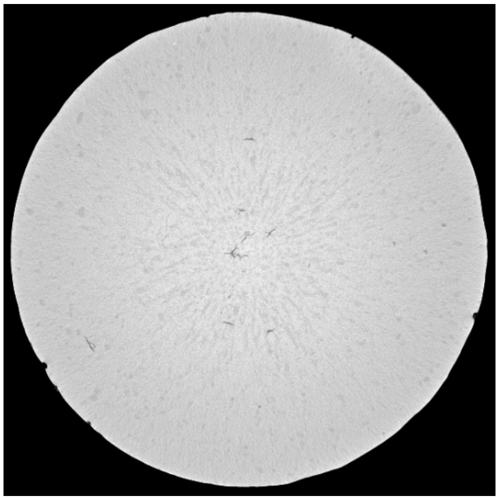	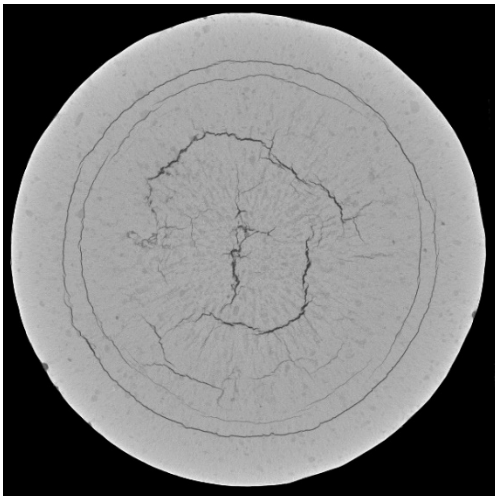

Sample #	Frozen	Freeze-Dried
58-2 (frozen at -20°C, pre-chilled)	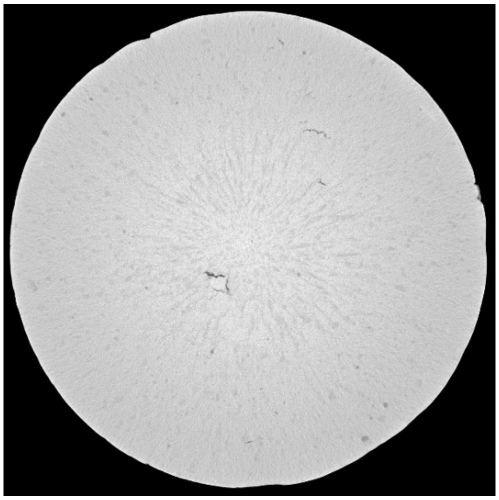	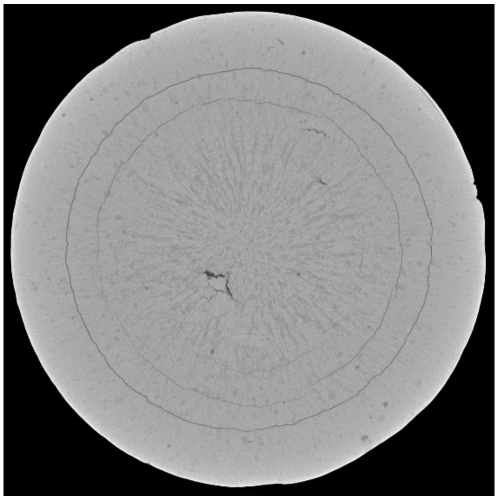

When comparing the xy-slices from the sample reconstructions, the presence of macroscopic cracks can be identified in the freeze-dried samples. The significant difference in the material density between ceramic and air phases results in a high visual contrast evident between the cracks and other voidage features, against the background of the solid particulate ceramic matrix. The morphology of the identified cracks is observed to vary between samples. Notably, in all of the dried samples, continuous concentric circular radial cracks are observed. Within the boundary of those radial cracks, additional discontinuous cracks are also observed, varying in size and severity between samples.

In contrast, when looking at the frozen samples, these macroscopic cracks are not visible. This enables us to identify that the freeze-drying process is the key step in the freeze-casting process responsible for the development of macroscopic internal cracks.

Examining the morphology of the cracks observed in the dried slices, in addition to the continuous radial cracking, there are also smaller discontinuous inner cracks that can be seen. These discontinuous cracks vary significantly in size, shape and severity, differing both within each sample, and differing when comparing across the set of dried samples. Both sample 58-1 and 58-2 were frozen and prepared under the same process conditions. In sample 58-1, severe internal cracks can be seen within the central region of the sample. By comparison, within sample 58-2, there is significantly less cracking visible in the same region. While some random variation is to be expected, this may suggest that there was variation in aspects of how these samples were handled or processed. In particular, it was identified that there were different varying intervals for each sample, between the time of freeze-casting, to the time of freeze drying. For sample 58-1, 12 days elapsed between freeze-casting and freeze-drying, while for sample 58-2, 18 days elapsed. While during this interval samples were stored in the ultra-low temperature freezer to avoid melting, it is proposed that this delay may have provided sufficient time for significant self-sublimation to occur.

Examining the tomograph slices for the frozen samples, minor internal defects can be observed. Some of these defects appear to be possible inclusions or clumps, while others appear to be small micro-cracks. Observing these same features in the dried sample, many of these defects appear to have been favourable for crack propagation, with the crack features preferentially passing through the major sites of defects observable in the frozen state, as seen in Table 7.4.b below. The discrepancies observed in the images below (e.g when compared to the later images in Table 7.4.f) is attributed to the lack of controlled drying and sample handling in the preparation of the earlier samples.

Table 7.4.b: Cross-section images of sample 57-2 (-80°C frozen in prechilled mould), showing development of defects in frozen state into favourable paths for crack propagation in the freeze-dried state. Composite images overlaid with varying transparency provided for clarity. Samples were NOT stored under controlled and consistent conditions, resulting in differences observable between samples.

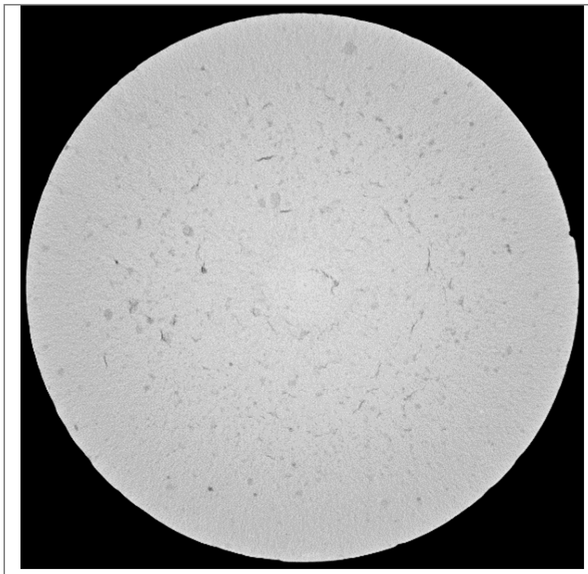 Frozen Sample	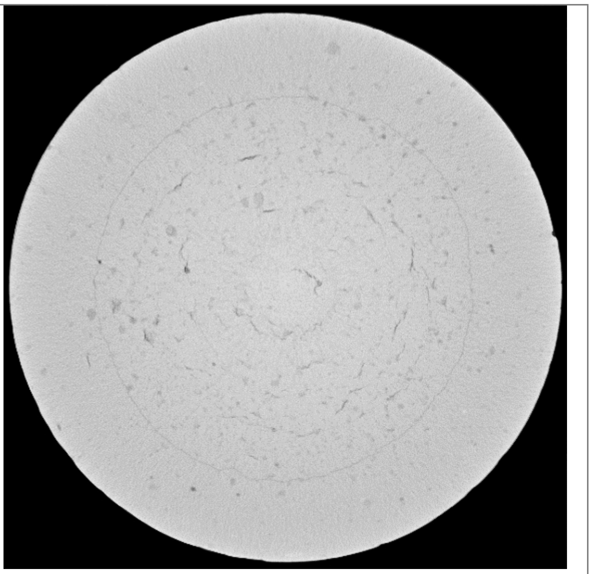 *Composite image:* Frozen Sample + Dried Sample Overlay at 25% Opacity
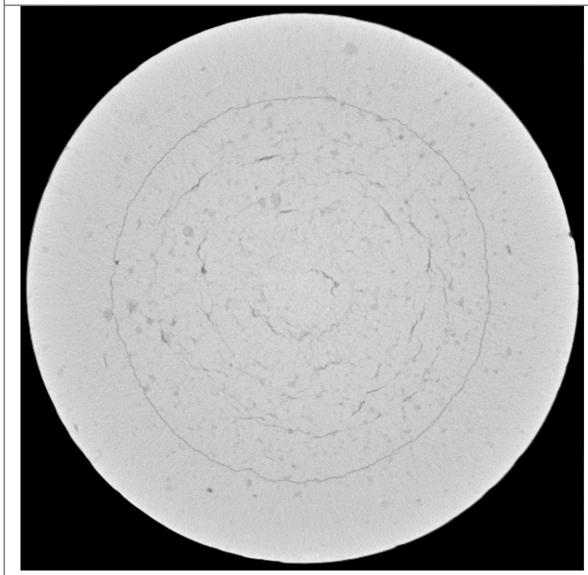 *Composite image:* Frozen Sample + Dried Sample Overlay at 50% Opacity	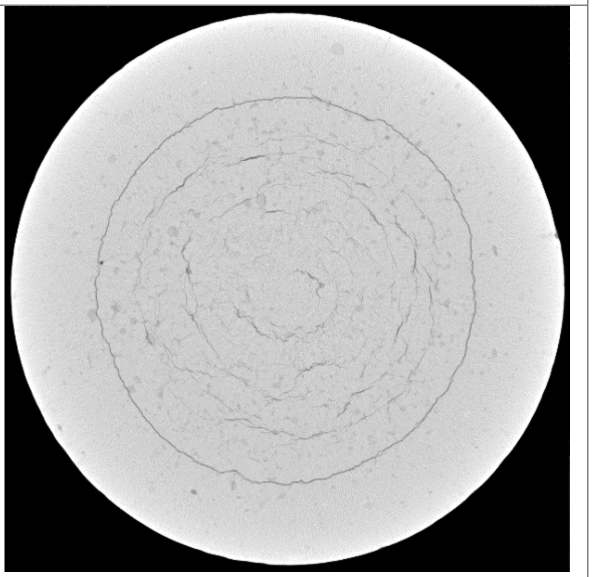 Dried Sample

The final sample of interest was cast with a single layer of Kapton tape film passing through the mould diameter, inserted prior to suspension injection. The imaging of the sample in the frozen state shows the clear separation between the mould halves. During imaging it was observed that the tape film was primarily adhered to the right side of the sample, although upon separating the halves, a small amount of material was observed to be stuck to the other tape side. It was not recorded which side of the tape originally carried adhesive before casting. As was observed in the previous (non-split) samples, here it is also true that in the frozen state no large voids or major defects are visible in the split sample, while in the dried state large internal cracks are now visible (see images in Table 7.4.cTable , below).

Table 7.4.c: Imaging of freeze-cast sample, cast with internal film, in both frozen and dried states

Sample #	**Frozen**	**-Freeze-Dried**
57-1 (frozen at -80°C, pre-chilled)	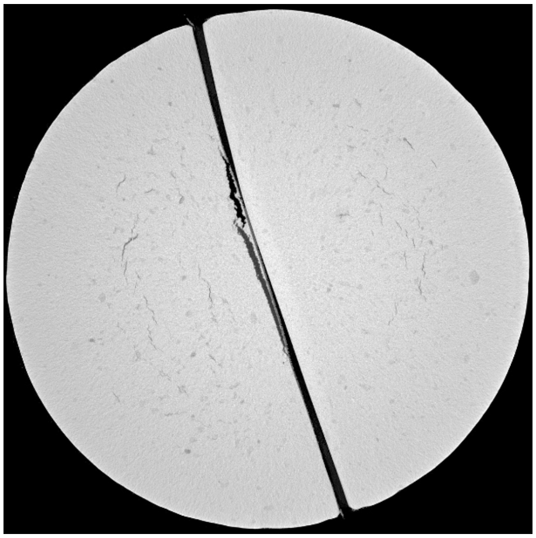	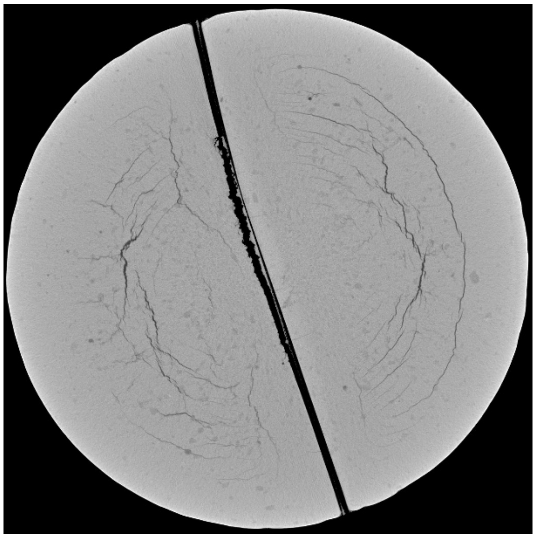

Comparing the internal cracks seen in the pre-split sample after freeze drying, with the cracks seen in undivided samples (e.g. Table 7.4.bTable), both similarities and differences can be observed. The general distribution of these cracks is similar, with the cracks generally preferring to propagate through the sample circumferentially in both the split and non-split samples. However, the development of these cracks in the pre-split sample appears to have been significantly affected or interrupted by the split-divider. It is notable that in the pre-split sample the cracks do not extend all the way to the internal cut surface, as the cracks taper off before reaching the interface of the split. In the previously examined freeze-dried samples, there appears to be a crack-free margin or boundary layer extending from the outer sample surface. This observation appears to also hold true for the split sample, where a crack-free margin in observed both from the outer circumference and the inner split surface.

Since the film divider used is both thin, and parallel to the direction of freezing, there should not be any significant change in the heat transfer within the sample during freezing, and as such minor changes in heat transfer from the addition of the divider were not considered as a factor responsible for the significant change in crack distribution.

The absence of cracks in the region of the sample near the crack divider confirms that freezing rate velocity, or variations in freezing rate across the sample, are not directly related to the formation of cracks. It was previously confirmed that when examining the microstructure on a line path from the outer sample radius to the centre of the sample, the freezing rate will vary from fast to slow. Since the crack free regions near the sample divider extend continuously from the sample surface to the centre, passing through all regions of varying freezing rate in the sample, this confirms that freezing rate is not a primary factor driving crack formation. This also suggests that if other crack causing factors can be controlled, crack-free microstructure should be possible to achieve within the range of freezing rates observed here.

For this reason, freeze-drying appears to be the primary cause behind crack development. However, if the evolved crack morphology was to be solely due to the process of freeze-drying, then the expected crack pattern would also be different from that observed here. For the un-divided sample, concentric cracks are observed extending from the sample surface at regularly spaced intervals. This is due to the freeze-drying beginning from the sample exterior where the sample interfaces with ambient air, and with drying progressing over time towards the centre of the sample. From the imaging of the frozen pre-split sample, a relatively large gap (~100 μm) is already visible between the two sample halves, which should allow freeze-drying to also begin from the internal cut surface faces. For this reason, if this same pattern of crack development were maintained for the pre-split sample, then it could be expected that the crack pattern for the divided sample would resemble concentric semicircles (see, Figure 7.4.a below).

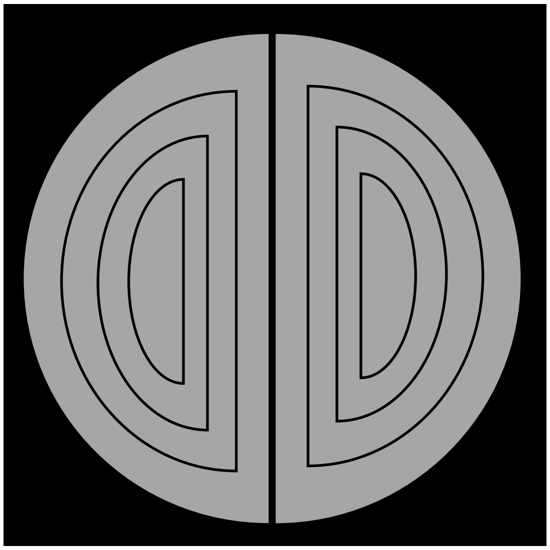

Figure 7.4.a :Schematic representation of crack pattern expected in freeze-dried sample with crack-divider.

The disagreement of the predicted crack distribution in Figure 7.4.a with the observed results shown in Table 7.4.c suggests that while the cracks are confirmed to evolve during the freeze-drying process, the development of the resulting freeze-dried crack morphology is not yet fully understood, and may be a product of both the freeze-drying process alongside as other contributing factors that remain to be identified.

Figure 7.4.b: Digital photo of sample 57-1 after imaging in the freeze-dried state was completed. Then the sample was split, and this image recorded. During the splitting, some material remained adhered to the tape film, which can be seen in the centre region of the right sample half. The internal surface is generally very smooth, like the tape surface.

7.4.2 Experiment 2: Examining effect of freeze-drying rate on cracking microstructure

For this experiment a set of two samples were prepared (Set A), with each sample dried via one of two different methods; fast-drying in a freeze-dryer, and slow-drying in a freezer. This experiment was then repeated in order to produce a second set of samples (Set B). Specific care was taken to reproduce the same experimental conditions between the sets. The fast-dried samples were transferred to the freeze dryer within 24 h after freeze-casting was completed, in order to minimise any self-drying that could occur during temporary sample storage.

7.4.2.1 Tracking Drying Degree via Weight Measurements

A single batch of suspension was successfully prepared for this study, and the expected percentage weight of solvent as prepared was calculated as 11.2% by weight. However, due to some settling and deposition of ceramic on the walls of the container, and due to evaporation occurring during the dispensing of the suspension, the actual solids content of the suspension may vary slightly from the prepared concentration. A drying mass-lost test indicated the real solvent content of dispensed suspension was higher, at 13.0%. This measured solvent concentration was then used to predict the final drying weights of all samples, in order to confirm that drying was complete. By measuring the starting weight, and the weight loss over time, the "% degree of drying" can be calculated as the proportion of mass measured lost during drying, relative to the expected mass to be lost after drying, equal to the mass of solvent in the dispensed portion of suspension. From other sample mass lost tests, it was measured that typically around 0.1 g of solvent evaporated from liquid suspension within the first 60 seconds after casting, before freezing has completed. Since the starting weight of the sample is only recorded after demoulding, this initial solvent loss is not considered, and it is expected that the degree of drying will be slightly underestimated as a result. Since 0.1 g of solvent loss is approximately equal to 5% drying degree, an error of 5% was assumed for the degree of drying. As can be seen from Table 7.4.d below, weight tracking measurements of samples before and after fast freeze-drying allow us to calculate the drying degree. Since the calculated drying degree approached 100%, it was concluded that complete solvent removal had been successfully achieved.

Table 7.4.d: Weights of fast-dried samples before and after freeze-drying.

Sample #	Frozen Weight after Demoulding	Weight after Freeze-drying
59-2	15.4315 g	13.4613 g
	0 ±5% dried	98.5 ±5% dried
59-4	15.4983 g	13.5401 g
	0 ±5% dried	97.5 ±5% dried

For the slow dried sample, the samples were initially allowed to self-dry in the ultra-low temperature freezer at -80°C, with weight progress in Table 7.4.e below. However, weight measurements after 4 days (since demoulding) indicated that the rate of self-drying was very low, with a calculated degree of drying of 3%. These samples were then transferred to a conventional freezer at -15°C, and the rate of mass loss was observed to increase significantly. After 7 days, the samples were reweighed, and the calculated degree of drying approached 100%. The samples were kept in the freezer for one more week to verify complete drying. After 13 days the samples were weighed again, and the degree of drying did not increase significantly, so the samples were considered fully dried and ready for imaging.

Table 7.4.e: Weights of slow-dried samples over time during self-sublimation freeze-drying

Sample #	Frozen Weight after Demoulding	4 days	7 days	13 days
59-1	14.9253 g	14.8751 g	13.0685 g	13.0463 g
	0% dried	3% dried	96.0 ±5% dried	97.2 ±5% dried
59-3	14.9340 g	14.8845 g	13.1029 g	13.0878 g
	0% dried	3% dried	94.6 ±5% dried	95.4±5% dried

For imaging these samples, the same micro-CT imaging procedures were used as for the previous experimental sample set, and the internal crack morphologies were successfully captured after data reconstruction. Cross-section xy-plane images are presented below in Table 7.4.f comparing the internal crack morphologies between the two drying methods. Comparing the internal crack morphology between Set A and Set B, it is readily apparent that there is a high degree of similarity and consistency between the features observed between the sets, with distinct morphologies apparent for each drying method used. The similarity of cracks between sets provides good confidence that the primary conditions relevant to the formation of cracks were maintained consistently between the two sample batches.

Table 7.4.f: Cross-section of freeze-cast samples after freeze-drying via slow- and fast- freeze-drying. All samples fast-frozen using -80°C pre-chilled mould.

	Set A	**Set B**
Slow Dried (Freeze-dried in freezer at -15°C and ambient atmospheric pressure for 14 days)	**Sample 59-1** 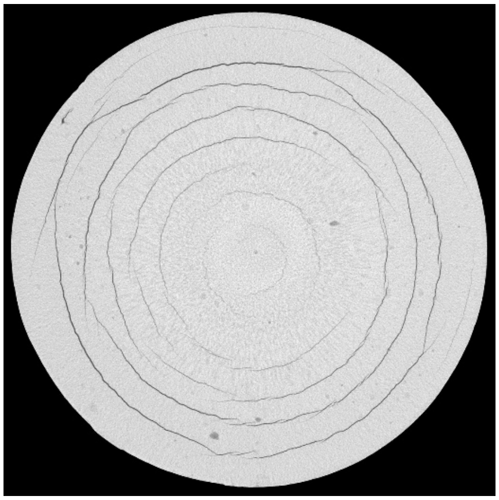	**Sample 59-3** 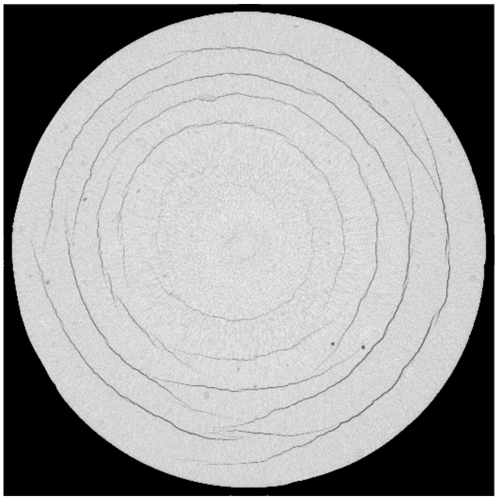
Fast Dried (Freeze-drier at 0.1mBar for 68 h)	**Sample 59-2** 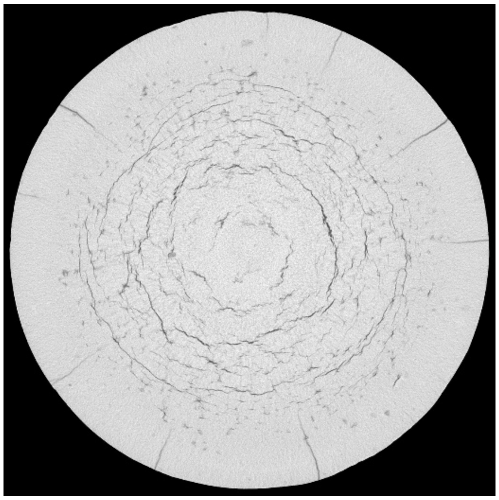	**Sample 59-4** 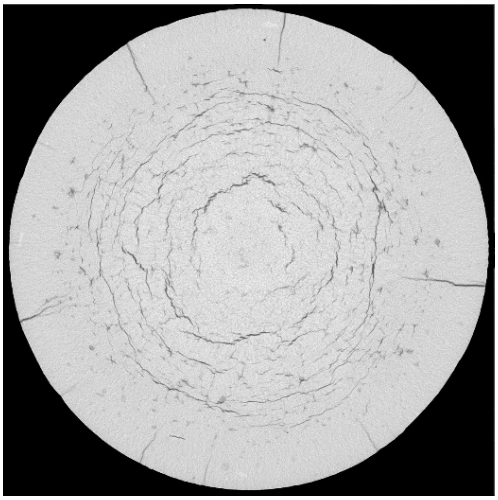

Examining the slow dried samples, the cracks appear as one style of continuous circular ring cracks, with a reasonably regular and consistent spacing evident between each crack ring ("onion-like cracking"). This crack pattern can be observed extending from the edges of the sample towards the centre, but the crack opening diameter varies. Cracks found toward the outside of the sample appear clearly defined, while cracks toward the centre become more difficult to differentiate from the solid phase due to limited imaging resolution available.

In contrast, the fast-dried samples display a significantly different cracking morphology, with two component cracking styles observed. Within the sample interior region, a high degree of cracking can be observed as short discontinuous cracks ("dispersed fracturing"). While these cracks are generally discontinuous, there does appear to be some ring or general circular alignment to these cracks. On the outer region of the fast-dried samples fewer cracks are observed, and the cracks that are present are parallel to the direction of freezing, and present as spoked radial cracks. These large radial cracks appear to be relatively spaced out, with the regions between the radial cracks being largely crack free.

The crack and solid phases can be segmented to create a pore volume network, and this can be re-rendered to reveal the crack morphology in 3D. While the high contrast between crack and solid phase assists in enabling clean segmentation, the captured resolution limits the segmentation to features larger than 20 μm (approx.). Longer connected cracks (as observed in the slow dried samples) were straight-forward to extract, due to their larger crack-opening diameter. Conversely, the fast-dried samples presented a challenge, as that crack network is comprised of many crack-like features that vary or taper in size, from large features (>40 μm), to small features that are below the imaging resolution.

Through image post-processing, some high aspect ratio features as thin as 5 μm can be identified and visualised. However small features were unlikely to be extracted accurately and as a result were excluded from quantitative analysis. Small (<25 μm diameter) disconnected void or pore objects were cleaned and removed from the 3D reconstructions used for illustration, in order to maintain clarity in the reconstruction, so as to help reveal both the general orientation and the connectivity between the primary crack-like features. Additionally, the freeze-casting process inherently produces small dendritic structures. Even though with fast-freezing these dendrites are below the imaging resolution, patterns from these structures become partially visible towards the centre region of these samples, and it is desirable that the dendritic features are not confused with crack-like features. Overall, a best effort was performed during post-processing to accurately identify and include large crack-like features in the pore-space segmentation, while smaller or more ambiguous features were typically excluded.

The design of the cylindrical moulds is intended to enable analysis with the assumption of primarily radial 1D freezing occurring from the mould wall inwards towards the sample centre. As can be seen from the full 2D xz-axis slices above, while the cracks mostly do extend vertically in the Z-axis, there is observable curvature to the cracking network near the top and bottom of the sample. For this reason, only a subsection extracted from the centre region of the sample is used and shown in the 3D visualisations shown below.

Visualisations of the internal crack and pore spaces are provided below for the two fast and slow dried samples. These images are obtained by taking a cylindrical slice from the centre region of the sample reconstruction. These 3D visualisations will also be made available as supplementary materials, with details to for provided in Appendix 11.1.

Finally, an exploration of the potential mechanisms for the development of these cracks with time, are presented and included in subsequent discussion sections of this chapter.

Figure 7.4.c: Images of 3D reconstruction of segmented pore space

Sample 59-3: Slow-Dried	**Sample 59-4: Fast-Dried**
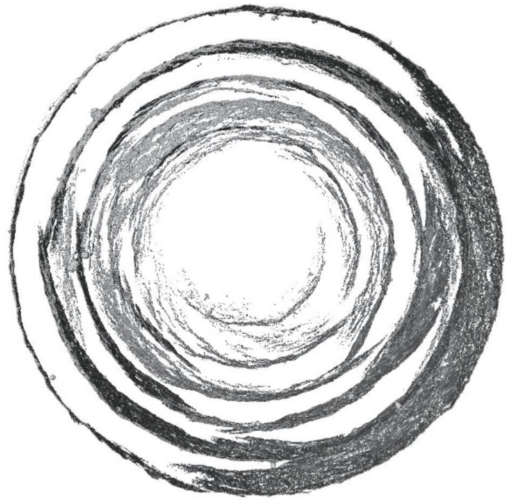	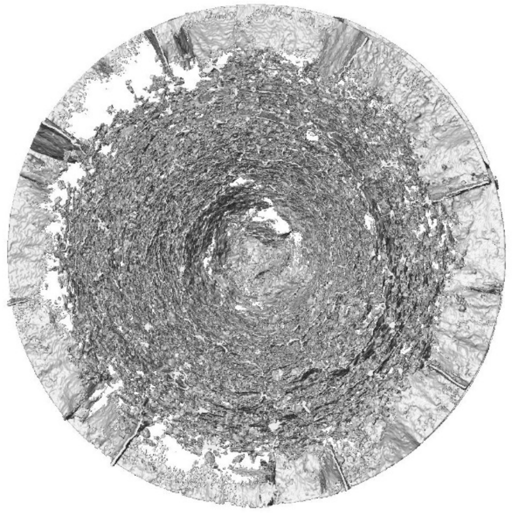

Sample 59-3: Slow-Dried	**Sample 59-4: Fast-Dried**
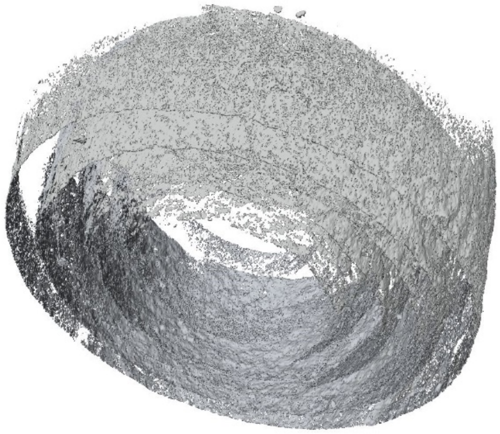	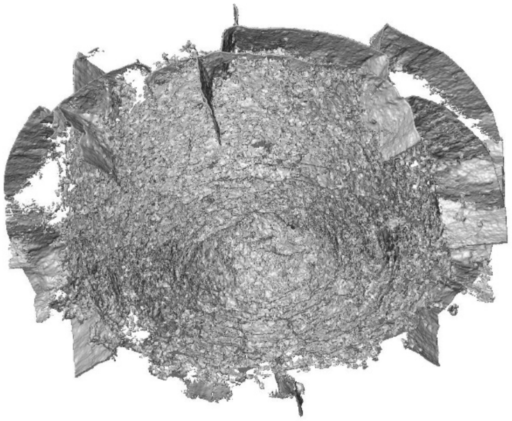
	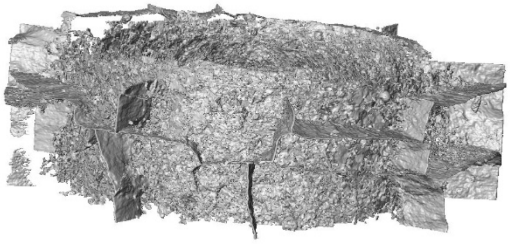
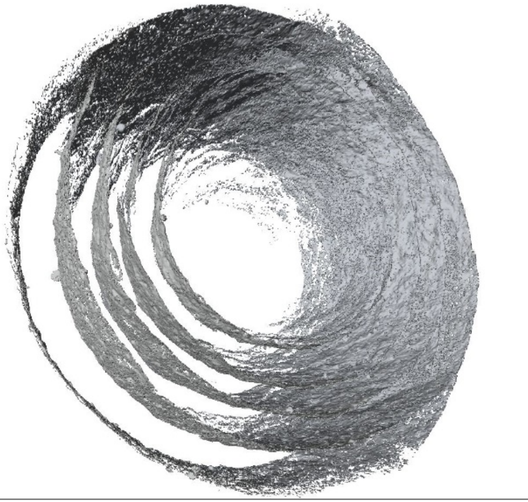	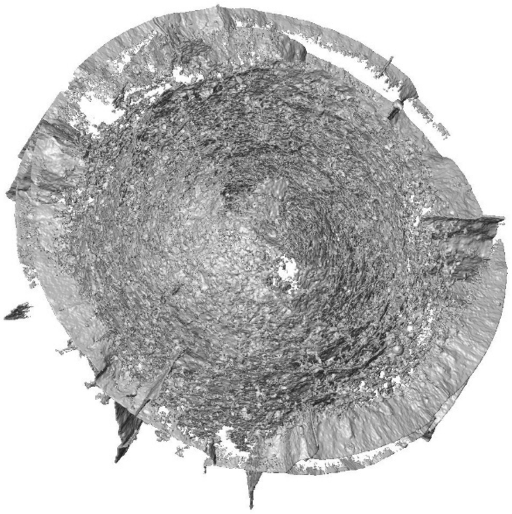

Sample 59-3: Slow-Dried	Sample 59-4: Fast-Dried
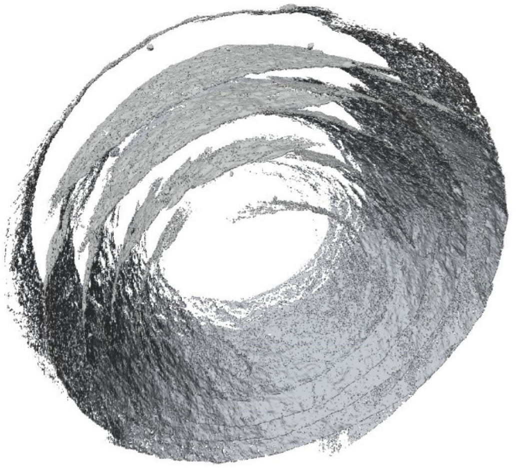	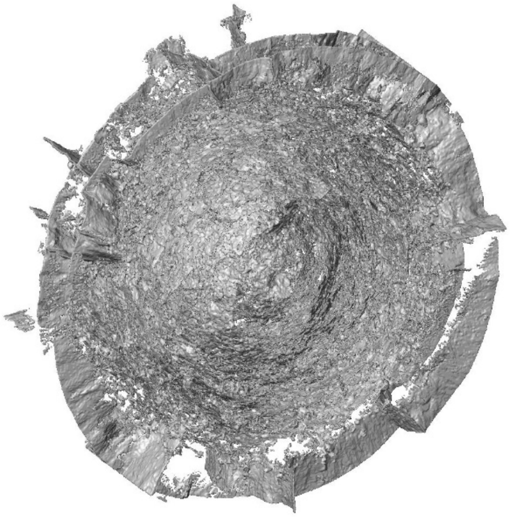
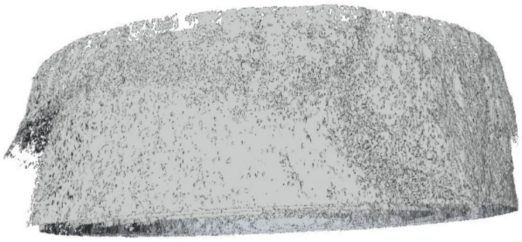	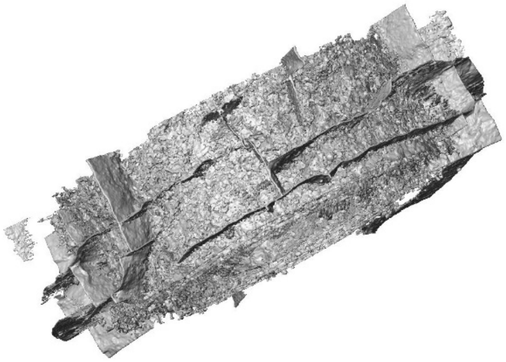
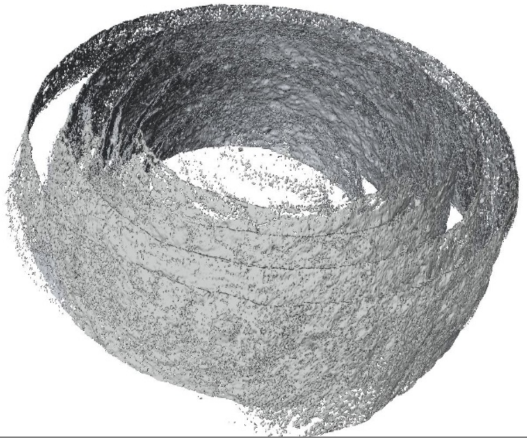	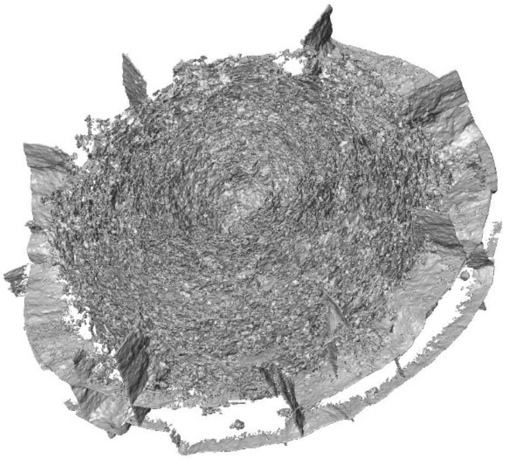

7.4.3 Experiment 3: Investigate the development of cracks during the identified process over time, using 4D imaging

For this experiment, one sample was successfully freeze-cast using a pre-chilled mould at -34°C. This sample was transported in a container with dry ice and imaged via Micro-CT using the previously described chilled sample platform. The time of imaging (t = 0 h) was 15 minutes after demoulding the frozen freeze-cast sample. After imaging, the sample was maintained on the chilled stage, and then reimaged at approximately exponentially increasing time intervals.

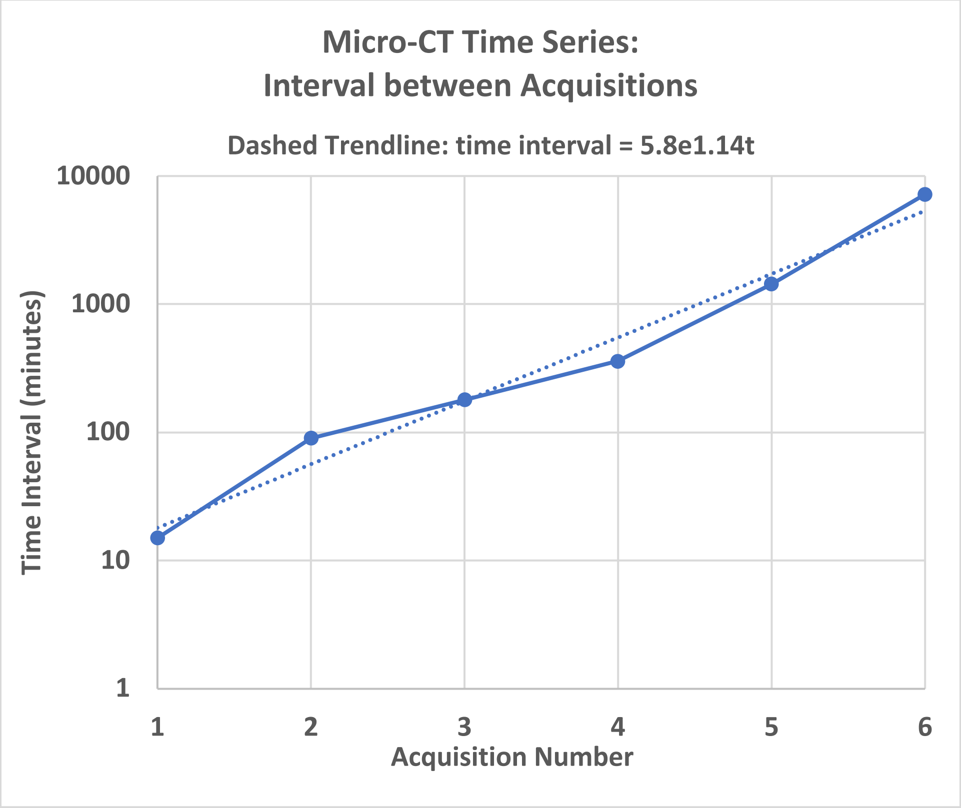

Figure 7.4.d: Plot of time interval between acquisitions vs acquisition number, showing exponential relationship.

Cross-section xy-axis slices taken from the 3D reconstruction are shown below.

Figure 7.4.e: Time series of cross-section images obtained for freeze-cast sample undergoing ambient-pressure freeze drying (self-sublimation)

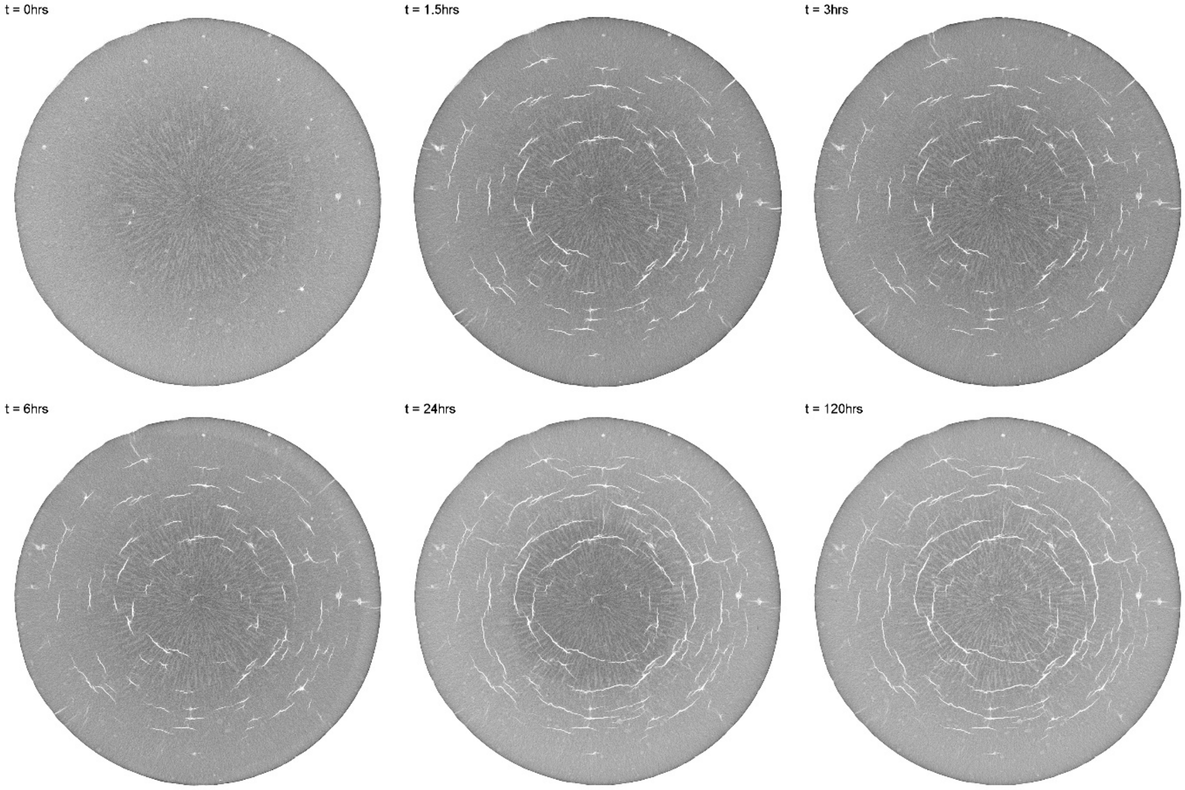

By examining the acquired time series, three main time-dependant observations can be made.

1. Firstly, the internal cracks visibly increase in severity with each time interval.
2. Secondly, there is a dark ring visible, that progressively shrinks in size with each time interval.
3. Lastly, there is a minor change in the diameter of the sample from image to image.

7.4.3.1 Crack propagation over time

The time-step slices above clearly show that the most significant change in the crack distribution occurred between the initial scan, where only minor internal cracking and flaws are evident, and the second scan, where significant internal cracking is now apparent.

By overlaying the first and second scans (Figure 7.4.f below), it is apparent that many of the cracks visible in the second scan have propagated from areas with identifiable flaws visible within the first scan.

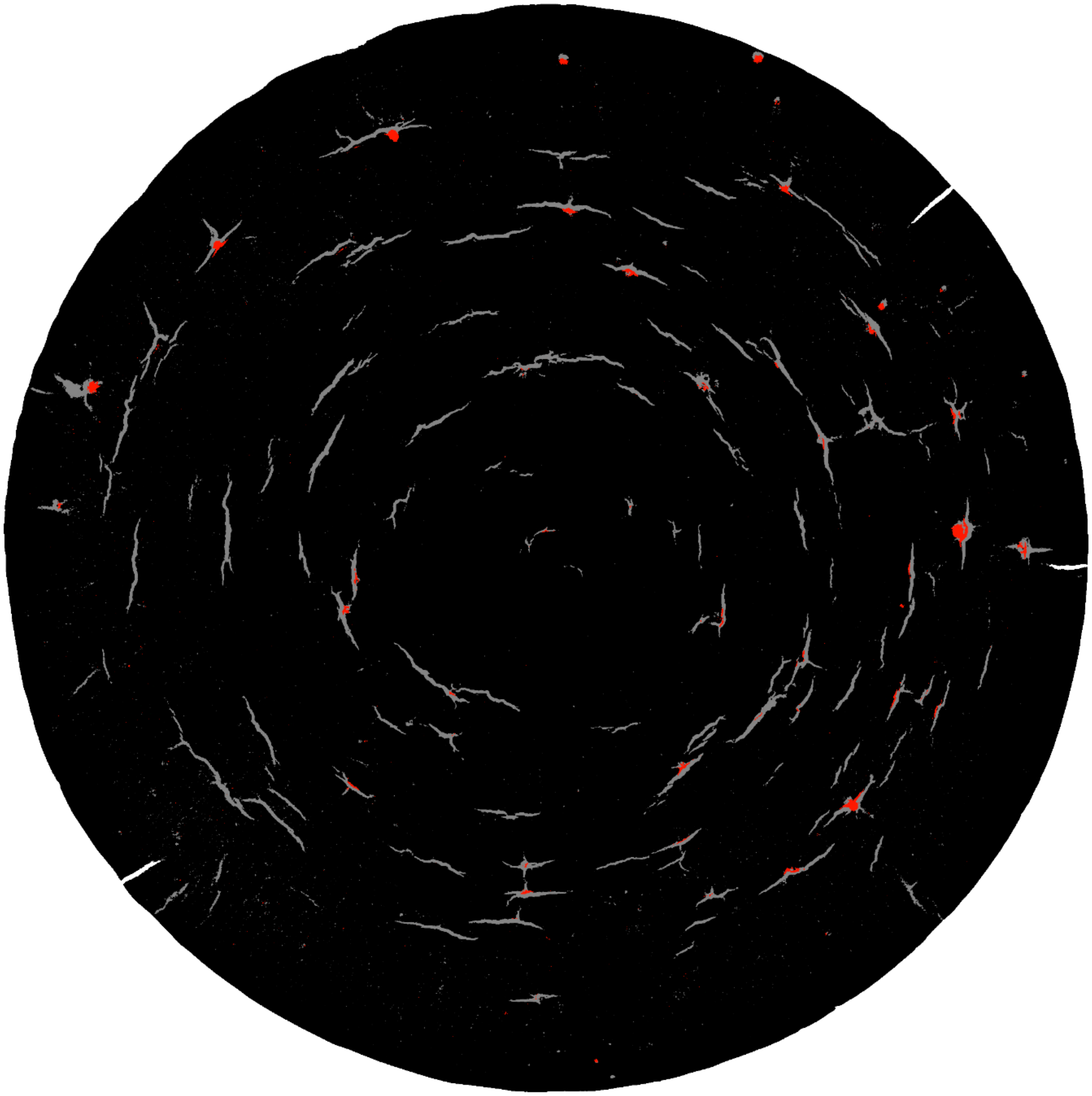

Figure 7.4.f: Composite image highlighting the development of cracks between scans at t=0 and t=1.5 h. The porosity present in the initial scan is highlighted in red.

The progressive development of these cracks was observed to continue throughout the imaging time-series. By generating another comparison overlay between the second and the final scans it was possible to identify that most of the cracks continue to grow in length from existing cracks, with only a minority of new crack formation occurring at new sites. This observation is predicted by fracture mechanic theory, as propagation and growth of existing cracks is more thermodynamically favourable than new crack formation in undamaged substrate.

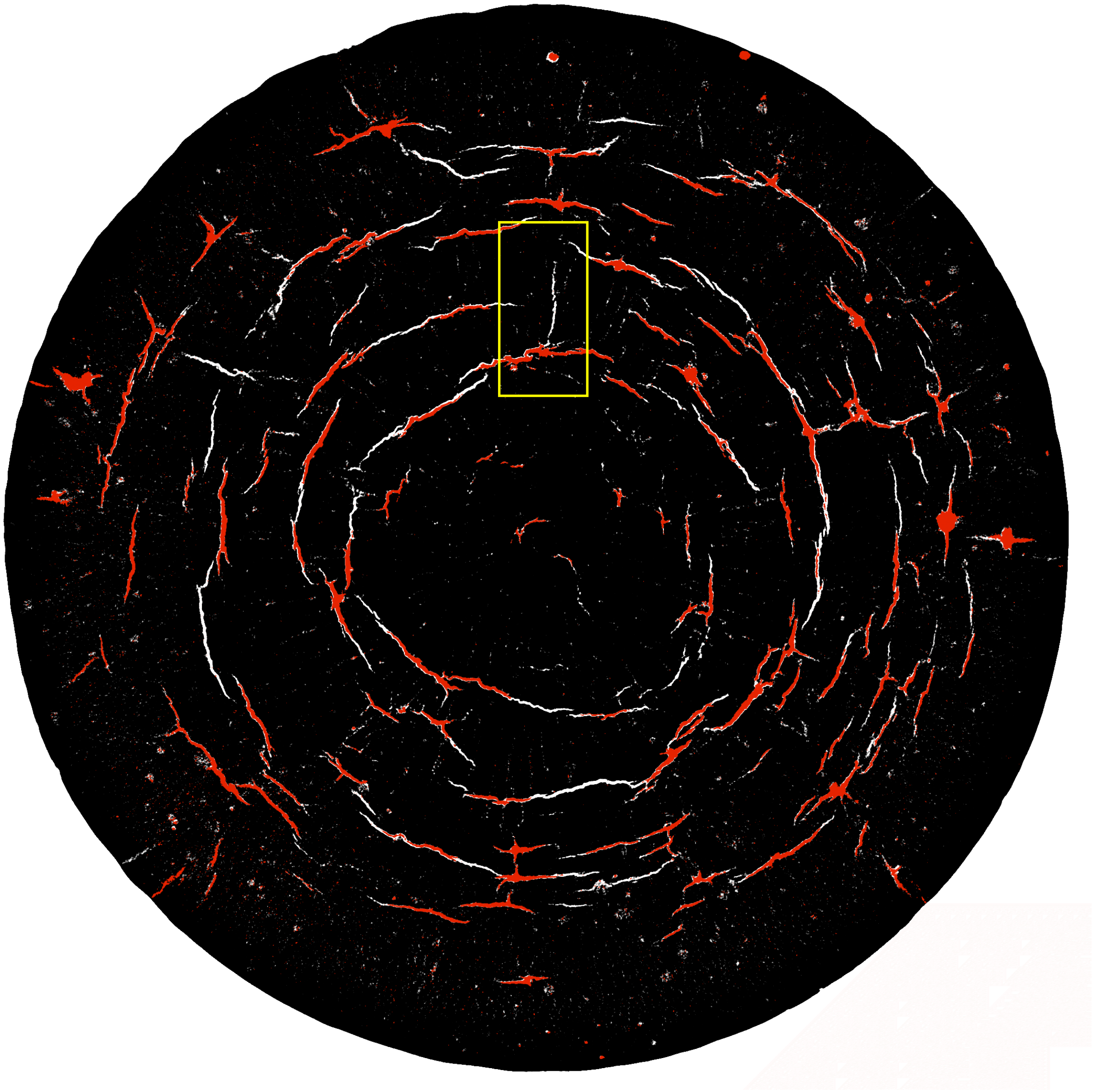

Figure 7.4.g: Composite image highlighting the development of cracks between scans at t=1.5 h and t=120 h. The earlier scan porosity is highlighted in red, with further crack development visible in white. Radial crack of note highlighted in yellow.

When examining the orientations of new crack formations it was observed that the majority of new cracks maintain consistency with the previous observations, with radial "spoked cracks" observed towards the sample periphery, and with concentric circular or arc “onion-like cracking” observed towards the sample centre region. However, select exceptions to these localised cracking styles can be observed in Figure 7.4.g, above.

Of note, one large radial crack was observed to developed closer in towards the sample interior. This specific crack (highlighted in yellow in Table 7.4.f, with enlarged views shown below in Table 7.4.g) was noted as developing along a dendritic pore line, with the dendritic pore structure formed during freezing being identifiable from the first scan.

Examining this specific pore in the 3D context (see Figure 7.4.h below) from the final timestep scan, it was apparent that the fully-developed crack has propagated from a single dendrite, to become a small radial vertical “sheet” crack.

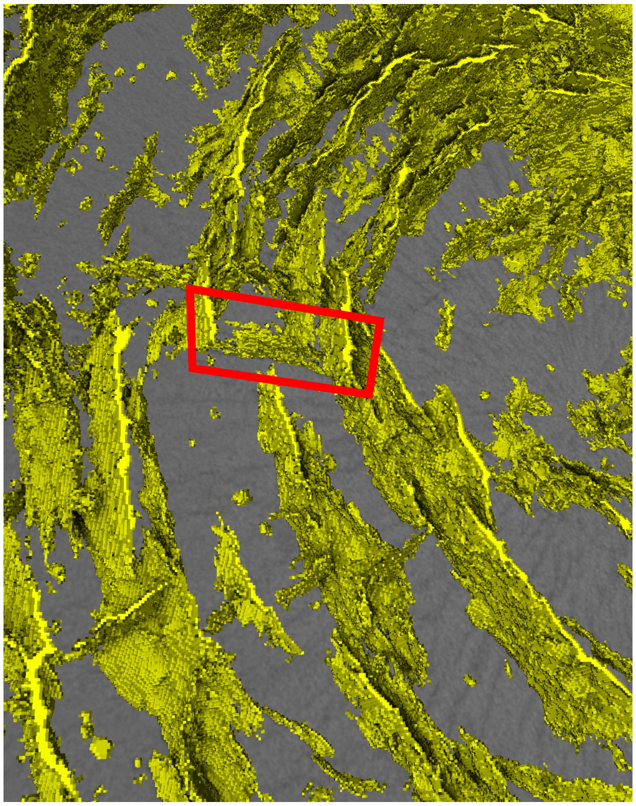

Figure 7.4.h: Oblique view of 3D slice showing the interior radial crack, from the t=120 h , crack highlighted in red

Table 7.4.g: Enlarged views of interior radial crack, showing development along dendritic pore path, with crack highlighted in red.

	Frozen State (Scan 1, t = 0 h)	**Dried State (Scan 6, t = 120 h)**
Raw image (contrast applied)	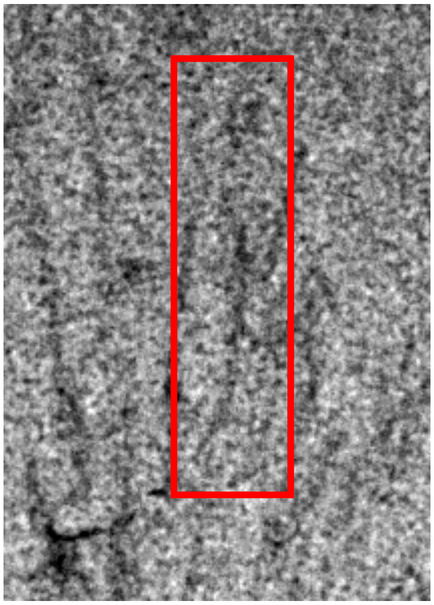	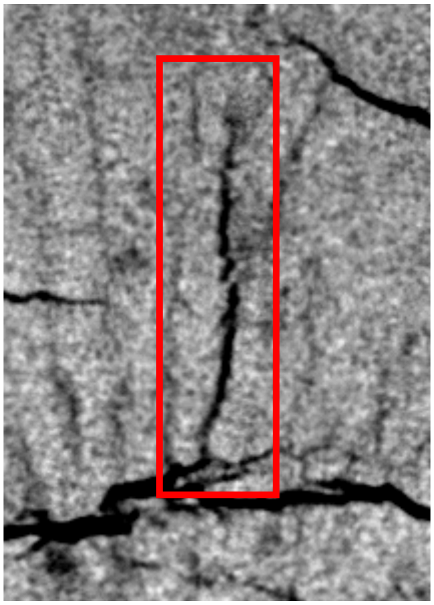
Processed image (post-processed and annotated to highlight dendrites pore paths in yellow)	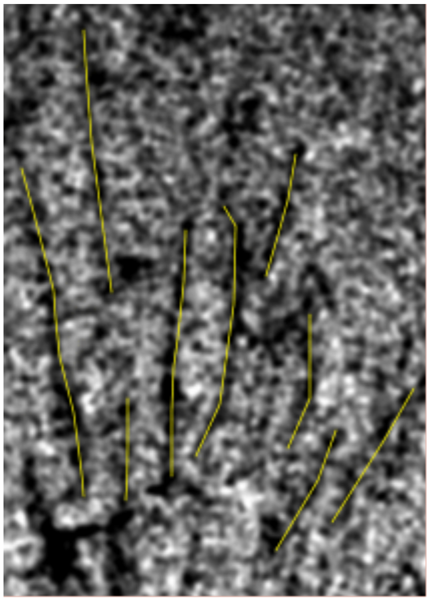	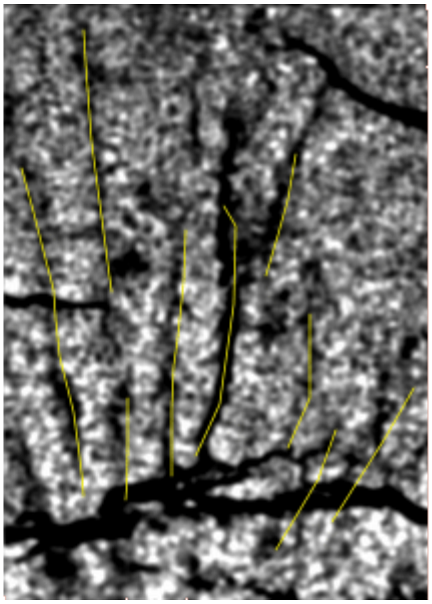

7.4.3.2 *Progression of Freeze-Drying Front*

In addition to the propagation of cracks, examining the freeze-drying time series reveals other time-dependant changes. Since these images are acquired via X-ray, changes in brightness in the image are associated with variances in apparent solid density. In the images below, (Figure 7.4.i and Figure 7.4.j below) darker regions correspond to regions of higher density, while lighter regions correspond to regions of lower density, with pores and cracks highlighted in white. During the drying of the sample, the loss of solvent from the particle matrix results in a reduction in sample weight, and thus a corresponding reduction in the apparent solid density should also be observable.

Examining the time series, at t =3 h a dark circular ring can be seen around the outer edges of the sample. Over subsequent time steps this ring progressively grows inwards, and this behaviour corresponds well with what could be expected during freeze drying, with sublimation progressively occurring at the ice/air interface and progressively moving towards the sample centre over time. It is notable that the transition interface remains sufficiently sharp to identify the interface location at subsequent time steps. It is apparent from Figure 7.4.i and Figure 7.4.j below, that although the cracking occurs during drying, in this case, the cracks actually occur in the frozen portion of the material. The mechanism behind this is discussed in section 7.5.3.

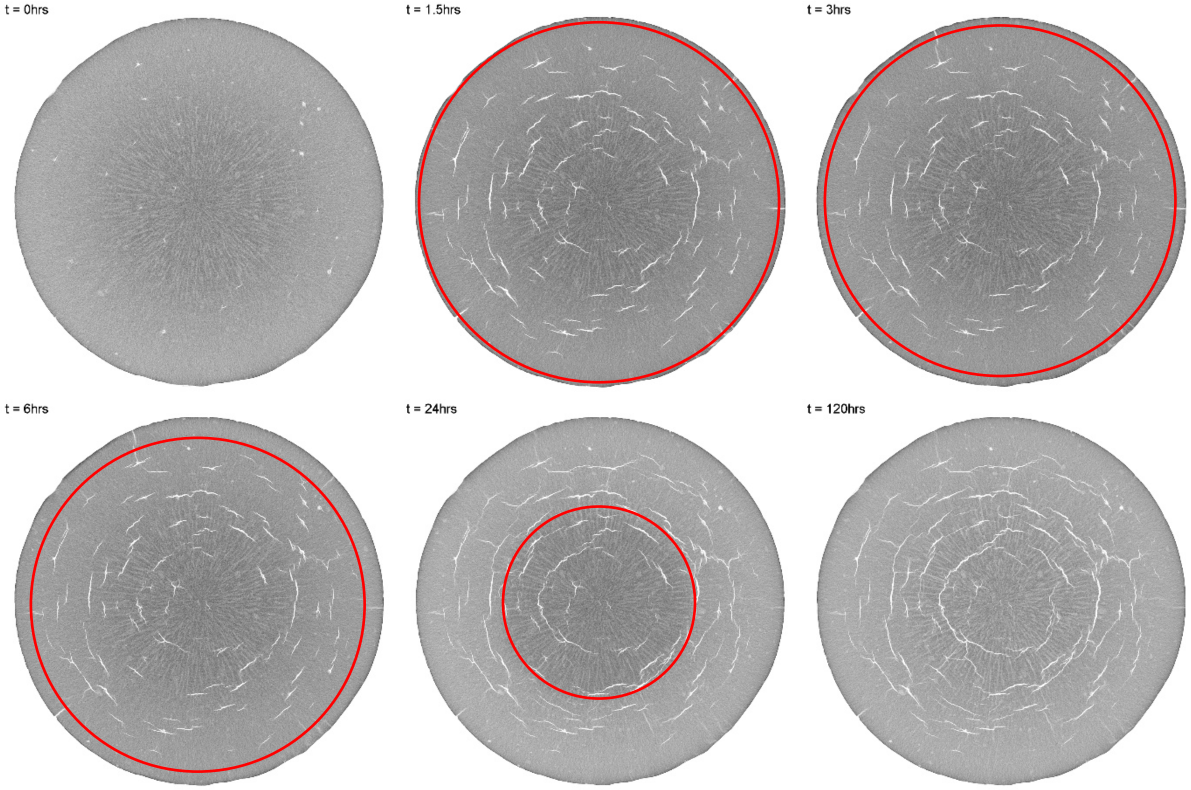

Figure 7.4.i: XY-slices from Micro-CT reconstruction time-series from t=0 h to 120 h. Apparent freeze-drying front progression outlined with red ring.

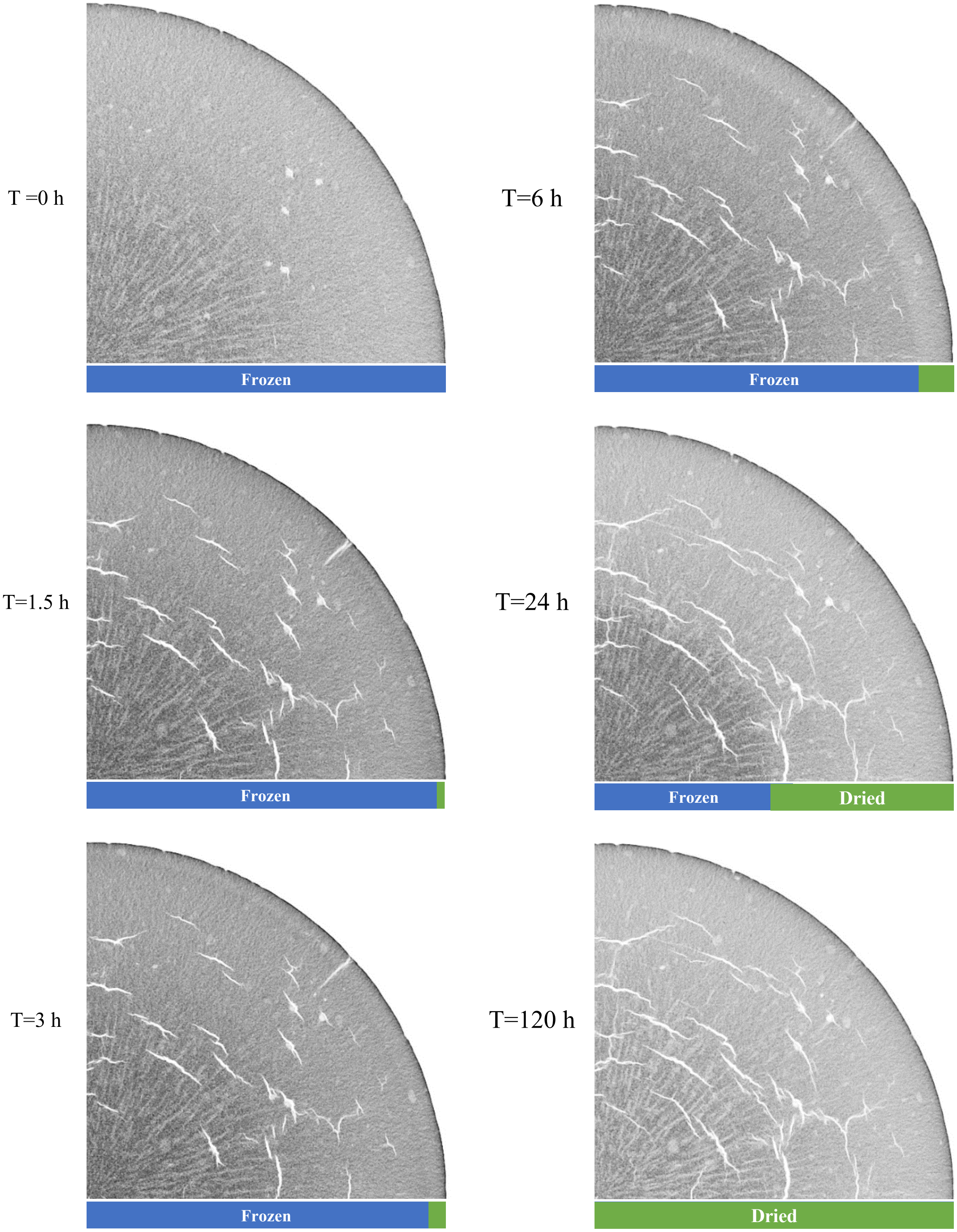

Figure 7.4.j: Close up of XY-slices from Micro-CT reconstruction time-series from t=0 h to 120 h indicating progression of freeze-drying front.

7.4.3.3 Volume change during Freeze-drying

During the progression of the time series, a minor change in the sample volume can be observed. By segmenting the external border of the sample against the background air, the area of each cross-sectional slice can be calculated (px^2). The value for area can then be used to calculate the average radius of the sample, and the relative expansion or contraction of the sample over the time series can then be plotted.

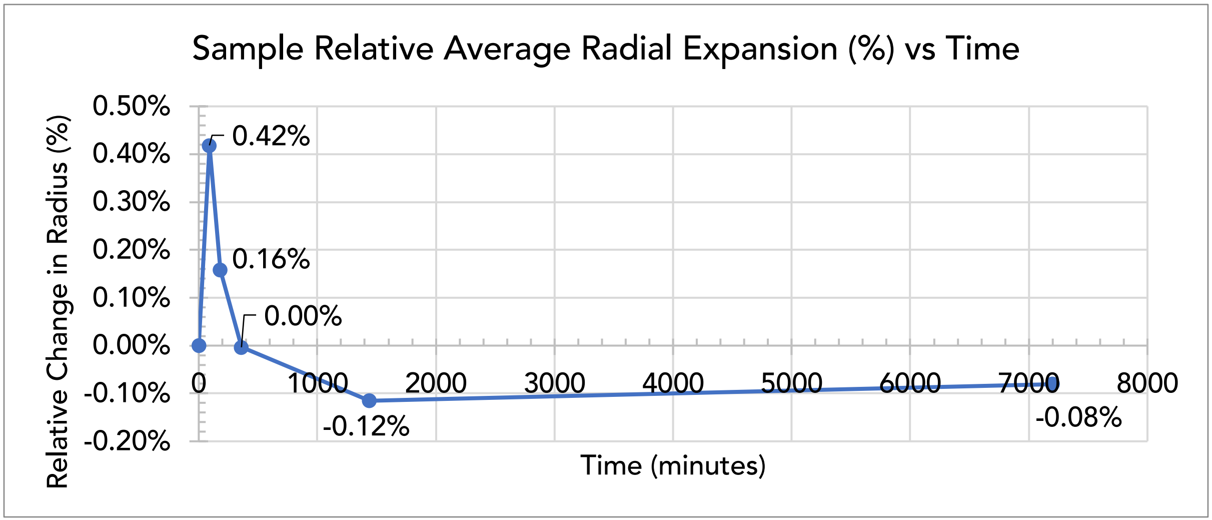

Figure 7.4.k: Sample Relative Average Radial Expansion (%) vs Time

In addition, the internal porosity can also be segmented and excluded, allowing the total solid cross-sectional area to be tracked through the drying process.

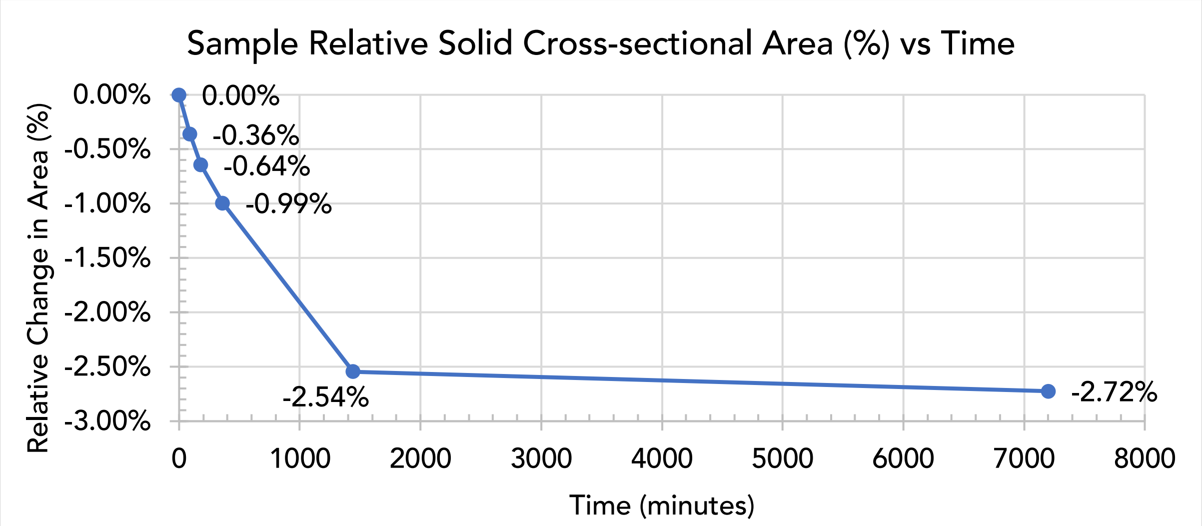

Figure 7.4.l: Sample Relative Solid Cross-sectional Area (%) vs Time

7.4.4 Experiment 4: Investigate the effect of freezing rate on the crack morphology observed within slow freeze-dried samples.

So far, the previous experiments have revealed new understandings relating to both the development of cracks during the freeze-drying process, and the role of the freeze-drying process conditions on generated crack morphologies. This final experiment investigates the relationship between the rate of suspension solidification during freezing and resulting internal crack morphologies following slow freeze-drying.

Samples were successfully freeze-cast at -40°C using both ambient and pre-chilled moulds, to examine slow-freezing and fast-freezing conditions respectively. Slow drying was performed at ambient pressure and -20°C temperature, for a duration of 10 days. The degree of drying was calculated via the measurement of sample weights, in order to confirm the completion of slow drying. The sample weights, recorded before and after drying, are provided in Table 7.4.h.

Table 7.4.h: Exp. 4 Sample Slow Freeze Drying Weight change

Sample	Frozen Weight (g)	Dried Weight (g)	Degree of Drying
76-1	17.3870	15.5351	91%
76-2	17.8058	15.9224	91%
76-3	17.7180	15.8778	89%
76-4	16.7355	14.9889	89%
76-5	16.7274	15.0446	86%
76-6	17.5303	15.6820	90%

Samples were imaged via micro-CT in the frozen state on a chilled plate, and successfully re-imaged after the completion of slow drying.

Fast Frozen State **After Slow Drying**

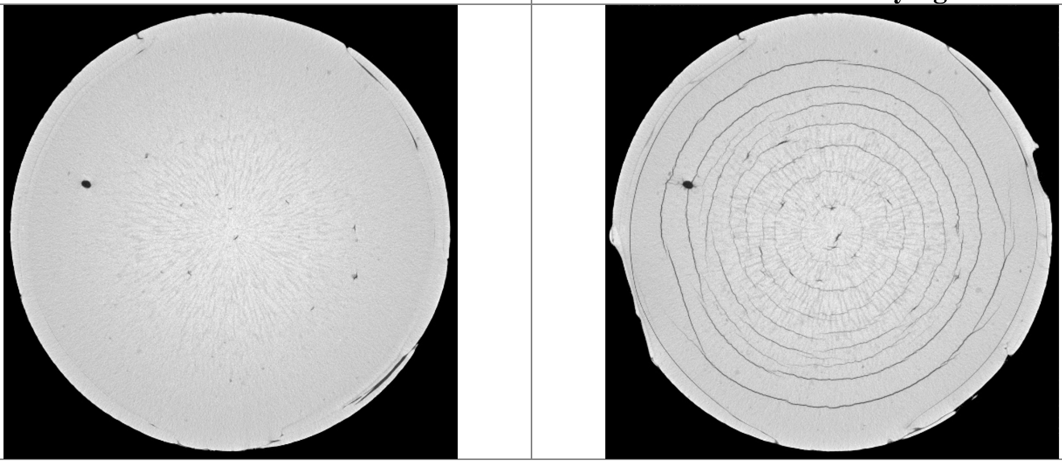

Sample 76-1

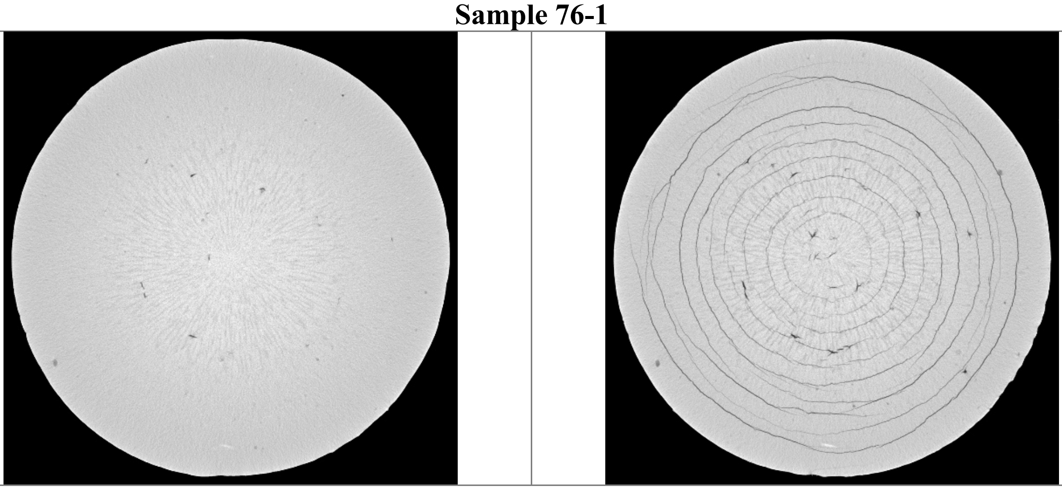

Sample 76-2

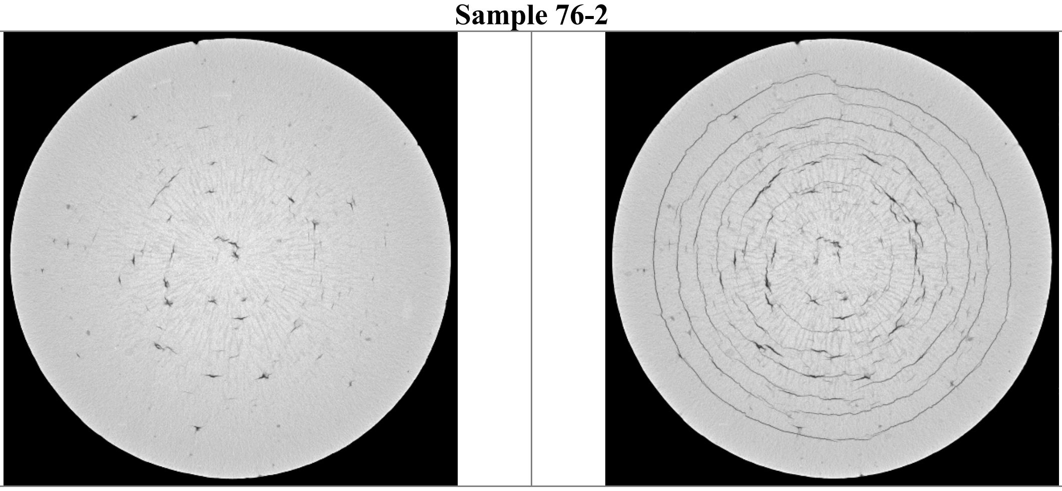

Sample 76-3

Figure 7.4.m: Micro-CT imaging of fast-frozen samples with slow freeze-drying, before and after drying

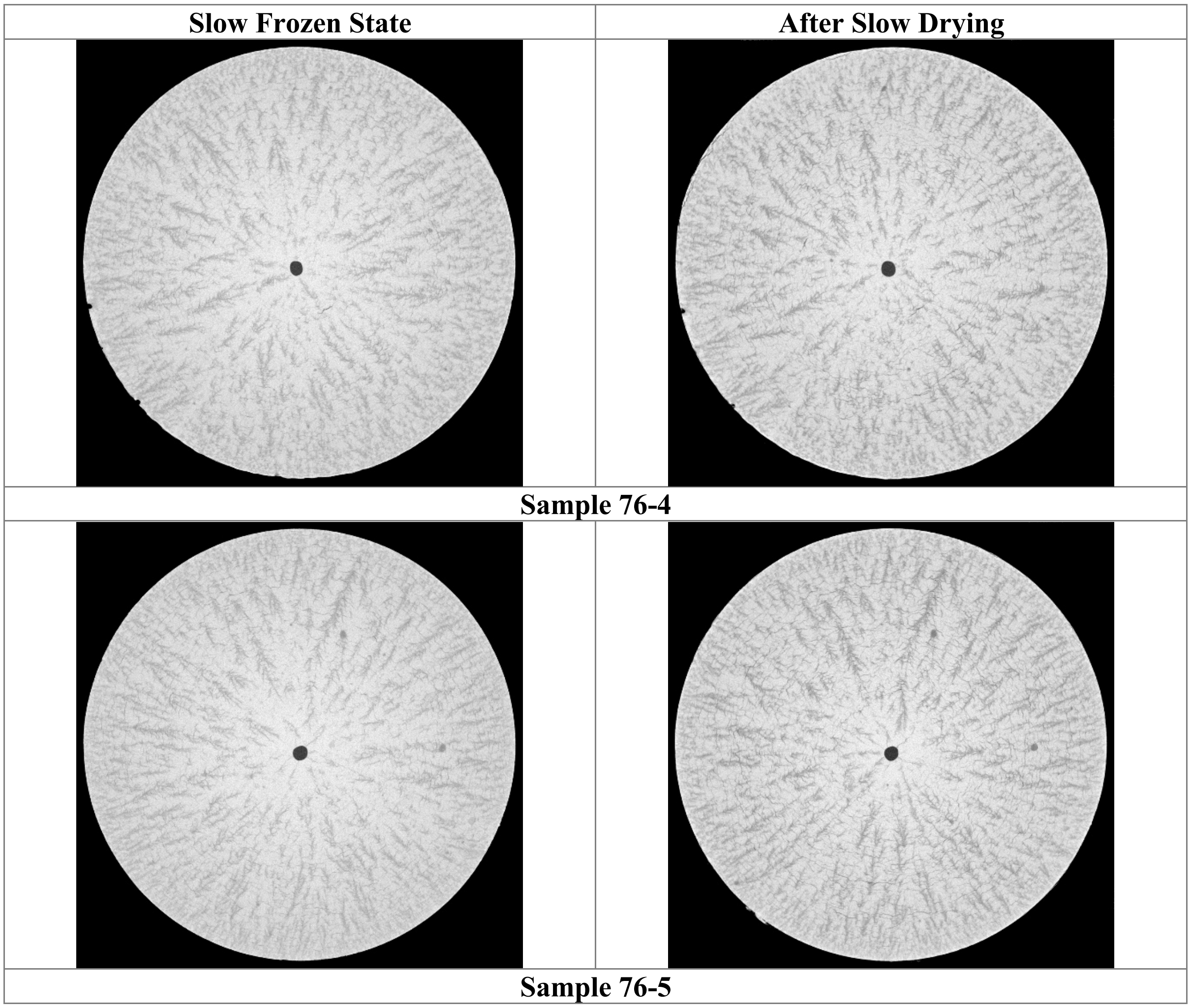

Figure 7.4.n: Micro-CT imaging of slow-frozen samples with slow freeze-drying, before and after drying

7.5 Discussion

7.5.1 Expt. 1: Cracking occurs during drying not freezing

The results from Expt. 1 demonstrated how micro-CT imaging can be used successfully to examine the internal structure of fragile green-body freeze-cast samples. In this way, non-destructive examination avoids the need for bisque firing and mechanical sectioning. Additionally, the use of a chilled stage successfully enabled samples to be examined in the frozen state. The solidification of alumina suspensions have previously been examined via X-ray radiography and tomography [114, 145, 146]. However, this study was performed with a conventional laboratory (not beamline) micro-CT setup, with use of a simpler commercially available chilled stage.

From the sample micro-CT reconstructions obtained from Expt. 1, the comparison of as-frozen and freeze-dried conditions clearly confirmed that the internal cracks observed within samples develop during the freeze-drying process. Since freeze-drying is a key step within the freeze-casting process, this discovery provided the motivation for the subsequent experiments; to examine the freeze-drying process and explore whether control of the freeze-drying process conditions could achieve a different outcome.

When comparing internal crack structures between samples prepared under similar conditions, major differences were identified between the observed internal crack networks. These discrepancies suggested that while the process conditions were not deliberately varied, other significant factors existed and had not been controlled, such as inconsistent handling, or time-sensitive factors such as cold storage time. The possibility was identified of a slow "self-freeze-drying" process occurring while samples were in storage at low temperature and ambient pressure.

7.5.2 Expt. 2: Influence of drying rate on cracking

In Expt. 2, care was taken with samples to ensure they were prepared, handled and treated consistently. In contrast with the results seen Expt. 1, in this study consistent results were obtained for samples prepared under the same conditions (fast-freezing in pre-chilled mould), and this consistency obtained in the observed results suggests that the key process parameters involved were successfully controlled. In this study the slow "self-freeze-drying" hypothesis was also tested, and it was confirmed that complete self-freeze-drying was achievable, even while under low-temperature conditions. By measuring the weight of samples, it was determined that under these conditions full self-freeze-drying could be achieved within two weeks.

This second study also enabled the comparison of slow freeze-drying samples against fast (conventional) freeze-drying samples. Examining the internal crack geometries, it was observed that both fast and slow freeze-drying methods resulted in severe internal cracking, but that the distribution of cracks differed significantly between fast and slow freeze-drying regimes. Slow drying resulted in concentric continuous circular cracks ("onion cracking"), while faster drying resulted in a high number of smaller discontinuous cracks in a similar circular arrangement. In addition, under fast drying additional radial cracks were observed propagating from the sample surface towards the sample centre, and these radial cracks were not observed in the slow dried samples. Examining the 3D reconstructions of the internal crack network amplifies the apparent distinction between the two morphologies. In the 3D space, the radial cracks can be observed to be extensive than simply radial planes, but exist on two perpendicular orientations. The visualisations of the slow-dried sample further demonstrate the contiguous nature of the onion-like cracks.

While the mechanisms driving development of these crack morphologies are not able to be directly identified from these results at present, the existence of the radial cracks suggests that either the forces, or the material properties of samples differ during freeze drying under these different drying regimes. During freeze-drying the material properties of the samples are time dependant, and so will change significantly as drying progresses from frozen-state to green-body. In the same way, during drying the sample material properties are also unlikely to be isotropic, as drying progresses from the outside of the sample towards the centre.

Since it is known that there is a significant difference in the rate of drying between fast and slow freeze-drying, it was thought possible that under varied drying rates, the time-dependant and anisotropic variation in material properties could result in different combinations of both stress distribution and material strength. In this way, even though no additional crack-driving forces are introduced, the ability of the material to resist these forces would differ under different drying regimes, potentially resulting in differing crack distributions, as observed. However, this hypothesis does not eliminate the possibility that additional crack-driving forces are present during either of these regimes, but these forces remain to be identified.

7.5.3 Expt. 3: When, where and how cracks occur

With confirmation that cracks develop during freeze-drying (Expt. 1) and indication that the crack development varies with freeze-drying rate (Expt. 2), Expt. 3 was setup to enable the study of progressive crack development in the time domain, during slow freeze-drying. By utilising the chilled sample stage, a freeze-cast sample was successfully able to be maintained in the frozen state over a period of five days, while undergoing slow self-freeze-drying, with simultaneous periodic micro-CT acquisitions.

The slow-drying conditions in this study differ to previous slow-drying samples. With the sample placed on the micro-CT chiller stage, the sample was still held at ambient atmospheric pressure. However, the environmental temperature experienced by this sample during slow drying was significantly higher (approx. -5°C) than the in-freezer temperature used for the slow-drying of previous samples (approx. -15°C). As a result, this was expected to result in a relative increase in the rate of self-drying.

Examining the time series of micro-CT reconstructions, progressive changes in apparent density can be observed within the sample over time, beginning from the outer sample surface and propagating towards the centre as a ‘freeze-drying front’. From these observations it was able to be determined that the sample was fully dried within the five-day study period; as predicted, the duration for complete drying under these conditions was significantly reduced under these conditions in comparison with previous slow-drying operations. From a commercialisation or practical standpoint, if slow freeze-drying (at ambient pressure) is identified as a required process step, a five-day drying period is a significant improvement over the 13 days previously required for slow freeze-drying of the same samples stored at lower temperatures.

Considering the specific freeze-drying conditions here (-5°C, ambient pressure), the actual rate of drying in this condition could be reasonably expected to be located between the rates of the previous slow-drying and fast-drying conditions. When examining the final dried crack network of this sample, the crack morphology observed appears to have similarities with features from both fast-drying and slow-drying regime samples. The relatively warmer temperature of the Micro-CT stage may mean that the thermal conditions are actually more similar to the fast freeze-drying conditions.

While fully continuous ring cracks were not observed, as in the previous slow freeze-drying, the length of the circumferential cracks was significantly longer than the shorter cracks observed in higher counts within the fast freeze-drying samples. Similarly, when considering the radially oriented cracks observed in the outer region of the fast-dried sample, these too were also observed in the studied sample, but by comparison had a significantly reduced crack length. Observing the internal crack network with features from both fast and slow freeze-drying, within a sample produced under slow drying (ambient pressure) conditions, suggests that there may be no significant difference in the range of crack-driving forces present during the different drying regimes.

Examining the time-series of sample reconstructions, it was previously observed that the progression of sample drying (from exterior to sample centre) did not correlate with the development of cracks. Instead, the cracks can be seen to develop and appear across the sample simultaneously, with the cracks are clearly visible in the second timestep where the sample is still mostly frozen. This finding firmly disproves the hypothesis that cracks could only develop in the dried region of the sample, where the sample mechanical properties would be expected to be weaker. In turn, this also indicates that even in the frozen state the sample lacks the mechanical properties to resist all crack development forces.

From Griffith's crack criterion for brittle fracture, it is reasonable to expect that areas around dendritic pores would be favoured preferentially as crack nucleation zones, relative to the continuous substrate. It could be expected that since there is an existing continuous exposed surface area within dendritic pores, this would reduce the energy requirement for crack development, resulting in dendritic pores being favoured as paths for the subsequent development of cracks. The specific example crack highlighted previously in Table 7.4.g suggests that this remains true.

The dendrites in the centre region of the fast-frozen samples have also been previously noted to be larger than the dendrites at the outer surfaces of the sample, due to the slower freezing front velocity. However, even in the fully dried state, it is evident that of the large number of identifiable dendrites that are oriented radially, the majority have not developed into cracks. Instead, most cracks observed within the inner region of the sample are consistently circumferential/tangential (perpendicular to the dendritic pores). This indicates that the crack-forming stresses were highly directional and not random, which in turn generated the need for a new hypothesis to be developed, regarding the distribution of stresses within samples occurring during the drying process, and the mechanisms behind the formations of these internal cracks..

7.5.3.1 Development of circumferential cracks

Assuming a Mode 1 fracture opening, the primary orientation of the cracks (circumferential) would suggest that some tensile force had occurred in the radial direction. This could occur under two scenarios; either (a) if the outer sample region was to expand and thus pull away from the centre region, or (b) if the inner sample region was to shrink, pulling away from the outer region inwards towards the sample centre. Examples of these two cases are illustrated in Figure 7.5.a on the following page.

Scenario (a) Crack formation via expansion of outer ring during freeze drying.	Scenario (b) Crack formation via shrinkage of centre during freeze drying.
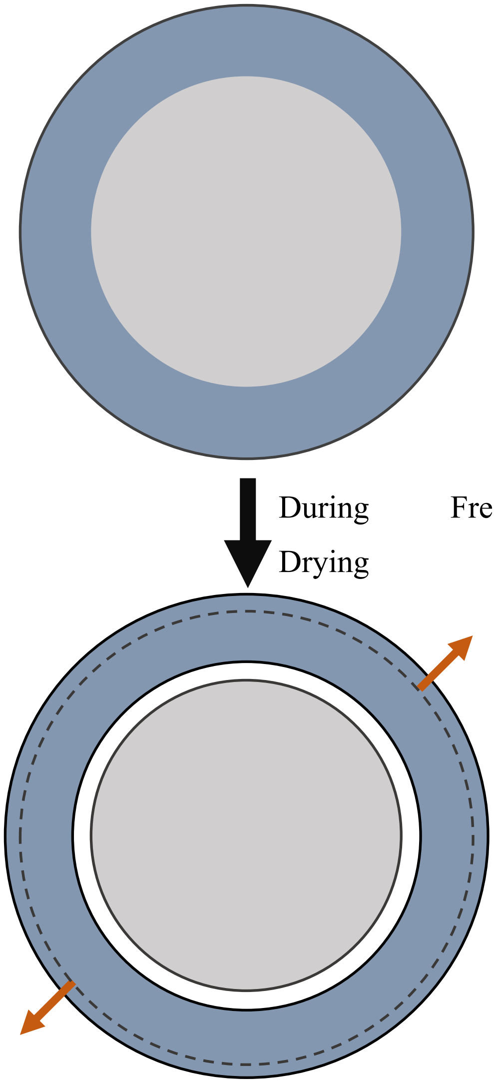 During Freeze Drying	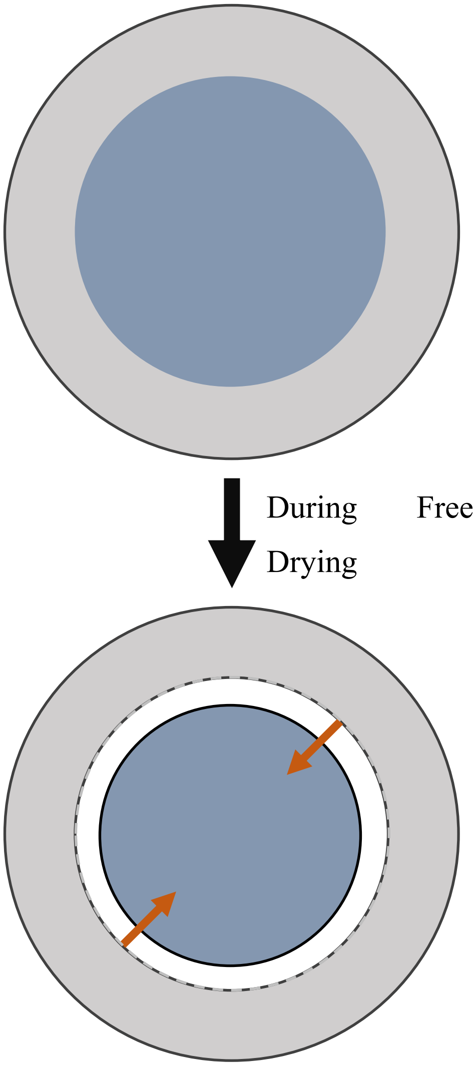 During Freeze Drying

Figure 7.5.a: Comparison of possible sample volume changes generating circumferential ring-like cracking

If any cracks (formed via the proposed methods above) are to be attributed to the freeze-drying process, then the likely origin cause of the cracks could be speculated. Since freeze-drying progresses from the outside of the sample towards the centre, if any sample volume changes are to be observed due to freeze-drying, it would be expected that this would occur at the outer region of the sample first. For this reason, the mechanism (a) appears more plausible in the context of generating circumferential cracking during freeze-drying.

When considering the possible causes for this outer-region expansion, the primary hypothesis involves volume change on solvent phase-change: during solvent solidification, the solvent (cyclohexane) undergoes a negative volume change. This shrinkage generates a compressive residual stress within the sample that develops from the outer region of the sample, and then accumulates towards the centre of the sample. Then, during freeze-drying, the sublimation of solvent progressively relieves the residual compressive force, resulting in expansion of the sample beginning from the outside region.

Additionally, during freezing under fast freezing conditions (very low freezer temperature), after solidification has completed in any region, in that local area the sample can then continue to cool further below the solidification temperature. This will result in further thermal shrinkage of the sample, thus resulting in additional compressive stress being exerted on the centre region of the sample during the remaining sample solidification. Meanwhile, the non-frozen regions will remain at or around the solvent freezing temperature until solidification occurs.

Considering the freezing progress of the sample over time, the outer sample region will solidify first, and thus, will shrink the most, developing the highest residual compressive stress, oriented inwards toward the sample centre. The inner sample regions will solidify last, and while subjected under the compressive stress exerted by the outer regions. Thus, a gradient of residual stress could be expected to be formed. This is represented schematically on Figure 7.5.b on the following page.

The proposed diagram below correlates best to samples under fast-freezing conditions. Under slow freezing conditions, the typically higher freezer temperature and higher ambient temperature mould would result in a reduction in the magnitude of thermal gradient developed across the sample during freezing, and thus the compressive stresses imparted from this effect would be reduced. However, the volume change on solidification, and those associated stresses, would still be expected to occur.

1. Liquid suspension	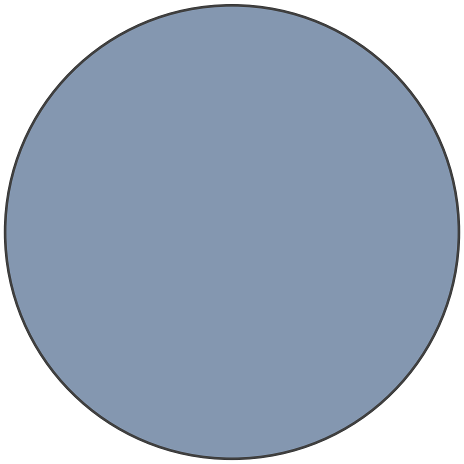
2. Partially frozen sample	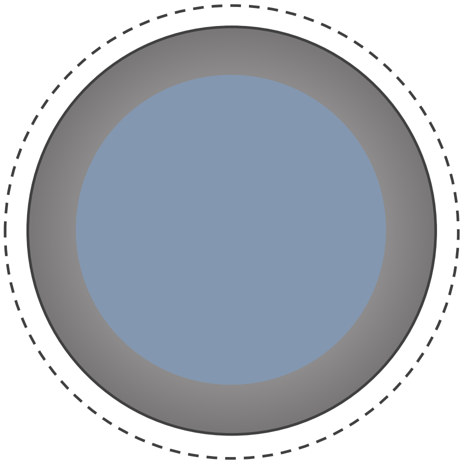
3. Completely frozen sample	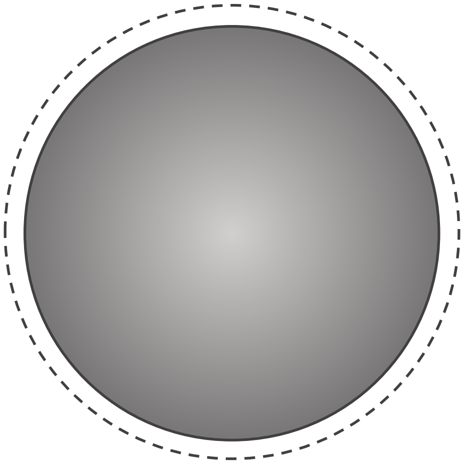

Figure 7.5.b: Illustration of development of high outer-edge formed residual stresses during fast freezing

While it may appear clear that there are avenues for residual stresses to be imparted into the frozen samples, a definitive mechanism for the subsequent evolution of cracks remains unverified. The sample studied in the time-series demonstrated the disconnection between the measurable drying of the sample over time, and the evolution of internal cracks, with the propagation of internal cracks significantly outpacing the freeze-drying process. This could potentially indicate that the development of cracks is more strongly tied to the sample experiencing significant changes in temperature, and the associated inhomogeneous thermal expansion of the sample. For example, the sample initially warms up rapidly on the micro-CT analysis stage after being removed from low-temperature frozen storage. Circumferential cracks could plausibly develop to alleviate accumulated internal residual stress from sample thermal expansion, as shown in Figure 7.5.c below.

Figure 7.5.c: Schematic showing proposed mechanism behind progressive development of circumferential cracking during freeze-drying

3. Completely frozen sample under residual compressive stress. Sample has shrunk due to being at low temperature, with original sample size at room temperature shown in dashed line.	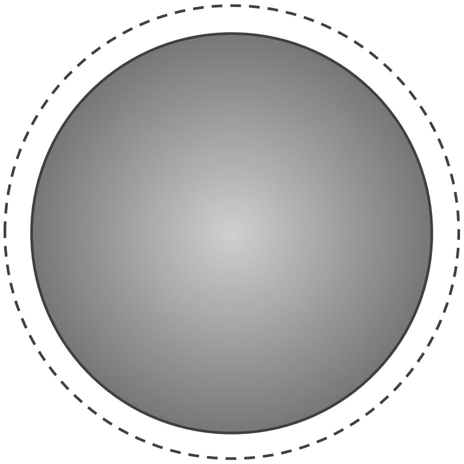
4. Sample begins to warm up and thus expand. Higher residual stress on outer regions result in greater expansion. The selective expansion of outer regions then sets up tensile forces towards internal regions. Simultaneously or sequentially, it also begins to freeze-dry from outside in. This both reduces local material strength, and the removal of solvent template provides opportunity for the residual stress to be relaxed by cracks.	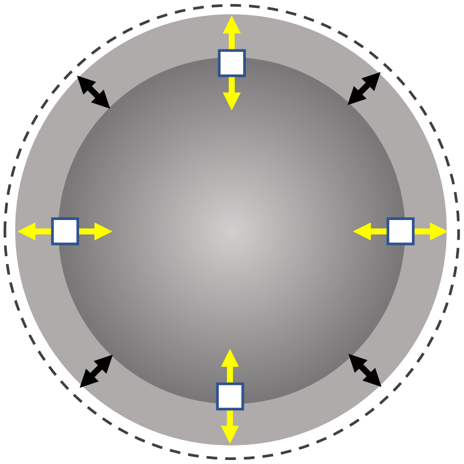

5. Expansion continues as sample warms up, resulting in unopposed internal stress increases. Freeze drying also progresses.	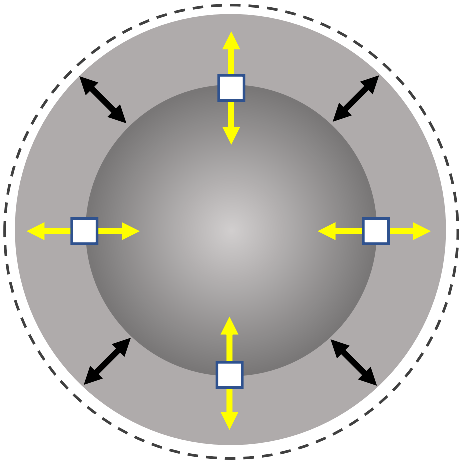
6. Tensile force exceeds local material strength and crack develops.	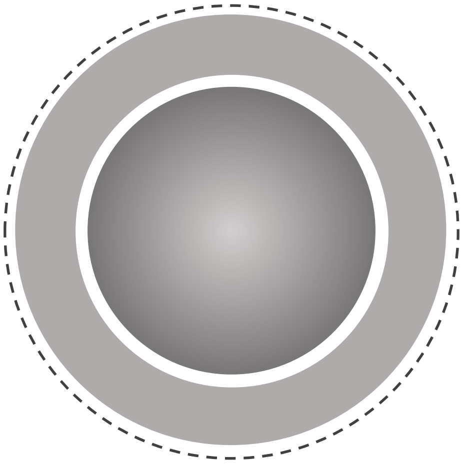
7. As inner sample region continues to expand and dry, the cycle repeats based on remaining residual stress within inner sample region.	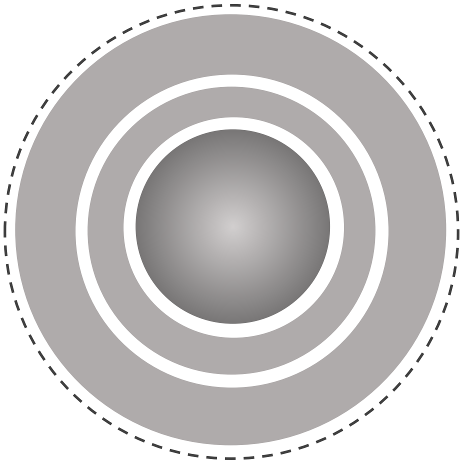

Overall, while the proposed mechanism for internal sample expansion forces and circumferential cracking may be plausible, at present this mechanism remains to be definitively verified. Other cracking aspects, such as the contiguous nature of the slow-dried circumferential cracks, and the fragmented morphology of the fast-dried cracks, could be speculated as being related to the rate of crack development, but further investigation and verification is still warranted in these areas.

7.5.3.2 Development of radial cracks

In addition to the circumferential cracks, in the fast-dried samples there was also an evolution of perpendicular radial, or ‘spoked’ cracks, that in most cases primarily formed in only the outer regions of the sample. It is proposed that these radial cracks could occur due to competing rates between thermal expansion, and freeze-drying.

Under a low vacuum, the rate of freeze-drying will be higher than at ambient pressure, whilst the rate of sample warming will largely be unaffected. A high initial rate of freeze-drying could result in the outer portion of the sample drying before significant thermal expansion occurs. As thermal expansion does begin to occur, the dried outer region does not contain solvent to expand, and so the expansion begins from beyond the dried zone. This expansion places a tensile hoop stress on the already dried region, which could be expected to result in a form of radial cracking, as observed. If at this point the rate of thermal expansion overtakes the rate of freeze drying, then the cycle will not repeat, and conventional circumferential cracks will be produced instead by the previously outlined mechanism.

The proposed mechanism for internal radial crack formation is illustrated schematically in Figure 7.5.d.

Figure 7.5.d: Progressive development of radial and circumferential cracking during freeze-drying

3. Completely frozen sample (under residual compressive stress)	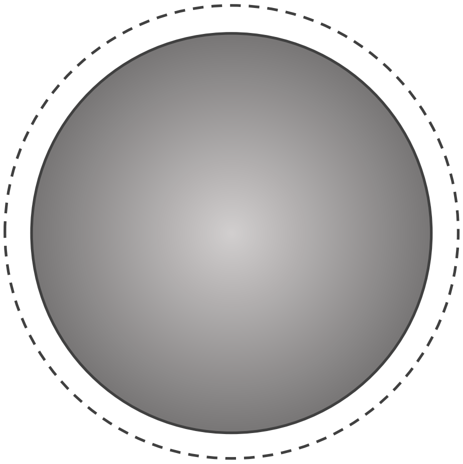
4. Sample under fast drying begins to freeze dry rapidly from outer regions first, before thermal expansion occurs.	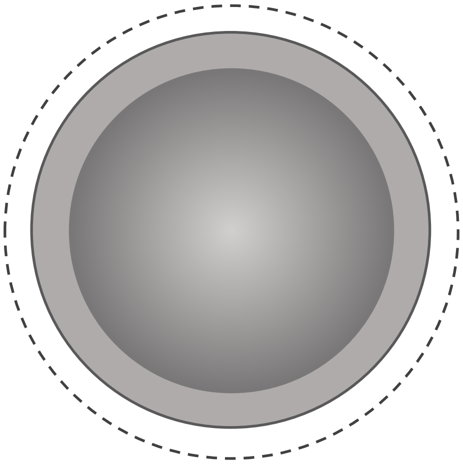
5. Thermal expansion rate increases and freeze-drying rate decrease. This results in expansion of centre region of sample, placing outer region into tensile hoop stress.	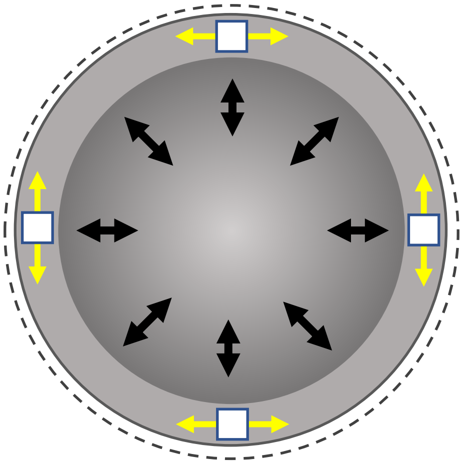

6. Tensile force exceeds local material strength and crack develops.	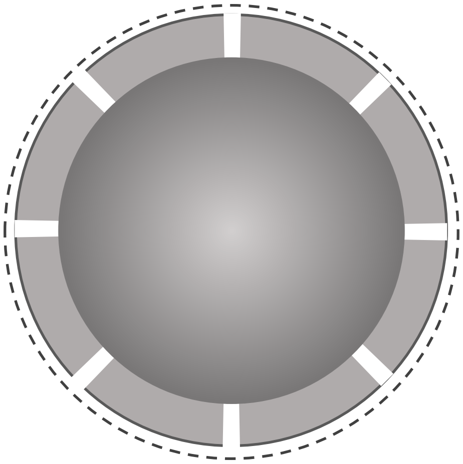
7. As sample continues to expand and dry, the drying rate reduces towards sample centre. Since freeze-drying causes sublimative cooling of sample, a reduced drying rate results in higher rate of thermal expansion. Thermal expansion within remaining frozen phase overtaking rate of drying. This results in circumferential cracking mode now being favoured, as in Figure 7.5.c.	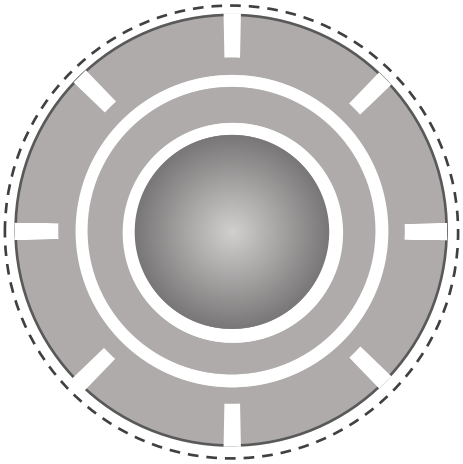

7.5.3.3 Sample volume changes during freeze-drying

From the theories of crack development above, it appears that thermal expansion may play a significant result in crack formation. As a result, it is reasonable to expect some measurable thermal expansion of the sample to occur during the freeze-drying process.

Since fast-freezing is used to minimise the size of crystal growth during solidification, this means that the temperature at the time of solidification is significantly lower than ambient temperature. For solvent removal via fast freeze-drying, this occurs at the sublimation temperature of the solvent, which is significantly warmer than the sample solidification temperature. This difference in temperature will result in some early thermal expansion of the sample as it warms up, *before* drying is completed. In this case the outer part of the sample will warm up first and try to expand away from the colder (near isothermal) core. This would cause a tensile stress in the radial direction which could initiate the onion like cracks observed. In contrast, for solvent removal via slow drying, this occurs at the lower temperature. Under those conditions, the sample is likely to warm up less, and thus expand less, followed by further expansion *after* drying is completed, when the dried sample is brought back to room temperature.

Examining the observations in Expt. 3, the micro-CT reconstruction slices can be measured in order to calculate the changes in sample volume over time. The initial expansion of the sample by 0.4% after the first time-step is followed by a subsequent retreat back to the original size, followed by a further slight shrinkage. The initial sample expansion appears to correlate well with the first visible presentation of the internal cracks, and this appears to reinforce the proposed theory of crack-formation originating due to early sample thermal warming and expansion upon drying.

However, the cause of the subsequent shrinkage is not immediately identifiable. This may be attributable to the loss of frozen solvent during drying, but further investigation is required.

7.5.4 Expt. 4: How freezing rate influences cracking during drying

In Expt. 4, the role of freezing rate is investigated in the context of slow drying.

Firstly, in all samples studied, the slow-frozen samples were consistently observed to feature a pore in the centre of the sample. With proper injection mould design (e.g. sample sprue and feeders), it is expected the presence of this large pore may be avoided or mitigated.

For the reconstructions obtained for samples in the frozen state, the slow-frozen samples are seen to have large internal dendritic pores visible. When examining the dried-state reconstructions, these dendrites appear to have disrupted the propagation of the continuous circumferential ring cracks, as were previously observed in the fast-frozen-slow-dried samples. For these slow-frozen samples, there are no large continuous cracks observed in the dried-state reconstructions, instead, numerous small inter-dendritic cracks are seen to have developed. These inter-dendritic cracks are homogenous in both their small size and distribution across the sample. This demonstrates that the solvent crystal distribution and resulting microstructure that is created during freezing, has a significant role to play in directing the generation of cracks during freeze drying. It appears that the resulting dendritic solvent crystals formed under slow freezing have dendritic arm diameters that are large, and as a result are favourable as nucleation points for crack growth. It is also observable that the cracks that form are primarily oriented in the circumferential direction; this is consistent with cracks observed within samples prepared under fast-freezing and dried via slow drying.

The distribution of numerous small, distributed cracks rather than few large cracks may mean that during sintering densification may improve the sample mechanical properties to achieve a better result than compared to samples with large internal cracks. However, the previous study (Chapter 6, Study of freezing-rate and microstructure via dense freeze-casting, page 71) indicated that for slow-frozen samples a lower final bulk density was achieved after sintering, and previous close examination of slow-frozen samples revealed that the large dendritic pores are unable to densify significantly (under pressureless sintering) and remain visible in the microstructure after sintering.

7.6 Conclusions

The primary result from this study series, is the conclusive identification that the freeze-drying process is responsible for the macroscale internal crack evolution observed in dense freeze-cast samples. Micro-CT imaging was used to demonstrate successfully that samples in the frozen state do not have cracks present, while freeze-dried green body samples have severe internal cracking.

In addition, it was found that the rate of freeze-drying also significantly affected the morphology and connectivity of the internal crack network formed during freeze-drying. For this reason, care was required to ensure samples were treated as “time-sensitive”, with controls in place to maintain consistent storage conditions from sample to sample. Even under low temperature and ambient pressure conditions, freeze-drying can occur slowly, and when examining the internal crack networks after drying is completed, continuous circumferential cracking is observed. Under high vacuum and at ambient temperature freeze-drying is rapid, with many discontinuous circumferential cracks observed, in addition to radially oriented cracks near the sample outer diameter.

Examination of crack morphology within samples produced under varying freezing rates indicated that the dendritic pore/crystal network does affect crack propagation during freeze drying. Slow-frozen samples with large dendritic systems provide a network convenient for crack propagation, resulting in many small cracks found connected to dendritic pores after freeze-drying. In contrast, fast-frozen samples with fine dendritic pores form large cracks that are not aligned with the pore network.

Examining a time-series of Micro-CT reconstructions during slow freeze-drying demonstrated that the **evolution of cracks does not correlate with the progressive degree of sample drying**, but rather, the formation of crack may be aligned with thermal expansion of the sample as it warms from storage temperatures to drying temperatures. Further investigation is required to verify the specific mechanism responsible for driving internal crack formation, such as examining the residual stresses imparted into the frozen sample during freezing.

8 Study of modified suspension composition for mitigation of freeze-drying cracks

8.1 Aims

In consideration of the previous discovery that samples produced via dense freeze-casting typically display severe internal cracking, applications for dense freeze-casting as a potential near-net shaping process would appear to be critically limited. The previous study clarified the evolution of these cracks, identifying that these internal cracks develop during the freeze-drying process. The purpose of this study is to investigate the relationship of suspension composition on both pore microstructure, and internal crack development, specifically examining alternative solvents and additives, with a goal of identifying strategies for crack mitigation and prevention.

8.2 Introduction

In the preceding chapters, it was identified that the internal cracks observed within dense freeze cast samples develop during the freeze-drying process step. Additionally, modifying the freeze-drying process step conditions did not yield elimination of cracks. Subsequently, the present challenge is to explore other possible avenues for mitigating the development of cracks during freeze-drying.

While freeze-drying was identified as the process that caused the development of cracks, the previous study did not confirm the specific forces responsible during freeze-drying. Freeze-drying was observed to progress over time from the outside of the sample surface towards the centre, while the development of cracks occurred simultaneously across all areas of the sample, and are identifiable throughout the sample even shortly after the start of the freeze-drying process. This suggests that there may be other factors (e.g. thermal expansion) that contribute to the generation of internal stresses, though the underlying cause remains speculative. Despite the lack of a proven mechanism, the presence of internal cracks in these samples indicates significant internal forces are present during the freeze-drying process, with these forces exceeding the strength of the material.

From this observation, two possible pathways towards elimination or reduction of these cracks can be identified; either by reducing the magnitude of the crack-generating forces, or alternatively by increasing the strength of the material sufficiently to withstand these forces. In this chapter, both avenues are explored independently, through different changes to the suspension composition.

8.3 Part A: Effect of Binder Addition to Suspension on Dense Freeze-Casting Cracks

8.3.1 Background

During the production of dense freeze-cast samples, the properties of the sample change significantly at each step, from the original powdered ceramic feedstock, to a viscous liquid, and (ideally) through to a dense sintered ceramic component.

The development of cracks was identified as occurring during the freeze-drying process, during which the sample undergoes a transition from a frozen state, into a green-body state. In the frozen state, the frozen solvent provides the primary mechanical strength to the sample. However, after drying the loss of the frozen scaffold results in a significant decrease in the mechanical strength of the green-body sample. Instead, in the green body state the primary particulate bonding forces are provided by the polymeric dispersant, which acts as a weak adhesive binder.

In this first study, the effect of binder addition was studied, looking at the impact on green-body mechanical sample strength. The intention of this incorporation being to sufficiently increase the mechanical strength, to support the ability of the material to resist the apparent crack-generating forces experienced during freeze-drying.

While this method of adding a binder may draw comparisons with the gel-casting process, the primary difference remains that the binder does not undergo an irreversible reaction during freezing, and melting the sample after freeze returns the suspension to a completely liquid state. Instead it is solely the solidification of the solvent that enables the binder to function, to add mechanical strength to the shaped component, both in the frozen and into the green-body states after drying. In gel-casting, the proportion of gelation agent may vary widely, typically between 2-5 wt.% [152, 153] to amounts exceeding 12 wt.%[154], with higher quantities of additive introducing complexities into the burn-out phase required during sintering to eliminate binder residues. By contrast, for freeze-casting the intention is to minimise the amount of binder required, with the priority being to maintain clean binder burn out (minimise residual carbon content), and to maximise the ceramic proportion by weight in the green-body sample[155].

8.3.1.1 Binder Selection

When selecting a binder, consideration must be given to ensure that is miscible or soluble in the carrier solvent selected. Following previous work, cyclohexane was selected for this study, which is a non-aqueous and non-polar solvent. For aqueous-based suspensions, common binders for freeze-casting include Polyvinyl-alcohol (PVA)[156–158], Glycerol[56], and various proprietary acrylic resins[8]. For non-aqueous solvent ceramic suspensions similar families of binders are also applicable, commonly including Polyvinyl-alcohol (PVA) and Poly-vinyl-butyral (PVB)[159, 160]. While few binders have been explicitly demonstrated for non-aqueous freeze-casting, a range of commercial acrylic polymer or co-polymer resins are commonly used in non-aqueous tape casting, such as those from the Paraloid® and Elvacite® product families respectively [85, 155, 161]. Polystyrene has been demonstrated as a freeze-casting binder with camphene solvent [41], and polystyrene polymer is also soluble in the selected carrier solvent, cyclohexane[162]. The binder selected for this study was Elvacite 2045 (Lucite Intl., Billingham, UK) which is an acrylic resin that is ideal for highly-loaded ceramic suspension processing applications[32], and specifically offers clean burn out upon sintering[163]. Elvacite 2045 is a high molecular weight isobutyl methacrylate polymer, that is also readily soluble in cyclohexane [85].

8.3.2 Method

8.3.2.1 Optimising Suspension Composition

With the addition of binder, the suspension viscosity increases, and this can introduce challenges when seeking to achieve fast injection of suspension into the mould during freeze-casting. Since the suspension with added binder is more viscous, the combined quantity of binder and ceramic powder must be limited to ensure a suitable viscosity was maintained for the injection of suspension. The relationship of binder addition and suspension viscosity was examined using a rheometer, enabling the maximum practical binder loading amount to be determined. This way, the strength of the green body samples can be maximised, while minimising effects on sample casting. As the suspensions from previous studies were highly loaded at 55 vol.% solid ceramic powder, further additions of Elvacite to those suspensions increased the viscosity to the point where well-dispersed suspension preparation was not possible, and rheological behaviour became paste-like. For this reason, the ceramic powder solids concentration was reduced to 54 vol.% in this study. Alumina AKP-15 (Sumitomo Chemical Co. Ltd, Tokyo Japan) ceramic powder was used for this study, with an average (mean) particle size of 0.7 µm. Suspension preparation process was identical, except for the addition of binder to the carrier solvent, well mixed, prior to the addition of ceramic material to suspension.

Additionally, one of the primary project goals was defined early on as minimising the solid fraction of any additives within the suspension, to avoid compromising the maximum bulk density achievable after pressureless sintering. For this reason, it was decided that only binder additions up to 1 wt.% binder addition would be explored, alongside a fixed 0.9 wt.% of Hypermer A70 dispersant.

8.3.2.2 Measuring effect of binder addition on mechanical strength

To establish the effect of binder addition to suspension formulation, a range of suspensions were prepared using the standard cyclohexane-based suspension formulation, with different concentrations of Elvacite binder added. From these suspensions, a set of green-body samples were prepared using varying concentrations of binder, via slip casting onto plaster sheets, in cylindrical moulds of 34.5 mm in diameter, and approximately 8mm in thickness. Slip cast samples were removed from plaster sheets after 4 hours, then left to dry in an oven at 80°C for 24 h.

The mechanical strength of samples was then measured, in order to determine the quantitative relationship between binder addition and the corresponding increase in mechanical strength.

The tensile strength of samples was measured indirectly, using the diametral compression test [164] method on an Instron 5848 MicroTester with 2 kN load-cell (Illinois Tool Works Inc., Norwood, MA, USA). The diametral compression test, also known as the “indirect tensile test” or “Brazilian test”, well suited for indirectly determining the tensile strength of particulate materials with both low absolute tensile strength values, and with low values for the ratio of tensile strength relative to compressive strength. This test involves compression of a circular disk through the vertical diameter, which in turn generates a tensile force perpendicular to the axis of compression. The failure point is taken to be the tensile failure of the material, thus allowing the indirect tensile strength (σ_t) of the material to be calculated be the following formula[164]:

$$\sigma_t = \frac{2F}{\pi D t}$$

For the formula above, F is the compression force, D is the sample diameter, and t is the sample thickness.

Figure 8.3.a: Diametral compression diagram (left), photo of experimental setup (right)

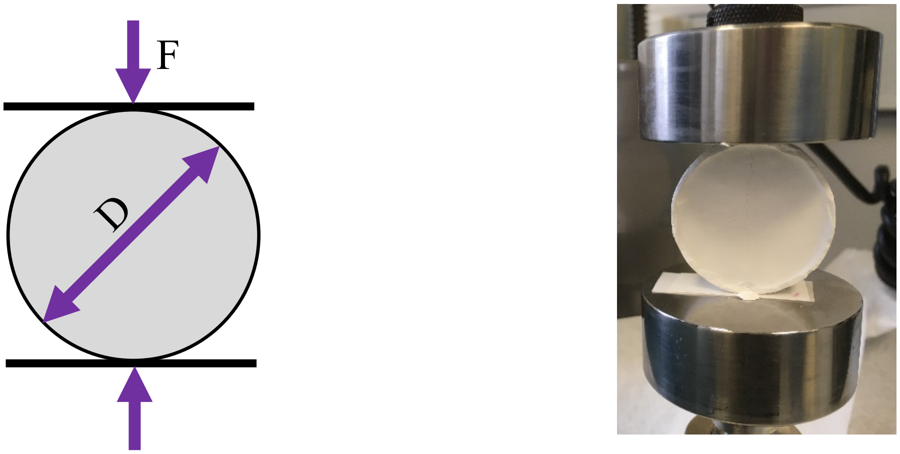

In order to calculate the effective tensile strength accurately, both the compressive failure stress, and the contact area must be recorded. Dual layer pressure sensitive contact films (Sensor Products Inc., Madison, NJ USA) were used to record the contact area, and these were placed below the sample before compression is started. When the pair of films is contacted under load, microcapsules release a reactive dye that reveals the area of load under contact. By using this technique an accurate record of the contact area dimensions can be obtained, in order to enable the contact angle under load to be calculated. Additionally, inspection of the contact area can be used to identify if there was any discrepancy or anomaly in the sample contact (e.g. uneven or partial contact under load) can be identified. From the values for contact angle and compressive yield stress, the effective tensile yield stress (fracture toughness) can then be calculated from a force balance. This setup allowed the mechanical strength of the slip-cast samples with varying binder to be measured.

8.3.2.3 Freeze-casting & Sample Examination

The optimised composition suspension with binder was then used to prepare dense freeze-cast samples, under both fast and slow freezing rates. The standard 20 mm cylindrical sample casting mould was used, as in previous chapters. Those samples were then freeze-dried, and then imaged via micro-CT. XY-slices through each sample were then extracted from the Micro-CT reconstructions, enabling the internal crack distribution to be compared between the samples with binder and the binder-free samples. In this way, the resulting effects of binder addition on internal cracking from dense freeze-casting were able to be determined.

8.3.3 Results

8.3.3.1 Binder Addition to Suspension: Rheological Results

Rheological testing of the suspension with varying binder addition yielded several observations. Firstly, the 54 vol.% ceramic solids concentration reference suspension (without Elvacite) was observed to be mildly shear-thinning, and relatively low in viscosity. As seen in Figure 8.3.b below, the addition of even a relatively minimal 0.25 wt.% of Elvacite, resulted in a significant increase in viscosity. At low shear rates (<1 s^{-1}) the viscosity increased by almost an order of magnitude, whilst at high shear rates (>500 s^{-1}) the increase in viscosity was significantly less noticeable. Due to the strong shear thinning behaviour observed, with more vigorous mixing it was possible to still prepare a well-dispersed suspension for all the selected concentrations. Since a suspension with 1 wt.% Elvacite as prepared was still sufficiently fluid to prepare a well-dispersed suspension, the solids concentration of 54 vol.% was evaluated as suitable and was used for the following sample studies with Elvacite.

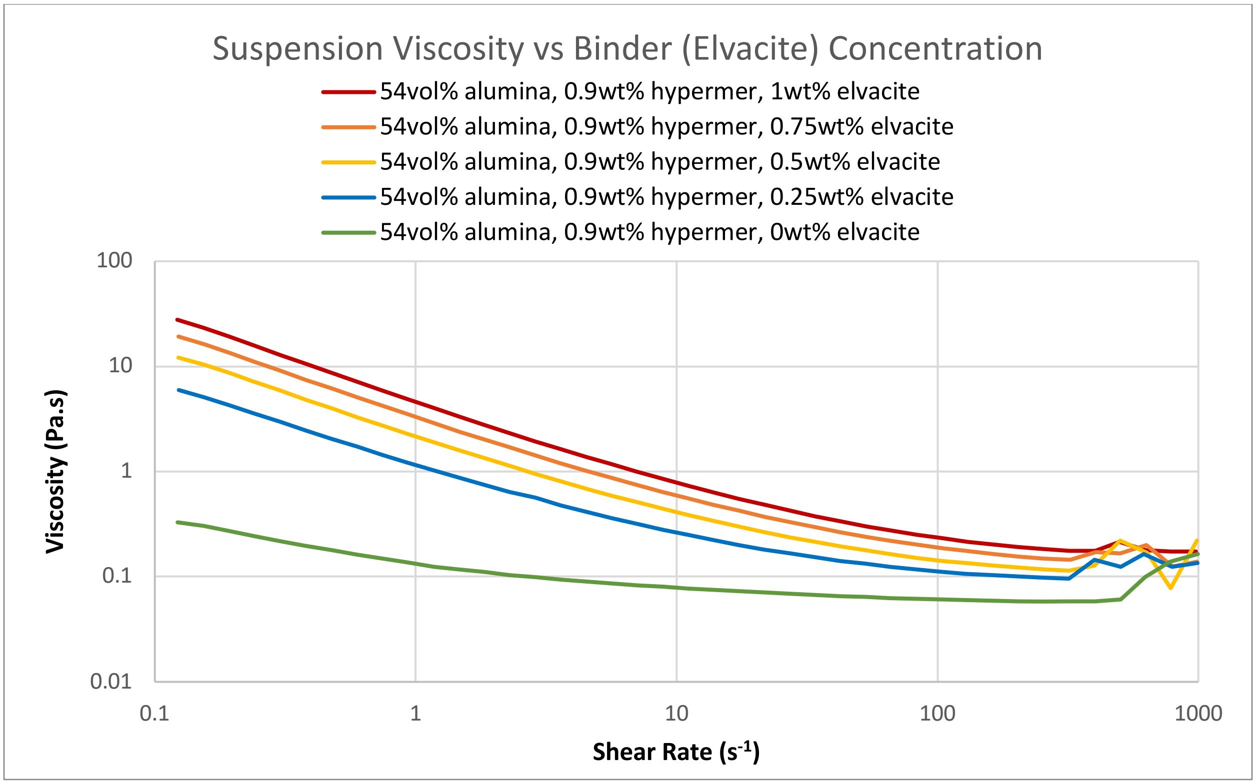

Figure 8.3.b: Rheology of highly loaded non-aqueous Alumina suspensions with binder, showing Viscosity (Pa.S) vs Shear Rate (s^{-1}) for a range of Elvacite binder concentrations from 0 to 1.00 wt.%.

8.3.3.2 Binder Addition to Suspension: Effective Tensile Fracture Strengths

The set of suspensions was successfully prepared, from 0 to 1 wt.% Elvacite, in 0.25% increments. It was observed that the suspension viscosity significantly thickened with each increase in binder added. Similarly, for each suspension formulation, a clear trend was observed with increasing binder content resulting in a corresponding increase in the magnitude of measured forces required for fracture.

For each sample tested, both the contact pattern on the pressure film and force-time profile were inspected to ensure valid results were obtained. If uneven contact was made, this would affect the distribution of stresses within the sample, which in turn could invalidate key assumptions made for diametral compression testing [165–167]. Both the dimensions of the sample and the dimensions of the contact pattern on the compression test films were inspected after each compression test, and in cases where the film indicated less than 85% of the sample thickness made contact during testing, those results were excluded. Multiple samples were tested until a minimum of five valid measurements were obtained for each condition.

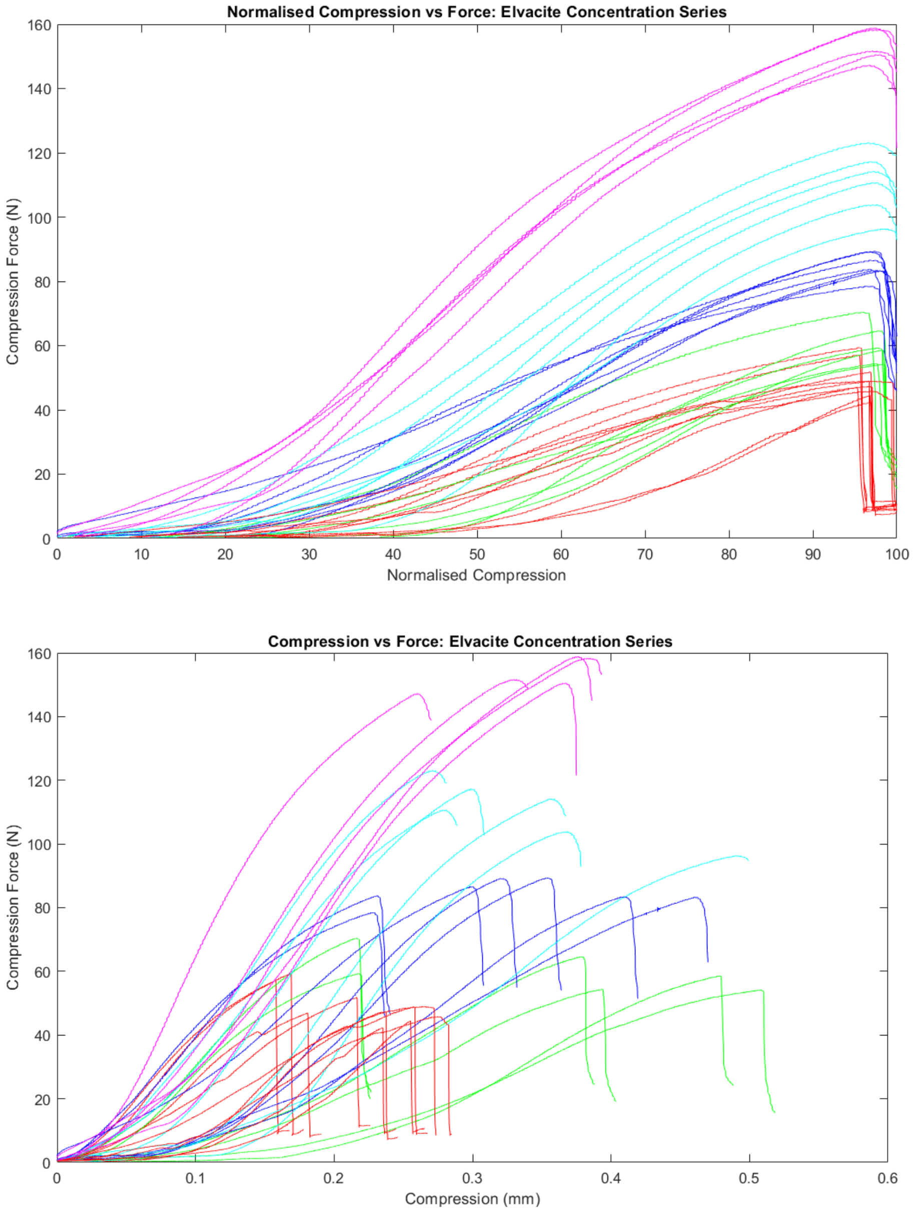

Red =No Elvacite, Green = 0.25 wt.%, Blue = 0.5 wt.%, Cyan = 0.75 wt.%, Magenta = 1 wt.%

Figure 8.3.c: Normalised compression vs. Compression Force (N), Sample compression (mm) vs Compression force (N), top and bottom plots respectively.

In Figure 8.3.c above, the raw compression plots are presented for each sample, displaying the recorded compression force (N) against compression displacement (mm), for each of the Elvacite binder concentrations. The upper plot shows the compression distance normalised, while the lower plot shows a direct plot of force against compression distance, as measured by the displacement of the universal test machine. Some of the variation that can be seen between samples within the same

Elvacite set can be attributed to variations in coupon thickness between samples, and it should be noted that thickness variation is both measured and accounted for when calculating the material's tensile stress for each sample.

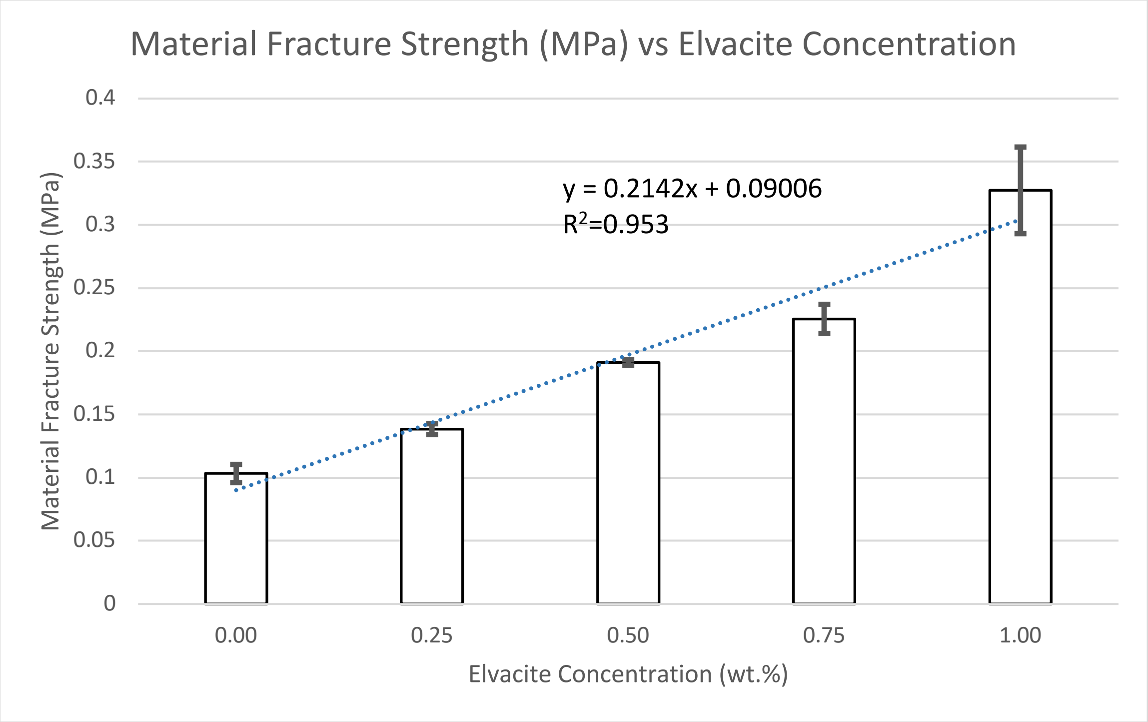

Figure 8.3.d: Material Fracture Strength (MPa) vs Elvacite Concentration (wt.%), with linear fit regression.

The results seen in Figure 8.3.d above indicate a strong linear relationship between fracture strength and binder addition, with consistent increase in mechanical strength observed with each corresponding increase in binder addition. With 1.0 wt.% binder addition, the green-body mechanical strength is seen to increase by a factor of 3.0x relative to the strength of the sample without binder addition. This indicates that significant increase in mechanical strength can be achieved with only a minor addition of binder to the suspension. Based on this increase on green body mechanical strength, it is worthwhile to evaluate the effect this has on the severity and configuration of internal freeze-cast sample cracks after freeze-drying.

8.3.3.3 Freeze-casting micro-CT results

A suspension was successfully prepared using 54 vol.% ceramic solids and 1 wt.% addition of Elvacite to maximise the strength of green bodies. This suspension was used to prepare a set (batch #120) of six freeze-cast samples. All samples were frozen at -40°C, but both pre-chilled and ambient moulds were used to vary the freezing rate (fast or slow freezing) between samples. Within this sample set the freeze-drying rates were varied, with both fast and slow freeze-drying methods used. The freeze-dried samples were then imaged via Micro-CT, with cross-section slices in Table 8.3.a below taken from the centre of the sample 3D reconstructions.

While it was found that 1 wt.% was the practical limit for a suspension with 54 vol.% solids, additional insights may be obtained when studying the effect with further additions of Elvacite. However, at those solids concentrations further additions of Elvacite are unviable, as it results in an increase in suspension viscosity beyond an acceptable level for casting. For this reason, an additional 2 wt.% Elvacite suspension was prepared, but using a suspension formulated with a lower 50 vol.% solids concentration. This new suspension possessed a suitable viscosity for freeze-casting test coupons to be prepared. The conditions used for this set of samples (batch #121) was identical to the previous batch, and are summarised again in and Table 8.3.b below.

Table 8.3.a: Freeze-Cast Samples with Elvacite – Set A (Batch 120) with 54 vol.% solids content, 1 wt.% Elvacite

Sample #	Freezing Rate	Drying method	Micro-CT X-Y Slice
A1	**Fast** -40°C prechilled mould	**Fast** Freeze-Dryer	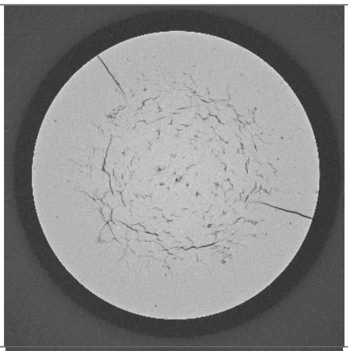
A2	**Fast** -40°C prechilled mould	**Fast** Freeze-Dryer	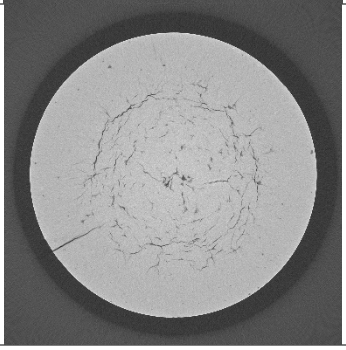
A3	**Fast**	**Slow**	*Not Imaged*
A4	**Fast**	**Slow**	*Not Imaged*
A5	**Slow** -40°C ambient mould	**Fast** Freeze-Dryer	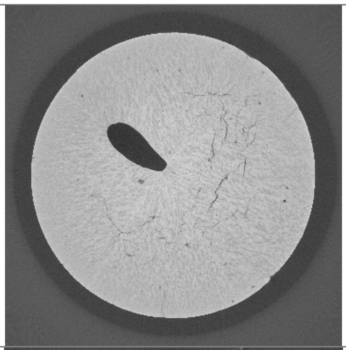
A6	**Slow** -40°C ambient mould	**Fast** Freeze-Dryer	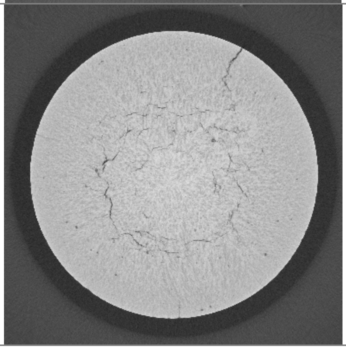

Table 8.3.b: Freeze-Cast Samples with Elvacite – Set B (Batch 121) with 50 vol.% solids content, 2 wt.% Elvacite

Sample	Freezing Rate	Drying method	Micro-CT X-Y Slice
B1	**Fast** -40°C prechilled mould	**Fast** Freeze-Dryer	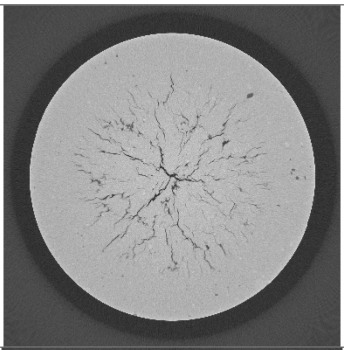
B2	**Fast** -40°C prechilled mould	**Fast** Freeze-Dryer	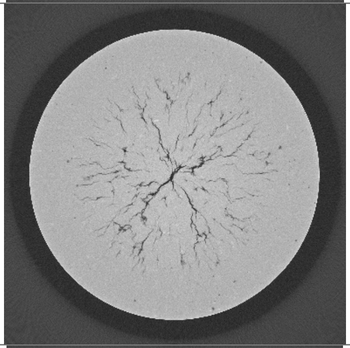
B3	**Fast** -40°C prechilled mould	**Slow** Dried in freezer	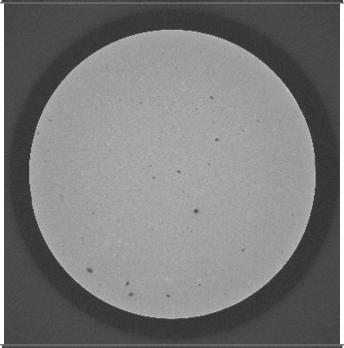
B4	**Fast** -40°C prechilled mould	**Slow** Dried in freezer	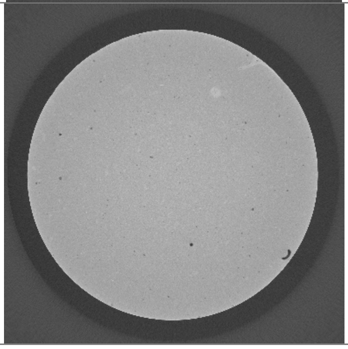

B5	**Slow** -40°C ambient mould	**Fast** Freeze-Dryer	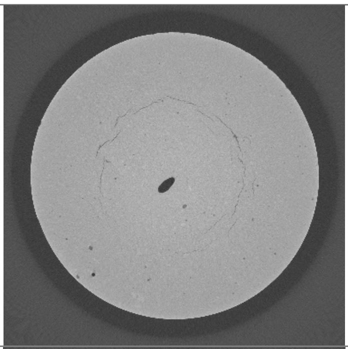
B6	**Slow** -40°C ambient mould	**Fast** Freeze-Dryer	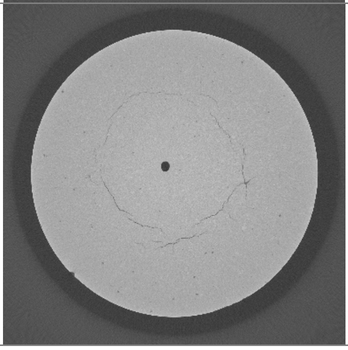

8.3.4 Discussion

8.3.4.1 Suspension Composition & Rheological Behaviour

For highly-loaded suspensions, it has been shown that shear-thinning rheological behaviour is typically observed[98], and this is observed in the original suspension without binder. When examining the effect of adding binder on the suspension rheology, the most significant was observed between the initial 0.25 wt.% Elvacite in comparison to the suspension without binder. In the suspension with Elvacite binder, a significant increase in shear thinning behaviour was evident, due to a marked increase in viscosity at low shear rates. By comparison, subsequent additions of Elvacite resulted in a less significant overall incremental increase on viscosity, with minor continued increases in viscosity at low-shear rates. As a result, the overall trend observed demonstrated that as the concentration of Elvacite increased, the shear-thinning behaviour continued to become more prominent.

This is in contrast with the previous studies, where increases in solids loading of ceramic particulates in suspension resulted in an overall viscosity increase, and an increase in shear thinning behaviour was not observed. The difference between these two observations is consistent with previously observed behaviours for binder addition, which can result in binder-particle bridging[168]. The addition of high molecular weight Elvacite polymer not only increases the loading in the suspension, but also affects the inter-particle interactions. As an acrylic polymer, Elvacite features functional groups, which in suspension will also be likely to affect the inter-particle attractive DLVO forces. These attractive interactions are weak and easily disrupted, so their effect is primarily observed under static or low-shear conditions[169].

Higher viscosities are generally undesirable, as they increase mechanical work requirements, and prevent higher solids loadings from being able to be well-dispersed. However, this shear-thinning behaviour is somewhat desirable, as high viscosity at low shear will serve to further prevent settling of particles in suspension, while the minimal increase in viscosity at high shear should not be prohibitive for rapid suspension injection into moulds.

While not quantitatively measured, increasing the Elvacite addition beyond 1 wt.% was found to result in a thick paste that was unsuitable for freeze-casting. Instead, by reducing the solids concentration to 50 vol.%, it was possible to add 2 wt.% Elvacite to achieve a suspension suitable for casting.

8.3.4.2 Binder Addition to Suspension: Compressive Fracture Strengths

The result from the diametral compression test series clearly demonstrate the increase in the green-body tensile strength that can be achieved with the addition of a binder to the suspension composition. The quantitative results show that a green-body material tensile strength increase of 100% can be achieved with approximately 0.5 wt.% Elvacite addition, and that the relationship between Elvacite addition and material strength appears to be relatively linear.

The limiting factor for further Elvacite addition beyond 1 wt.% remains maintaining acceptable rheological properties, unless the concentration of solids is significantly reduced to compensate. As a result, it would be expected that even higher increases in green body strength would be possible, if the need for a high solids concentration could be relaxed. This results in a trade-off, where there is the need to find an optimal compromise between the required Elvacite addition for achieving a desired material strength, and the with the suspension composition, where a high solids loading is desired to achieve a maximum bulk density of the final sintered product.

It should be noted that the mechanical tests were performed using slip-cast test coupons, and were not freeze-cast; the mechanical strength of the freeze-cast samples has not been measured, and would like differ from slip-cast samples due to internal porosity.

8.3.4.3 Freeze-cast sample Micro-CT Results

Examining the internal features from the 3D sample reconstructions, different internal microstructures are observed for samples prepared under different conditions. Both freezing rate and freeze-drying rates are observed to have significant effects; in alignment with the results observed from the previous chapters. Due to limitations with the equipment, for this study 40°C was the lowest possible temperature achievable on the freezer used. For this reason, the resulting freezing rate would be expected to be between the -20°C and -80°C conditions previously used.

The samples produced under fast-freezing and fast-drying represent the most rapid method for part production, and for this reason, this would the most desirable process condition to use for mass production. However, examining samples A1 and A2, significant internal and radial cracks are still visible in the cross-section reconstructions. As shown in Table 8.3.c below, in comparison to pre-chilled samples from the previous chapter, the severity of cracking on the Elvacite sample is slightly reduced, but the two radial cracks present appear to have opened wider than on the sample without binder.

Image	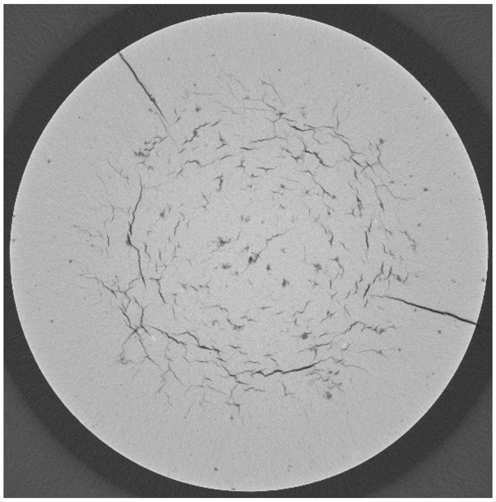	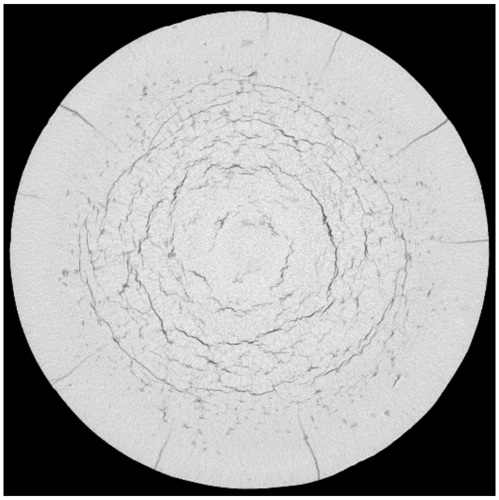
Sample	A1: -40°C, prechilled, fast dried	59-2: -80°C, prechilled, fast dried

Table 8.3.c: Binder study with Fast freezing and fast drying

The presence of cracks within the sample with binder indicates that the cracking forces are still overcoming the strength of the material. For this reason, a second set of samples was also prepared and studied, with ceramic solids concentration reduced to 50 vol.%, but with the binder content increased to 2 wt.%. From the tensile mechanical study, it was previously observed that there was a strong linear trend between material tensile strength and binder addition.

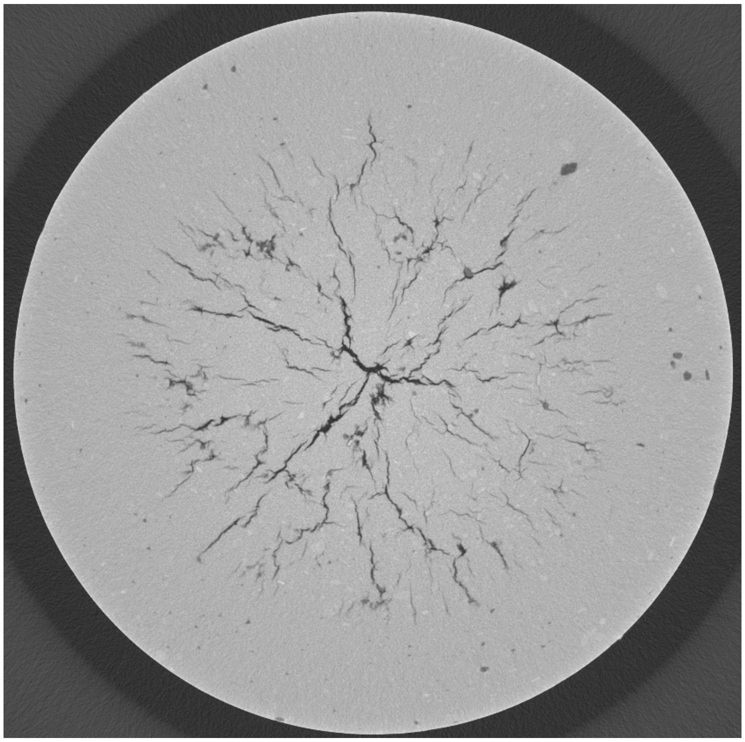

Figure 8.3.e: Sample B1, showing inner-crack concentration

When examining the 2 wt.% binder sample B1 and B2, internal cracks are still clearly present. It can be noted that no outer radial cracks are observed in any of the 2 wt.% B series of samples, but instead in samples B1 and B2 a concentration of cracks are observed toward the centre region of the sample. In addition, the cracks appear to be oriented towards the centre of the sample, rather than around the circumference. This suggests that a significant change occurs with the distribution of cracking forces following the further addition of Elvacite, but this change may be attributable to either the higher Elvacite addition, or to the lower relative solids concentration

Examining the slow-frozen and fast-dried samples (A5, A6, B5, B6), it is evident that the samples with binder display a significant reduction in the severity of sample cracking. Again, the increase in binder concentration further improves the part quality, as samples B5 and B6 display only one ring crack. The porosity of the slow-frozen Elvacite samples after drying also appears to be significantly reduced compared to previous slow frozen samples without binder. Previously, large dendritic structures were visible for slow-frozen samples, which after drying were visible as dendritic pore structures. In this case, the addition of Elvacite appears to have also resulted in a degree of cryoprotection, interrupting the crystal developments, and resulting in a finer distribution of pores present after drying. Even though the cracks are reduced here, the presence of even minor cracks in a formed part is still fatally prohibitive for most engineering applications. Further increasing the binder content in suspension may further reduce the cracking severity, this would be likely to necessitate a corresponding reduction in the solids loading, which is undesirable for achieving a high sintered bulk density. Finally, some of the slow-frozen and fast dried samples also display some large internal pores. The slow freezing allows time for air bubbles to enter, and it is likely that these pores are due to the simplistic mould design that was used, and it is expected that pores like this would not be occur for a commercial moulding process with more sophisticated mould design.

The final sample set to discuss are the fast-frozen and slow-dried samples, B3 and B4. Here, it can be observed that these samples do not have internal cracks or pores, but the samples appear to be well reproduced from the mould. This finding reiterates that even with binder addition, the rate of drying is a key parameter that should be well controlled for commercial dense freeze-casting process. While successfully cast for this study, future studies should carry out further tests to investigate the minimum Elvacite concentration for achieving crack free microstructure. Furthermore, it would be appropriate for future studies to examine the effect of binder addition on green-body microstructure and pore morphology by bisque firing and SEM imaging, as well as to measure the bulk density achieved for fully sintered samples.

8.3.5 Conclusion

This study was successfully able to demonstrate that with binder addition, the strength of the material can be increased sufficiently to mitigate crack formation in freeze-cast samples under specific conditions. The binder selected was Elvacite 2045, offering good burn-out characteristics, and good compatibility with non-aqueous solvents. It was found that by using fast-freezing, slow-drying, and 2 wt.% binder that a dried body could be successfully formed free of internal cracks.

The quantitative effect of binder addition on mechanical properties was measured, with an indirect tensile test on slip-cast green body samples. A strong linear relationship was found between Elvacite concentration and tensile strength, with over 200% increase in tensile strength observed at 2 wt.% binder addition. In addition to an increase in mechanical strength, the addition of binder was observed to offer a cryoprotective role. Samples prepared under slow-freezing conditions with binder addition did not display the typical large dendritic pores, instead it appeared that the binder disrupted crystal growth resulting in a more refined pore microstructure in the dried green-body.

However, the addition of binder had the disadvantage of significantly increasing the suspension rheology. As a result, in this study, the increase in viscosity at 2 wt.% Elvacite required that the solids concentration correspondingly be reduced, from 54 vol.%, to 50 vol.%. For this reason, it is suggested that future studies investigate the minimum binder required to achieve crack-free parts, in addition to investigating the bulk density of samples and resulting microstructures following pressureless sintering.

8.4 Part B: Effect of Alternative Carrier Solvent on Dense Freeze Casting Cracks

8.4.1 Background

During the previous time-lapse study of freeze-drying, it was observed that the development of cracks over time did not correspond with the progression of the freeze-drying front through the sample. Instead, significant cracking was observed to occur early during drying, within regions of the samples that appeared to still be frozen. Since frozen samples regions still contain the carrier solvent in the solid phase, this suggested that the role of the carrier solvent should be investigated with respect to both microstructural development, and internal cracking phenomena.

For this second study, the carrier solvent used in the suspension was substituted with a different carrier solvent, to explore whether the properties of the solvent affect the resulting cracks in any aspect. Specifically, there are two material-dependant properties that are plausibly relevant to crack formation, these being material thermal expansion coefficients, and volume expansion on material phase change. Thermal expansion and volume expansion would both result in internal forces generated during the freeze-casting process, which could result in residual stresses imparted into samples during solvent solidification. For example, it has been recommended that volume change on freezing is less than 10% [32].

The consequences of this solvent substitution are expected to affect several other aspects of the freezing and freeze-drying processes, due to significant differences in physical, chemical and mechanical properties between these solvents. In addition to changes to thermal expansion coefficients and volume changes on freezing, differences in solvent vapour equilibrium will also affect the rates of sublimation drying. The chemical polarity and molecular conformation will also affect the behaviour during freezing, consequently affecting the frozen solvent microstructure that is templated during freeze-casting, which could also affect the freeze-drying performance. Finally, the viscosity of the solvent, the thermal conductivity, and the freezing temperature will affect the practical aspects of freeze-casting, such as the maximum freezing-rates achievable, the time required to inject the suspension into the mould, and the maximum practical solid loading in suspension.

8.4.1.1 Alternative Solvent Selection

The selection of an alternative solvent that is well-suited for freeze casting should take into consideration many of the factors identified above. Attention should also be given to examine the potential hazards and risks introduced by new materials, as many solvents are hazardous or toxic. From the literature, few other solvents have been explored for non-aqueous ceramic freeze casting, including camphene[9, 78], tert-butyl alcohol[119, 170–172], napthalene-camphene[65, 77, 173], and cyclooctane[174]. Other suggested solvents include phenol, caprolactam, dioxane, neopentyl alcohol[32, 54]. Selected properties for some of these solvents are tabulated below.

Table 8.4.a: Properties of various alternative freeze-casting carrier solvents

Solvent	**Freezing Temperature**	**Coefficient of Thermal Expansion**	**Volume Change on Freezing**	**Pore Geometry Style**
Cyclohexane	6.5°C [104]	$6.0 * 10^{-4}$°C^{-1}	-5.2% [32]	Dendritic[174]
Cyclooctane	14°C [175]	N/A	-6% [176, 177]	Dendritic[174]
Camphene	52.6°C [178]	N/A	-3% [87]	Dendritic [78]
Tert-Butyl Alcohol (TBA)	25.5°C [179]	N/A	Low [55]	Hexagonal / Honeycomb
Naphthalene-Camphene	31°C[65]	N/A	N/A	Disordered / Lamellar [65]
Neopentyl alcohol	55.0°C [180]	N/A	-9.9% [32]	N/A
Dioxane	11.8°C [181]	N/A	N/A	Dendritic [174]
Caprolactam	69°C [182]	N/A	-6.5% [32]	N/A
Phenol	39.5°C [183]	N/A	-6.5% [32]	N/A

In addition to property data, pore geometry has also been listed for the solvents above; when directionally frozen, most solvents display a strong tenancy to produce frozen crystals with an inherent shape, resulting in characteristic pore geometry for each solvent. Each pore geometry style provides both benefits and drawbacks, depending on the application for which the material or part is intended. For example, TBA is the most frequently used non-aqueous carrier solvent explored within freeze-casting studies, typically for typically highly-porous applications [53], and it was considered for this study as an alternative carrier solvent. TBA has a tendency to produce highly elongated non-dendritic crystals, resulting in hexagonal or 'honeycomb-like' pores[55], and this is ideal for achieving high mass-transport for filters or porous applications. However, for dense-body applications TBA's tendency to produce elongated pores has potential to exacerbate anisotropy in the final part, or result in differential shrinkage during sintering. Conversely, dendritic-pore formers such as cyclohexane are regarded as less desirable for some high porosity applications, as dendrites can produce dead-end pores, that reduce material transport through a material[77]. However, for developing homogenous dense components, dendritic pores appear desirable, as they are regarded as offering the most isotropic microstructure. It should also be noted that some variation in the evolved pore geometry may still be observable for different solvent and dispersed phase combinations[55, 174].

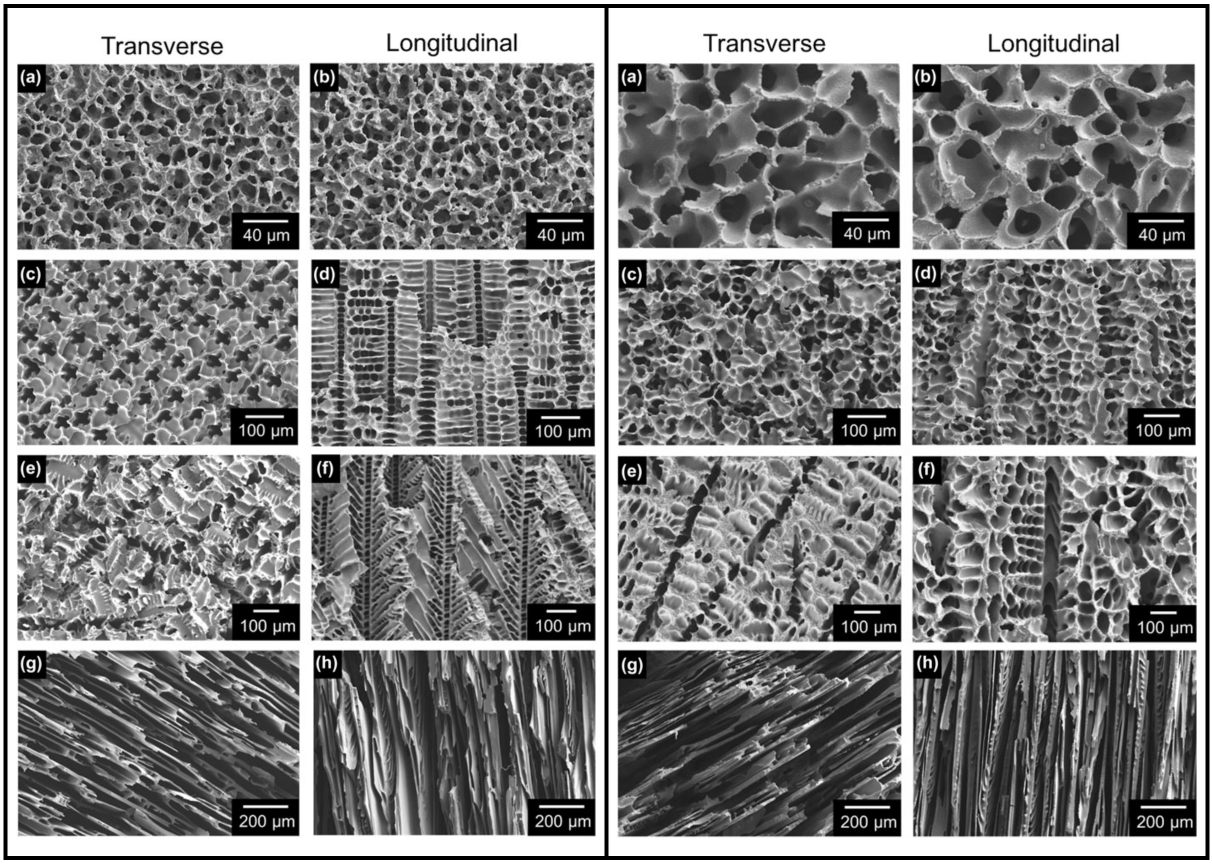

Figure 8.4.a: Transverse and Longitudinal views of pores formed by (a, b) cyclooctane, (c, d) cyclohexane, (e, f) dioxane, and (g, h) dimethyl carbonate, in both Alumina ceramic suspension (left) and SiOC pre-ceramic polymer solution (right). Reproduced from Naviroj et al.[174]

For this study, cyclooctane was selected for study as the alternate carrier solvent, being a similar non-aqueous and non-polar solvent to cyclohexane, with a similarly accessible phase transition temperature, low viscosity, and few indications of severe toxicity or environmental incompatibility. The referenced volume change for cyclooctane on freezing is also similar to cyclohexane, and both are known to produce relatively isotropic dendritic pores[174].

8.4.2 Method

The established cyclohexane-based ceramic suspension used in previous studies was reformulated using cyclooctane solvent as the carrier. With this new formulation, a set of suspensions were prepared across a range of solids-loading values between 20 to 60 vol.%, for rheological testing. A highly-load cyclooctane-based suspension was prepared, balancing the need for both maximal solids-loading and acceptable viscosity for freeze-casting. This suspension was then used to prepare a set of freeze-cast samples for further study. These samples were freeze-cast under both fast and slow freezing rates, freeze-dried by both fast and slow drying regimes. Samples were then examined via micro-CT, being imaged both before freezing by using a chilled stage, as well as afterwards after the completion of freeze-drying. Inspection of the sample reconstructions via micro-CT enabled the internal crack structures to be inspected, and these reconstructions can be directly compared with previous samples prepared from cyclohexane-based suspensions.

8.4.3 Results

8.4.3.1 Rheological Results

Cyclooctane did not present a significant challenge for the preparation of highly loaded suspensions. For suspension preparation, a similar 1 wt.% of Hypermer A70 dispersant was used (relative to the ceramic loading weight), and this dispersant was found to be readily soluble in cyclooctane. While the viscosity of cyclooctane solvent itself appears to be visibly higher than cyclohexane, after the addition of dispersant and ceramic media the rheological behaviour of the suspension was found to be generally similarly or slightly less viscous, than equivalent suspensions prepared with cyclohexane carrier solvent.

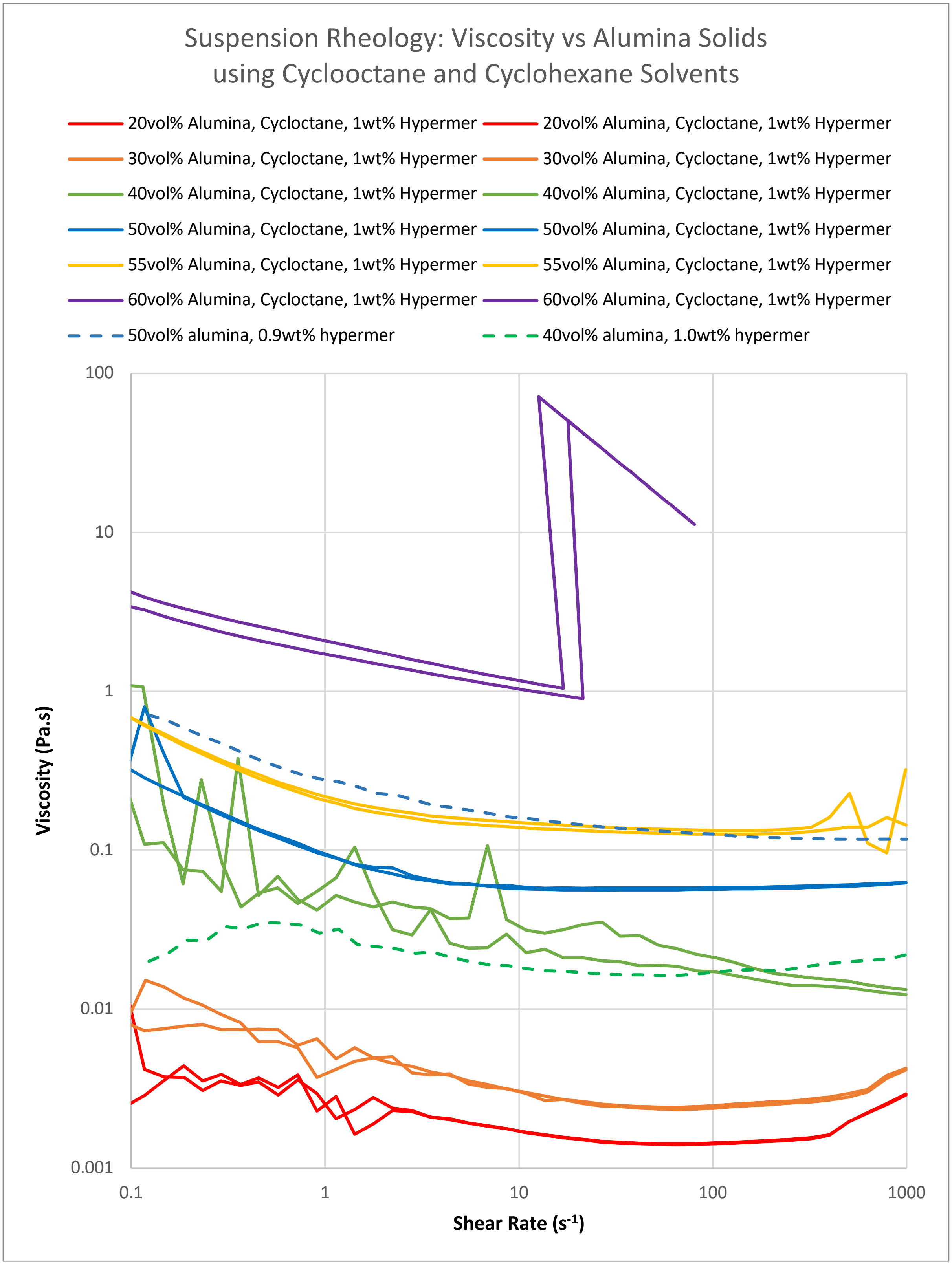

Figure 8.4.b: Rheology of highly-loaded Alumina non-aqueous suspensions, cyclooctane based: solids concentration vs viscosity

8.4.3.2 Freeze Casting and micro-CT results

A selection of the samples was prepared from Cyclooctane based suspensions, and were examined via micro-CT, before and after freeze drying. Cross sections from the sample reconstructions are presented below in Table 5, listed alongside the conditions used to prepare the sample. Only four samples were imaged in the frozen state, with two samples for each of the freezing-rate conditions examined: slow freezing and fast freezing, with ambient temperature and pre-chilled temperature moulds respectively. Samples were also prepared to explore both fast and slow freeze-drying rates, using a freeze-dryer, or by leaving samples to self-sublimate in a freezer at ambient pressure, respectively. Since the melting point of cyclooctane is higher than for cyclohexane, and the vapour pressure is lower, slow freeze drying was performed in a conventional fridge maintained at 0°C.

Table 8.4.b: Freeze-Cast Samples prepared with Cyclooctane-based suspension, varying freezing rate and drying rate.

Sample	Frozen micro-CT	Freeze-dried micro-CT
75-1: Fast-freezing, Fast-drying - Pre-chilled mould, frozen in -35°C freezer - Freeze-dried under vacuum in freeze-dryer, ambient temperature.	N/A	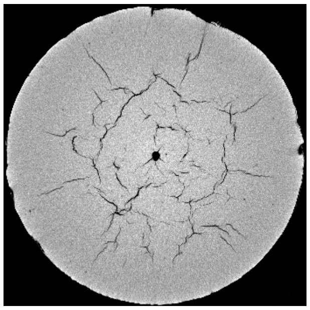
75-3: Fast-freezing, Fast-drying - Pre-chilled mould, frozen in -35°C freezer - Freeze-dried under vacuum in freeze-dryer, ambient temperature.	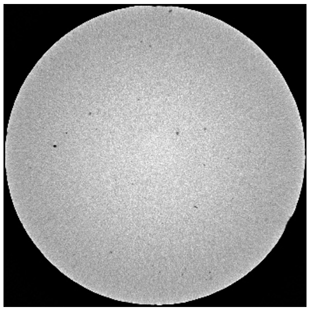	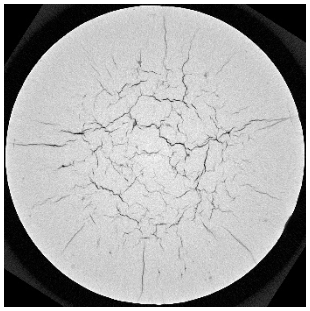
75-4: Fast-freezing, Fast-drying - Pre-chilled mould, frozen in -35°C freezer - Freeze-dried under vacuum in freeze-dryer, ambient temperature.	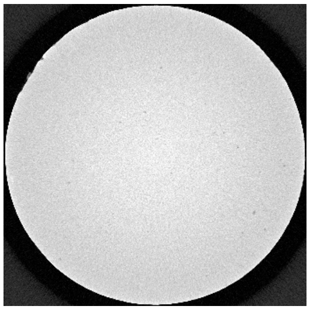	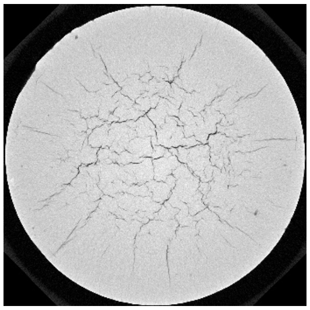
75-5: Slow-freezing, Fast-drying - Ambient mould, frozen in -30°C freezer - Freeze-dried under vacuum in freeze-dryer, ambient temperature.	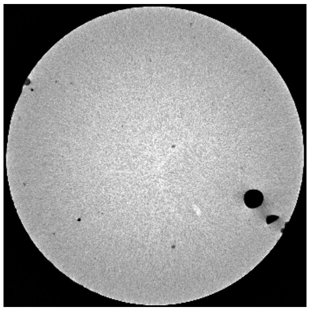	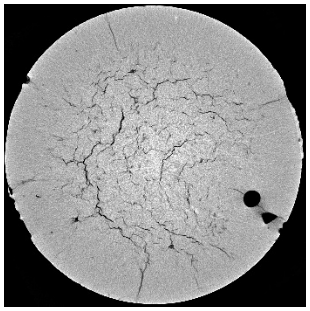

75-6: Slow-freezing, Fast-drying • Ambient mould, frozen in -30°C Freezer • Freeze-dried under vacuum in freeze-dryer, ambient temperature.	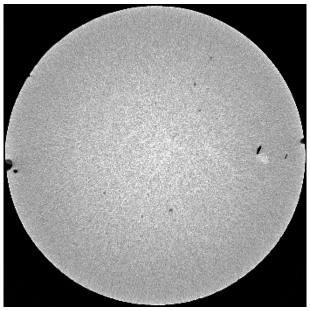	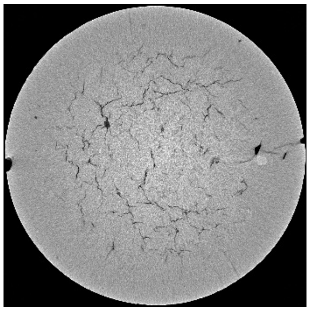
77-7: Fast-freezing, Slow-drying • Pre-chilled mould, frozen in -40°C Freezer • Freeze-dried in fridge at ambient pressure, low temperature (0°C)	N/A	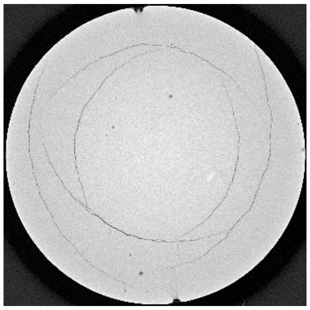
77-8: Slow-freezing, Slow-drying • Ambient mould, frozen in -40°C Freezer • Freeze-dried in fridge at ambient pressure, low temperature (0°C)	N/A	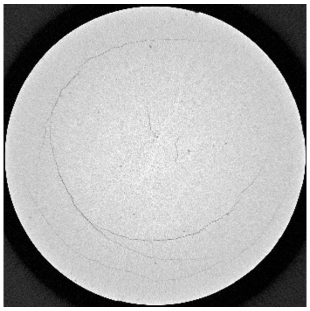

8.4.4 Discussion

These early tests were successful in demonstrating the use of cyclooctane as an alternative solvent carrier for dense freeze casting. The suspension viscosity was similar in comparison to cyclohexane-based suspensions at the same solids loading. As was achieved using cyclohexane, a stable and highly loaded ceramic suspension was still able to be prepared using cyclooctane up to 60 vol.%, using the same Hypermer A70 dispersant. However, for practical freeze-casting of samples, a lower solid-loading of 55 vol.% was required, in order that the suspension viscosity was suitably fluid for rapid injection (high-shear) into casting moulds. Freeze-casting of samples was also successfully demonstrated, with test samples able to be frozen in moulds for shaping, before undergoing solvent removal via sublimation (freeze-drying) without melting.

8.4.4.1 Examination of Internal Cracking

Non-destructive examination of internal features was performed using micro-CT imaging, with samples studied in both frozen and dried states, to confirm the effect of freeze-drying on cyclooctane freeze-cast parts. Matching of internal microstructural features was used to enable the comparison of sample cross sections before and after freeze-drying. Examination of frozen-state sample reconstructions reconfirmed that for samples in the frozen-state no internal cracking is evident with cyclooctane carrier solvent. However, for samples that had undergone freeze-drying, yet again internal cracks were visible under all sample conditions studied after freeze-drying via either fast or slow drying regimes. Examining the dried reconstructions of cyclooctane samples, these can be compared against the results obtained from samples prepared with cyclohexane-based suspensions from previous chapters.

Comparing the internal crack network of the cyclooctane and cyclohexane fast-frozen, fast dried samples (see Figure 8.4.c below), similarities and differences can be observed. For both samples, there are two distinct crack feature-types evident, with outer radial 'spoked' cracking, and inner discontinuous cracking. The outer radial cracking on the cyclohexane sample extends to the sample surface, exposing those cracks from the outside, while for the cyclooctane sample, most of the radial cracks do not reach the surface of the sample, which is unexpected. Comparing the internal central-region cracks, significant differences are visible, with cyclohexane sample displaying cracks that are largely concentric, while the cyclooctane sample cracks do not appear to show any preferential orientation or alignment. This could be due to differences in dendritic propagation during freezing, or differences in dendrite sizes evolved, with cracks preferentially following the paths of larger dendrites seen in cyclohexane, while the pores in cyclohexane may not be as strongly aligned, or as clearly defined.

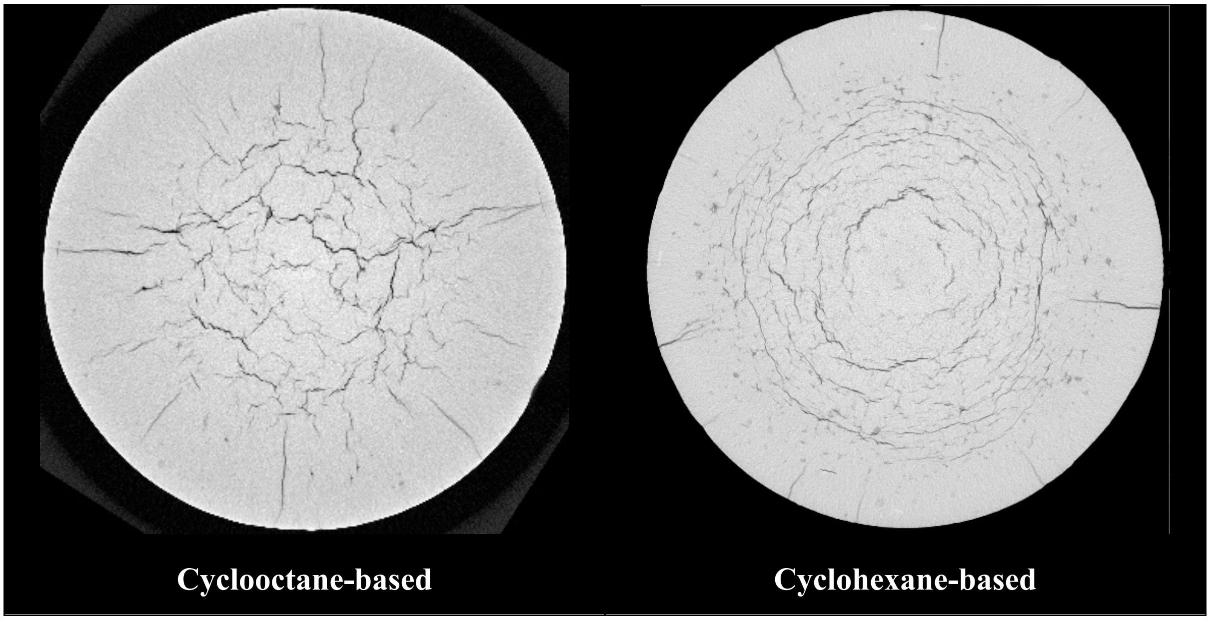

Figure 8.4.c: Comparison of cyclooctane (left) and cyclohexane (right) fast frozen, fast dried samples, frozen at -35°C and -80°C respectively.

When drying samples via slow-drying, again, a significant difference is observed between cyclohexane-based and cyclooctane-based samples. As was seen with cyclohexane, with cyclooctane again different cracking modality is observed when using slow-drying sublimation rather than fast-drying in a freeze-dryer. An example comparison is shown in Figure 8.4.d below. Again, as for cyclohexane samples, slow-dried samples displayed longer continuous cracks extending circumferentially. In contrast with cyclohexane samples, the cracks in cyclooctane samples appear to extend as arcs crossing through the sample, rather than as circumferential cracks of constant radius. The arcs appear to be connected, with many of the cracks extending inwards from the outer arc cracks, at small angles of incident. This pattern of crack configuration (with inner cracks appearing to terminate when reaching outer cracks) would appear to suggest that cracks formed by a mechanism that developed cracks from the outside of the sample, inwardly. These arc-cracks also appear to be consistent for both fast and slow freezing rates, though a larger number of samples would be appropriate to confirm these observations. In addition, the slow-dried samples appear to have a significantly reduced overall severity of cracks, in comparison with cyclohexane-based samples.

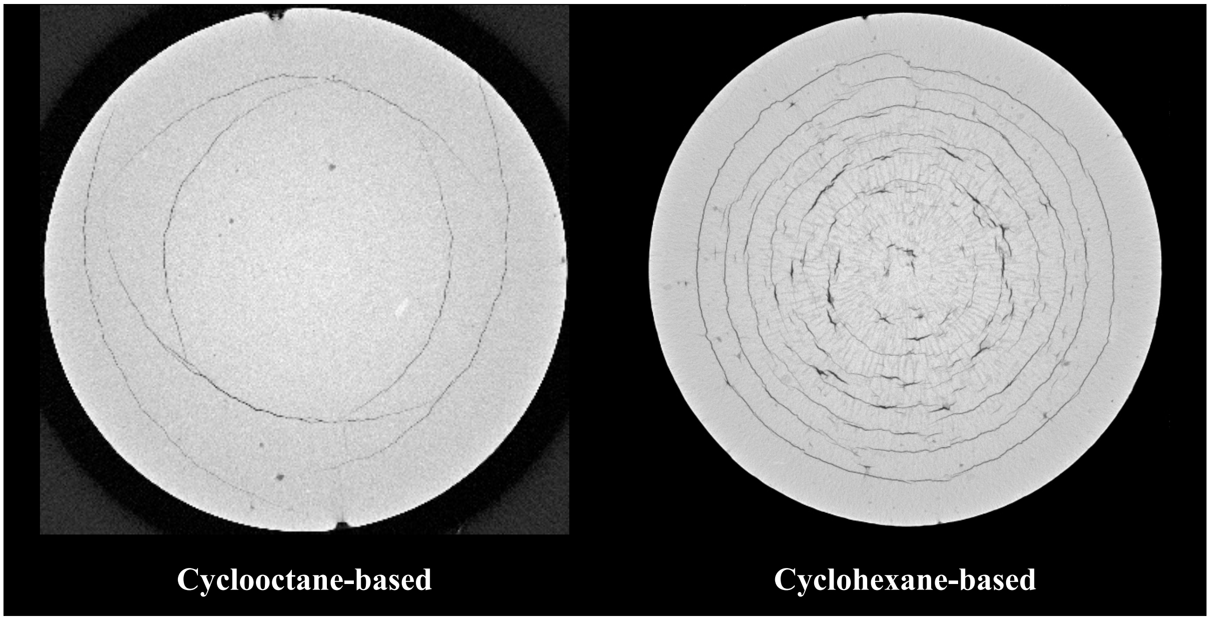

Figure 8.4.d: Comparison of cyclooctane (left) and cyclohexane (right) fast-frozen, slow-dried samples.

When examining the slow-frozen samples produced using these solvents, significant differences can be observed in the dendrite microstructure formation. Examining Figure 8.4.e below, the cyclohexane sample shows visible dendritic growth and branching oriented towards the sample centre. Those dendrites are large enough to be identifiable even at the relatively low resolution of the micro-CT reconstruction (>10µm). By contrast, examining the cyclooctane sample, no significant dendrites can be observed.

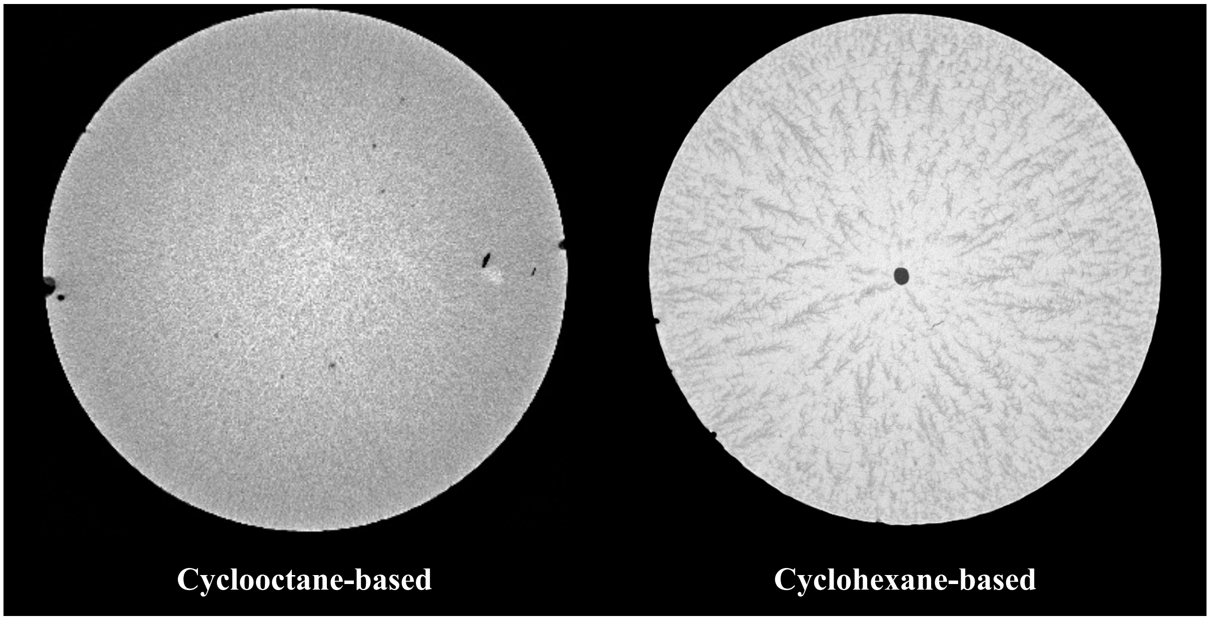

Figure 8.4.e: Comparison of cyclooctane (left) and cyclohexane (right) slow-frozen sample, imaged in frozen state.

The lack of apparent visible dendrites in the cyclooctane samples may simply be due to inspecting at a low resolution. Bisque-firing and SEM examination will provide answers regarding the geometry of pores within dense freeze-cast cyclooctane samples, and it is possible that this would offer insights into the reason for the discrepancy between the cracking morphologies observed.

A lack of large pores in the cyclooctane samples would be an advantage for dense freeze-casting, and it is expected to enable a high bulk density to be achieved after sintering, but this remains to be examined. With cyclohexane, as the thickness of objects increases, the freezing rate at the centre of the part decreases, resulting in larger pores, and in turn resulting in porosity in the final parts. If cyclooctane is used instead, it may be possible to freeze-cast through thicker geometry parts before large crystal growth becomes significant, avoiding macro pore evolution. Further investigation would be valuable in this area, specifically, to examine the sintered pore microstructure of cyclooctane samples prepared under different freezing conditions with high-resolution SEM imaging, and to examine the relationship of freezing rate and pore sizes with this solvent.

Finally, it is a limitation of this study that a wider range of carrier solvents were not able to be explored in a similar methodology beyond cyclohexane and cyclooctane. Araki & Halloran [65] clearly demonstrated the ability to precisely tailor a desirably 'disordered or 'discontinuous' pore geometry through the use of a eutectic solvent mixture. Based on the results of that paper, and the significant differences observed between the two similar solvents explored within this study, further exploration of binary solvent mixtures and resulting freeze-cast pore microstructures could have the potential to offer another method for tailoring porous microstructure, which could assisting towards optimising the dense freeze casting process for the production of high-density ceramic components.

8.4.5 Conclusion

Cyclooctane was successfully demonstrated as a non-aqueous carrier solvent in the freeze-casting of dense ceramic suspensions. It was found to be suitable for preparing highly loaded ceramic suspensions with acceptable rheology, performing similar to cyclohexane in this regard. However, with regards to the primary goal of producing dense freeze-cast samples that are free of cracks, this was not achieved, as all dried samples had significant cracking evident internally.

Under fast freeze-drying conditions, similar internal crack morphologies to were also observed with cyclooctane as with cyclohexane carrier solvent, with both radial external cracking and discontinuous internal cracking. Under slow-drying conditions a significant reduction in cracking was observed, although elongated arc cracks still permeated the outer regions of the samples.

It was noted however, that with cyclooctane-based suspension under slow-freezing conditions, the development of large dendritic pores was not observed, unlike those seen following the slow-freezing of cyclohexane. This tends to suggest that cyclooctane is a better option than cyclohexane for using freeze-casting, as will enable the production of larger complex-shaped components while maintaining more homogenous pore microstructures throughout. Further testing is required to explore the limits of these findings, and future studies of cyclooctane-based freeze-casting would be valuable to further understand the crystal growth and microstructural evolution occurring during freeze-casting of highly-loaded cyclooctane suspensions.

9 Conclusions

This thesis critically evaluated the potential suitability of the freeze-casting process to produce dense, complex near-net shaped ceramic components.

The primary limitation of this process previously identified, was the presence of internal cracks within dense freeze-cast samples. For dense freeze-casting to be at all viable for commercial applications, it would naturally be required that the cause of the cracks was identified, and that a strategy be found for crack mitigation. To address each of the original research goals, specific aspects of the process were examined individually in separate studies. For each of the areas that were studied, a summary of the key research findings and outcomes are presented below. In addition, where significant research gaps were identified in the scope of this project, recommendations are provided regarding areas for future research.

9.1 Demonstration of Freeze-casting Process for Shaping of Dense Ceramic Components

To those familiar with the typical results of the freeze-casting process and the literature within this field, the goal of producing dense components via a freeze-casting process may at first seem counterproductive, perhaps appearing to put a 'square peg in round hole'. Being an inherently pore-forming process, it can be acknowledged that this is inherently in opposition to the goal of maximising part bulk density. However, sufficient examples from literature have been reviewed within this thesis that demonstrate that dense parts can be achieved partly as a result of densification processes occurring during sintering[33, 64, 112].

9.1.1 Chapter 5: Preliminary Study of Dense Freeze-casting Process

As the freeze-casting process as the process itself is inherently pore-producing, through the removal of frozen solvent crystals by sublimation, it is unsurprising that freeze-casting research attention has primarily focused on production of porous components. With this context, applying such a process with the goal of producing dense components may appear incongruent. However, it is known that during final sintering, pore features below a critical size threshold undergo pore elimination, resulting in densification to increase the bulk density of the final component.

Observations in literature demonstrated the capability to tailor the size of solvent crystal features through control of freeze-casting process parameters, with the intent to use this control to template a suitable pore microstructure as desired[55]. For this study, a fine micropore microstructure optimised for densification was pursued via efforts to maximise both suspension solids-loading and solidification freezing-rates.

9.1.1.1 Findings & Recommendations

In preparing a highly loaded ceramic suspension, the primary limitation for ultimate solids loading was determined to be rheological flow requirements for injection moulding. A highly loaded ceramic suspension was successfully prepared, using a non-aqueous carrier solvent, with 0.9 wt.% of dispersant, and solid ceramic particle loadings up to 55 vol.%. The carrier solvent, cyclohexane, offers a favourable combination of properties that make it suitable for use with this process, including an accessible freezing-point, a high-vapour point, and a low viscosity. Under this formulation, the resulting highly loaded suspension possessed an acceptably fluid rheology for smooth and rapid (~5 s) manual injection moulding via syringe. In addition, in comparison to aqueous carrier solvent, using a non-aqueous carrier solvent both enables compatibility with both oxide and non-oxide materials, and avoids the typically large crystals formed when freezing aqueous suspensions.

Fast freeze-casting was achieved using a cylindrical aluminium mould, offering large thermal mass and high thermal conductivity. The mould was first pre-chilled to -80°C in an ultra-low temperature freezer before suspension was rapidly injected into the mould. Under these conditions, the thermal measurements via in-situ thermocouple indicated that sample solidification completed in less than a minute.

After solidification, this was followed by rapid solvent removal via sublimation in a freeze-dryer, to produce a resulting 20mm diameter cylindrical green body sample.

Suspensions were prepared from both alumina (oxide) and titanium carbide (TiC), non-oxide) ceramic powders, and the resulting dense freeze-cast samples were pressureless sintered in air and vacuum furnaces for each material, respectively. The sintered densities achieved were 97.8% of the maximum theoretical density (T.D) for alumina, and 94.9% of T.D for TiC, validating the preliminary study hypothesis that dense (or near-dense) complex shaped samples can be produced using the dense freeze-casting process, and demonstrating this capability in both oxide and non-oxide materials.

With respect to the shaping capabilities of the process, a selection of complex-shaped samples was successfully produced via dense freeze-casting into silicone confectionary moulds. The resulting castings displayed excellent reproduction of both the details and features of the mould, as well as retaining a perceptible degree of the mould surface texture. The results seen offer confidence that precise near-net shape moulds could be created for mass-production of complex shaped components.

Internal examination of these complex-shaped samples revealed extensive internal cracking. While undesirable, these results validated past experimental results, where cracking was identified within dense-freeze-casting attempts using ZrB_2-based suspensions. The verification of internal cracking occurring with other ceramic materials confirmed that internal-cracking was the primary challenge to overcome, in order for dense-freeze-casting to have any potential or viability for practical uses.

9.1.1.2 Future study

An area for further study regarding shaping capabilities would be to examine the effect of residual stresses from freeze-casting, and whether specific features could cause artifacts during casting, or other potential issues that arise during densification such as warping. Other practical limitations from complex shaping were also not explored: If a pre-chilled mould is used for fast freezing, this has the potential to limit the aspect ratio of features or the minimum feature size possible to cast, as the suspension may freeze before mould filling has completed. Additional investigation may also be required for parts with multiple mould filling ports, to ensure that the regions where two feed streams blend does not form defects, gaps, or result in incomplete filling.

One of the reasons that a simple cylindrical mould geometry was selected, was the high degree of rotational symmetry offered: this geometry can be approximated as equivalent to a one-dimensional line; a path from external surface to mould centre. This in turn provides an avenue to simple heat and mass-transfer process simulations, either on a 1D simulation, a 2D cylindrical and symmetrical geometry, or a full 3D cylindrical geometry. While work was begun in the area of modelling, it has not been completed, and for this reason has not been included within this thesis.

9.2 Develop understanding of factors responsible for microstructural control

In this study, the boundaries and limitations for practical process operation of dense freeze-casting were explored.

9.2.1 Chapter 6: Study of Freezing-rate and microstructure via Dense Freeze-casting

The first question investigated in chapter 6 was whether the freezing-rate used was sufficiently high to achieve the desired microstructure with micro-pores; that is, having pores small enough in size, that they undergo complete densification during sintering, to yield a fully dense final product.

A broader range of solidifications rates were explored in this second study by using both pre-chilled and ambient temperature moulds. By controlling the freezer temperature, it was demonstrated possible to achieve a range of freezing rates across two orders of magnitude. After freeze-drying, sintering, cutting and polishing the test samples, SEM imaging was used to inspect the sintered microstructure evolved.

9.2.1.1 Findings & Recommendations

As expected, the microstructures observed varied across the range of solidification conditions explored, with significant differences observed between the bulk phase microstructures for fast-frozen and slow frozen samples.

When examining fast-frozen samples, in the areas of the sample where freezing was fastest (at the mould surface), a near fully dense microstructure was successfully obtained, showing a homogenous near dense fine-grained microstructure with a minimal amount of residual homogenously distributed fine micro-porosity (<5 µm); approximately on the same size length scale as the sintered grain size. However, the pore size was not constant, as an increasing gradient in pore size (and change of microstructure) was observed from the radius to the sample centre. Examining the slow-frozen samples cast in ambient temperature moulds, the microstructure was visibly different, with large dendritic pores visible across the sample, oriented towards the sample centre. This study demonstrated that for small pores to be produced using this suspension formulation, that pre-chilled moulds were essential to achieve a sufficiently high freezing rate.

A known limitation of this study was that a simple casting setup was used, with no ability to dynamically control the freezing rate during solidification. As a result, localised variation in pore sizes was observed within samples. This is unsurprising; in comparison to the mould material, the sample material has a significantly lower thermal conductivity, and the thermal resistance results in a significant decrease in cooling rate corresponding with distance away from the mould surface. As a result, maintaining the same fine microporous microstructure homogenously throughout a bulk part is not possible with the system used; as even under the highest freezing rate conditions used in these studies, the microporous (dendrite-free) dense zone only extends approximately 1000µm from the sample surface. Thus, for a process required to produce fully dense parts, this would appear to impose a practical limit on the maximum defined thickness of the part features that could be formed.

9.2.1.2 Future study

While not explored in this study, it is noted that further incremental increases in freezing rate would be possible, for example by using copper moulds or cryogenic liquid cooling to further increase the rate of cooling. However, doing so would introduce new challenges, and in a commercial process the additional process cost and complexity would be likely prohibitive; and doing so would still only be likely to result in incremental improvements in the thickness of the near-dense microporous zone in the sample. Finally, this study only explored sintering via pressureless-sintering; it may be that with use of HIP-ing or other pressure-sintering processes, the remaining porosity in fast-frozen samples may be able to be eliminated, or further minimised.

The limitation of the thickness of the dendrite-freeze zone may be able to be extended if techniques can be identified to disrupt or slow the growth of large dendritic crystals, such as through addition of a cryoprotectant, or though exploration of other carrier solvents. For this reason, any avenues which provide cryoprotective effects in freezing of non-aqueous solvents would be valuable to investigate in future studies.

9.2.2 Chapter 7: Study of drying rate and cracking in freeze-casting

The identification of internal cracking was evaluated as a critical issue for dense freeze-casting to have potential for commercial applications. The initial hypotheses for the formation of internal cracks was attributed to the sintering processes, but after similar cracks were observed in bisque fired samples, this theory was disproved, and a new hypothesis was required. For this study close attention was given to the freeze-drying process, which was examined in detail. This study was enabled through access to micro-CT imaging, in conjunction to a chilled sample stage. This technique permitted the non-destructive internal examination of samples both before and after freeze-drying, in both the frozen and green states respectively.

9.2.2.1 Findings & Recommendations

Through this study it was possible to conclusively show that the freeze-drying process is the primary cause responsible for the evolution of internal sample cracking observed in dense freeze-cast samples. Internal reconstructions of frozen samples showed that they did not possess internal cracks, while after freeze-drying severe internal cracks were clearly evident.

The second key discovery was that the conditions during freeze-drying also affected the formation of the internal crack network; time, pressure and temperature all influenced the configuration and morphology of the final internal cracks. These factors are all related to the rate of freeze-drying, in driving the interfacial equilibrium occurring at the frozen solvent surface, that is responsible for the sublimative solvent removal processes from solid to gas. Two primary rates were explored: fast freeze-drying performed in a commercial freeze-drying under high vacuum and at ambient temperature, and slow freeze-drying, performed by placing samples in a freezer at low temperature and ambient pressure. For each of these drying regimes, characteristic patterns were observed in the internal cracks that develop. Samples that undergo fast drying typically develop extensive networks of discontinuous internal cracking in the simple centre region, as well as radially oriented cracks that develop near the sample surface. In contrast, slow-dried samples typically develop circumferential cracks, that are both fewer in number, and more continuous and connected in nature. This confirmed the time-sensitive nature of crack development during freeze-drying.

After clarifying the role of freeze-drying in internal crack formation, attention was returned to the role of freezing-rate affecting crack development, and it was confirmed that dendrites can also affect the development of cracks. For slow-frozen samples with large internal dendrites, those dendrites appear to offer a more favourable path for stress relief, resulting in small cracks consistently propagating from existing dendritic pores. In comparison, for faster-frozen samples with smaller dendritic pores, other pathways were favoured that often were not aligned with the existing pores.

Having definitively identified the process step responsible for crack formation, the following research goal was to elucidate the mechanism responsible by which cracks are generated, in context of the eventual goal being to minimise or prevent the formation of internal cracks. To observe the development of cracks within a sample during freeze drying, a time-lapse was recorded, using the chilled stage in the micro-CT to perform slow drying of a test sample, while taking 3D acquisitions periodically. This time-series successfully demonstrated that the progression of the drying front from the outside of the sample towards the centre, was not connected with the development of internal cracks. Instead, internal cracking was observed to start early in the process and rapidly progress to completion, well before the drying front was observed to make significant process. From these results it was evident that crack formation did not occur due to sample freeze-drying directly, as cracks were seen to develop within frozen-state sample material.

9.2.2.2 Future study

Possible causes behind the forces that generate cracks in freeze-drying samples have been posited from the evolved crack networks, such as being due to sample warming and thermal expansion after removal from freezer, or from or residual stresses introduced during rapid solidification. However, further investigation in this area is still needed as these hypotheses have not been tested, and the specific cause(s) have not yet been definitively identified; the proposed causes could be individually studied, thus and confirmed or eliminated.

Cyclohexane is also known to have multiple solid crystal configurations depending on temperature, and the effect of these confirmations on expansion and contraction of frozen highly loaded suspensions remains to be studied.

9.2.3 Chapter 8: Study of modified suspension composition for mitigation of freeze-drying cracks

This final chapter explored the potential to mitigate crack formation during freeze-drying, by modifying the suspension formulation. Two separate avenues were explored independently for this study: (A) adding a binder to increase strength and resist cracking forces, and (B) using an alternative carrier-solvent to examine the effect of solvent selection on internal cracking.

9.2.3.1 Part A: Effect of Binder Addition to Suspension on Dense Freeze-Casting Cracks - Findings & Recommendations

Addition of binder was shown to enable successful production of crack-free samples, under specific processing conditions.

First, the suspension was modified with the addition of a binder agent, to help increase the mechanical strength of samples, and thus resist the formation of cracks. A commercial acrylic resin, Elvacite 2045, was selected as a binder, as it is soluble in non-aqueous solvents and offers clean burn-out during sintering. This binder was found to be soluble in cyclohexane, however, the addition of binder was found to significantly increase the suspension viscosity. To maintain an acceptable rheology for injection casting, for 1 wt.% Elvacite the maximum solid suspension loading was required to be lowered from 56 vol.% to 54 vol.%, while for 2 wt.% Elvacite the loading was reduced further to 50 vol.%.

Test coupons were produced by slip-casting suspensions with Elvacite addition varied between 0 to 1 wt.%, with a linear relationship observed between the proportion of Elvacite addition and mechanical strength. A 1 wt.% addition of Elvacite resulted in an increase in mechanical strength over 3x of samples without binder. Due to the low mechanical strength of green body samples, the fracture strength of samples was measured using a diametral compression test, as a proxy for measuring measure effective tensile strength.

A set of samples were successfully freeze-cast using the suspension with 1 wt.% binder, under a range of conditions, using both slow and fast freezing methods, using fast freeze-drying. For samples produced with fast-freezing, internal cracks were still present, but a reduction in cracking severity was observed. For samples freeze-cast under slow-freezing conditions, formation of large dendrites appeared to be suppressed, and the resulting crack morphology was similar to those from fast-freezing. A second set of samples were cast with 2 wt.%. Elvacite, and 50 vol.% solids loading, and for these samples different results were obtained. For fast freezing with fast drying, the cracks appeared to be reduced in number, but increased in severity, and concentrated towards the sample centre. For samples with slow freezing, the effect of dendritic growth suppression appeared to be even greater, with dendrites no longer visible at the imaged resolution in Micro-CT. Those samples also displayed significantly reduced cracking.

Finally, a 2 wt.% Elvacite sample was prepared using fast-freezing, and slow drying, and this sample did not display any internal cracking after drying.

The addition of binder to the suspension composition appears to show significant potential to benefit dense freeze-cast samples. As can be seen, the addition of Elvacite was successful in helping to both mitigate and minimise the formation of internal cracks during the freeze-drying of samples. In addition, the incorporation of Elvacite was observed to further minimise the size of solvent dendrites formed, which may help to achieve a more homogenous microstructure in the final sintered sample. It remains to be tested, whether the addition of binder and other additives negatively affects the final bulk density achievable or reduces the final mechanical properties.

9.2.3.2 Future study

Closer examination of these samples should be performed after sintering, to measure the achieved sintered bulk density, and to inspect the internal microstructure formed after both binder burnout (via bisque firing), and after full sintering. Further optimisation of the suspension composition may also be possible, to help reduce the proportion of binder required, and to maximise the suspension solid loading. It may be possible to injection mould using a higher solid loading, if using a higher-pressure suspension feeder for injection.

9.2.3.3 Part B: Effect of Alternate Carrier Solvent on Dense Freeze-casting Cracks - Findings & Recommendations

While the process step where cracking was successfully identified, and the effect of cracking successfully mitigated via binder addition, the primary cause of the cracks remains unconfirmed. Since cracking is observed during the freeze-drying process, and this known to be where the solvent is removed, the involvement of the solvent in crack formation was considered. An alternative solvent, cyclooctane, was demonstrated for dense freeze-casting in place of cyclohexane. Cyclooctane was used with the same dispersant added, to prepare a highly loaded Alumina suspension of suitable viscosity. This cyclooctane suspension was then successfully used to perform dense freeze-cast samples via the same method, but with solidification occurring at a different temperature. The effect of variations in both freezing-rate and drying-rate on internal cracks were again explored for the cyclooctane system, but after dense freeze-casting was performed it was verified via micro-CT that under the conditions explored, internal cracking was present in all cyclooctane-based samples after drying.

Most aspects of crack evolution were confirmed to be similar as seen in cyclohexane-based samples. It was verified that no cracking was present in the frozen state, and in fast-dried samples a similar distinct two regions of cracking by different modes were identified, with both outer radial cracking and inner discontinuous cracking regions observed. Slow cracking was again also found to reduce the severity of internal cracking. Unlike cyclohexane, slow-dried cyclooctane samples possessed elongated internal arc cracks, that appeared to develop from the outside of the sample, inwards, unlike the concentric circular cracks observed in slow-dried cyclohexane samples.

The use of cyclooctane was observed to have a key influence on the sample microstructure, as unlike the cyclohexane samples, none of the cyclooctane samples displayed sufficiently large dendritic crystals to be identified at the resolution imaged via Micro-CT. This would suggest that cyclooctane, at least under highly loaded suspension conditions, does not form large dendrites as rapidly as cyclohexane. If confirmed, this property would be desirable for dense freeze-casting, as for the forming of large or thick components, as freezing-rate decreases, the size of internal pores increases. A solvent that resists rapid formation of large crystals during solidification would increase the viable thickness of dense complex shaped parts.

9.2.3.4 Future study

From this brief study, cyclooctane appears to be a viable solvent alternative to cyclohexane for dense freeze-casting, but it has not been extensively explored for dense freeze-casting. It still remains to explore the crystal growth of cyclooctane in highly loaded suspensions, to characterise the green microstructure (through bisque firing and SEM imaging), and to measure the sintered final bulk density achieved.

The success observed with avoiding cracks through the addition of Elvacite binder and slow drying also, could be explored with cyclooctane, to see if this method of crack mitigation is solvent independent. The mechanical strength of dried cyclooctane samples could also be measured for comparison.

Finally, beyond the findings obtained from single solvents, suspensions prepared with miscible binary solvent mixtures could be of significant interest to study. Previous studies with solvent mixtures have shown interesting transitions in microstructure evolved under freezing conditions at high solids loadings, and it remains to be seen if cyclohexane and cyclooctane could be well suited for such a study.

9.3 Final Comments

At the commencement of this thesis, it was expected to some degree, that dense freeze-casting would operate in a relatively narrow process window, in terms of suitable parameters for producing successful components. Further exploration may be appropriate to refine the process further, but it may become apparent that even if technically capable, the process itself is both too complex and too inflexible to be used for a broader range of ceramic shaping applications. However, there could be great value to be able to integrate dense freeze-casting techniques with traditional porous freeze casting processing, to produce highly engineered composite or dual-phase materials.

It is also somewhat unsatisfying at present, to be unable to definitively pinpoint the mechanism behind crack formation during freeze-drying. From the results obtained through this thesis, this mechanism has managed to avoid specific identification as it appears to be affected by many properties and parameters to varying degrees. While fascinating to explore and study, and with the potential to yield insights across a range of fields, this kind of parameter sensitivity does not lend easily to developing a robust process for commercial applications. However, with the key issues of internal cracking potentially resolved, the dense freeze-casting process appears to still offer a unique capability for near-net complex shaping, that while possibly challenging to master, could be plausibly scaled to mass production.

10 References

1. Leo S. Colloidal Processing of Difficult-to-densify Ceramics. Department of Chemical and Biomolecular Engineering, The University of Melbourne; Melbourne, Australia; 2015
2. Deville S, Saiz E, Tomsia AP. Ice-templated porous alumina structures. *Acta Mater*. 2007;55(6):1965–1974. https://doi.org/10.1016/j.actamat.2006.11.003
3. Wang F, Yao D, Xia Y, Zuo K, Xu J, Zeng Y. Porous SiC ceramics prepared via freeze-casting and solid state sintering. *Ceram Int*. 2016;42(3):4526–4531. https://doi.org/10.1016/j.ceramint.2015.11.143
4. Liu X, Wu J, Luo B, Zhang L, Lai Y. Porous Cu foams with oriented pore structure by freeze casting. *Mater Lett*. 2017;205:249–252. https://doi.org/10.1016/j.matlet.2017.06.011
5. Fukushima M, Yoshizawa Y. Fabrication of highly porous nickel with oriented micrometer-sized cylindrical pores by gelation freezing method. *Mater Lett*. 2015;153:99–101. https://doi.org/10.1016/j.matlet.2015.04.029
6. Deville S. Freeze-Casting of Porous Biomaterials: Structure, Properties and Opportunities. *Materials*. 2010;3(3):1913–1927. https://doi.org/10.3390/ma3031913
7. Yoon B-H, Choi W-Y, Kim H-E, Kim J-H, Koh Y-H. Aligned porous alumina ceramics with high compressive strengths for bone tissue engineering. *Scr Mater*. 2008;58(7):537–540. https://doi.org/10.1016/j.scriptamat.2007.11.006
8. Chen J, Liu G, Button TW. Mechanical properties of porous TiO2 ceramics fabricated by freeze casting process. *Adv Appl Ceram*. 2013;112(7):436–441. https://doi.org/10.1179/1743676113Y.0000000099

9. Araki K, Halloran JW. Porous Ceramic Bodies with Interconnected Pore Channels by a Novel Freeze Casting Technique. *J Am Ceram Soc*. 2005;88(5):1108–1114. https://doi.org/10.1111/j.1551-2916.2005.00176.x

10. Carter CB, Norton MG. Ceramic Materials: Science and Engineering. 2nd ed. New York: Springer-Verlag; 2013 https://doi.org/10.1007/978-1-4614-3523-5

11. Tallon C, Franks GV. Recent trends in shape forming from colloidal processing: A review. *J Ceram Soc Jpn*. 2011;119(1387):147–160.

12. Coxworth B. High-tech material used to create a thin, flat fisheye lens. *New Atlas*. 2020.

13. The Market Correspondent. Global Gallium Nitride (GaN) Substrates Industry Report Expected Massive Growth By 2020 – 2026. *Mark Corresp*. 2020.

14. Lovatt A, Shercliff H. Material Selection Charts: Strength-Density. *Mater Sel Process*. 2002.

15. Piero M. Guide to Display Assembly Macbook Unibody: The Benefits of the Unibody Construction. *Bright Hub*. 2020.

16. Gantt C. HTC to continue metal unibody chassis for its future smartphone products. *TweakTown*. 2013.

17. Kamps HJ. Apple is an exception to nearly every rule. *TechCrunch*. 2018.

18. Boch P, Nièpce JC. Ceramic Materials: Processes, Properties, and Applications. Wiley; 2010

19. Apple, Inc. Apple Watch Edition. 2017.

20. Matsuyuki N, Memering DN, Waniuk TA, Takagi K, Ely CM. Yttria-Sensitized Zirconia. United States US20180079686A1. 2018.

21. Rahaman MN. Ceramic processing. Boca Raton, Fla. : London : CRC/Taylor & Francis, c2007.; 2007

22. Kingery WD, Bowen HK, Uhlmann DR. Introduction to Ceramics. John Wiley & Sons; 1976

23. Basu B, Balani K. Advanced Structural Ceramics. Wiley; 2011

24. Richerson DW, Lee WE. Modern Ceramic Engineering: Properties, Processing, and Use in Design, Fourth Edition. CRC Press; 2018

25. Tallon C, Chavara D, Gillen A, *et al.* Colloidal Processing of Zirconium Diboride Ultra-High Temperature Ceramics. *J Am Ceram Soc*. 2013;96(8):2374–2381. https://doi.org/10.1111/jace.12383

26. Rice RW. Ceramic Fabrication Technology. Taylor & Francis; 2002

27. Leo S, Tallon C, Stone N, Franks GV. Near-Net-Shaping Methods for Ceramic Elements of (Body) Armor Systems. *J Am Ceram Soc*. 2014;97(10):3013–3033. https://doi.org/10.1111/jace.13192

28. Hengst RR, Heichel DN, Holowczak JE, Taglialavore AP, McEntire BJ. A comparison of forming technologies for ceramic gas-turbine engine components. Vol. 2. Brussels, Belgium: 1990 https://doi.org/10.1115/90-GT-184

29. Binner J. Advanced Ceramic Processing and Technology. Noyes Publications; n.d.

30. Lange FF. Powder processing science and technology for increased reliability. *J Am Ceram Soc*. 1989;72(1):3–15.

31. Bengisu M. Engineering Ceramics. Springer; 2001

32. Adams RW, Karas AE, Novich BE, Sundback CA. Complex ceramic and metallic shaped by low pressure forming and sublimative drying. 1991.

33. Leo S, Jukes L, Pinches S, Tallon C, Franks GV. Freeze casting for near-net-shaping of dense zirconium diboride ceramics. *J Am Ceram Soc*. 2018;101(7):2770–2785. https://doi.org/10.1111/jace.15451

34. Park H, Choi M, Choe H, Dunand DC. Microstructure and compressive behavior of ice-templated copper foams with directional, lamellar pores. *Mater Sci Eng A*. 2017;679:435–445. https://doi.org/10.1016/j.msea.2016.10.057

35. Chino Y, Dunand DC. Directionally freeze-cast titanium foam with aligned, elongated pores. *Acta Mater*. 2008;56(1):105–113. https://doi.org/10.1016/j.actamat.2007.09.002

36. Mah T-I, Keller KA, Kerans RJ, Cinibulk MK. Reduced Cracking in Oxide Fiber-Reinforced Oxide Composites via Freeze-Dry Processing. *J Am Ceram Soc*. 2015;(5):1437. https://doi.org/10.1111/jace.13500/abstract

37. Hu X, Yang L, Li L, Xie D, Du H. Freeze casting of composite system with stable fiber network and movable particles. *J Eur Ceram Soc*. 2016;36(16):4147–4153. https://doi.org/10.1016/j.jeurceramsoc.2016.05.049

38. Guo R, Shen P, Sun C, Wang Y, Shaga A, Jiang Q. Processing and mechanical properties of lamellar-structured Al–7Si–5Cu/TiC composites. *Mater Des*. 2016;106:446–453. https://doi.org/10.1016/j.matdes.2016.06.008

39. Shaga A, Shen P, Guo R-F, Jiang Q-C. Effects of oxide addition on the microstructure and mechanical properties of lamellar SiC scaffolds and Al–Si–Mg/SiC composites prepared by freeze casting and pressureless infiltration. *Ceram Int*. 2016;42(8):9653–9659. https://doi.org/10.1016/j.ceramint.2016.03.052

40. Hautcoeur D, Lorgouilloux Y, Leriche A, *et al.* Thermal conductivity of ceramic/metal composites from preforms produced by freeze casting. *Ceram Int*. 2016;42(12):14077–14085. https://doi.org/10.1016/j.ceramint.2016.06.016

41. Koh Y-H, Lee E-J, Yoon B-H, Song J-H, Kim H-E, Kim H-W. Effect of Polystyrene Addition on Freeze Casting of Ceramic/Camphene Slurry for Ultra-High Porosity Ceramics with Aligned Pore Channels. *J Am Ceram Soc*. 2006;89(12):3646–3653. https://doi.org/10.1111/j.1551-2916.2006.01311.x

42. Maxwell WA Francisco, AC, Gurnick, RS,. Preliminary investigation of the “freeze-casting” method for forming refractory powders. Washington, DC: National Advisory Committee for Aeronautics; 1954

43. Deville S. Ice-Templating and Freeze-Casting: Control of the Processes, Microstructures, and Architectures. In: Deville S, ed. *Freez. Colloids Obs. Princ. Control Use Appl. Mater. Sci. Life Sci. Earth Sci. Food Sci. Eng.* Cham: Springer International Publishing; 2017:351–438. https://doi.org/10.1007/978-3-319-50515-2_6

44. Deville S. Ice-templating, freeze casting: Beyond materials processing. *J Mater Res*. 2013;28(17):2202–2219. https://doi.org/10.1557/jmr.2013.105

45. Shao G, Hanaor DAH, Shen X, Gurlo A. Freeze Casting: From Low-Dimensional Building Blocks to Aligned Porous Structures—A Review of Novel Materials, Methods, and Applications. *Adv Mater*. 2020;32(17):1907176. https://doi.org/10.1002/adma.201907176

46. Fu Q, Rahaman MN, Dogan F, Bal BS. Freeze-cast hydroxyapatite scaffolds for bone tissue engineering applications. *Biomed Mater Bristol Engl*. 2008;3(2):025005. https://doi.org/10.1088/1748-6041/3/2/025005

47. Wegst UGK, Schecter M, Donius AE, Hunger PM. Biomaterials by freeze casting. *Philos Trans R Soc Lond Math Phys Eng Sci*. 2010;368(1917):2099–2121. https://doi.org/10.1098/rsta.2010.0014

48. Yang DY, Wei GH. Research the Performance of Alumina Insulation Material by Freeze-Drying. *Key Eng Mater*. 2012;512–515:527–530. https://doi.org/10.4028/www.scientific.net/KEM.512-515.527

49. Fukasawa T, Deng Z-Y, Ando M, Ohji T, Goto Y. Pore structure of porous ceramics synthesized from water-based slurry by freeze-dry process. *J Mater Sci*. 2001;36(10):2523–2527. https://doi.org/10.1023/A:1017946518955

50. Zheng J, Salamon D, Lefferts L, Wessling M, Winnubst L. Ceramic microfluidic monoliths by ice templating. *Microporous Mesoporous Mater*. 2010;134(1–3):216–219. https://doi.org/10.1016/j.micromeso.2010.05.012

51. Yook S-W, Jung H-D, Park C-H, *et al.* Reverse freeze casting: A new method for fabricating highly porous titanium scaffolds with aligned large pores. *Acta Biomater*. 2012;8(6):2401.

52. Moritz T, Richter H-J. Ceramic Bodies with Complex Geometries and Ceramic Shells by Freeze Casting Using Ice as Mold Material. *J Am Ceram Soc*. 2006;89(8):2394–2398. https://doi.org/10.1111/j.1551-2916.2006.01081.x

53. Scotti KL, Dunand DC. Freeze Casting: A Review of Processing, Microstructure and Properties via the Open Data Repository, FreezeCasting.net. *ArXiv171000037 Cond-Mat Physicsphysics*. 2017.

54. Occhionero MA, Novich BE, Sundback CA. Forming of complex high performance ceramic and metallic shapes. US5047181 A. 1991.

55. Deville S. Freezing Colloids: Observations, Principles, Control, and Use: Applications in Materials Science, Life Science, Earth Science, Food Science, and Engineering. Cham: Springer International Publishing; 2017 https://doi.org/10.1007/978-3-319-50515-2

56. Sofie SW, Dogan F. Freeze Casting of Aqueous Alumina Slurries with Glycerol. *J Am Ceram Soc*. 2001;84(7):1459–1464. https://doi.org/10.1111/j.1151-2916.2001.tb00860.x

57. Zhang Y, Hu L, Han J, Jiang Z. Freeze casting of aqueous alumina slurries with glycerol for porous ceramics. *Ceram Int*. 2010;36(2):617–621. https://doi.org/10.1016/j.ceramint.2009.09.036

58. Wildhack S, Aldinger F. Freeze Casting of Aluminium Nitride. *Adv Sci Technol*. 2006;45:407–412. https://doi.org/10.4028/www.scientific.net/AST.45.407

59. Liu R, Xu T, Wang C. A review of fabrication strategies and applications of porous ceramics prepared by freeze-casting method. *Ceram Int*. 2016;42(2, Part B):2907–2925. https://doi.org/10.1016/j.ceramint.2015.10.148

60. Nelson I, Naleway SE. Intrinsic and extrinsic control of freeze casting. *J Mater Res Technol*. 2019;8(2):2372–2385. https://doi.org/10.1016/j.jmrt.2018.11.011

61. Shanti NO, Araki K, Halloran JW. Particle Redistribution During Dendritic Solidification of Particle Suspensions. *J Am Ceram Soc*. 2006;89(8):2444–2447. https://doi.org/10.1111/j.1551-2916.2006.01094.x

62. Tang J, Chen YF, Wang H, Liu HL, Fan QS. Preparation of Oriented Porous Silicon Carbide Bodies by Freeze-Casting Process. *Key Eng Mater*. 2005;280–283:1287–1290. https://doi.org/10.4028/www.scientific.net/KEM.280-283.1287

63. Stolze C, Janoschka T, Schubert US, Müller FA, Flauder S. Directional Solidification with Constant Ice Front Velocity in the Ice-Templating Process. *Adv Eng Mater*. n.d.;18(1):111–120. https://doi.org/10.1002/adem.201500235

64. Wildhack S, Rixecker G, Aldinger F. Processing of Aqueous Aluminum Nitride Suspensions with High Solid Loading. *J Am Ceram Soc*. 2005;88(9):2391–2395. https://doi.org/10.1111/j.1551-2916.2005.00467.x

65. Araki K, Halloran JW. Room-Temperature Freeze Casting for Ceramics with Nonaqueous Sublimable Vehicles in the Naphthalene–Camphor Eutectic System. *J Am Ceram Soc*. 2004;87(11):2014–2019. https://doi.org/10.1111/j.1151-2916.2004.tb06353.x

66. Leo S, Tallon C, Franks GV. Aqueous and Nonaqueous Colloidal Processing of Difficult-to-Densify Ceramics: Suspension Rheology and Particle Packing. *J Am Ceram Soc*. 2014;n/a-n/a. https://doi.org/10.1111/jace.13220

67. Naviroj M, Miller SM, Colombo P, Faber KT. Directionally aligned macroporous SiOC via freeze casting of preceramic polymers. *J Eur Ceram Soc*. 2015;35(8):2225–2232. https://doi.org/10.1016/j.jeurceramsoc.2015.02.013

68. Araki K, Halloran JW. New Freeze-Casting Technique for Ceramics with Sublimable Vehicles. *J Am Ceram Soc*. 2004;87(10):1859–1863. https://doi.org/10.1111/j.1151-2916.2004.tb06331.x

69. Acree (Jr.) WE, Chickos JS. NIST Chemistry WebBook. Gaithersburg MD: National Institute of Standards and Technology; n.d.

70. DDBST GmbH. Vapor Pressure of Cyclohexane. *Dortm Data Bank DDB*. 2010.

71. Durkee JB. Cleaning with Solvents. 2nd ed. In: Kohli R, Mittal KL, eds. *Dev. Surf. Contam. Clean.*, 2nd ed. Oxford: William Andrew Publishing; 2008:479–577. https://doi.org/10.1016/B978-0-323-29960-2.00011-3

72. DDBST GmbH. Cyclooctane. *Dortm Data Bank DDB*. 2010.

73. Maryott AA, Smith ER. Table of Dielectric Constants of Pure Liquids. U.S. Government Printing Office; 1951

74. Dannhauser W, Cole RH. Dielectric Properties of Liquid Butyl Alcohols. *J Chem Phys*. 1955;23(10):1762–1766. https://doi.org/10.1063/1.1740576

75. Lemmon EW, Huber ML. Thermodynamic Properties of n-Dodecane. *Energy Fuels*. 2004;18(4):960–967. https://doi.org/10.1021/ef0341062

76. Sedrez PC, Sanchez CJN, da Silva MJ, Barbosa JR. Dielectric Constant of Mixtures of Carbon Dioxide and n-Dodecane Between 283 K and 343 K. *Int J Thermophys*. 2020;41(2):26. https://doi.org/10.1007/s10765-019-2597-y

77. Lacerda LD, Souza DF, Nunes EHM, Houmard M. Macroporous alumina structures tailored by freeze-casting using naphthalene–camphor as freezing vehicle. *Ceram Int*. 2018;44(13):16010–16016. https://doi.org/10.1016/j.ceramint.2018.06.036

78. Miller SM, Xiao X, Faber KT. Freeze-cast alumina pore networks: Effects of freezing conditions and dispersion medium. *J Eur Ceram Soc*. 2015;35(13):3595–3605. https://doi.org/10.1016/j.jeurceramsoc.2015.05.012

79. Lasalle A, Guizard C, Leloup J, *et al.* Ice-Templating of Alumina Suspensions: Effect of Supercooling and Crystal Growth During the Initial Freezing Regime. *J Am Ceram Soc*. 2012;95(2):799–804. https://doi.org/10.1111/j.1551-2916.2011.04993.x

80. Peelen JGJ. Alumina: sintering and optical properties. Department of Chemical Engineering and Chemistry, Technische Hogeschool Eindhoven; Eindhoven; 1977

81. Sumitomo Chemical. Product Databook: High Purity Alumina. 2016.

82. Franks GV, Johnson SB, Dunstan DE. Methods of forming shaped articles from suspensions. EP1328386 B1. 2009.

83. Tanurdjaja S, Tallon C, Scales PJ, Franks GV. Influence of dispersant size on rheology of non-aqueous ceramic particle suspensions. *Adv Powder Technol*. 2011;22(4):476–481. https://doi.org/10.1016/j.apt.2011.04.011

84. Franks GV, Tallon C, Studart AR, Sesso ML, Leo S. Colloidal Processing: Enabling Complex Shaped Ceramics with Unique Multiscale Structures. *J Am Ceram Soc*. 2017;n/a-n/a. https://doi.org/10.1111/jace.14705

85. Lucite International. Elvacite 2045. 2014.

86. Deville S, Meille S, Seuba J. A meta-analysis of the mechanical properties of ice-templated ceramics and metals. *ArXiv150503333 Cond-Mat*. 2015.

87. Deville S. Freeze-Casting of Porous Ceramics: A Review of Current Achievements and Issues. *Adv Eng Mater*. 2008;10(3):155–169. https://doi.org/10.1002/adem.200700270

88. Desmond KW, Weeks ER. Influence of particle size distribution on random close packing of spheres. *Phys Rev E*. 2014;90(2):022204. https://doi.org/10.1103/PhysRevE.90.022204

89. Song C, Wang P, Makse HA. A phase diagram for jammed matter. *Nature*. 2008;453(7195):629–632. https://doi.org/10.1038/nature06981

90. Donev A, Cisse I, Sachs D, *et al.* Improving the Density of Jammed Disordered Packings Using Ellipsoids. *Science*. 2004;303(5660):990–993. https://doi.org/10.1126/science.1093010

91. Ferreira JMF, Diz HMM. Effect of Solids Loading on Slip-Casting Performance of Silicon Carbide Slurries. *J Am Ceram Soc*. 1999;82(8):1993–2000. https://doi.org/10.1111/j.1151-2916.1999.tb02031.x

92. Tarì G, Ferreira JMF, Fonseca AT. Influence of particle size and particle size distribution on drying-shrinkage behaviour of alumina slip cast bodies. *Ceram Int*. 1999;25(6):577–580. https://doi.org/10.1016/S0272-8842(98)00068-6

93. Teng WD, Edirisinghe MJ, Evans JRG. Optimization of Dispersion and Viscosity of a Ceramic Jet Printing Ink. *J Am Ceram Soc*. 1997;80(2):486–494. https://doi.org/10.1111/j.1151-2916.1997.tb02855.x

94. Singh BP, Jena J, Besra L, Bhattacharjee S. Selection and Optimization of Dispersant in Ceramic Slurry Processing by Different Techniques: Comparison, Correlation, and Standardization. *J Dispers Sci Technol*. 2007;28(7):1044–1052. https://doi.org/10.1080/01932690701523960

95. Lee BI, Rives JP. Dispersion of alumina powders in nonaqueous media. *Colloids Surf*. 1991;56:25–43. https://doi.org/10.1016/0166-6622(91)80112-2

96. Lee BI, Paik U. Dispersion of alumina and silica powders in non-aqueous media: Mixed-solvent effects. *Ceram Int*. 1993;19(4):241–250. https://doi.org/10.1016/0272-8842(93)90056-W

97. Setz LFG, Koshimizu L, de Mello-Castanho SRH, Morelli MR. Rheological Analysis of Ceramics Suspensions with High Solids Loading. *Mater Sci Forum*. 2012;727–728:646–651. https://doi.org/10.4028/www.scientific.net/MSF.727-728.646

98. Mueller S, Llewellin EW, Mader HM. The rheology of suspensions of solid particles. *Proc R Soc Lond Math Phys Eng Sci*. 2010;466(2116):1201–1228. https://doi.org/10.1098/rspa.2009.0445

99. Jeffrey DJ, Acrivos A. The rheological properties of suspensions of rigid particles. *AIChE J*. 1976;22(3):417–432. https://doi.org/10.1002/aic.690220303

100. Sushumna I, Gupta R k., Ruckenstein E. Effective dispersants for concentrated, nonaqueous suspensions. *J Mater Res*. 1992;7(10):2884–2893. https://doi.org/10.1557/JMR.1992.2884

101. Aminabhavi TM, Patil VB, Aralaguppi MI, Phayde HTS. Density, Viscosity, and Refractive Index of the Binary Mixtures of Cyclohexane with Hexane, Heptane, Octane, Nonane, and Decane at (298.15, 303.15, and 308.15) K. *J Chem Eng Data*. 1996;41(3):521–525. https://doi.org/10.1021/je950279c

102. Cruickshank AJB, Cutler AJB. Vapor pressure of cyclohexane, 25 to 75.degree. *J Chem Eng Data*. 1967;12(3):326–329. https://doi.org/10.1021/je60034a010

103. IHS Markit. Cyclohexane. *Chem Econ Handb CEH*. 2017.

104. National Library of Medicine, HSDB Database. Cyclohexane. *Toxicol Data Netw*. 2015.

105. Bingham E, Cohrssen B. Alicyclic Hydrocarbons. 6th ed. *Pattys Toxicol.*, 6th ed. Vol. 5. John Wiley & Sons, Inc; 2012:103.

106. Croda International Plc. Hypermer A70. 2018.

107. Stojanović BD, Skorokhod VV, Nikolić MV. Advanced Science and Technology of Sintering. Boston, MA: Springer US; 1999

108. Tang Y, Miao Q, Qiu S, Zhao K, Hu L. Novel freeze-casting fabrication of aligned lamellar porous alumina with a centrosymmetric structure. *J Eur Ceram Soc*. 2014;34(15):4077–4082. https://doi.org/10.1016/j.jeurceramsoc.2014.05.040

109. Tanurdjaja S. A new paradigm in near-net-shape advanced ceramic components processing: development of the novel processing technique. 2011.

110. Mohanty S, Das B, Dhara S. Poly(maleic acid) – A novel dispersant for aqueous alumina slurry. *J Asian Ceram Soc*. 2013;1(2):184–190. https://doi.org/10.1016/j.jascer.2013.05.005

111. Hong C, Du J, Liang J, Zhang X, Han J. Functionally graded porous ceramics with dense surface layer produced by freeze-casting. *Ceram Int*. 2011;37(8):3717–3722. https://doi.org/10.1016/j.ceramint.2011.04.119

112. Wildhack S, Aldinger F. Freeze Casting of Aluminium Nitride. *Adv Sci Technol*. 2006;45:407–412. https://doi.org/10.4028/www.scientific.net/AST.45.407

113. Peppin SSL, Elliott J a. W, Worster MG. Solidification of colloidal suspensions. *J Fluid Mech*. 2006;554:147–166. https://doi.org/10.1017/S0022112006009268

114. Deville S, Maire E, Bernard-Granger G, *et al.* Metastable and unstable cellular solidification of colloidal suspensions. *Nat Mater*. 2009;8(12):966–972. https://doi.org/10.1038/nmat2571

115. Porter Michael M., Niksiar Pooya, McKittrick Joanna, Franks G. Microstructural Control of Colloidal-Based Ceramics by Directional Solidification Under Weak Magnetic Fields. *J Am Ceram Soc*. 2016;99(6):1917–1926. https://doi.org/10.1111/jace.14183

116. Goehring L, Clegg WJ, Routh AF. Solidification and Ordering during Directional Drying of a Colloidal Dispersion. *Langmuir*. 2010;26(12):9269–9275. https://doi.org/10.1021/la100125v

117. Hu Z-J, Shen X-T, Geng S-L, Shen P, Jiang Q-C. 3D long-range ordered porous ceramics prepared by a novel bidirectional freeze-casting technique. *Ceram Int*. 2018;44(5):5803–5806. https://doi.org/10.1016/j.ceramint.2017.12.130

118. Bai H, Chen Y, Delattre B, Tomsia AP, Ritchie RO. Bioinspired large-scale aligned porous materials assembled with dual temperature gradients. *Sci Adv*. 2015;1(11). https://doi.org/10.1126/sciadv.1500849

119. Hu L, Wang C-A, Huang Y, Sun C, Lu S, Hu Z. Control of pore channel size during freeze casting of porous YSZ ceramics with unidirectionally aligned channels using different freezing temperatures. *J Eur Ceram Soc*. 2010;30(16):3389–3396. https://doi.org/10.1016/j.jeurceramsoc.2010.07.032

120. Lu K. Microstructural Evolution of Nanoparticle Aqueous Colloidal Suspensions During Freeze Casting. *J Am Ceram Soc*. 2007;90(12):3753–3758. https://doi.org/10.1111/j.1551-2916.2007.02000.x

121. Bluhm J, Ricken T, Bloßfeld M. Ice Formation in Porous Media. *Adv. Ext. Multifield Theor. Contin.* Springer, Berlin, Heidelberg; 2011:153–174. https://doi.org/10.1007/978-3-642-22738-7_8

122. Schollick JMH, Style RW, Curran A, *et al.* Segregated Ice Growth in a Suspension of Colloidal Particles. *J Phys Chem B*. 2016;120(16):3941–3949. https://doi.org/10.1021/acs.jpcb.6b00742

123. Waschkies T, Oberacker R, Hoffmann MJ. Investigation of structure formation during freeze-casting from very slow to very fast solidification velocities. *Acta Mater*. 2011;59(13):5135–5145. https://doi.org/10.1016/j.actamat.2011.04.046

124. Anderson AM, Worster MG. Periodic Ice Banding in Freezing Colloidal Dispersions. *Langmuir*. 2012;28(48):16512–16523. https://doi.org/10.1021/la303458m

125. Anderson AM, Grae Worster M. Freezing colloidal suspensions: periodic ice lenses and compaction. *J Fluid Mech*. 2014;758:786–808. https://doi.org/10.1017/jfm.2014.500

126. Naglieri V, Bale HA, Gludovatz B, Tomsia AP, Ritchie RO. On the development of ice-templated silicon carbide scaffolds for nature-inspired structural materials. *Acta Mater*. 2013;61(18):6948–6957. https://doi.org/10.1016/j.actamat.2013.08.006

127. Peppin SSL, Worster MG, Wettlaufer JS. Morphological instability in freezing colloidal suspensions. *Proc R Soc Lond Math Phys Eng Sci*. 2007;463(2079):723–733. https://doi.org/10.1098/rspa.2006.1790

128. Peppin SSL, Wettlaufer JS, Worster MG. Experimental Verification of Morphological Instability in Freezing Aqueous Colloidal Suspensions. *Phys Rev Lett*. 2008;100(23):238301. https://doi.org/10.1103/PhysRevLett.100.238301

129. Naviroj M, Wang MM, Johnson MT, Faber KT. Nucleation-controlled freeze casting of preceramic polymers for uniaxial pores in Si-based ceramics. *Scr Mater*. 2017;130:32–36.

130. Konstantinov VA, Revyakin VP, Sagan VV, Pursky OI, Sysoev VM. Thermal conductivity of solid cyclohexane in orientationally ordered and disordered phases. *J Exp Theor Phys*. 2011;112(2):220–225. https://doi.org/10.1134/S1063776111010092

131. Wisotzki KD, Würflinger A. PVT data for liquid and solid cyclohexane, cyclohexanone and cyclopentanol up to 3000 bar. *J Phys Chem Solids*. 1982;43(1):13–20. https://doi.org/10.1016/0022-3697(82)90167-6

132. Coussy O. Poromechanics of freezing materials. *J Mech Phys Solids*. 2005;53(8):1689–1718. https://doi.org/10.1016/j.jmps.2005.04.001

133. Fen-Chong T, Fabbri A, Thiery M, Dangla P. Poroelastic Analysis of Partial Freezing in Cohesive Porous Materials. *J Appl Mech*. 2013;80(2):020910-020910–8. https://doi.org/10.1115/1.4007908

134. MacKenzie AP. Factors Affecting The Mechanism Of Transformation Of Ice Into Water Vapor In The Freeze-Drying Process. *Ann N Y Acad Sci*. 1965;125(1):522–547.

135. Choi W, Jun S. Measurement of structural shrinkages of freeze dried chipping potatoes for crack modeling. *Food Sci Biotechnol*. 2013;22(4):967–972. https://doi.org/10.1007/s10068-013-0171-0

136. Turpin C. The Micro-Taphonomy of Cold: Differential Microcracking in Response to Experimental Cold-Stresses. *J Forensic Sci*. 2017;62(5):1134–1139. https://doi.org/10.1111/1556-4029.13406

137. Tian G, Lu Z, Miao K, Ji Z, Zhang H, Li D. Formation Mechanism of Cracks During the Freeze Drying of Gelcast Ceramic Parts. *J Am Ceram Soc*. 2015;98(10):3338–3345. https://doi.org/10.1111/jace.13761

138. Ullrich S, Seyferth S, Lee G. Measurement of Shrinkage and Cracking in Lyophilized Amorphous Cakes. Part I: Final-Product Assessment. *J Pharm Sci*. 2015;104(1):155–164. https://doi.org/10.1002/jps.24284

139. Ullrich S, Seyferth S, Lee G. Measurement of Shrinkage and Cracking in Lyophilized Amorphous Cakes. Part II: Kinetics. *Pharm Res*. 2015;32(8):2503–2515. https://doi.org/10.1007/s11095-015-1639-9

140. Ullrich S, Seyferth S, Lee G. Measurement of Shrinkage and Cracking in Lyophilized Amorphous Cakes Part 3: Hydrophobic Vials and the Question of Adhesion. *J Pharm Sci*. 2015;104(6):2040–2046. https://doi.org/10.1002/jps.24441

141. Ullrich S, Seyferth S, Lee G. Measurement of shrinkage and cracking in lyophilized amorphous cakes. Part IV: Effects of freezing protocol. *Int J Pharm*. 2015;495(1):52–57. https://doi.org/10.1016/j.ijpharm.2015.08.091

142. Réthoré J, Limodin N, Buffière J-Y, Roux S, Hild F. Three-dimensional Analysis of Fatigue Crack Propagation using X-Ray Tomography, Digital Volume Correlation and Extended Finite Element Simulations. *Procedia IUTAM*. 2012;4:151–158. https://doi.org/10.1016/j.piutam.2012.05.017

143. Zhao Y, Takhar PS. Micro X-ray computed tomography and image analysis of frozen potatoes subjected to freeze-thaw cycles. *LWT - Food Sci Technol*. 2017;79:278–286. https://doi.org/10.1016/j.lwt.2017.01.051

144. Deville S, Adrien J, Maire E, Scheel M, Di Michiel M. Time-lapse, three-dimensional in situ imaging of ice crystal growth in a colloidal silica suspension. *Acta Mater*. 2013;61(6):2077–2086. https://doi.org/10.1016/j.actamat.2012.12.027

145. Bareggi A, Maire E, Lasalle A, Deville S. Dynamics of the Freezing Front During the Solidification of a Colloidal Alumina Aqueous Suspension: In Situ X-Ray Radiography, Tomography, and Modeling. *J Am Ceram Soc*. 2011;94(10):3570–3578. https://doi.org/10.1111/j.1551-2916.2011.04572.x

146. Deville S, Maire E, Lasalle A, *et al.* Influence of Particle Size on Ice Nucleation and Growth During the Ice-Templating Process. *J Am Ceram Soc*. 2010;93(9):2507–2510. https://doi.org/10.1111/j.1551-2916.2010.03840.x

147. Deville S, Maire E, Lasalle A, *et al.* In Situ X-Ray Radiography and Tomography Observations of the Solidification of Aqueous Alumina Particle Suspensions—Part I: Initial Instants. *J Am Ceram Soc*. 2009;92(11):2489–2496. https://doi.org/10.1111/j.1551-2916.2009.03163.x

148. Deville S, Maire E, Lasalle A, *et al.* In Situ X-Ray Radiography and Tomography Observations of the Solidification of Aqueous Alumina Particles Suspensions. Part II: Steady State. *J Am Ceram Soc*. 2009;92(11):2497–2503. https://doi.org/10.1111/j.1551-2916.2009.03264.x

149. Debyn UK. CT Coolstage -20°C to +160°C for µXCT applications. *Deben UK – SEM Accessories Tensile Test*. 2019.

150. Kampschulte M, Erdmann G, Sender J, *et al.* The development and validation of micro-CT of large deep frozen specimens. *Scanning*. 2015;37(1):63–72. https://doi.org/10.1002/sca.21180

151. Stokes RH, Tomlins RP. Thermodynamic functions of melting for cyclohexane. *J Chem Thermodyn*. 1974;6(4):379–386. https://doi.org/10.1016/0021-9614(74)90168-2

152. Fanelli AJ, Silvers RD, Frei WS, Burlew JV, Marsh GB. New Aqueous Injection Molding Process for Ceramic Powders. *J Am Ceram Soc*. 1989;72(10):1833–1836. https://doi.org/10.1111/j.1151-2916.1989.tb05987.x

153. Nieto MI, Santacruz I, Moreno R. Shaping of Dense Advanced Ceramics and Coatings by Gelation of Polysaccharides. *Adv Eng Mater*. 2014;16(6):637–654. https://doi.org/10.1002/adem.201400076

154. Jiang D, Zhang J. Properties of Carbide Ceramics from Gelcasting and Pressure-less Sintering. *IOP Conf Ser Mater Sci Eng*. 2011;18(20):202001. https://doi.org/10.1088/1757-899X/18/20/202001

155. Henneck S, Lindner F, Kelnberger A, Nguyen H. Method for producing ceramic green compacts for ceramic components. United States US7713896B2. 2010.

156. Zuo KH, Zeng Y, Jiang D. Effect of cooling rate and polyvinyl alcohol on the morphology of porous hydroxyapatite ceramics. *Mater Des*. 2010;31(6):3090–3094. https://doi.org/10.1016/j.matdes.2009.12.044

157. Zuo KH, Zeng Y-P, Jiang D. Properties of Microstructure-Controllable Porous Yttria-Stabilized Ziroconia Ceramics Fabricated by Freeze Casting. *Int J Appl Ceram Technol*. 2008;5(2):198–203. https://doi.org/10.1111/j.1744-7402.2008.02190.x

158. Coimbra D, Greenwood R, Kendall K. Video-controlled tensile testing of alumina fibres and rods manufactured by colloidal processing. *J Mater Sci*. 2000;35(13):3347–3357. https://doi.org/10.1023/A:1004876801070

159. Su B, Button TW. A comparative study of viscous polymer processed ceramics based on aqueous and non-aqueous binder systems. *J Mater Process Technol*. 2009;209(1):153–157. https://doi.org/10.1016/j.jmatprotec.2008.01.046

160. Pollinger JP, Messing GL. Thermal Analysis of Organic Binders for Ceramic Processing. In: Snyder RL, Condrate RA, Johnson PF, eds. *Adv. Mater. Charact. II*. Boston, MA: Springer US; 1985:359–370. https://doi.org/10.1007/978-1-4615-9439-0_28

161. Dow Inc. Paraloid^{TM} B-44 100% Resin. *Dow Chem*. 2020.

162. Brandrup J, Immergut EH, Grulke EA, Abe A, Bloch DR. Polymer handbook. 4th ed. Wiley New York; 1999

163. Lucite International. Specialty Polymers and Resins: Coatings, Inks & Adhesives. 2020.

164. Hondros G. The evaluation of Poisson's ratio and the modulus of materials of low tensile resistance by the Brazilian (Indirect tensile) test with particular reference to concrete. *Aust J Appl Sci*. 1959;10(3):243–268.

165. Procopio A, Zavaliangos A, Cunningham J. Analysis of the Diametral Compression Test and the Applicability to Plastically Deforming Materials. *J Mater Sci*. 2003;38:3629–3639. https://doi.org/10.1023/A:1025681432260

166. Shang C, Sinka IC, Pan J. Modelling of the break force of tablets under diametrical compression. *Int J Pharm*. 2013;445(1–2):99–107. https://doi.org/10.1016/j.ijpharm.2013.01.032

167. Kaklis K, Agioutantis Z, Sarris E, Pateli A. A theoretical and numerical study of discs with flat edges under diametral compression (flat Brazilian test). 2005

168. Nagata K. Effect of functionalities of binders on rheological behavior of alumina suspensions and properties of green sheets. *J Ceram Soc Jpn*. 1993;101(1176):845–849.

169. Harrison G, Franks GV, Tirtaatmadja V, Boger DV. Suspensions and polymers - Common links in rheology. *Korea-Aust Rheol J*. 1999;11(3):197–218.

170. Dong S, Zhu W, Gao X, *et al.* Preparation of tubular hierarchically porous silicate cement compacts via a tert-butyl alcohol (TBA)-based freeze casting method. *Chem Eng J*. 2016;295:530–541. https://doi.org/10.1016/j.cej.2016.03.023

171. Tang Y, Qiu S, Wu C, Miao Q, Zhao K. Freeze cast fabrication of porous ceramics using tert-butyl alcohol–water crystals as template. *J Eur Ceram Soc*. 2016;36(6):1513–1518. https://doi.org/10.1016/j.jeurceramsoc.2015.12.047

172. Souza DF, Nunes EHM, Pimenta DS, *et al.* Synthesis and structural evaluation of freeze-cast porous alumina. *Mater Charact*. 2014;96:183–195. https://doi.org/10.1016/j.matchar.2014.08.009

173. Halloran J. Making Better Ceramic Composites with Ice. *Science*. 2006;311(5760):479–480. https://doi.org/10.2307/3843399

174. Naviroj M, Voorhees PW, Faber KT. Suspension- and solution-based freeze casting for porous ceramics. *J Mater Res*. 2017;1–11. https://doi.org/10.1557/jmr.2017.133

175. Ewing MB, Levien BJ, Marsh KN, Stokes RH. Excess enthalpies, excess volumes, and excess gibbs free energies for mixtures of cyclo-octane+cyclopentane at 288.15, 298.15, and 308.15 K. *J Chem Thermodyn*. 1970;2(5):689–695. https://doi.org/10.1016/0021-9614(70)90044-3

176. Domínguez I, Calvar N, Gómez E, Domínguez Á. Liquid–Liquid Extraction of Aromatic Compounds from Cycloalkanes Using 1-Butyl-3-methylimidazolium Methylsulfate Ionic Liquid. *J Chem Eng Data*. 2013;58(2):189–196. https://doi.org/10.1021/je300826t

177. Kiefte H, Askarpour V, Zuk J, Clouter MJ. Comparative Brillouin scattering study of .gamma.-oxygen and cyclooctane I: rotation-translation coupling effects. *J Phys Chem*. 1992;96(3):1449–1455. https://doi.org/10.1021/j100182a077

178. Rubinstein ER, Glicksman ME. Dendritic growth kinetics and structure II. Camphene. *J Cryst Growth*. 1991;112(1):97–110. https://doi.org/10.1016/0022-0248(91)90915-R

179. Bethell D, Cockerill AF. Mechanistic studies in strongly basic media. Part II. Indicator equilibria in t-butyl alcohol. *J Chem Soc B Phys Org*. 1966;(0):913–916. https://doi.org/10.1039/J29660000913

180. Straka M, van Genderen A, Růžička K, Růžička V. Heat Capacities in the Solid and in the Liquid Phase of Isomeric Pentanols. *J Chem Eng Data*. 2007;52(3):794–802. https://doi.org/10.1021/je060411g

181. Jancso G, Illy H, Staschewski D. Oxygen-18 and deuterium isotope effect on the freezing-point of dilute water + dioxan solutions. *J Chem Soc Faraday Trans 1 Phys Chem Condens Phases*. 1976;72(0):2203–2210. https://doi.org/10.1039/F19767202203

182. Gao Y, Liu J, Li Z, *et al.* Dichloroimidazolidinedione-Activated Beckmann Rearrangement of Ketoximes for Accessing Amides and Lactams. *J Org Chem*. 2018;83(4):2040–2049. https://doi.org/10.1021/acs.joc.7b02983

183. Chen K, Liu C, Deng L, Xu G. A practical Δ1-dehydrogenation of Δ4-3-keto-steroids with DDQ in the presence of TBDMSCl at room temperature. *Steroids*. 2010;75(7):513–516. https://doi.org/10.1016/j.steroids.2010.03.002

11 Appendices

11.1 Online Materials files

Digital files from this thesis will be made available online at:

https://samuelpinches.com.au/thesis

11.2 Freezing Rate Microstructure: Sample Images obtained via Digital Camera

The following images were obtained of the cut bisque-fired and fully fired alumina samples using a digital camera. More information on this image set is provided in the main text, in the results section.

Freezer T (°C)	Mould T (°C)	Sintering	Sample	Overview Image
-20°C	Ambient Mould	Bisque Fired	147	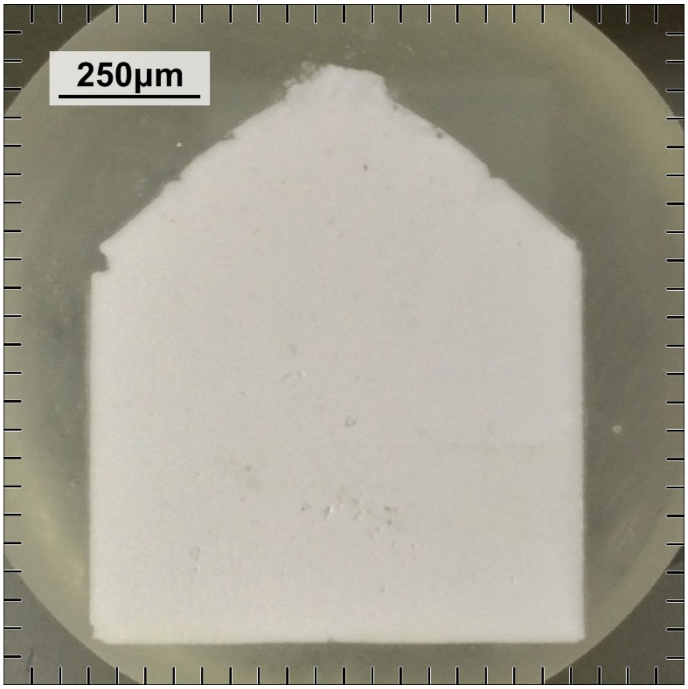
		Fully Sintered	148	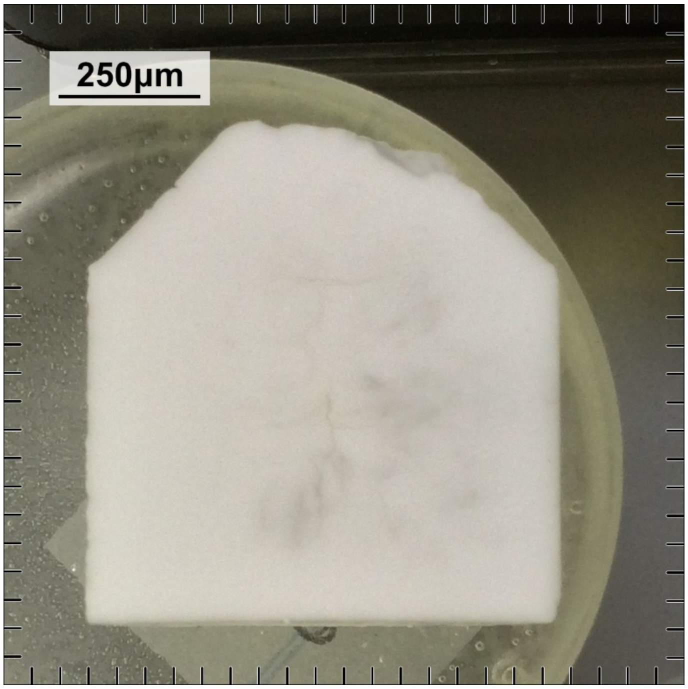

Freezer T (°C)	**Mould T (°C)**	**Sintering**	**Sample**	**Overview Image**
-20°C	Pre-Chilled Mould	Bisque Fired	162	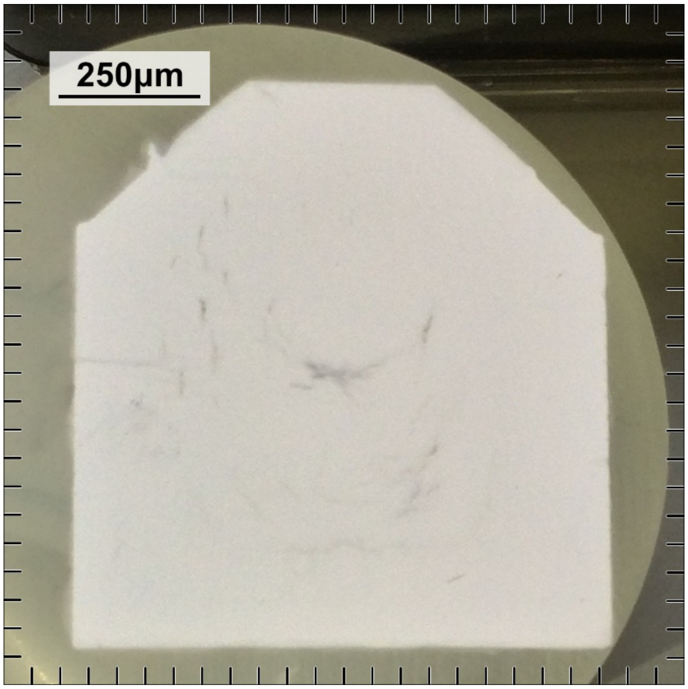
		Fully Sintered	163	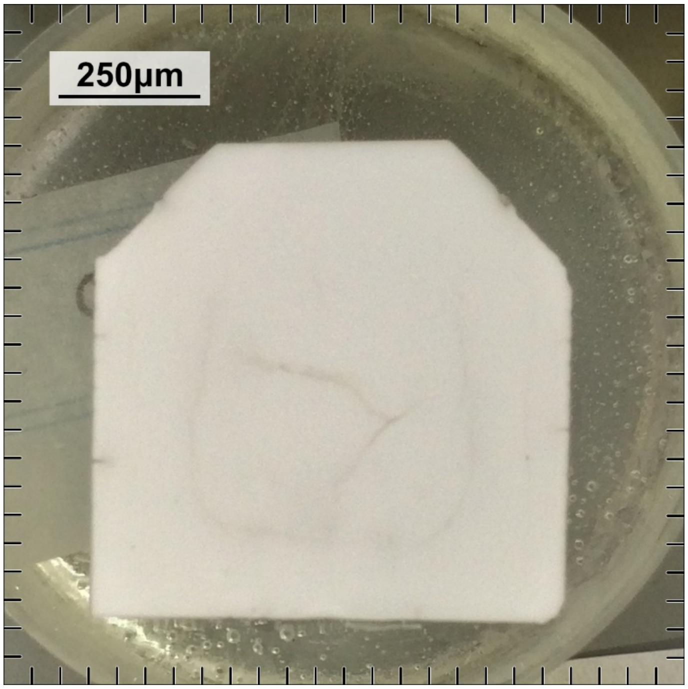

Freezer T (°C)	Mould T (°C)	Sintering	Sample	Overview Image
-40°C	Ambient Mould	Bisque Fired	141	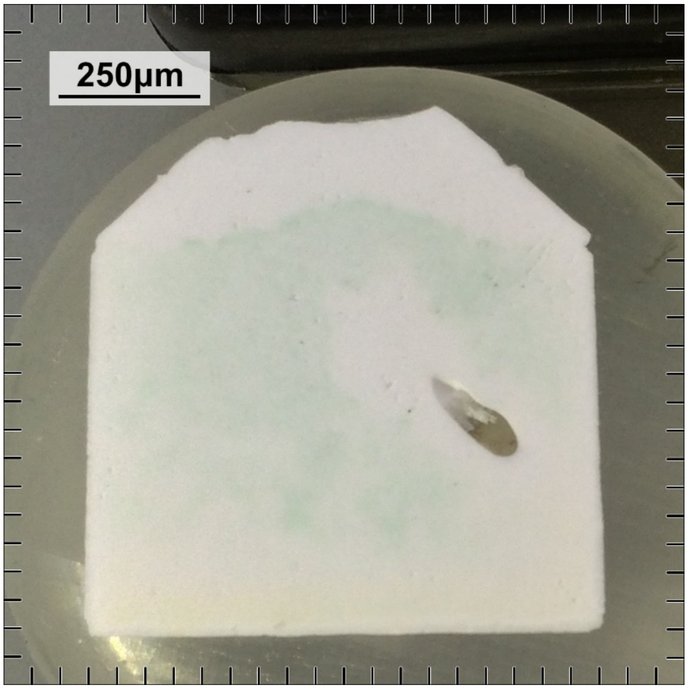
		Fully Sintered	142	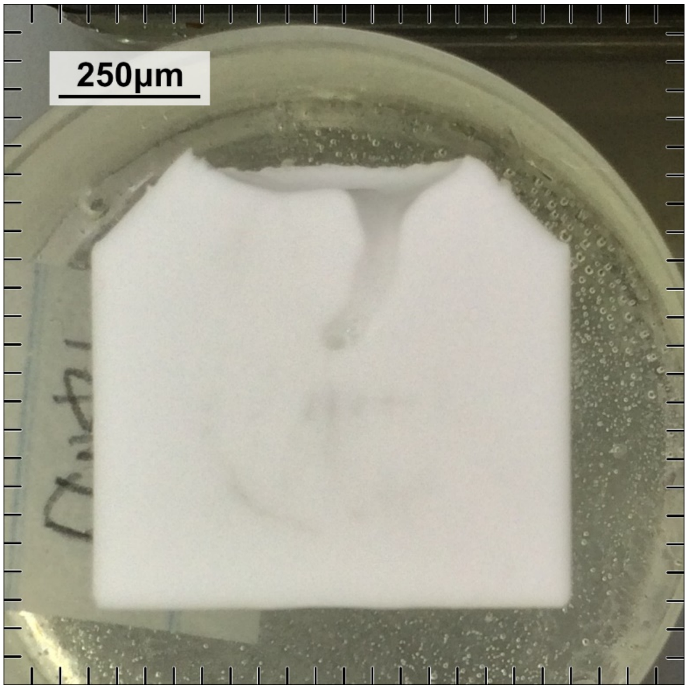

Freezer T (°C)	**Mould T (°C)**	**Sintering**	**Sample**	**Overview Image**
-40°C	Pre-Chilled Mould	Bisque Fired	153	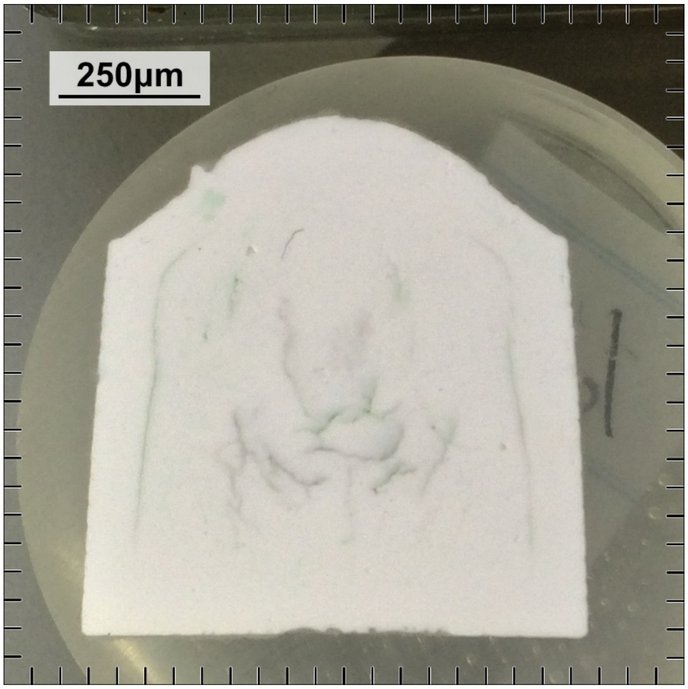
		Fully Sintered	155	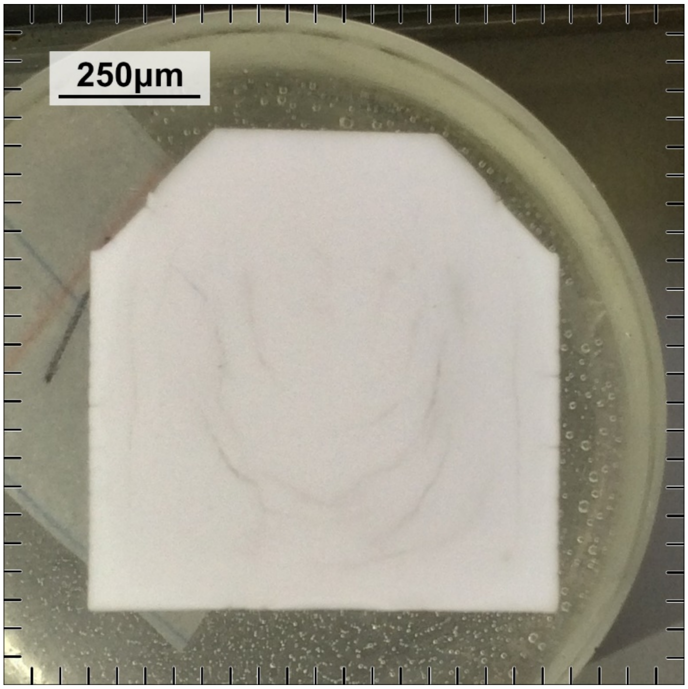

Freezer T (°C)	**Mould T (°C)**	**Sintering**	**Sample**	**Overview Image**
-80°C	Ambient Mould	Bisque Fired	134	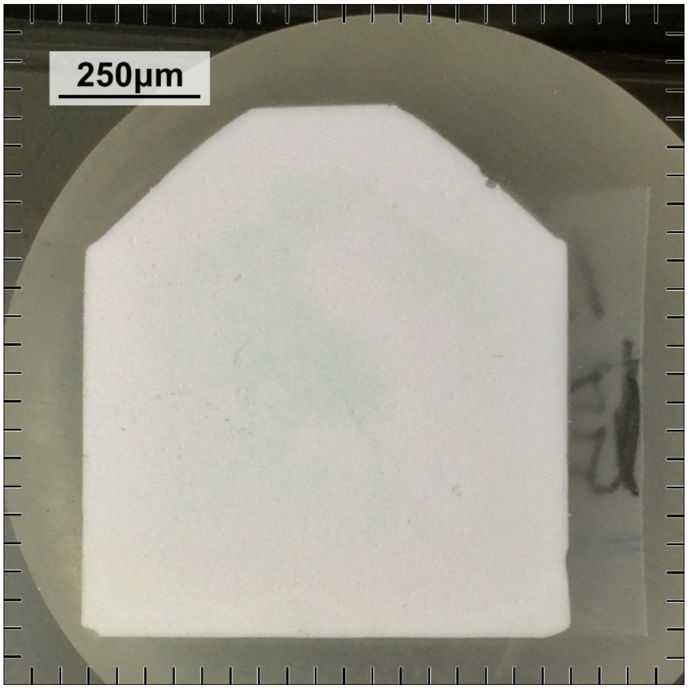
		Fully Sintered	135	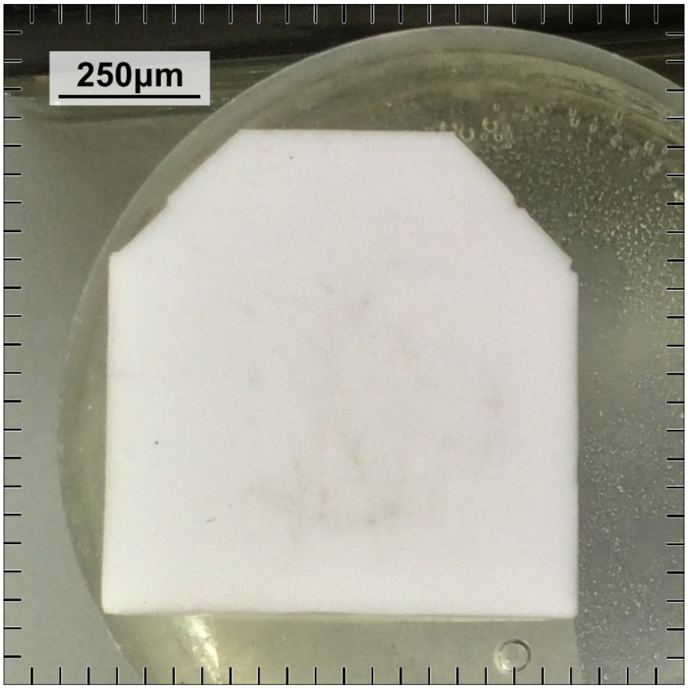

Freezer T (°C)	Mould T (°C)	Sintering	Sample	Overview Image
-80°C	Pre-Chilled Mould	Bisque Fired	167	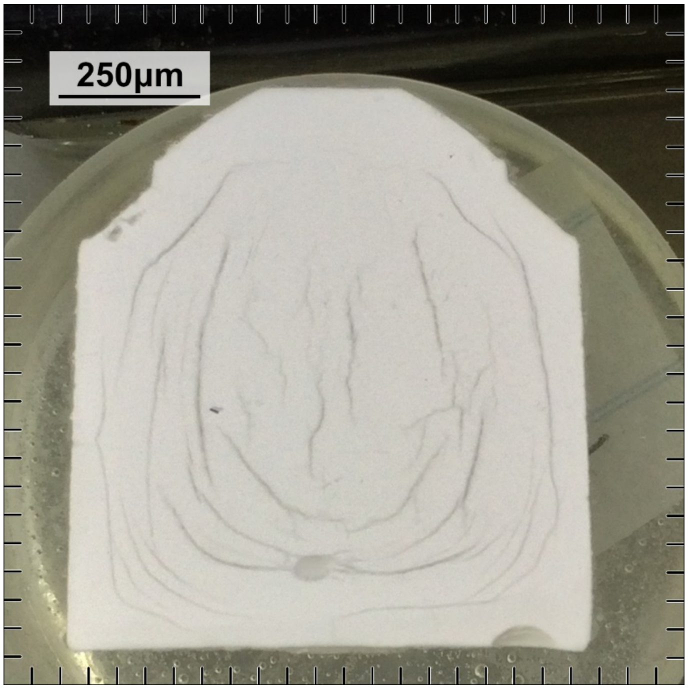
		Fully Sintered	168	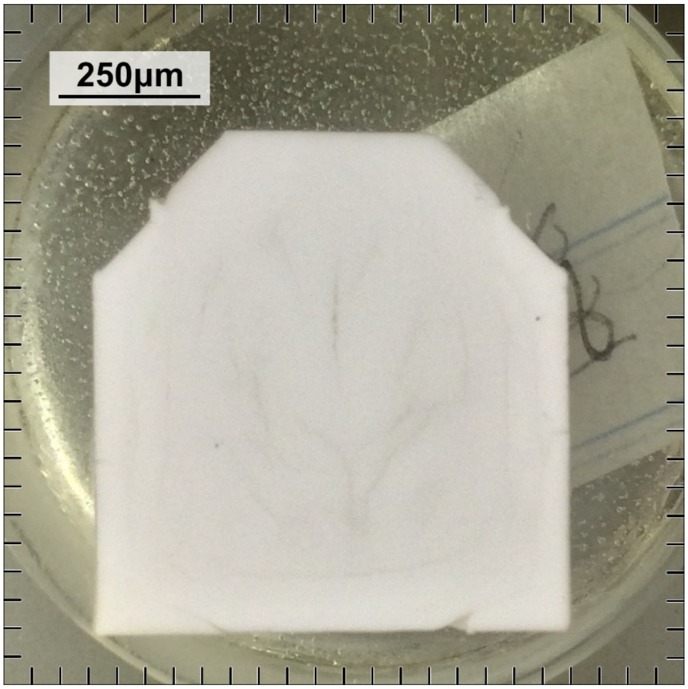

11.2.1 Freezing Rate Microstructure: Sample Images obtained via Microscope

The following images were obtained through a top-illuminated microscope equipped with a digital eyepiece. More details on this image set is provided in the main text within the results section.

Sample #'s	147 & 148	Bisque Sample Image 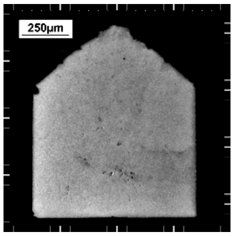	Sintered Sample Image 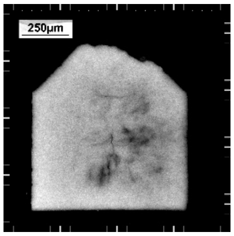
Freezer Temperature	-20°C	Mould Temperature	Ambient Mould
Bisque		Sintered	
Centre (5x)			
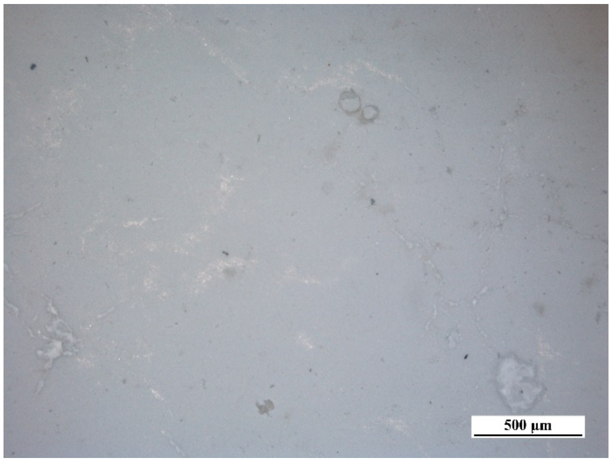		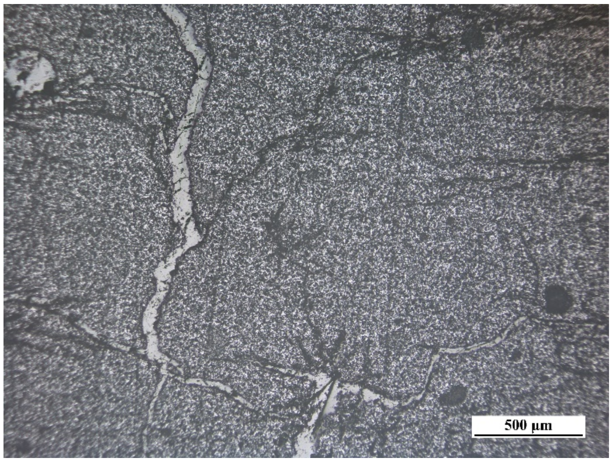	
Centre (20x)			

<table>
<tr><td>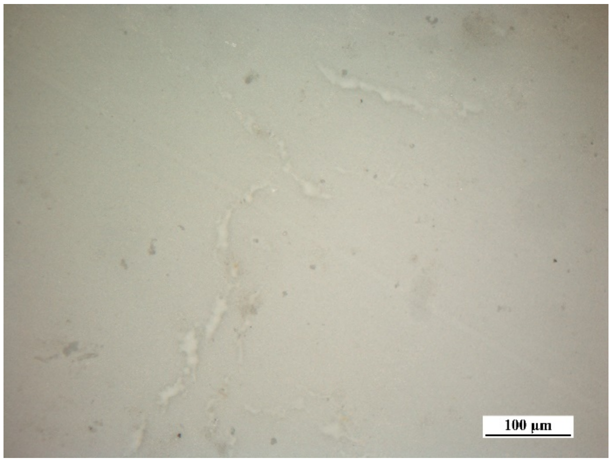 </td><td>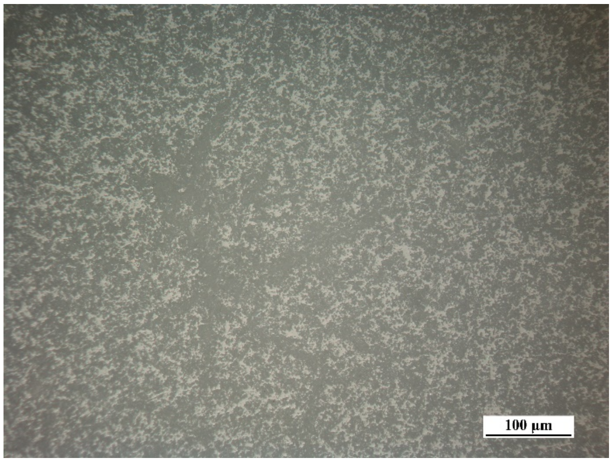 </td></tr>
<tr><td colspan="2">Edge (5x)</td></tr>
<tr><td>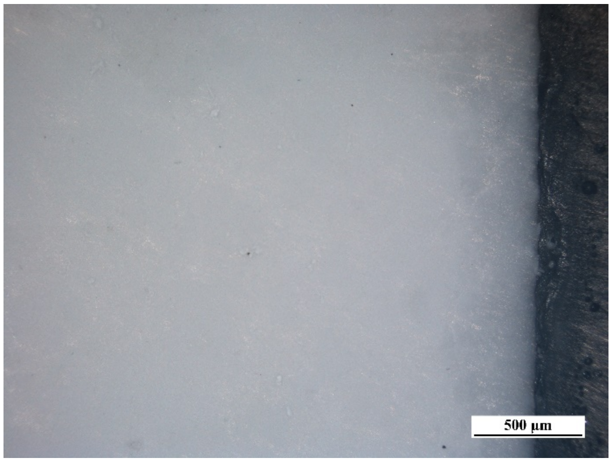 </td><td>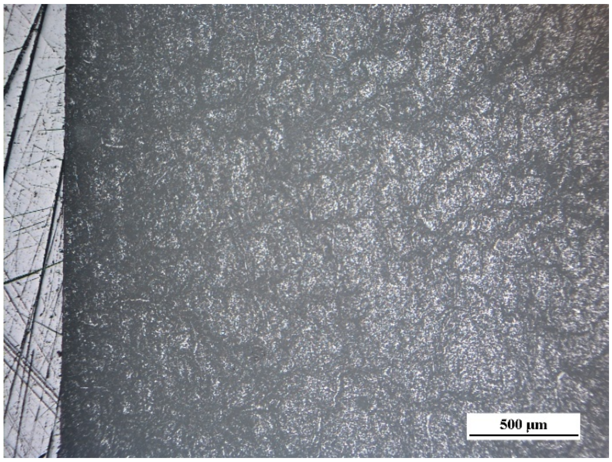 </td></tr>
<tr><td colspan="2">Edge (20x)</td></tr>
<tr><td>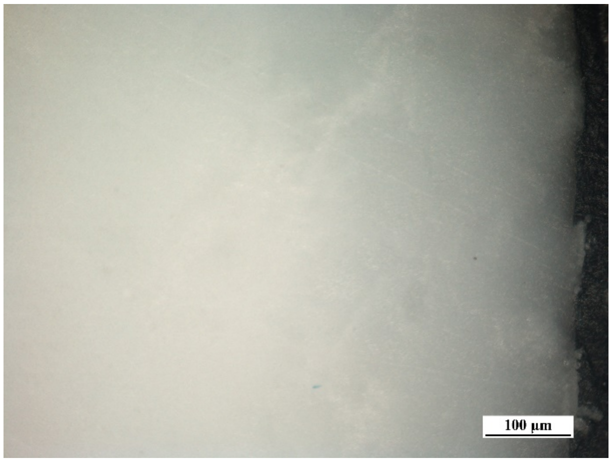 </td><td>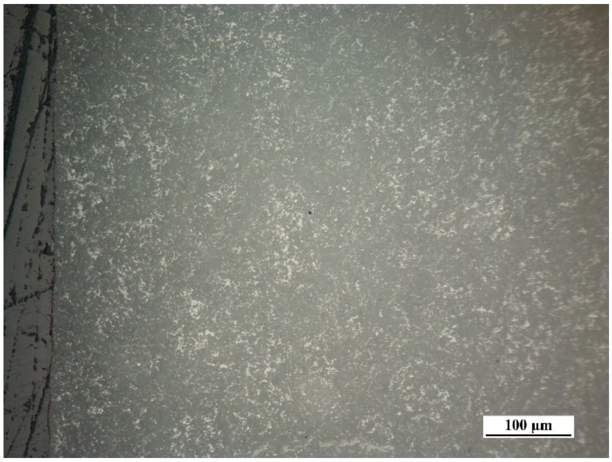 </td></tr>
</table>

<table>
<tr><td rowspan="2">Sample #’s</td><td rowspan="2">162 & 163</td><td>Bisque Sample Image</td><td>Sintered Sample Image</td></tr>
<tr><td>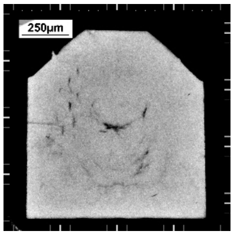 </td><td>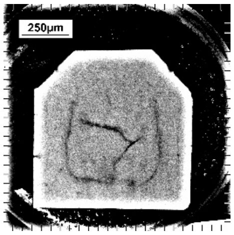 </td></tr>
<tr><td>Freezer Temperature</td><td>-20°C</td><td>Mould Temperature</td><td>Pre-chilled</td></tr>
<tr><td colspan="2">Bisque</td><td colspan="2">Sintered</td></tr>
<tr><td colspan="4">Centre (5x)</td></tr>
<tr><td colspan="2">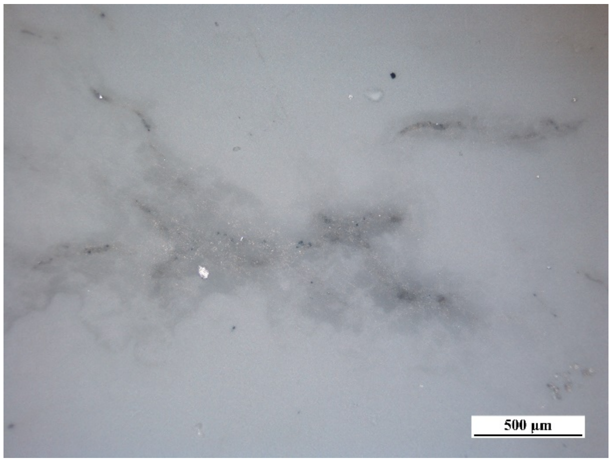 </td><td colspan="2">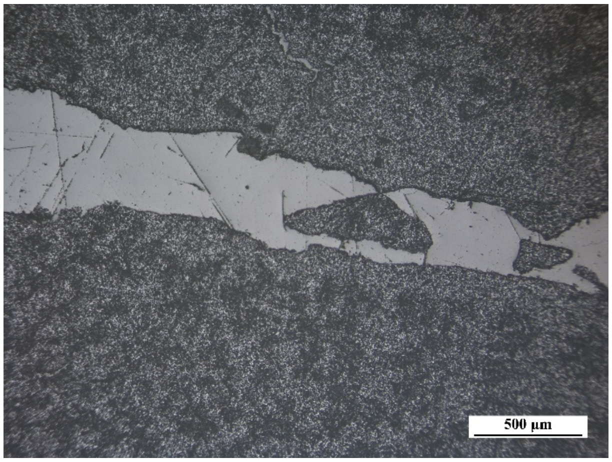 </td></tr>
<tr><td colspan="4">Centre (20x)</td></tr>
<tr><td colspan="2">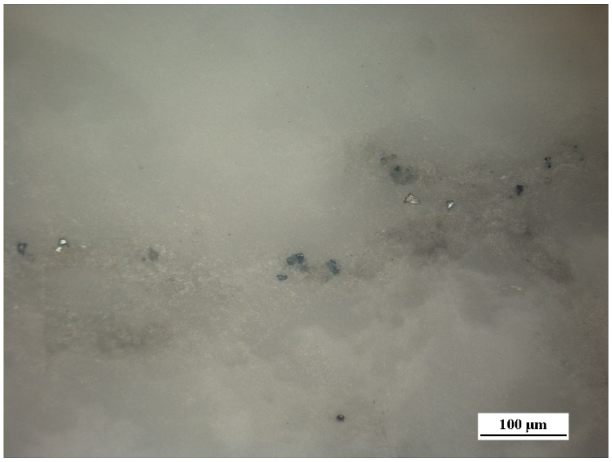 </td><td colspan="2">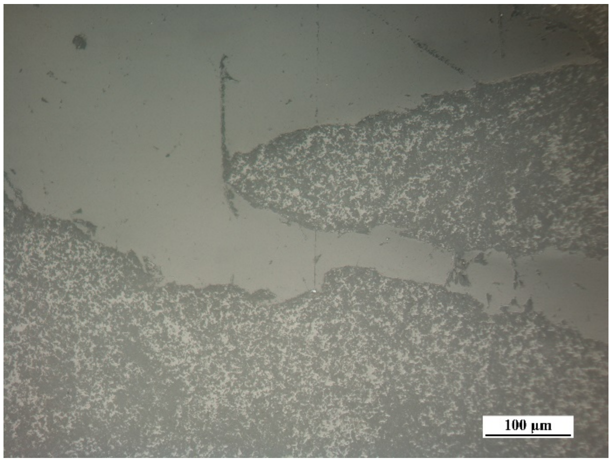 </td></tr>
</table>

Edge (5x)	
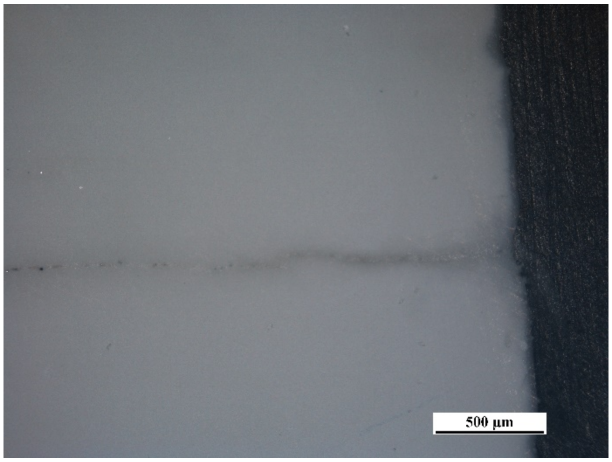	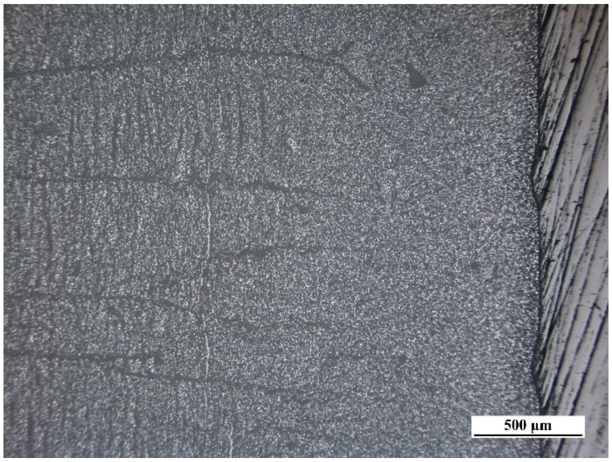
Edge (20x)	
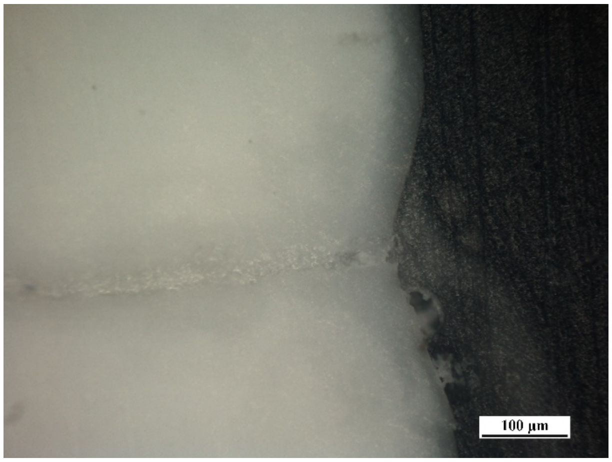	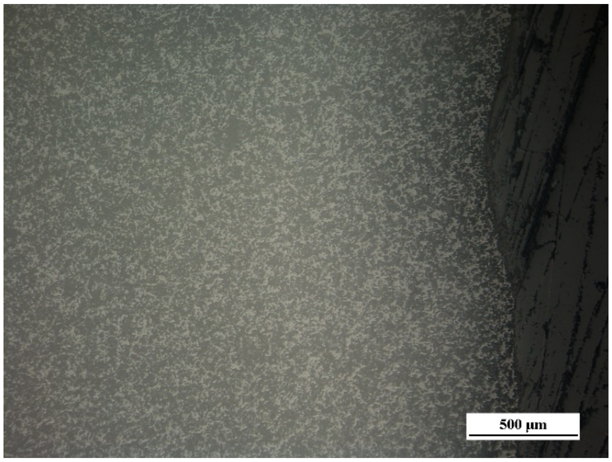

<table>
<tr><td>Sample #’s</td><td>141 & 142</td><td>Bisque Sample Image
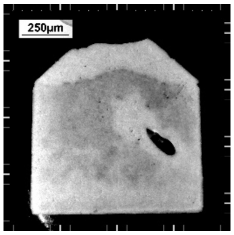 </td><td>Sintered Sample Image
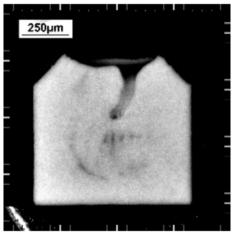 </td></tr>
<tr><td>Freezer Temperature</td><td>-40°C</td><td>Mould Temperature</td><td>Ambient Mould</td></tr>
<tr><td colspan="2">Bisque</td><td colspan="2">Sintered</td></tr>
<tr><td colspan="4">Centre (5x)</td></tr>
<tr><td colspan="2">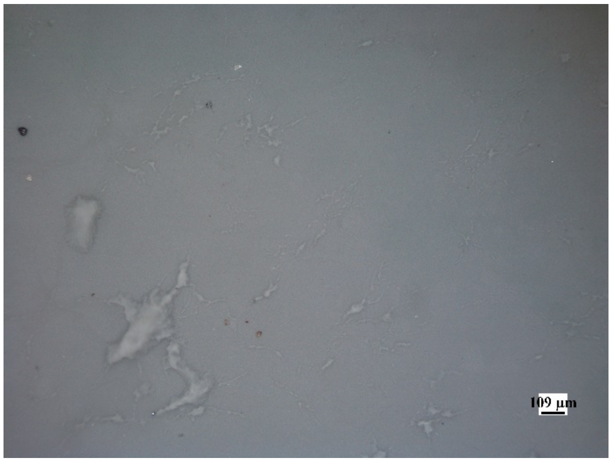 </td><td colspan="2">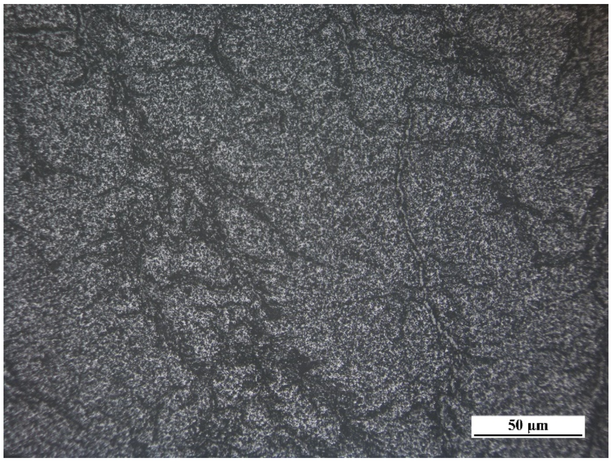 </td></tr>
<tr><td colspan="4">Centre (20x)</td></tr>
<tr><td colspan="2">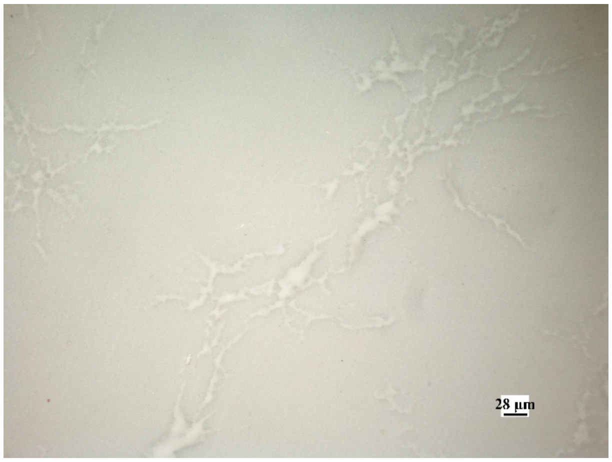 </td><td colspan="2">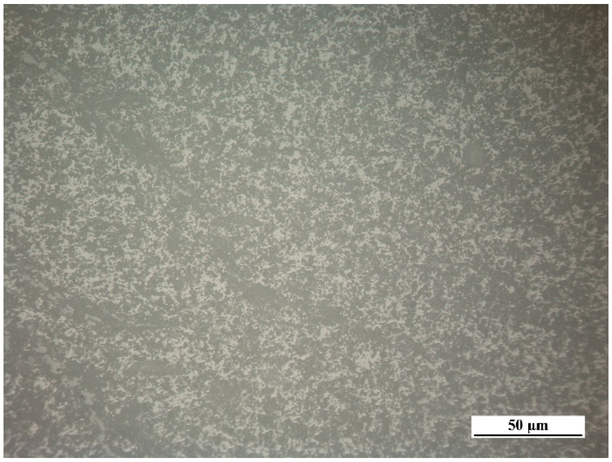 </td></tr>
</table>

Edge (5x)	
	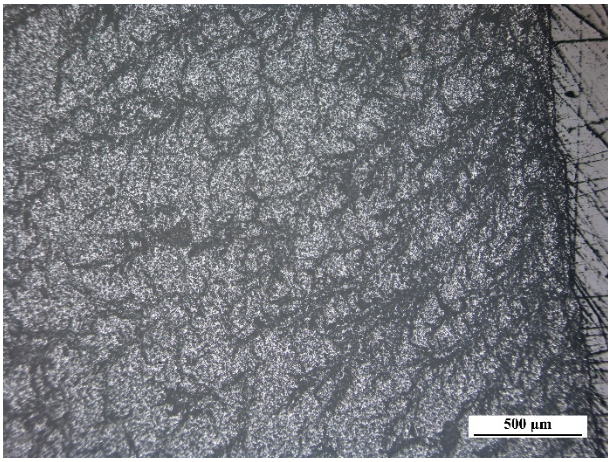
Edge (20x)	
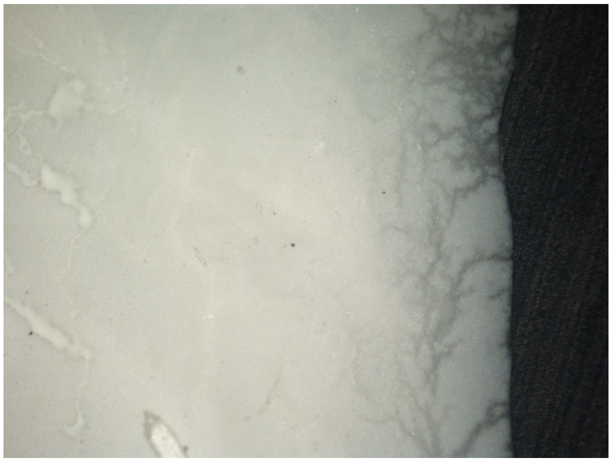	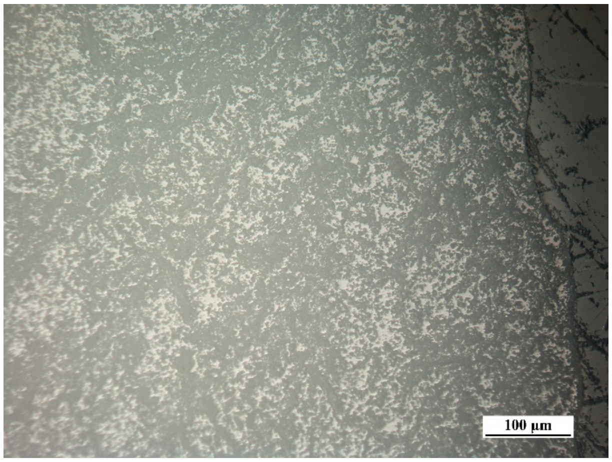

Sample #'s	153 & 155	Bisque Sample Image 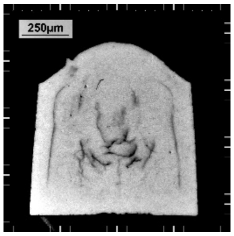	Sintered Sample Image 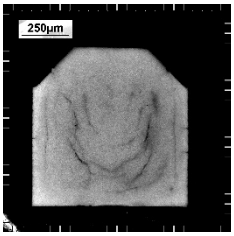
Freezer Temperature	-40°C	Mould Temperature	Pre-chilled
Bisque		Sintered	

<table>
<tr><td colspan="2">Centre (5x)</td></tr>
<tr><td>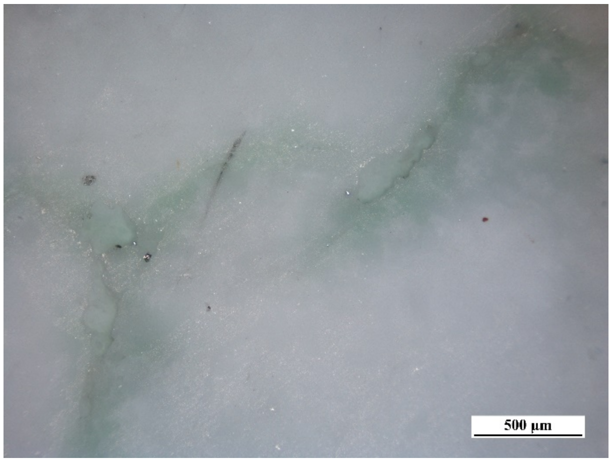
</td><td>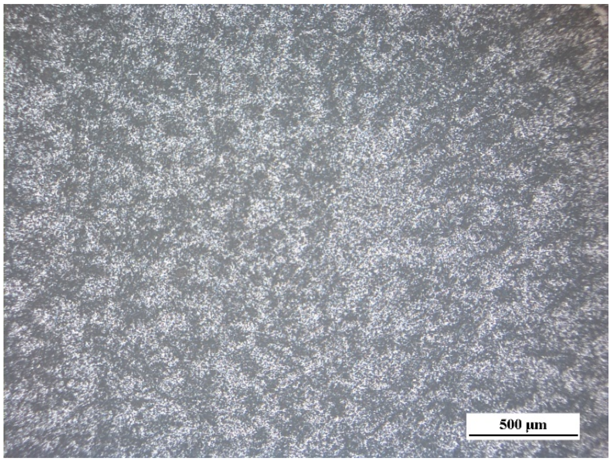
</td></tr>
<tr><td colspan="2">Centre (20x)</td></tr>
<tr><td>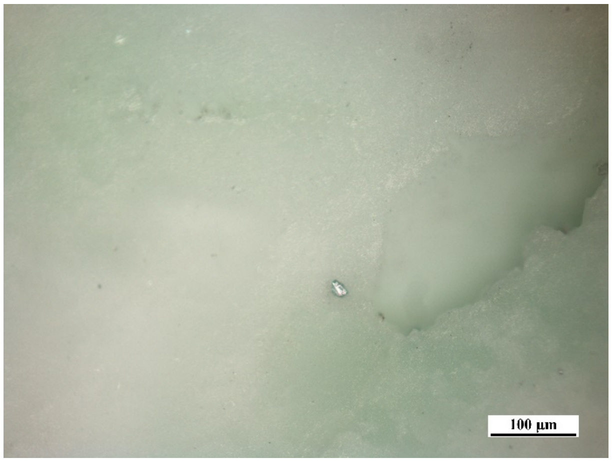
</td><td>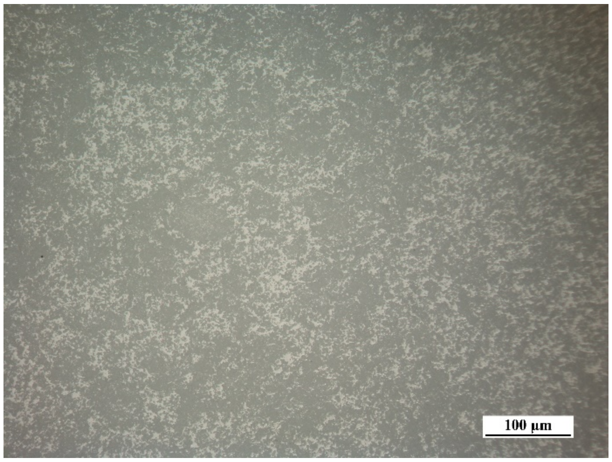
</td></tr>
<tr><td colspan="2">Edge (5x)</td></tr>
<tr><td>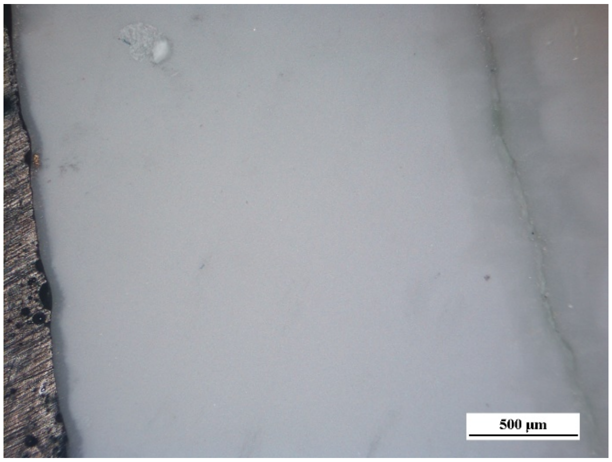
</td><td>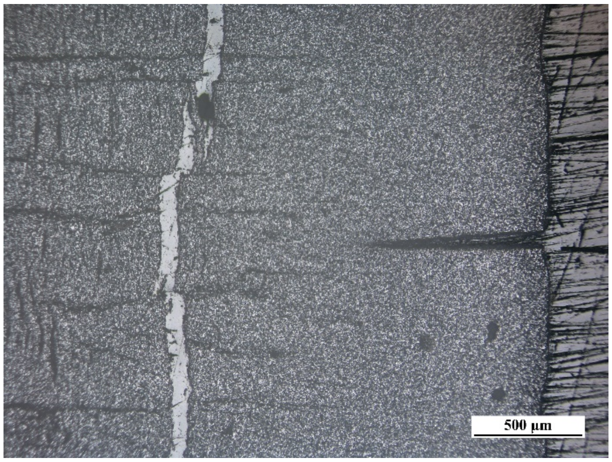
</td></tr>
</table>

Edge (20x)	
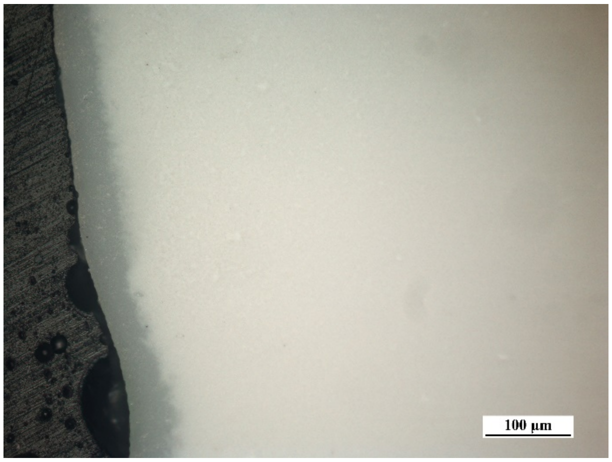	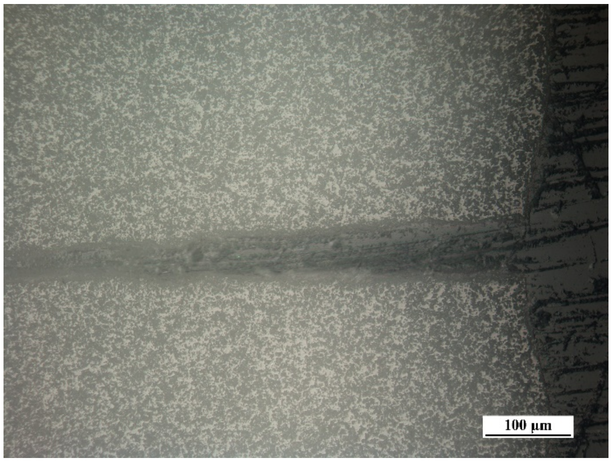

Sample #'s	134 & 135	Bisque Sample Image 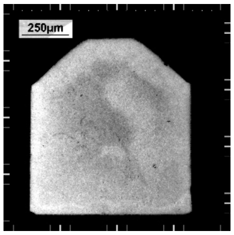	Sintered Sample Image 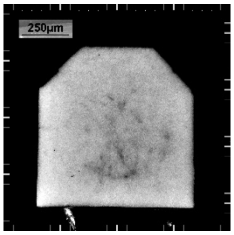
Freezer Temperature	-80°C	Mould Temperatures	Ambient Mould
Bisque		Sintered	
Centre (5x)			
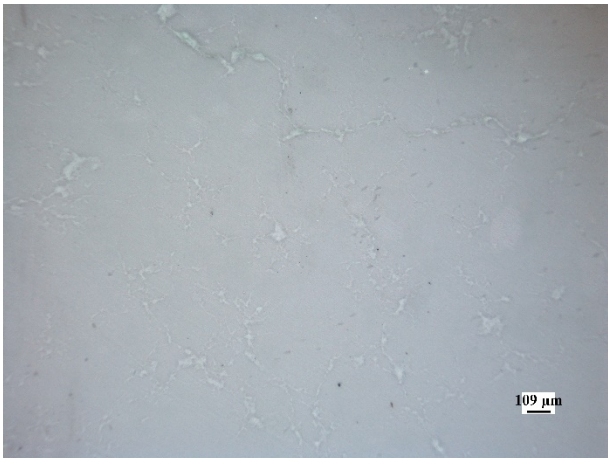		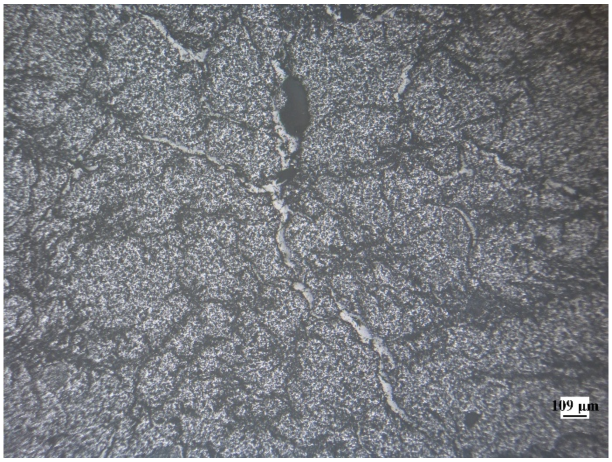	

Centre (20x)

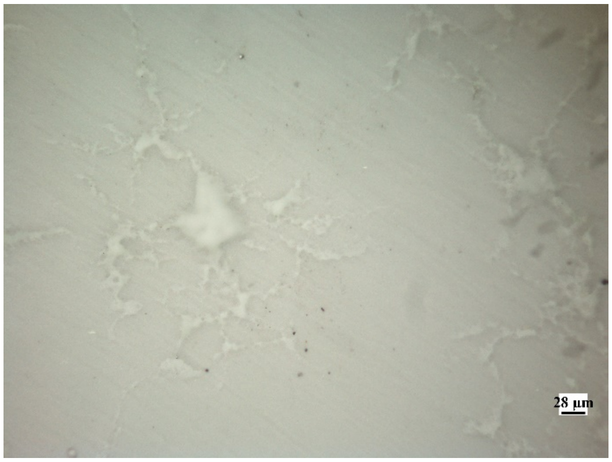

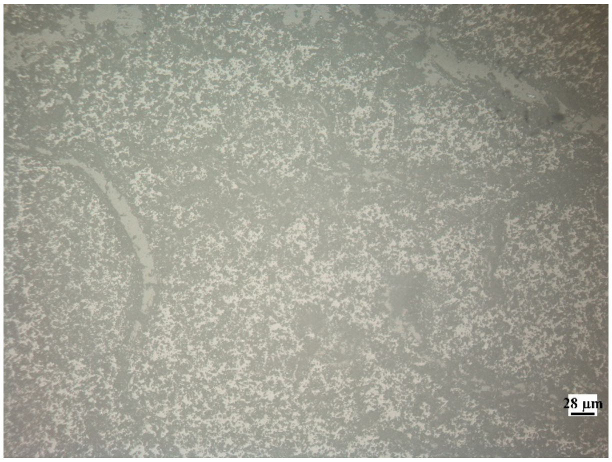

Edge (5x)

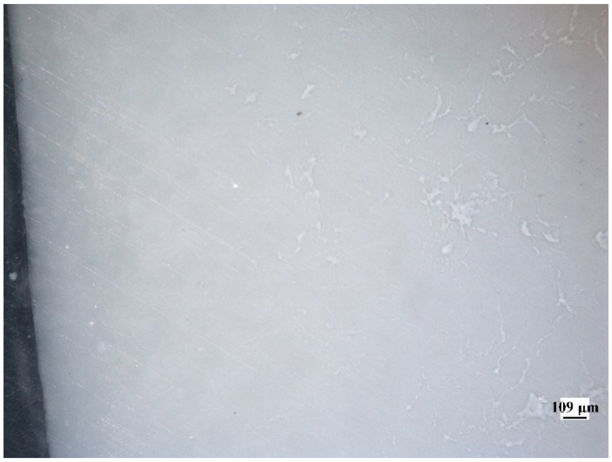

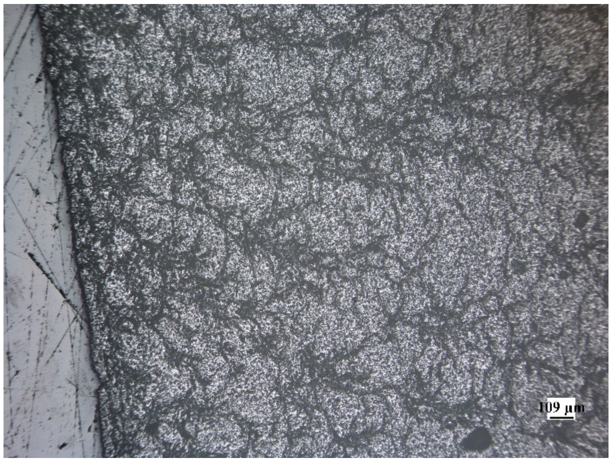

Edge (20x)

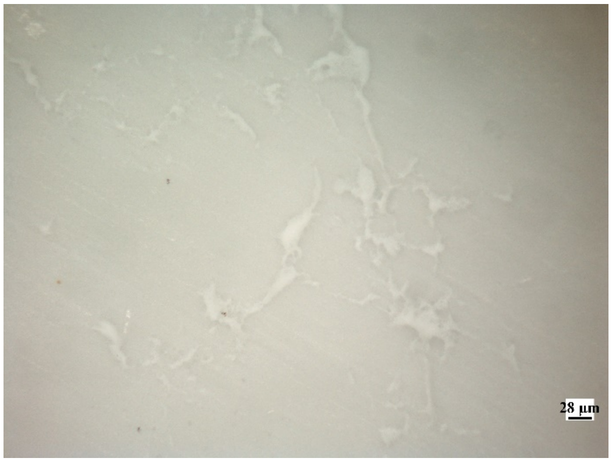

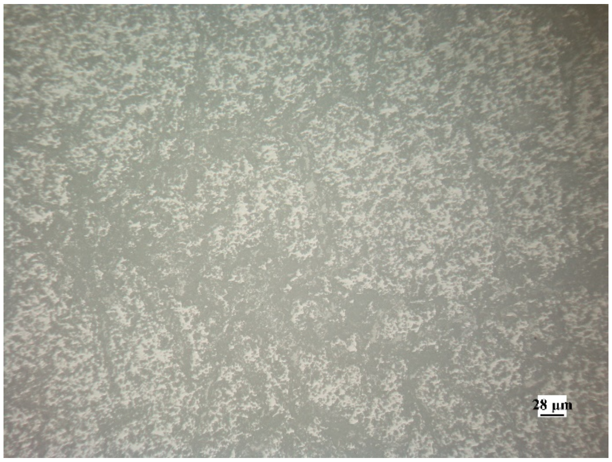

Sample #	167 & 168	Bisque Sample Image 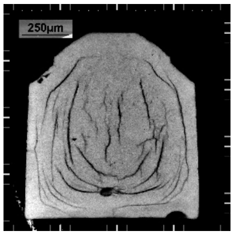	Sintered Sample Image 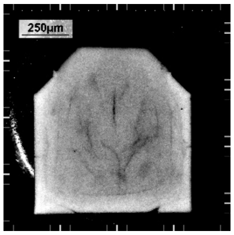
Freezer Temperature	-80°C	Mould Temperature	Pre-chilled
Bisque		Sintered	
Centre (5x)			
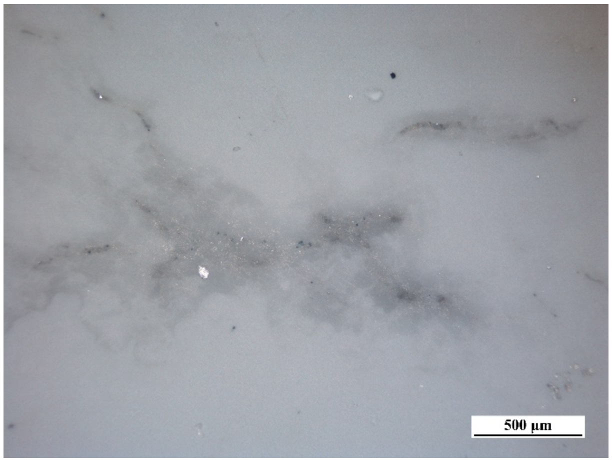		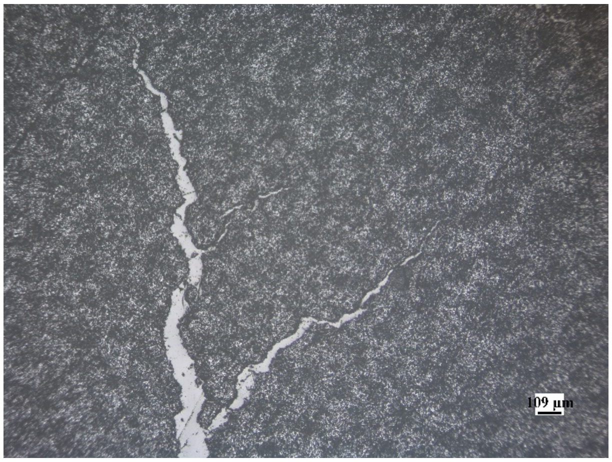	
Centre (20x)			
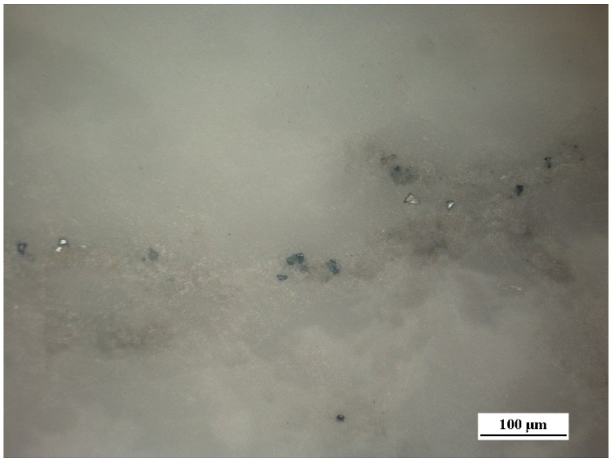		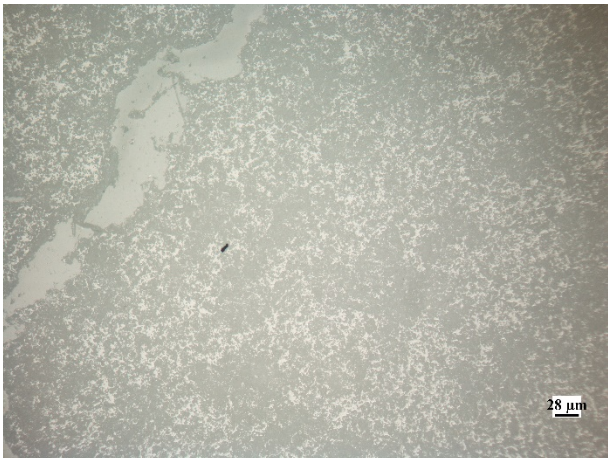	

Edge (5x)	
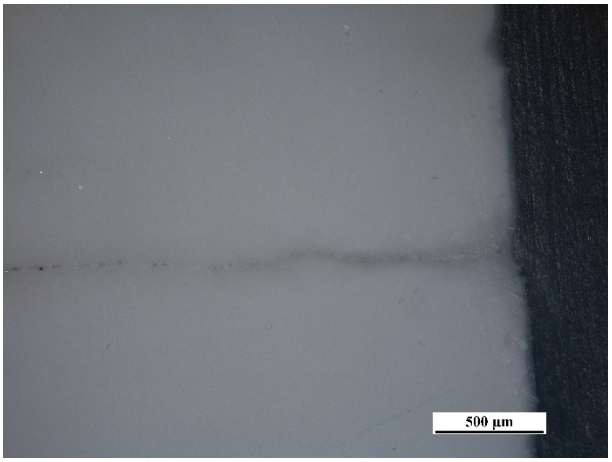	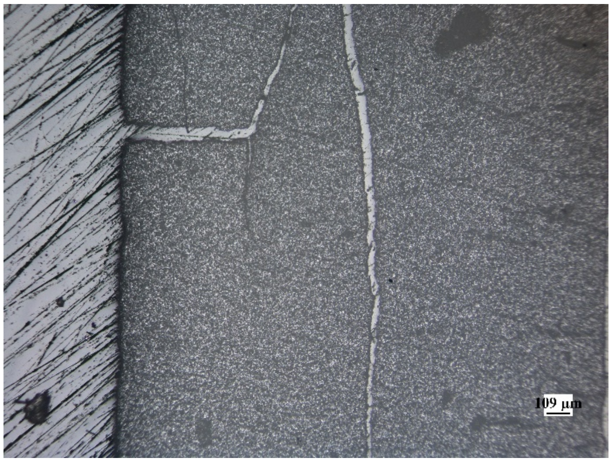
Edge (20x)	
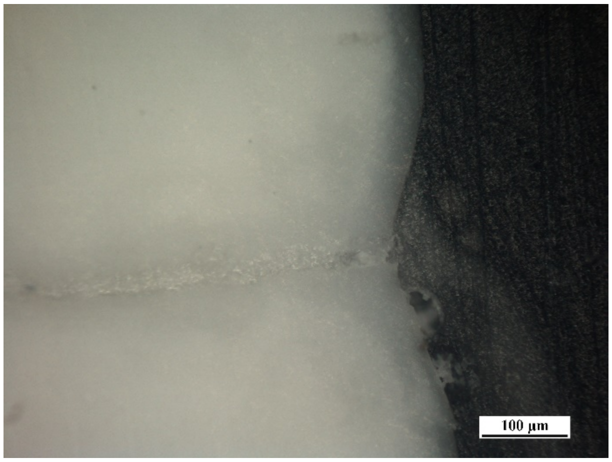	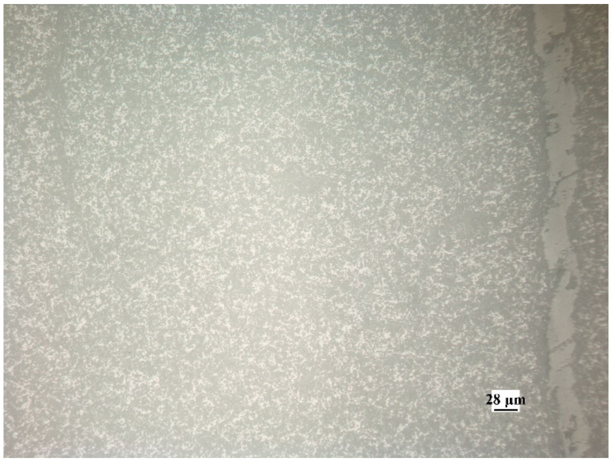

11.2.2 Sample Images Obtained via SEM

The following tables contain the images of the alumina samples, obtained under different freezing conditions. More information on this image set is provided in the main text within the results section.

Sample #’s	147 & 148	Bisque Sample Image 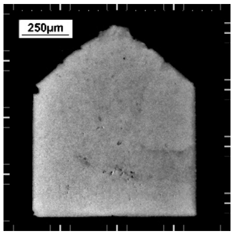 	Sintered Sample Image 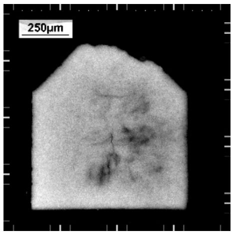
Freezer Temperature	-20°C	Mould Temperature	Ambient Mould

	Bisque	Sintered
Centre 100x	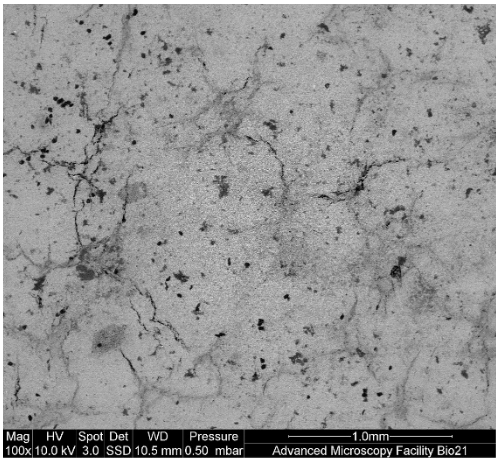 	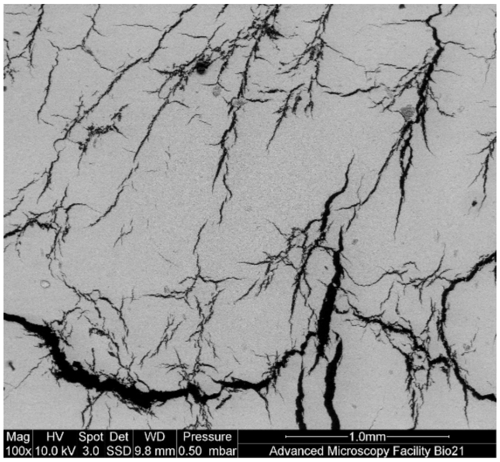
Centre 800x	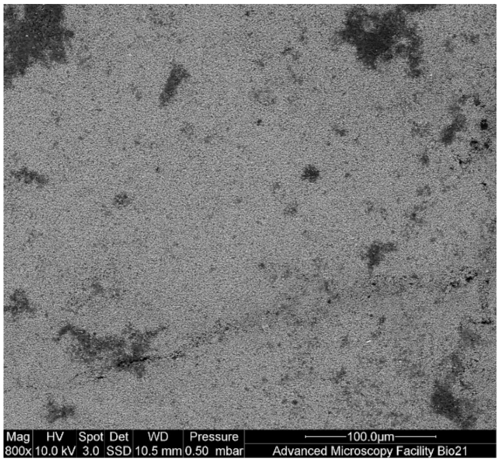 	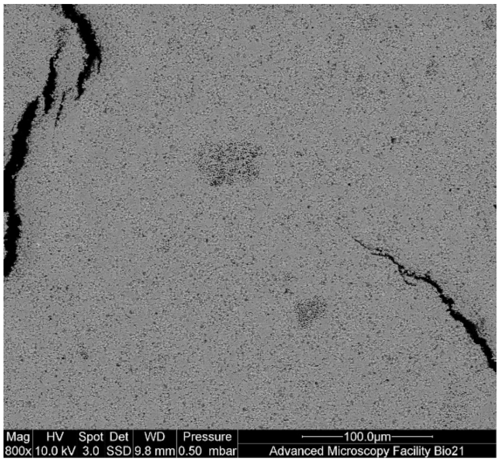

Centre 4000x	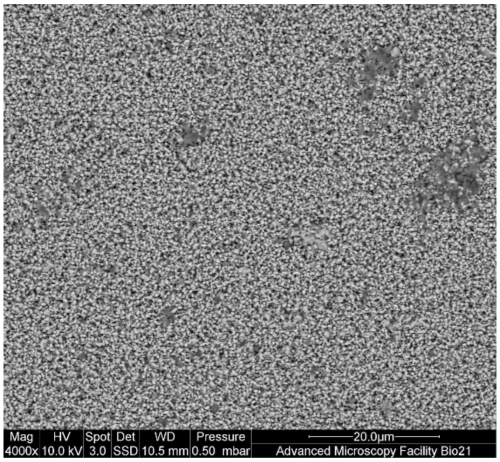	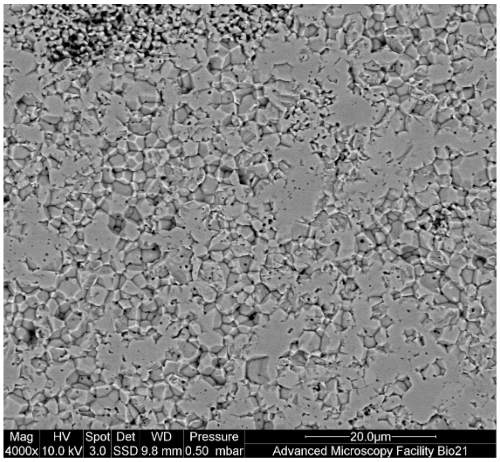
Bottom 100x	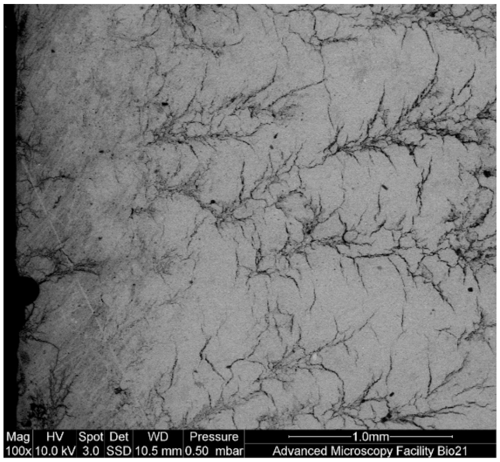	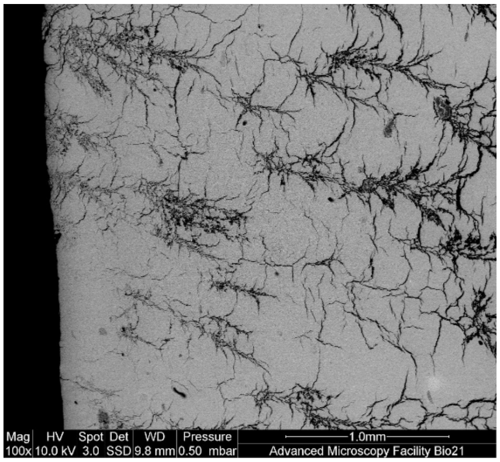
Bottom 800x	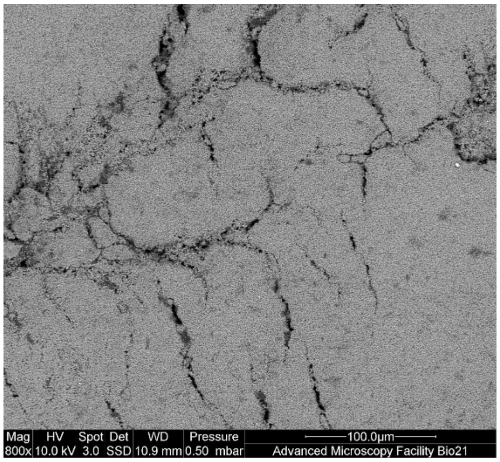	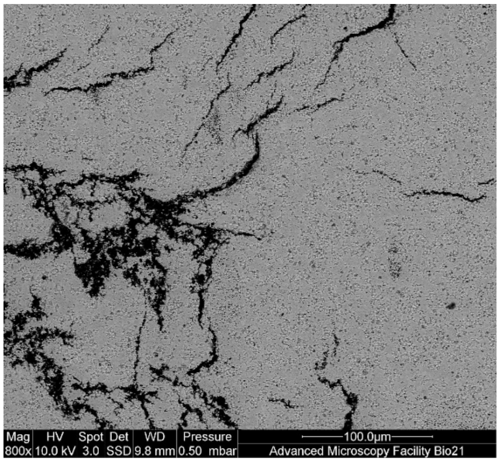

Bottom 4000x	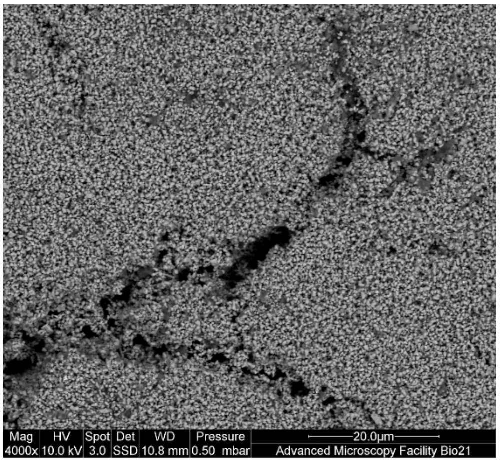	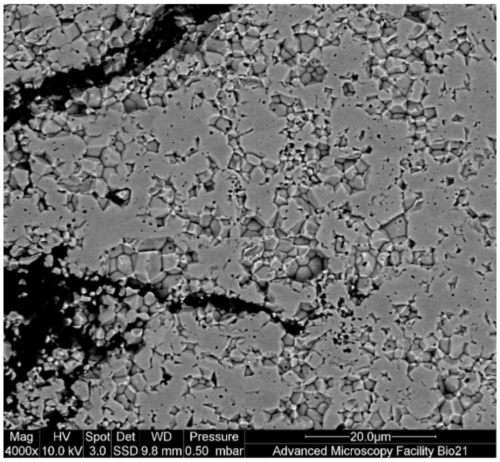
Corner 100x	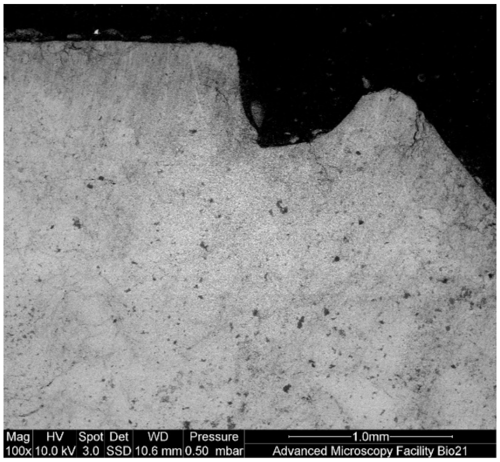	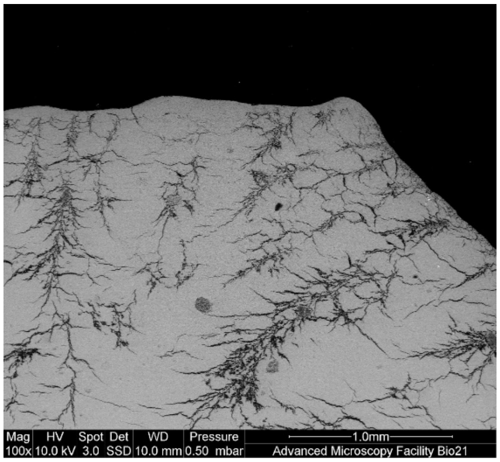

Corner 800x	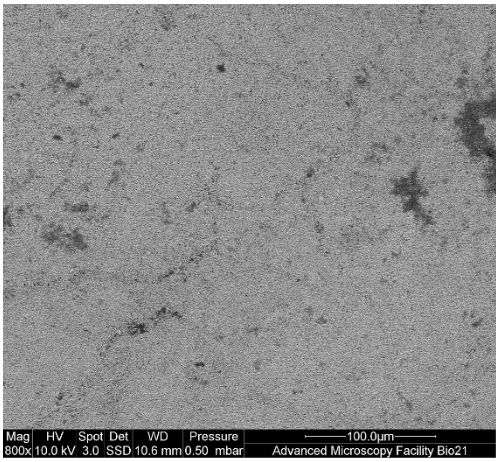	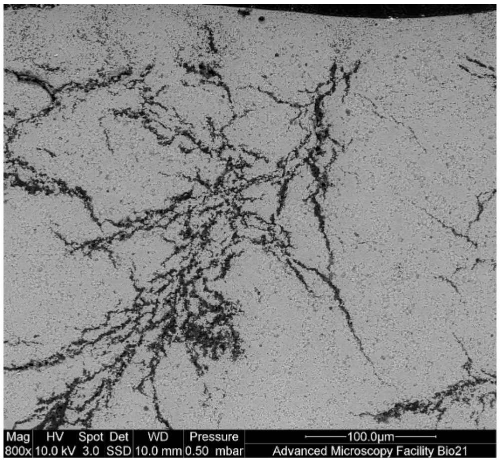
Corner 4000x	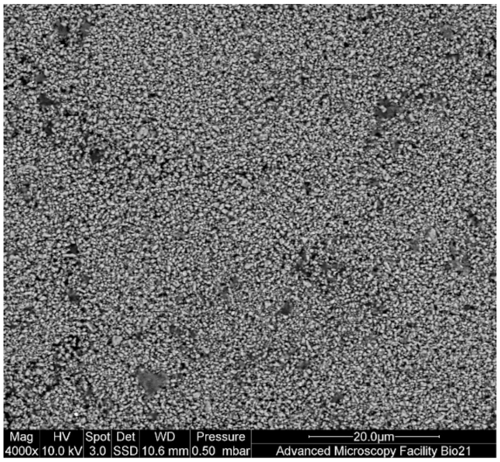	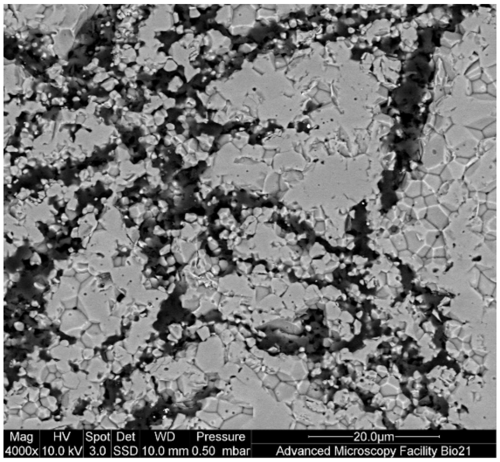

Sample #'s	162 & 163	Bisque Sample Image 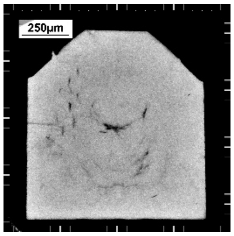	Sintered Sample Image 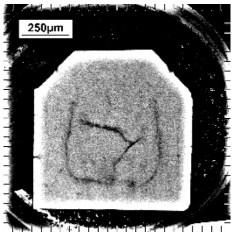
Freezer Temperature	-20°C	Mould Temperature	Pre-chilled
	Bisque		Sintered

Centre 100x	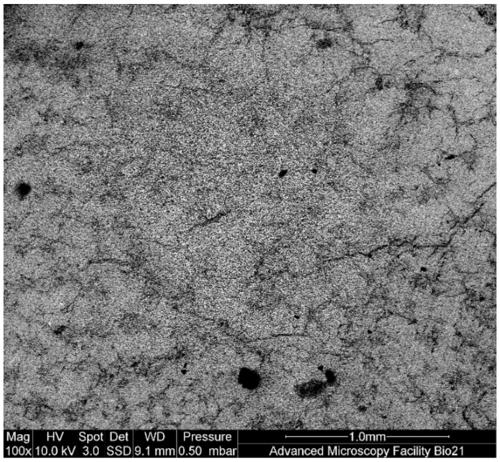	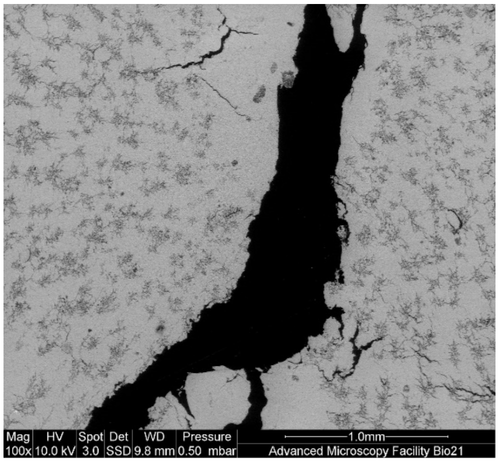
Centre 800x	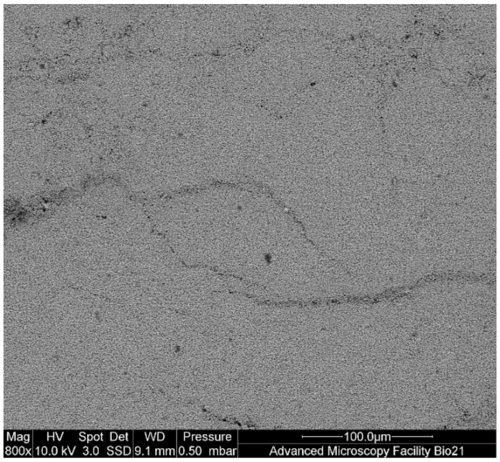	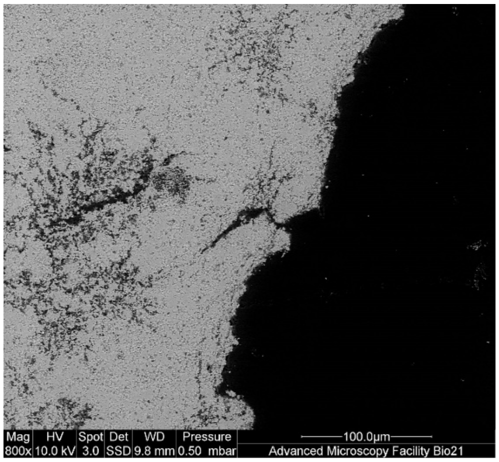
Centre 4000x	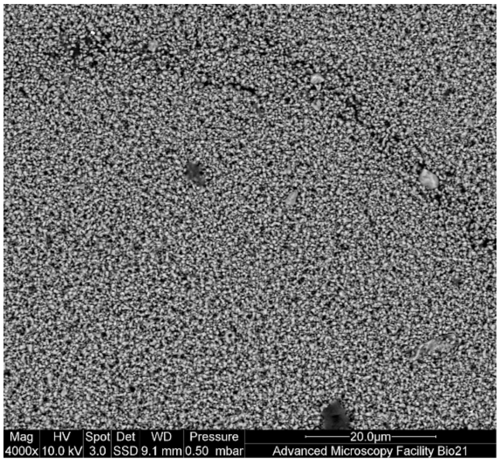	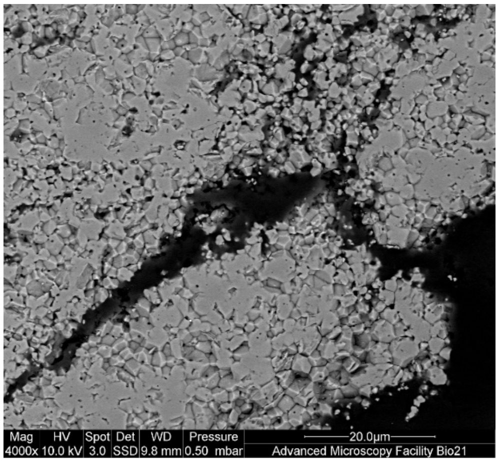

Bottom 100x	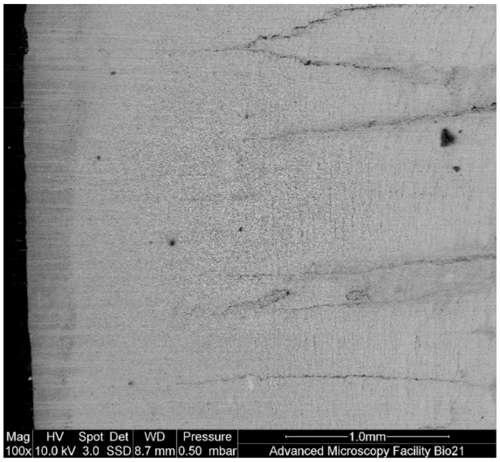	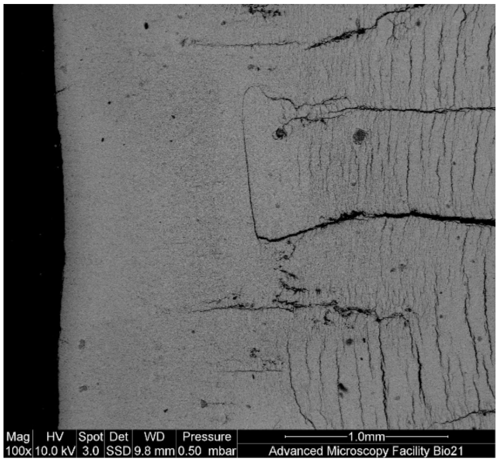
Bottom 800x	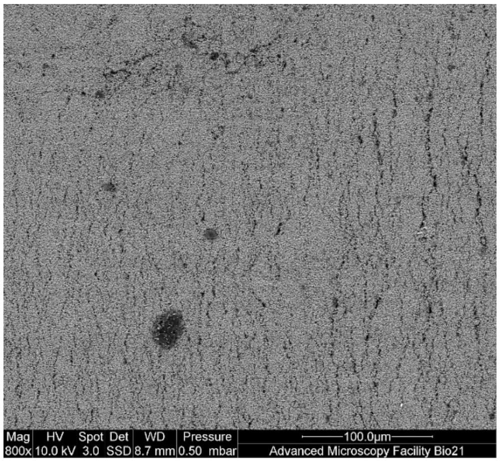	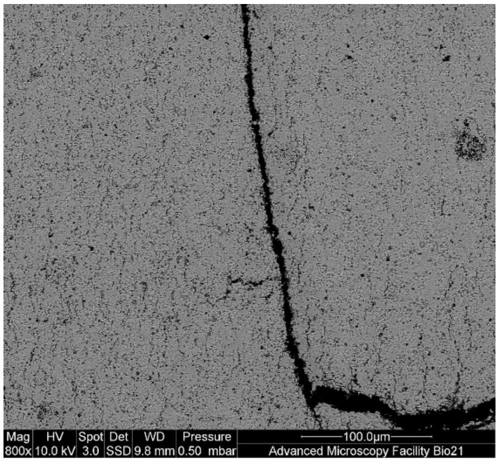
Bottom 4000x	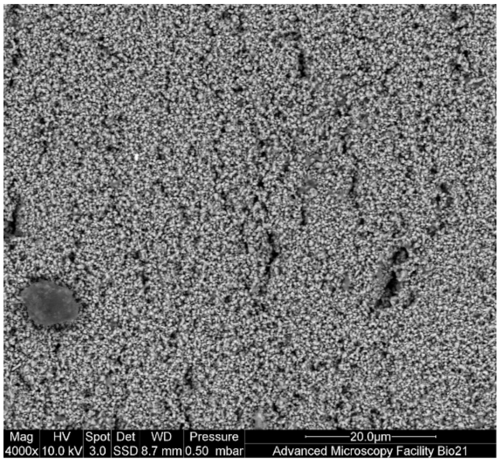	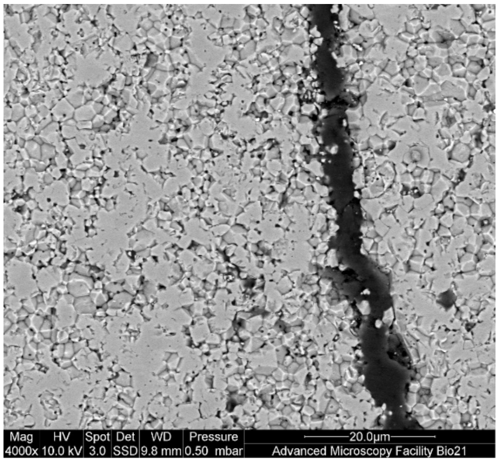

Corner 100x	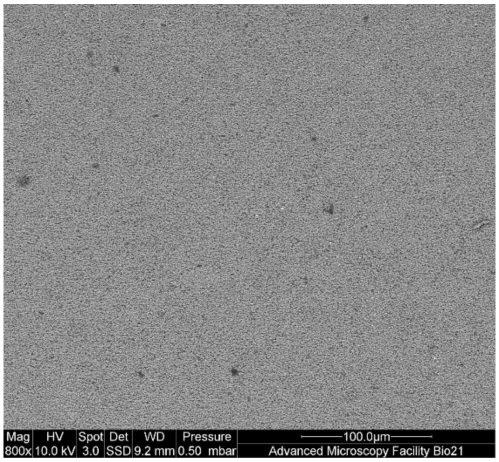	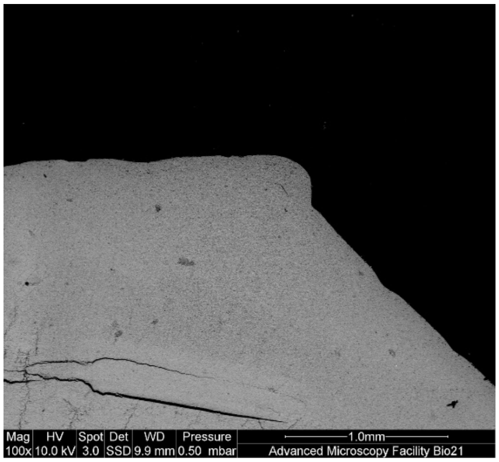
Corner 800x	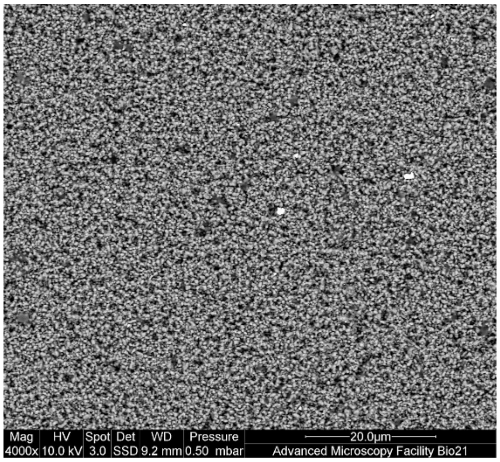	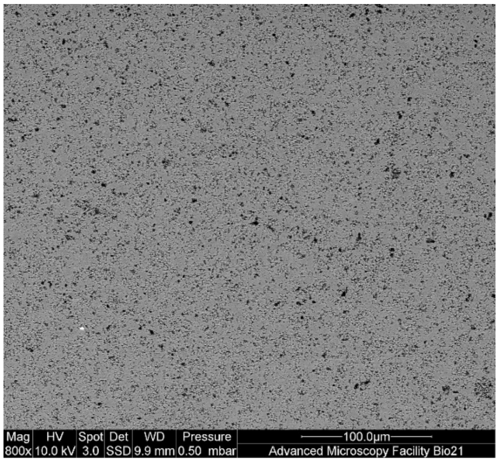
Corner 4000x	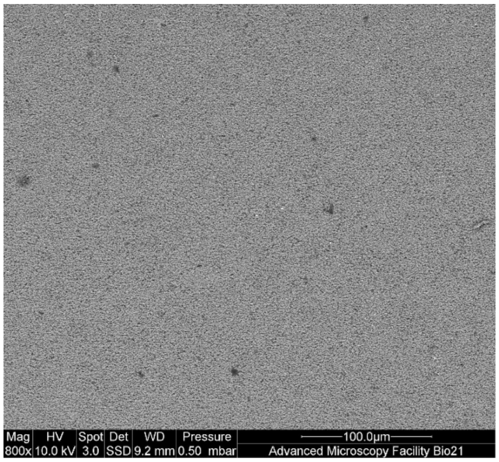	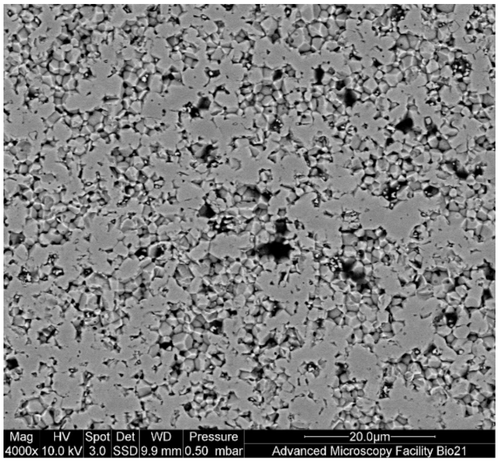

Sample #'s	141 & 142	Bisque Sample Image 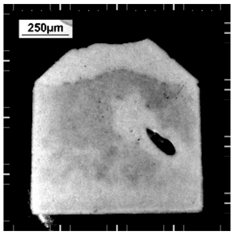	Sintered Sample Image 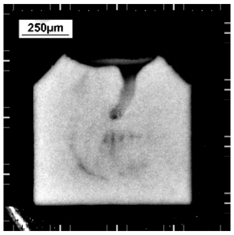
Freezer Temperature	-40°C	Mould Temperature	Ambient Mould
	Bisque	Sintered	
Centre 100x	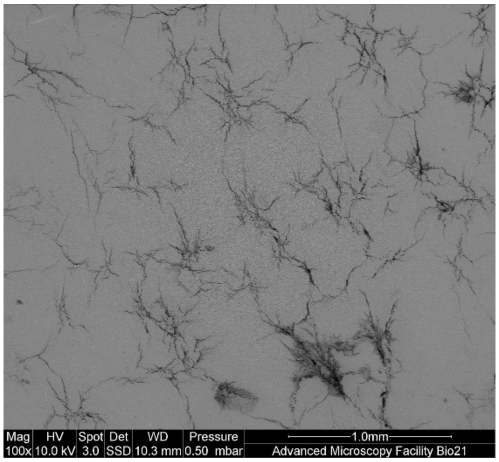	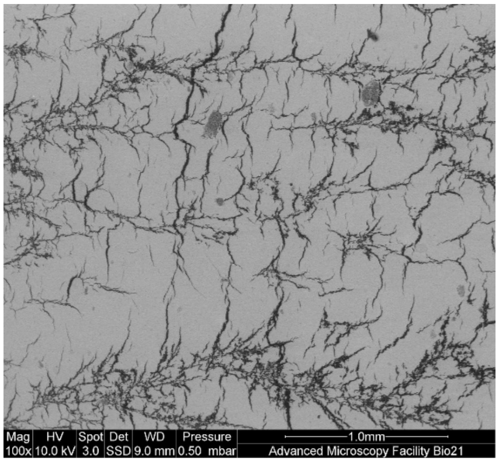	
Centre 800x	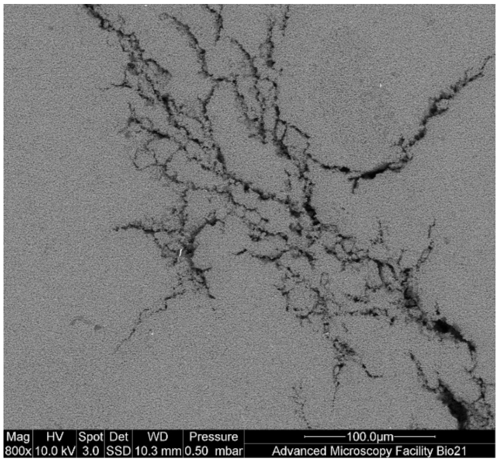	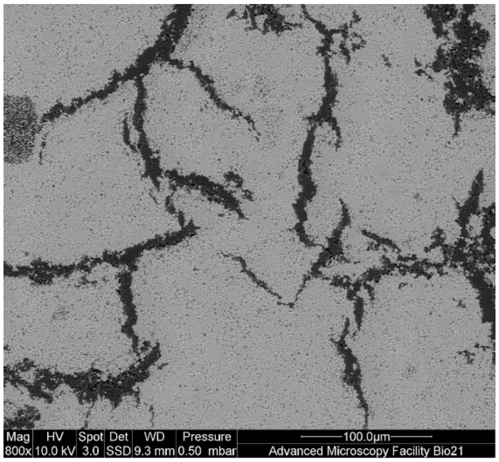	

Centre 4000x	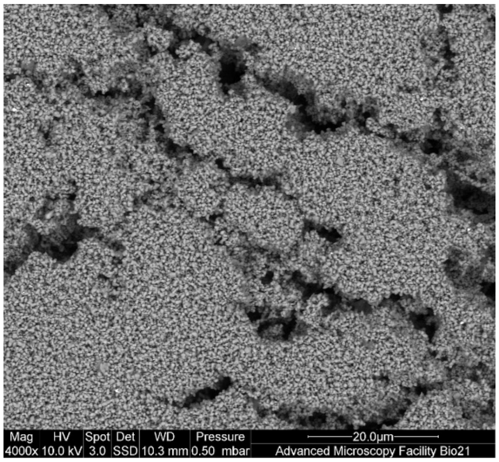	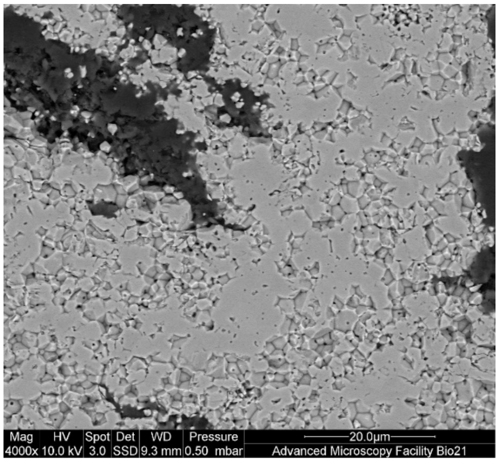
Bottom 100x	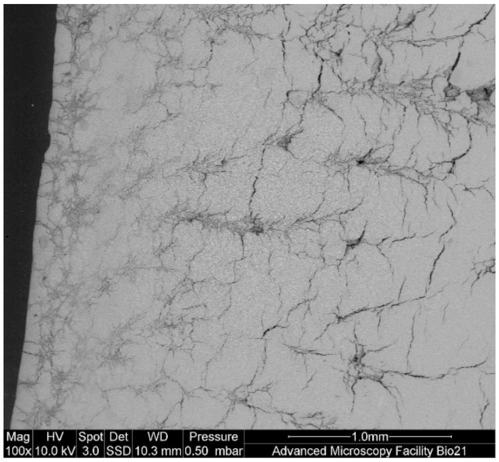	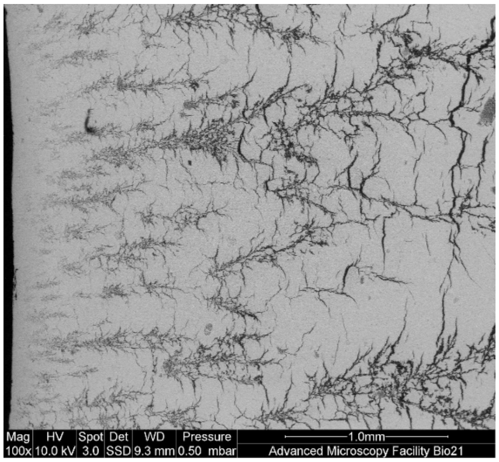
Bottom 800x	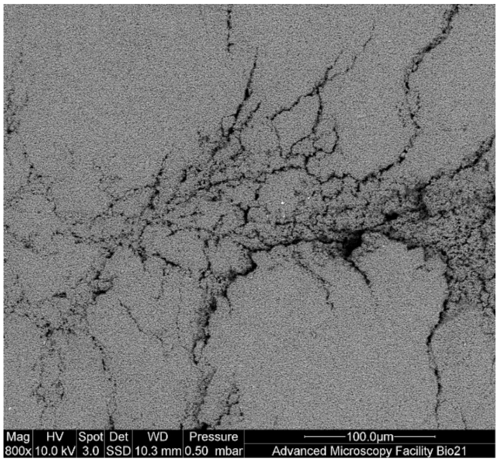	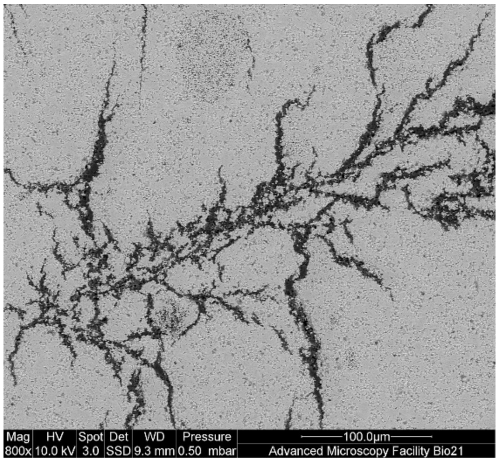

Bottom 4000x	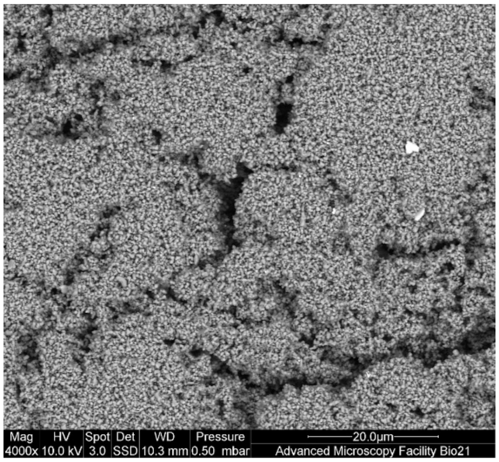	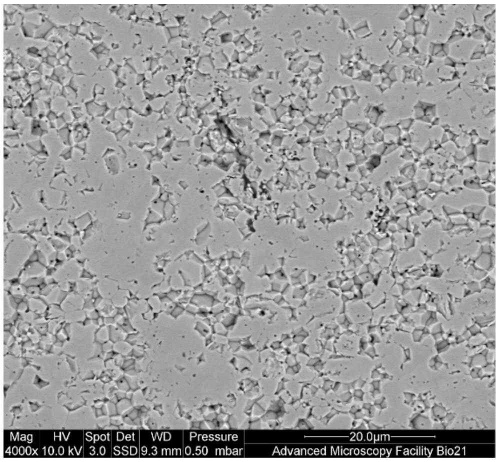
Corner 100x	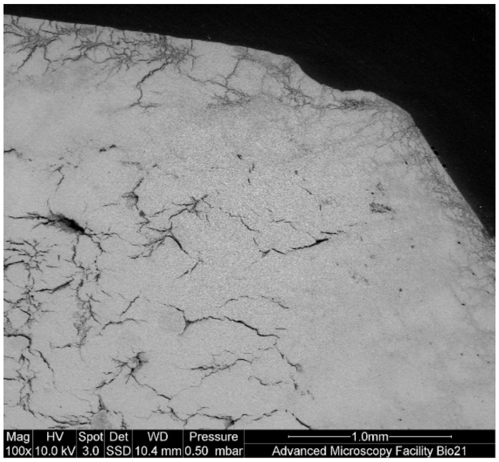	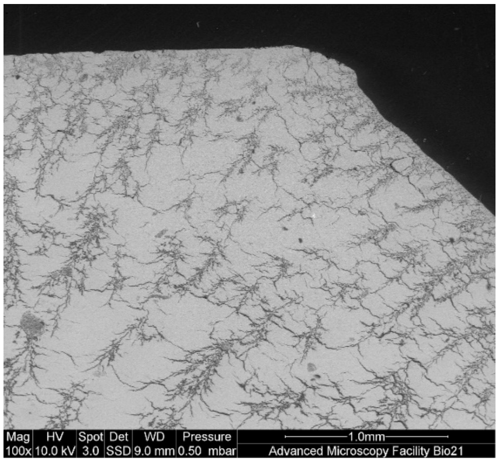
Corner 800x	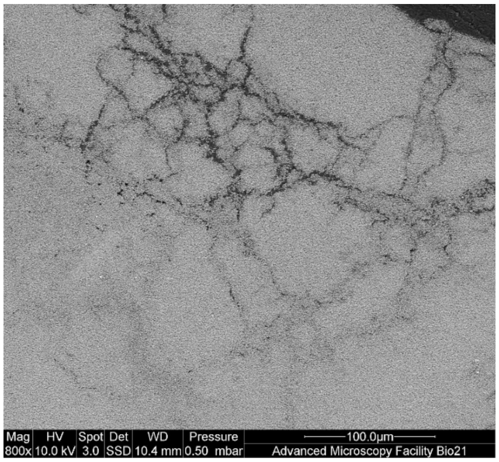	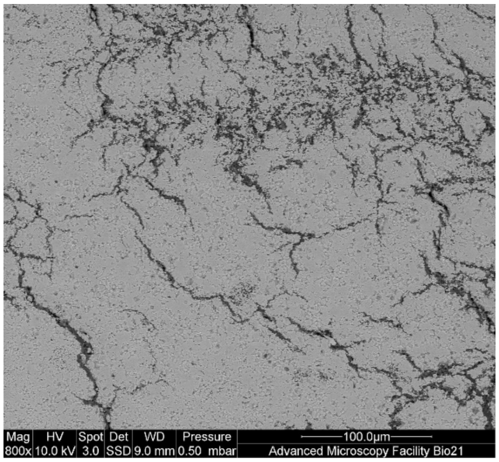

<table>
<tr><td>Corner 4000x</td><td>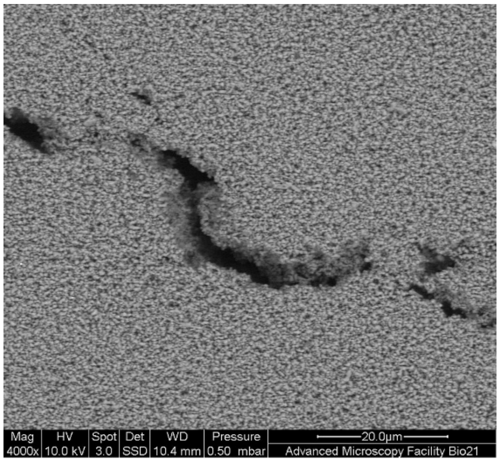 </td><td>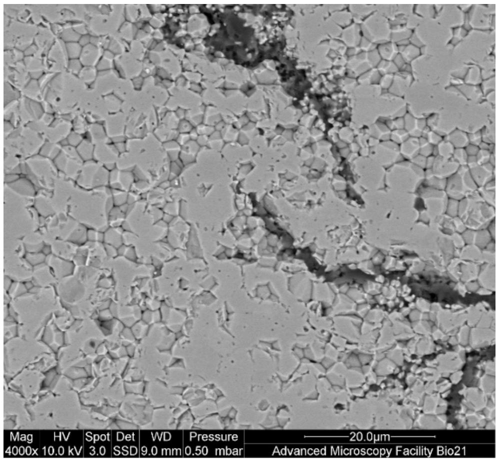 </td></tr>
</table>

<table>
<tr><td>Sample #’s</td><td colspan="2">153 & 155</td><td colspan="2">Bisque Sample Image
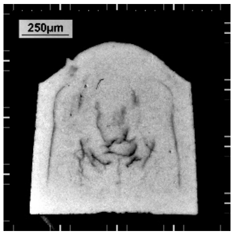 </td><td>Sintered Sample Image
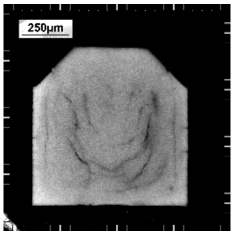 </td></tr>
<tr><td>Freezer Temperature</td><td>-40°C</td><td colspan="3">Mould Temperature</td><td>Pre-chilled</td></tr>
<tr><td></td><td colspan="3">Bisque</td><td colspan="2">Sintered</td></tr>
<tr><td>Centre 100x</td><td colspan="3">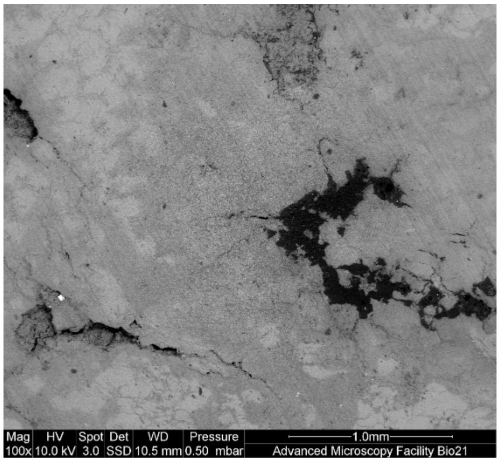 </td><td colspan="2">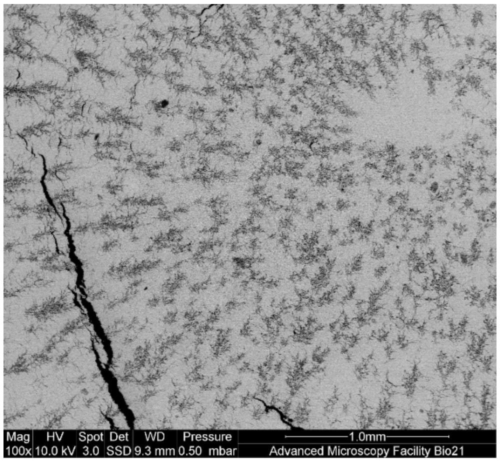 </td></tr>
</table>

Centre 800x	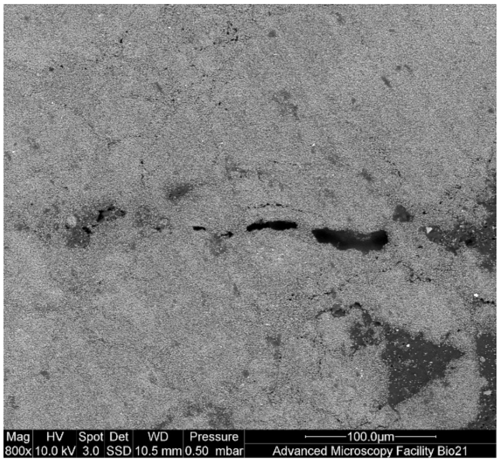	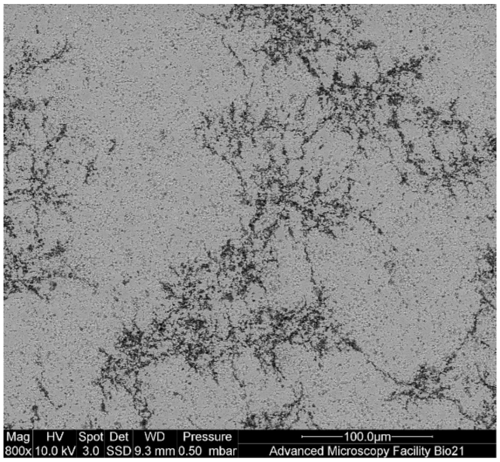
Centre 4000x	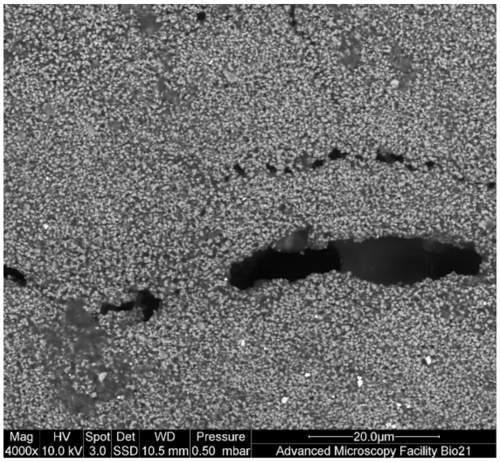	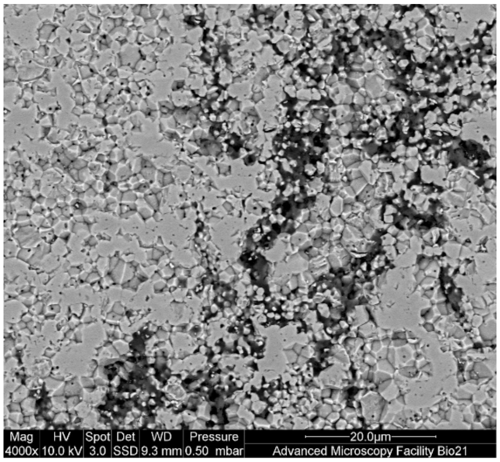
Bottom 100x	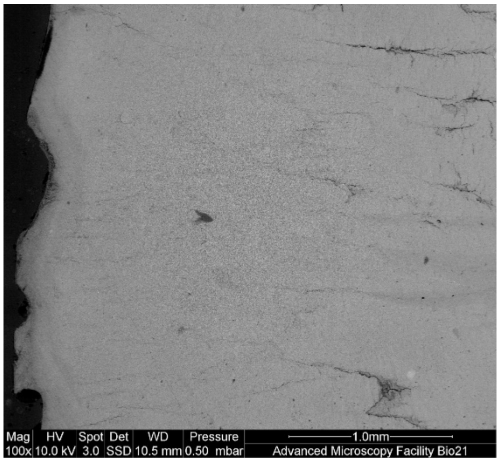	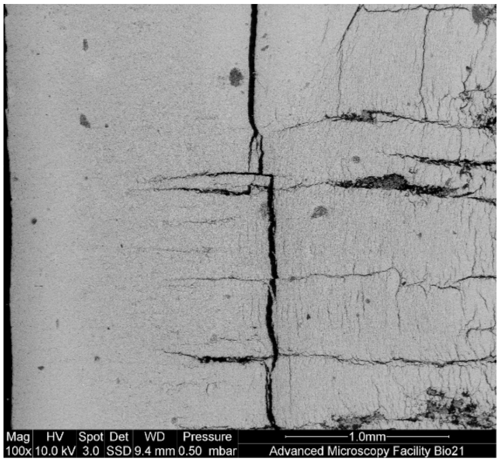

Bottom 800x	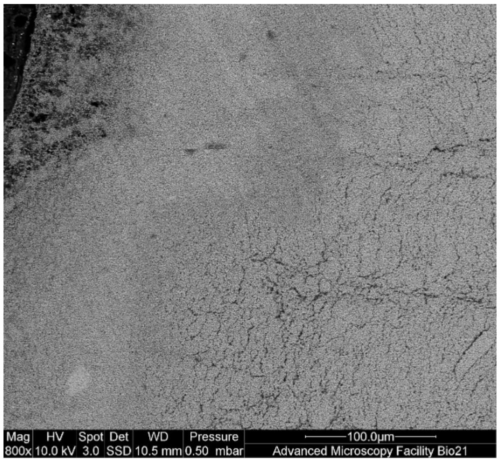	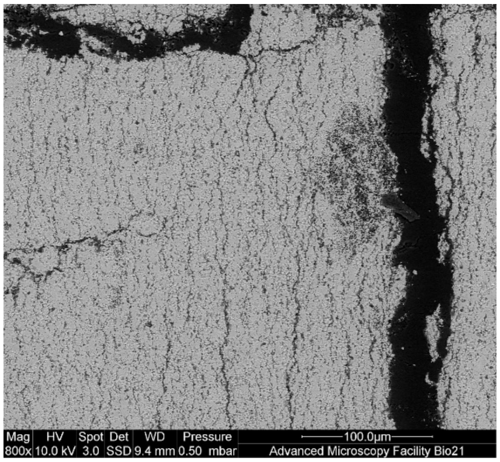
Bottom 4000x	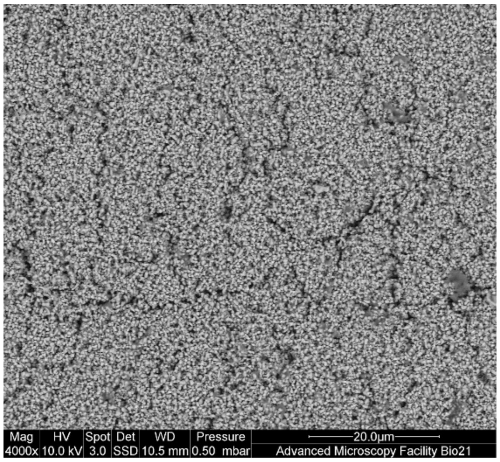	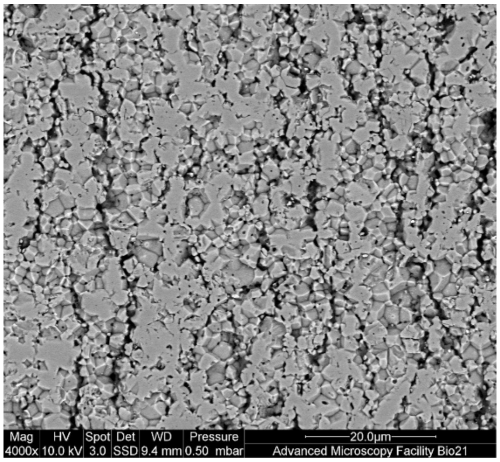
Corner 100x	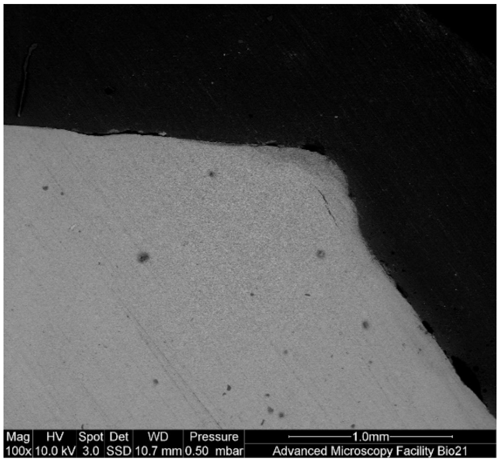	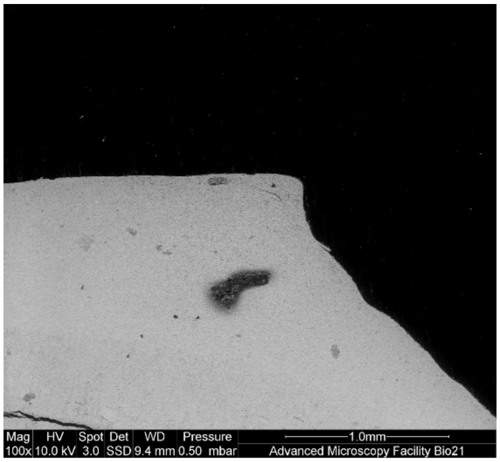

Corner 800x	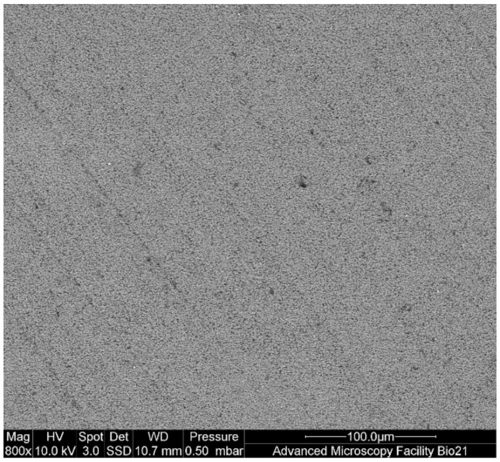	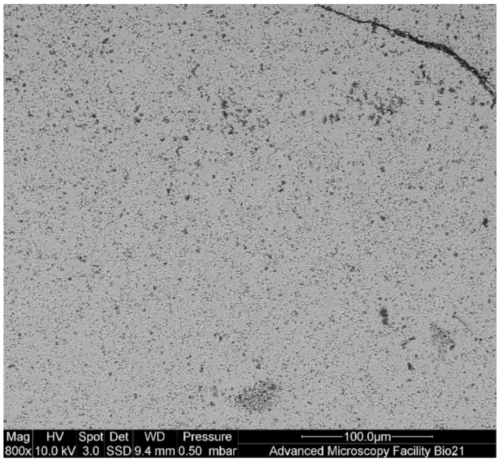
Corner 4000x	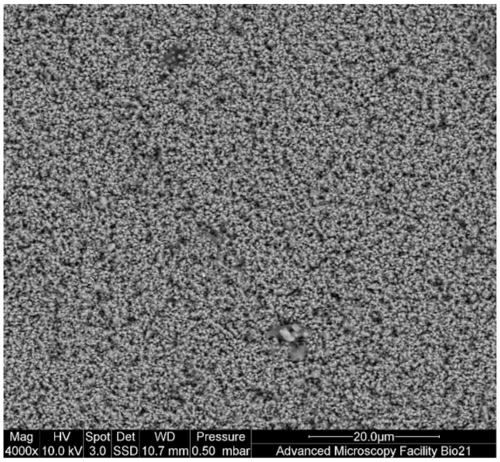	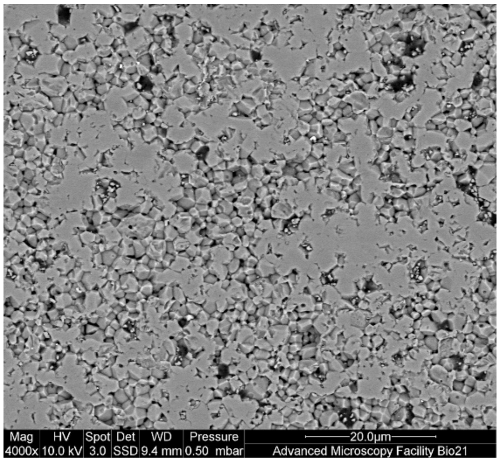

Sample #'s	134 & 135		Bisque Sample Image 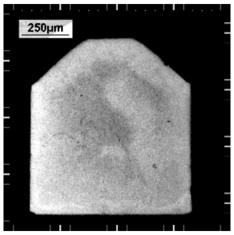	Sintered Sample Image 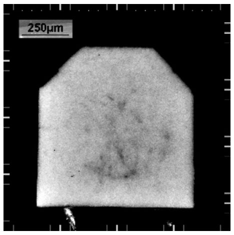
Freezer Temperature	-80°C	Mould Temperatures		Ambient Mould
	Bisque		Sintered	

Centre 100x	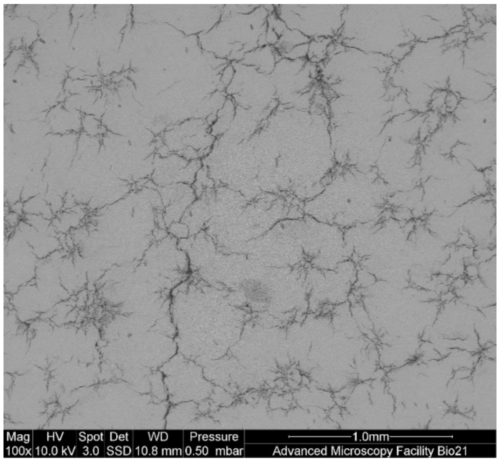	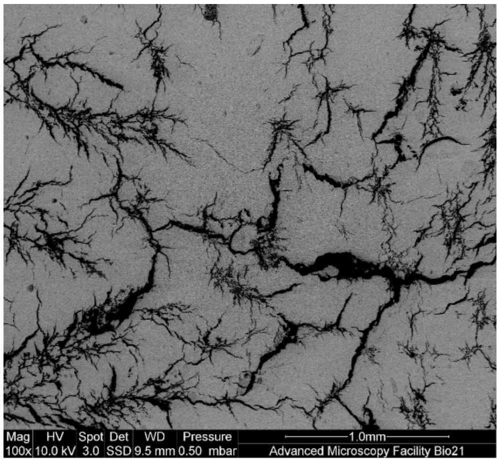
Centre 800x	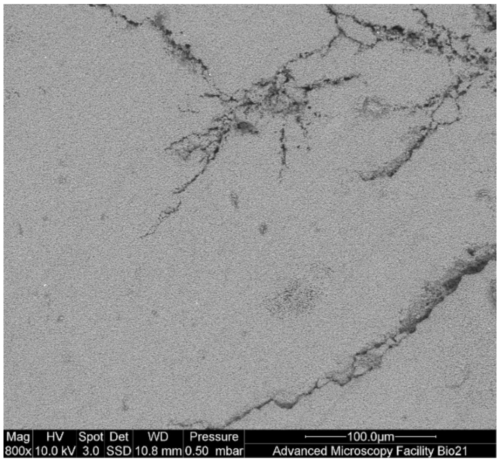	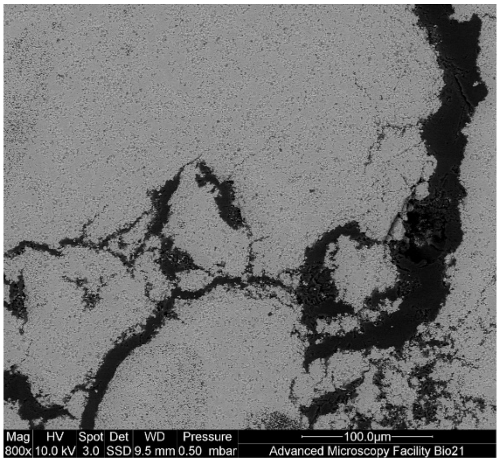
Centre 4000x	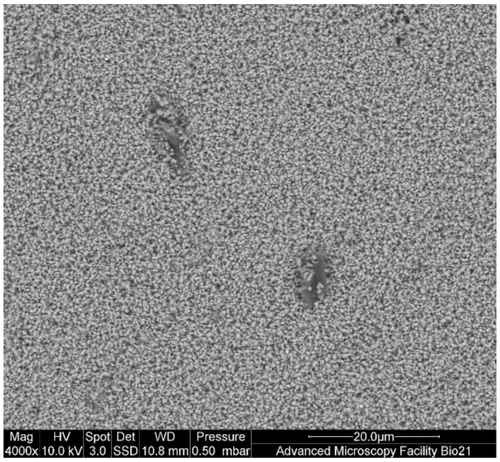	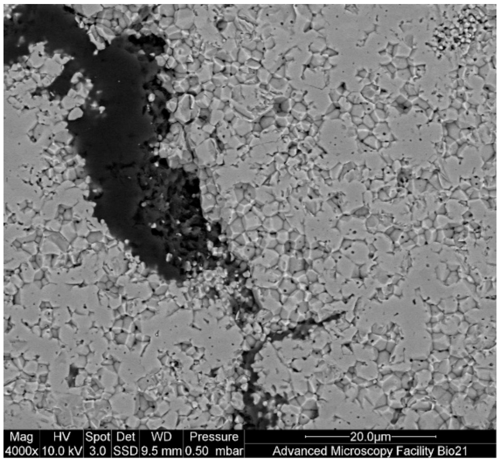

Bottom 100x	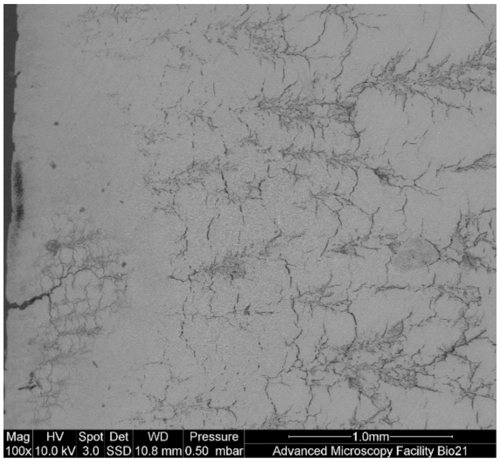	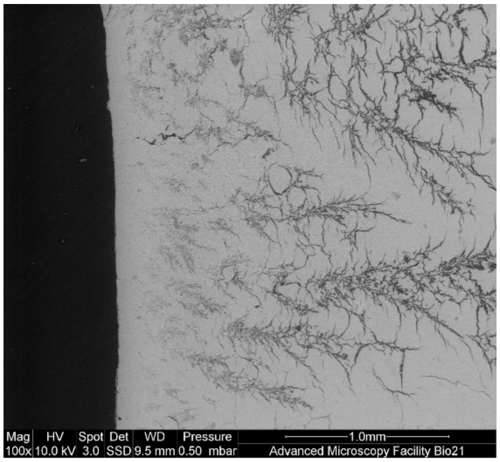
Bottom 800x	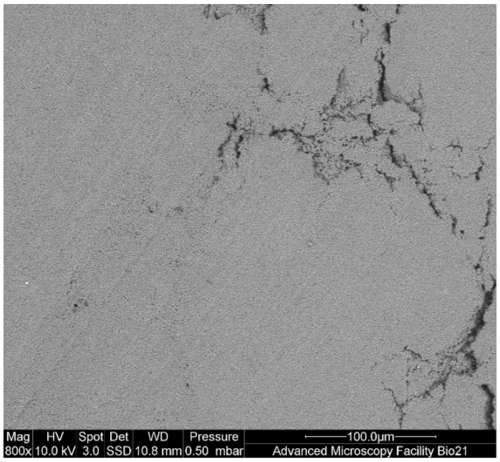	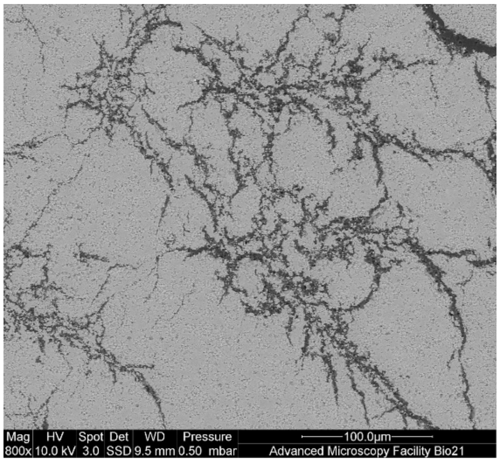
Bottom 4000x	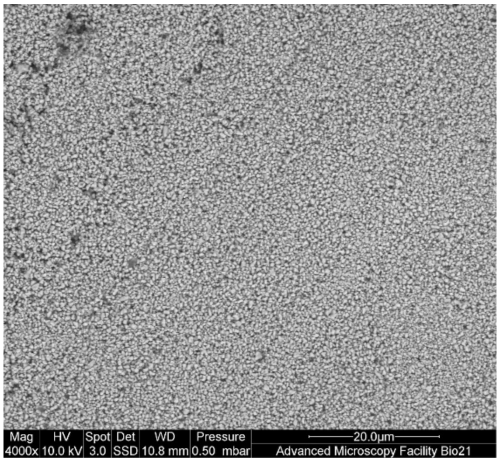	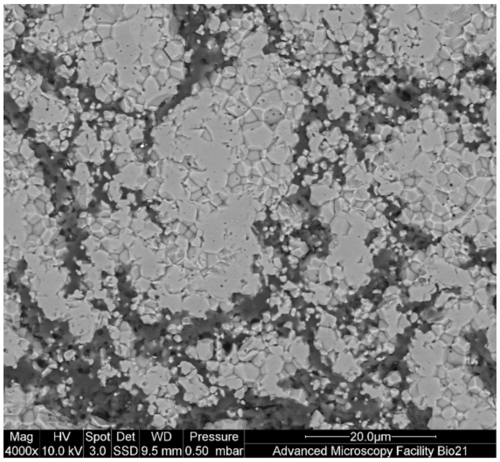

Corner 100x	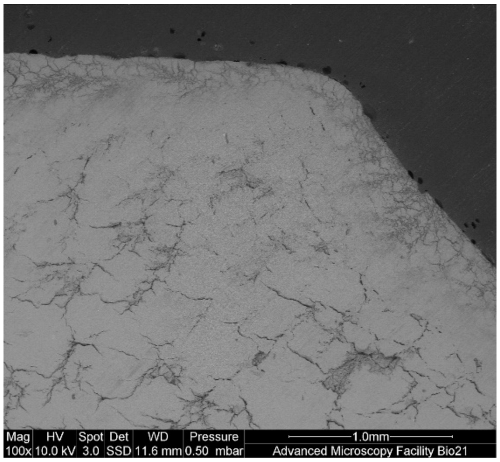	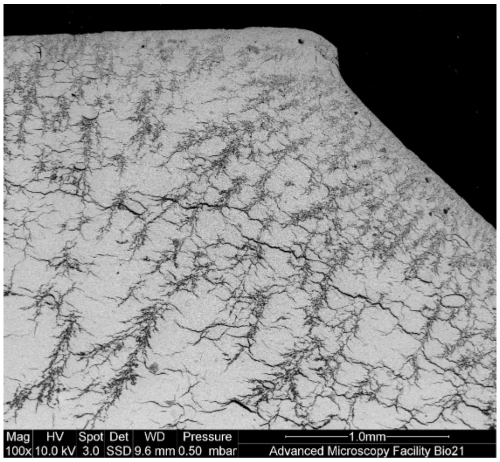
Corner 800x	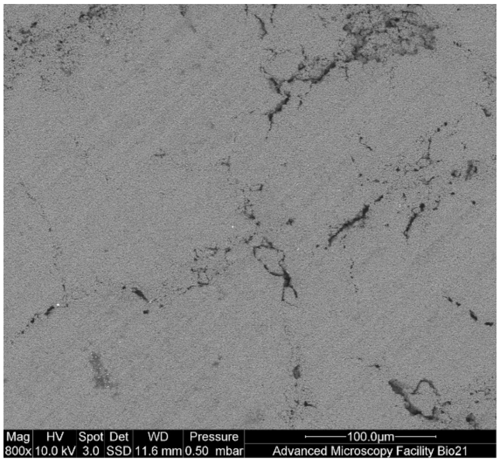	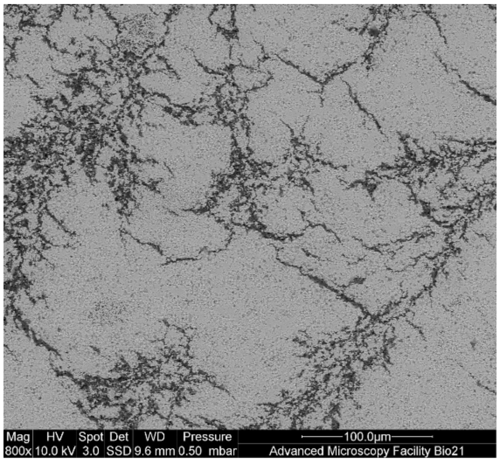
Corner 4000x	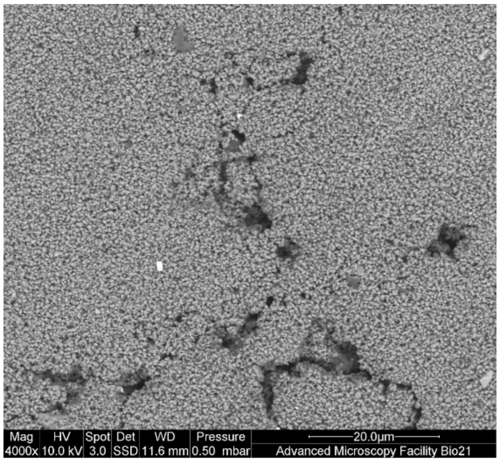	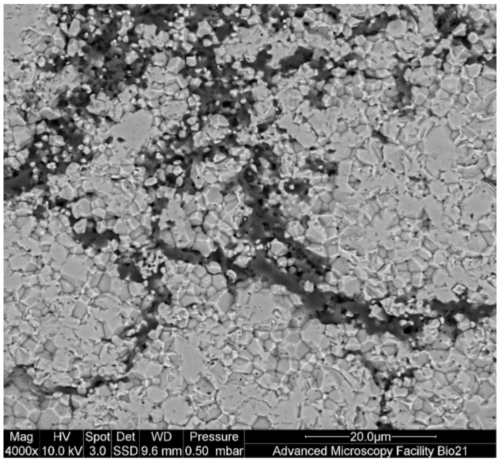

Sample #	167 & 168	Bisque Sample Image 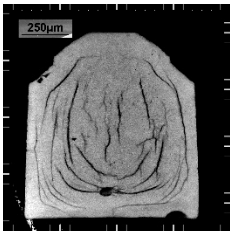	Sintered Sample Image 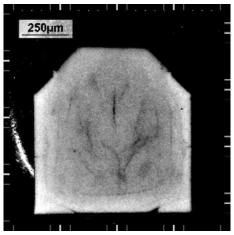
Freezer Temperature	-80°C	Mould Temperature	Pre-chilled

	Bisque	Sintered
Centre 100x	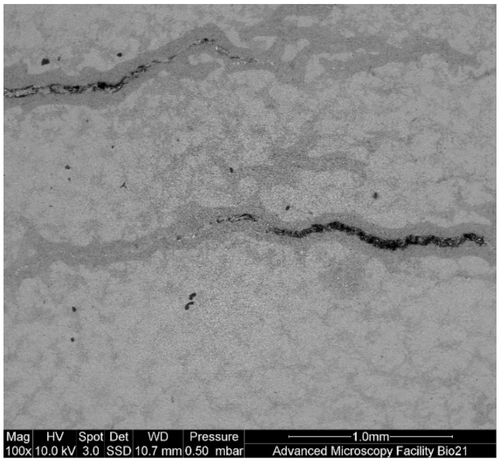	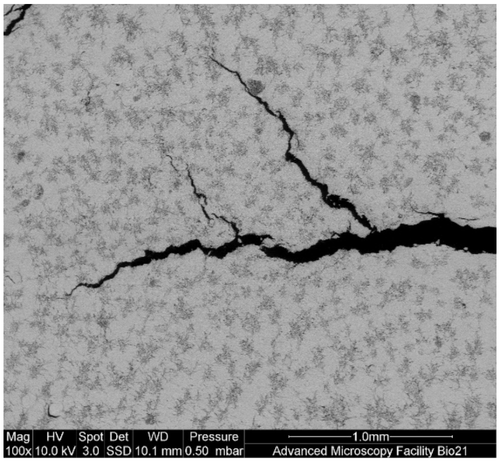
Centre 800x	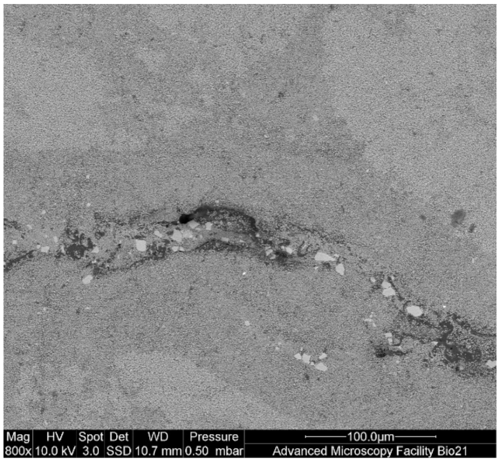	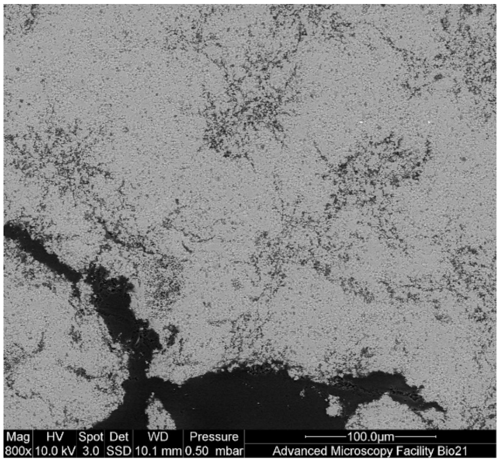

Centre 4000x	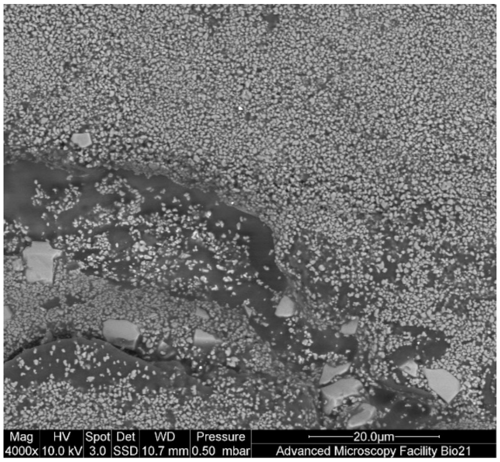	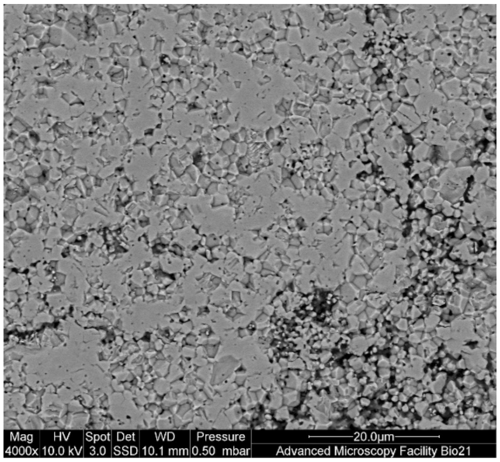
Bottom 100x	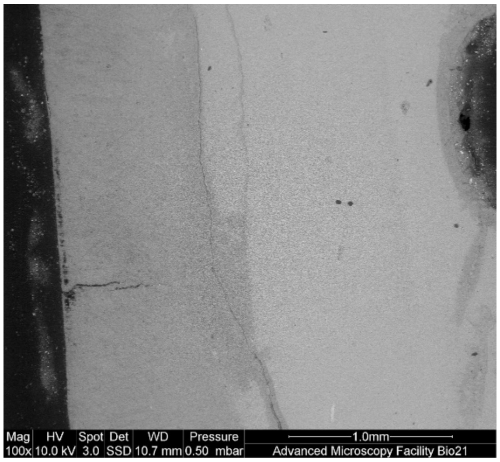	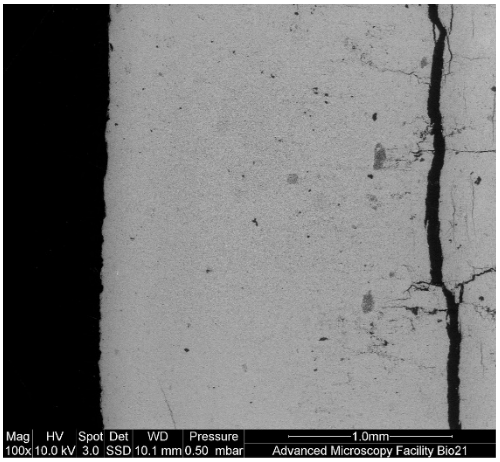
Bottom 800x	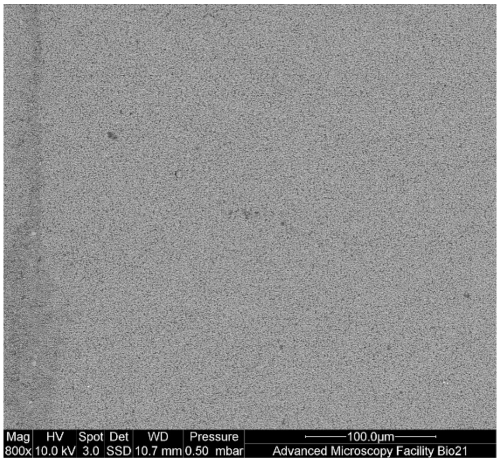	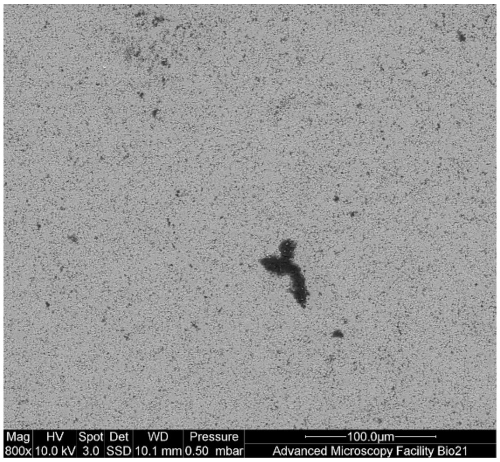

Bottom 4000x	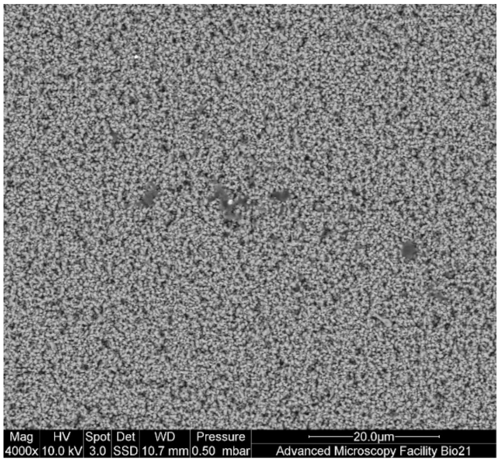	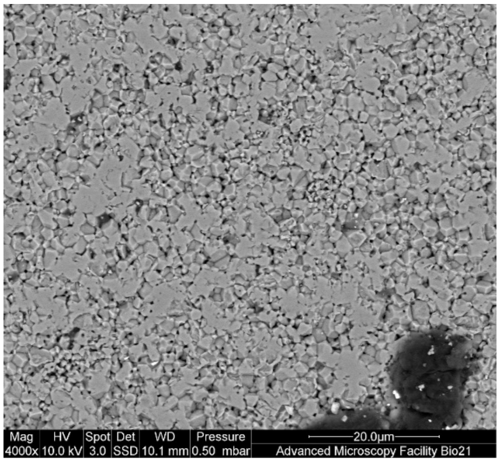
Corner 100x	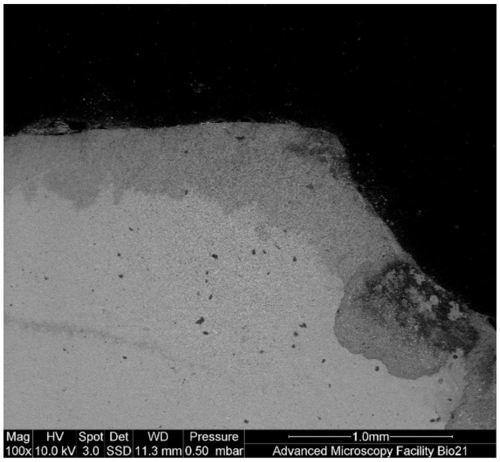	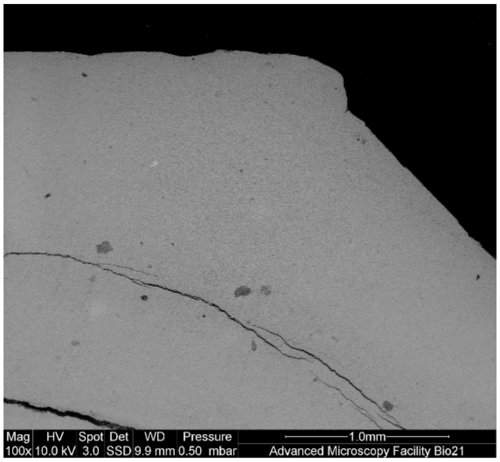
Corner 800x	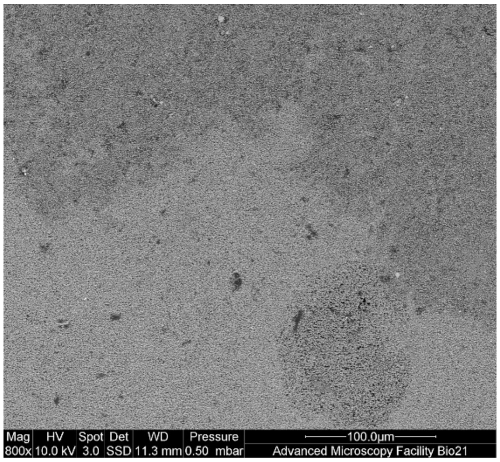	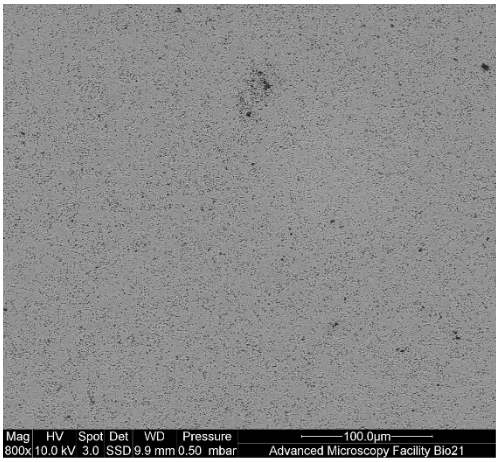

Corner 4000x	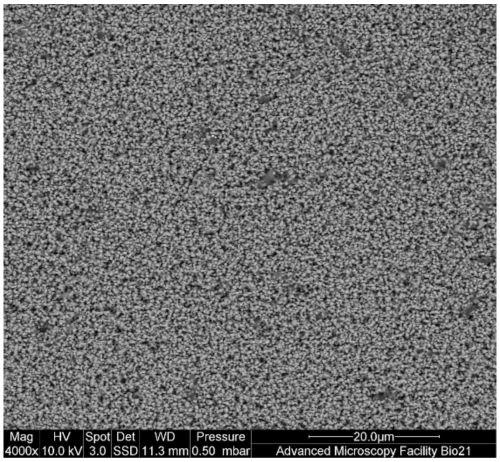	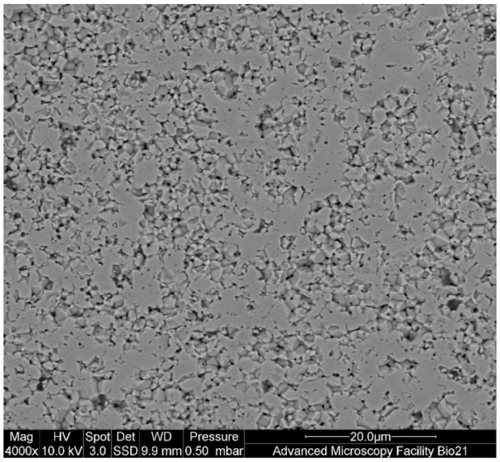

Sample #	167 & 168	Bisque Sample Image 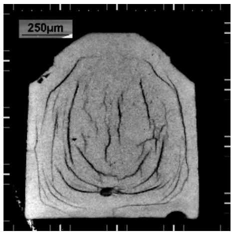	Sintered Sample Image 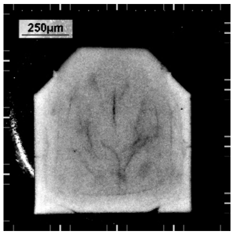
Freezer Temperature	-80°C	Mould Temperature	Pre-chilled
	Bisque	Sintered	
Centre 100x	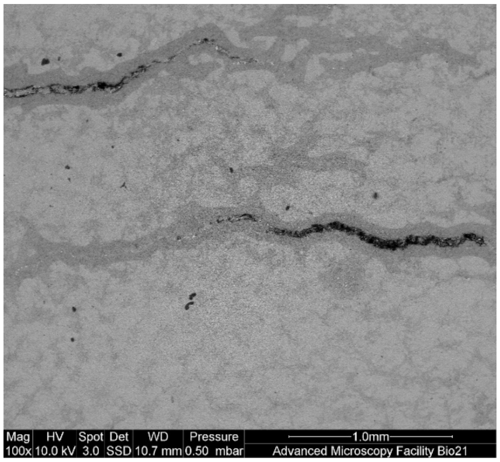	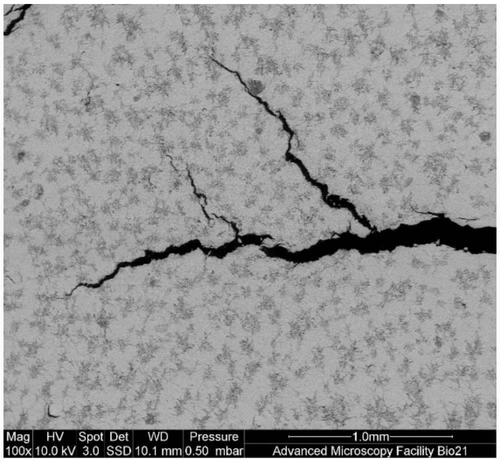	

Centre 800x	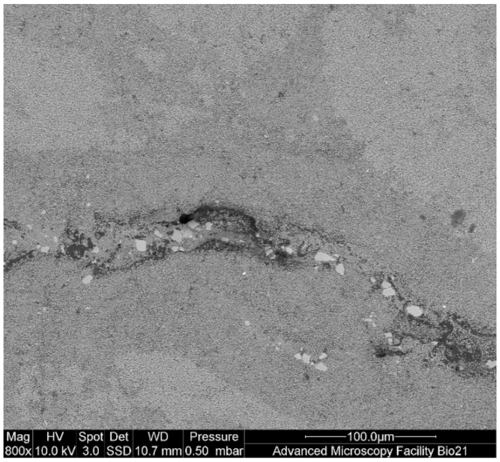	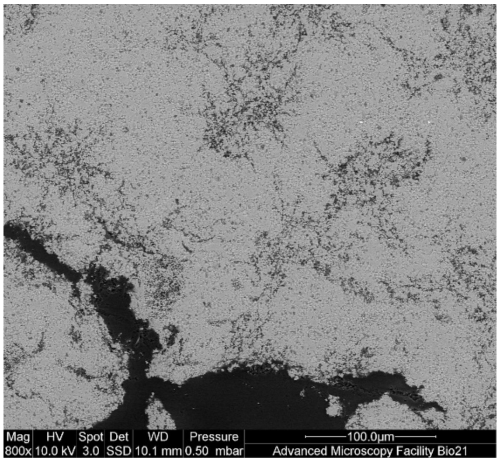
Centre 4000x	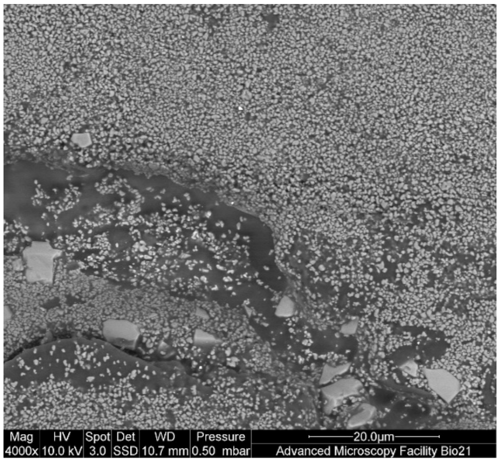	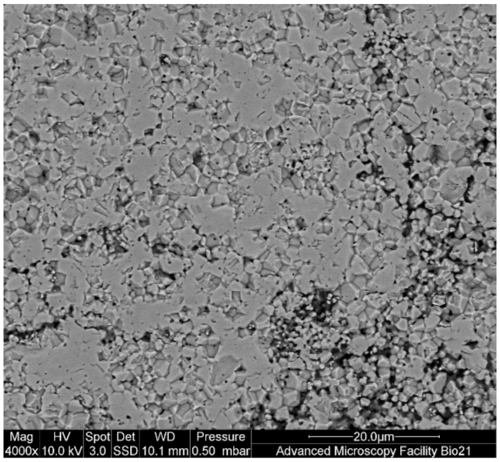
Bottom 100x	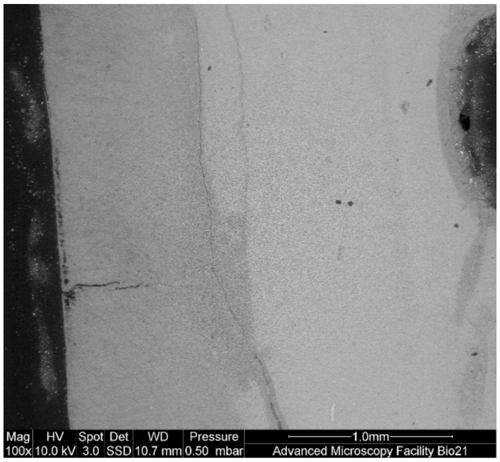	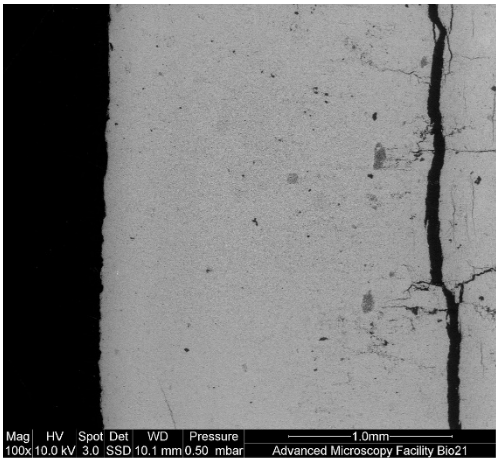

Bottom 800x	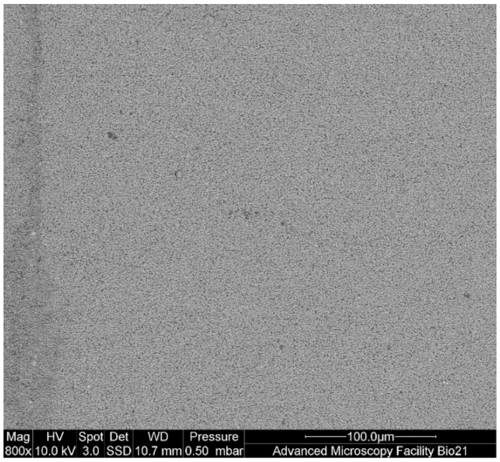	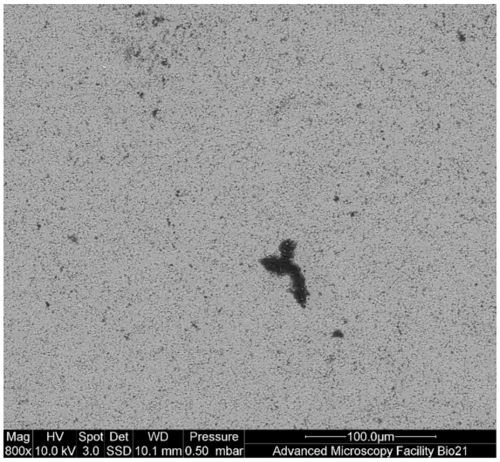
Bottom 4000x	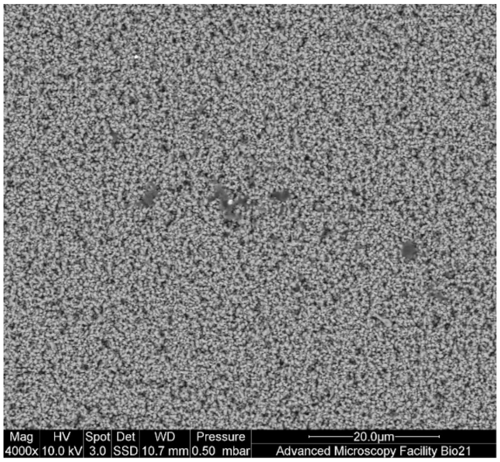	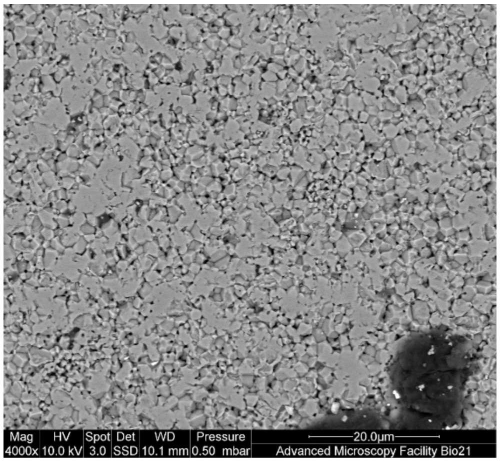
Corner 100x	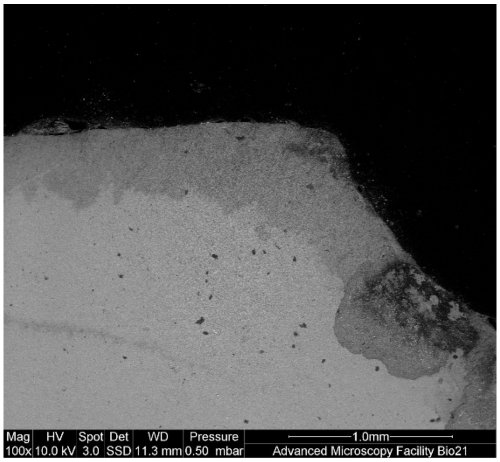	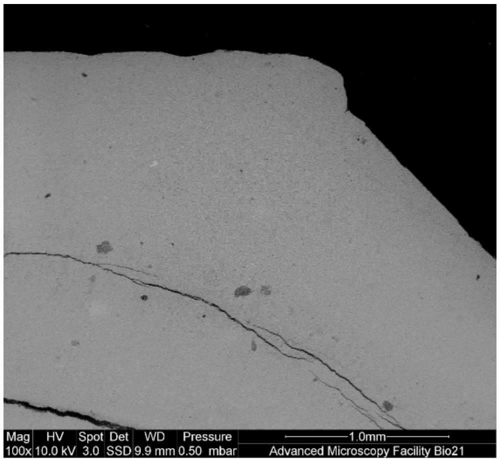

Corner 800x	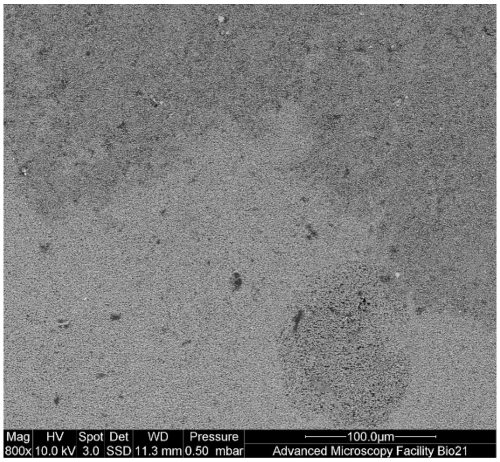	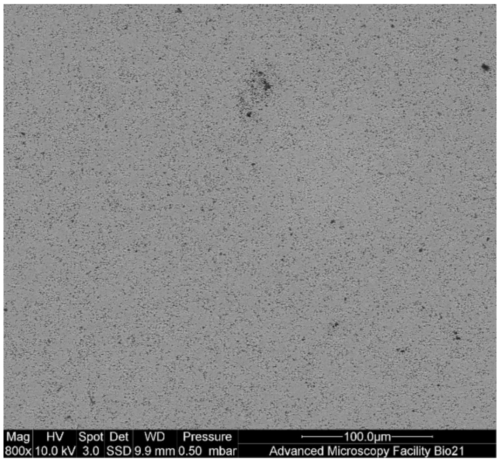
Corner 4000x